Leibniz-Institut
für Festkörper- und
Werkstoffforschung
Dresden

**TECHNISCHE
UNIVERSITÄT
DRESDEN**

Disentangling the Intrinsic Attributes and the Physical Properties in Cobalt-based Quaternary Heusler Compounds

Dissertation

zur Erlangung des akademischen Grades

Doctor rerum naturalium (Dr. rer. nat.)

Fakultät Mathematik und Naturwissenschaften

der Technischen Universität Dresden

vorgelegt von

Ahmad Omar

geboren am 20.01.1988; aus Indien

Dresden, September 2015

1. Gutachter: Prof. Dr. Bernd Büchner
2. Gutachter: Prof. Dr. Andreas Hütten

Tag der Einreichung: 4. September, 2015
Tag der Verteidigung: 25. February, 2016

"Nobody should assume that what I am saying is true. It is not given to us to know what is true in this sense. But everybody knows that I write this scientific treaty in an implicit unwritten understanding among the scientists that I can be absolutely believed to be what I believe."

- J. Bronowski

'Origins of Knowledge and Imagination'

Yale University Press, USA 1978

Contents

Introduction

Towards understanding the material-property correlation

Heusler compounds are classically ternary intermetallics (X_2YZ) with a wide range of interesting properties, which are closely related to the cubic structure of the material. In addition, several exotic physical phenomena have been predicted for different compositions in the family, but have not been experimentally realized. By and large, the lack of success in realization of various properties are due to the issues with intrinsic material attributes, which have been difficult to resolve as the relationship between them is not well understood.

Ever since the discovery of the first Heusler compound Cu_2MnAl, disentangling the material-property correlation in the Heusler compounds has been a fundamental point of research. The quest has increased manifold as new Heusler compounds with novel properties continue to be predicted and synthesized. One such property is half-metallic ferromagnetism, where in the electronic structure, there is a finite density of states at the Fermi level along one spin direction while a band-gap exists at the Fermi level along the other spin direction. Such a feature should lead to interesting physical properties such as a considerably large magnetoresistance, which is quite in demand in the field of spintronics. Cobalt-based Heusler compounds are one of the more promising candidates for half-metallicity. Unfortunately, most materials which have been predicted to be half-metallic ferromagnets have not been verified, even at low temperature, let alone a fully spin-polarized material at room temperature. Aside from exploring new materials, it is pertinent to understand why or why-not the existing systems work. Understanding the evolution and effect of various intrinsic attributes of a sample such as the structure, defects and possible chemical disorder, on the extrinsic properties is the main point which this work addresses.

The present work is based on quaternary Heusler compounds, where one of the elements is partially substituted with an additional element (For example, $X_2Y'_{1-x}Y''_xZ$ and so on). Although there have been various reports on quaternary substitutions, they gained prominence since late 1990s as the effect of substitution could be explored to possibly tune the electronic structure [1, 2] and physical properties [3, 4] and may as well lead to evolution of new properties [5, 6]. Therefore, quaternary compounds allow the possibility to tune the properties such as Curie temperature, band gap etc., as

desired. This is important towards understanding the fundamental physics of the system in general, and has a significance from the technological point of view.

In this work, a study on two different Co-based quaternary Heusler systems is presented, both of which have been predicted to be robust half-metallic ferromagnets [5–10] but so far have not been experimentally realized. Majority of the issues with experimental realization of novel properties, particularly with Heusler compounds, relates to thermodynamic instability of the compound itself as well as the stability and attainability of a fully ordered $L2_1$ structure. In each system, the aim was to tackle the interplay between an intrinsic attribute and its effects on the physical properties, in order to get further insight on the material-property correlation.

The first system that is studied is the $Co_2Cr_{1-x}Fe_xAl$ series of Heusler compounds. The system is fraught with inconsistencies in physical properties, with regards to the theory. There are hints of chemical inhomogeneity in the system, which was the starting point of our work. The underlying aim of the work has been to shed light on the relationship between the thermodynamic instabilities, which may exist at different temperature regimes, and the evolving properties. Furthermore, a better understanding of the phase transformations in the system has allowed us to develop a recipe to obtain a homogeneous phase-pure sample, and has led to a coherency between the theory and the observed physical properties. Thus, a new promising half-metallic ferromagnet in the $Co_2Cr_{1-x}Fe_xAl$ series is presented.

In the second part, the $Co_2FeAl_{1-x}Si_x$ system is presented, which unlike $Co_2Cr_{1-x}Fe_xAl$, does not suffer from the issue of chemical inhomogeneity. However, the observed physical properties are lacking in comparison to theory, as there is the issue of obtaining a highly ordered sample, and the order-disorder temperature regimes are also under debate. We have thus attempted to gain a better understanding of the ordering phenomena in $Co_2FeAl_{0.5}Si_{0.5}$, which has allowed us to achieve a significantly improved $L2_1$ order, in addition to an improved comprehension of the evolution of order during annealing and the subsequent cooling process.

We have thus made a considerable advancement towards greater evidence-based knowledge and a better understanding of the material-property correlation in $Co_2Cr_{1-x}Fe_xAl$ and $Co_2FeAl_{1-x}Si_x$ Heusler compounds.

Brief outline of present thesis

In Chapter 1, we have discussed the basics of structure and magnetism of Heusler compounds, and briefly commented on the structure-property relationship. In Chapter 2, the details of the sample preparation, specially the Floating Zone (FZ) technique, as well as the experimental techniques have been laid out. We have also discussed a couple of theoretical aspects with regards to the phase diagrams and sample preparation.

Chapter 3 deals with the $Co_2Cr_{1-x}Fe_xAl$ series. The chapter is divided into three sections. In

the first part, we have demonstrated the existence of a phase separation via low temperature transformation in the Co-Cr-Fe-Al system using FZ growth of selected compositions. In the second section, we discuss the extent of immiscibility in the phase diagram in order to better understand the phase dynamics. First, we explored the stability of the secondary phase along temperature observed in FZ-grown Co_2CrAl, through annealing experiments. Later, an alternate approach to optimize the composition of Co_2CrAl is employed and found to be successful in avoiding the transformation altogether. In the last section of the chapter, the concept of off-stoichiometry which was found to be successful, was applied to the case of $Co_2Cr_{0.6}Fe_{0.4}Al$. The FZ-growth of off-stoichiometric $Co_2Cr_{0.4}Fe_{0.4}Al_{1.2}$ was successful and homogeneous phase-pure material is obtained. Theoretical calculations and the various physical property measurements are shown to match well with theory, and thus, we have a promising new half-metallic ferromagnet in the $Co_2Cr_{1-x}Fe_xAl$ Heusler series.

In Chapter 4, we focussed on the ordering phenomena in $Co_2FeAl_{0.5}Si_{0.5}$, a stable, quaternary Heusler compound. Neutron diffraction on as-cast and annealed samples at toom temperature along with detailed high temperature *in situ* neutron powder diffraction experiment is presented. It was found that the order-disorder transition is spread over a large temperature range, in contrast to that reported in the literature [11, 12]. Based on the diffraction, the presence of antiphase domains and their evolution under different processing conditions is discussed, along with the effect on magnetic properties. Details of corresponding laboratory annealing based on the *in situ* experiment, are also presented. A significantly improved ordering as well as a reduction in defects is obtained on slow cooling of the sample post-annealing. Therefore, slow cooling after annealing as an optimized annealing procedure is discussed, with the possibility of extending the concept to other systems.

Finally, Chapter 5 presents a short summary and outlook.

Chapter 1

Background: Structure and Magnetism

1.1 Heusler compounds: A brief history

Long ago, in a land not so far away, it all began with an idea. And, as is always a necessity, a quantum of luck. At the dawn of the 20th century, Friedrich Heusler, a German mining engineer, was studying manganese-based intermetallic compounds. He was interested in ferromagnetic materials and was exploring new compositions. Till then, it was understood that at least one of the three magnetic elements, namely iron, nickel and cobalt, need to be present as a constituent to obtain a ferromagnetic material at room temperature. To his surprise, an alloy of copper, manganese and aluminium turned out to be ferromagnetic at room temperature, and the reports of this finding were published in 1903 [13, 14]. This scientific discovery, albeit iconic, garnered limited attention initially, as not much was understood behind the origin of the evolving ferromagnetism. Also, different samples showed different magnetic properties, which were somehow a function of the composition and heat treatment [15]. Over the next couple of decades, Heusler and others tried to explore the Cu-Mn-Al phase-space in order to optimize the composition with regards to magnetic properties [16]. Quite varied results were initially obtained, as depending on the composition and (or) subsequent heat treatment, the samples contained up to three different phases and showed varied magnetic behaviour [17–19].

In the beginning, it was understood that the ferromagnetism in Cu-Mn-Al alloy is due to a solid solution of $(CuMn)_3Al$, where the copper and manganese mole fraction could be varied to a large extent, while still showing measurable magnetization. Incidentally, strong ferromagnetism was observed in a narrow composition regime. In 1928-29, the ferromagnetic alloy was identified as the Cu_2MnAl composition with a body-centred cubic structure [20, 21]. Single crystals of Cu_2MnAl, and hence, the first Heusler single crystals, were grown and studied by Potter [22], who also described the atomic positions of the individual atoms. Once the structure was confirmed, further studies were done on Cu_2MnAl, e.g., under different annealing conditions [23], magnetoresistance and

magnetocaloric effects [24], resistivity, thermoelectric power and specific heat [25], ferromagnetic resonance absorption [26], and even as a catalyst [27].

During the early years, due to the unique magnetic properties, Cu_2MnAl was called the Heusler alloy. Later on, any compound with a corresponding structure as Cu_2MnAl, and a resulting X_2YZ composition, started being referred to as a Heusler compound, since the unique properties were found to be closely related to the specific arrangement of atoms in the crystallographic structure.

In the next few decades, different elemental combinations in the specific ratio of 2:1:1 were explored, but the interest in the community was limited. Some compositions were reported to contain multiple phases, whereas some were ferromagnetic and some were not [28–31]. Even after more than half a century, there was much to be understood about the structure and magnetism in Heusler compounds.

Research in the field of Heusler compounds picked up in the 1970s with the synthesis of certain elemental combinations, e.g., cobalt-based Heusler compounds, as they showed varied properties such as a much higher magnetization [32, 33] and antiferromagnetism [34]. Also, in the later half of the 20th century, derivative ternary compounds were discovered, which essentially had the same lattice as any Heusler compound X_2YZ but the lattice site of element X was half-filled. This resulted in an atomic proportion of 1:1:1 (XYZ), and the structure was defined with a separate space group. These XYZ compositions later became popular as 'half-Heusler' compounds and came under the umbrella of Heusler compounds. These 'half-Heusler' compounds also came along with their own interesting properties, e.g., antiferromagnetism [35]. During the same time, theory of magnetic moments and their relation to the structure was developed for Heusler compounds such as the Slater-Pauling rule, which is discussed later in this chapter. A greater understanding of the magnetism led to the prediction of new Heusler compounds with novel properties. All this development ushered in a pursuit of exotic physical phenomena and a thrust towards understanding the underlying principle of the evolving physics and its relation to the structure.

In the late 20th century, computational capabilities advanced considerably, and new techniques of theoretical calculations emerged. The research interest in Heusler compounds increased more or less exponentially, as varied elemental combinations in the specific atomic proportions and crystal structure could be explored on the basis of predictive calculations. This also paved way for better understanding of the nature of these materials as theoretical models could be developed and explored. Since the advent of the 21st century, as band structure calculations have became widespread, many more novel and exotic physical phenomena such as topological insulators, compensated ferrimagnetism and skyrmions, have been predicted in the class of Heusler compounds recently [36]. So far, more than a 1000 Heusler compounds have been either experimentally reported or predicted. A review by Graf et al. [37] nicely summarizes the plethora of properties and underlying structure-types that have been found or predicted in the huge family of Heusler compounds.

We shall move on to the background and first explain the structure and related aspects of Heusler compounds which play the most important role towards their interesting properties.

1.2 Structure and disorder

Heusler compounds have the X_2YZ stoichiometry, where the X and Y atoms are generally transition metals and Z is a main group element, commonly a metalloid. The structure is cubic, with space group $Fm\bar{3}m$ (225) and Pearson symbol *cF16*, in the fully ordered state. X atoms occupy $8c$ Wyckoff positions, whereas Y and Z occupy $4b$ and $4a$ Wyckoff positions, respectively. The structure can also be understood as four inter-penetrating face-centered cubic (fcc) lattices, two of X and one each of Y and Z atoms. This leads to the structure being understood as a super-cell of 8 body centred unit cells, with corners occupied by alternating Y and Z atoms, and X at the body centre of each of the unit cells. The structure is illustrated in Figure 1.1. Cu_2MnAl is the prototype system.

X₂YZ
cF16, *Fm̄3m* (225)

Z sublattice
fcc (4*a*)

Y sublattice (4*b*)
octahedral site

X sublattice (8*c*)
tetrahedral site
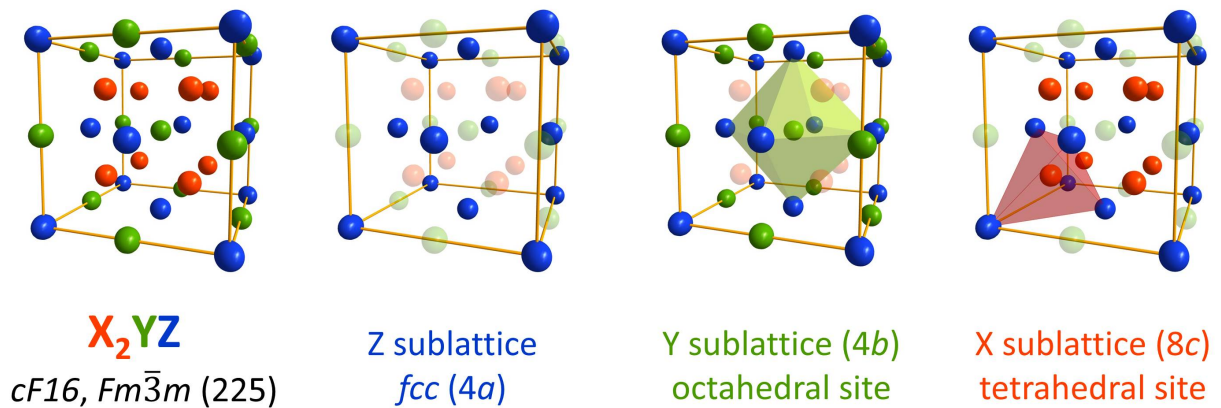
Figure 1.1: Crystal structure of Heusler compound X_2YZ showing the sublattices as well as the local environments at different Wyckoff positions.

For a simpler understanding, the structure can also be defined as a fcc unit cell of Z atoms with Y atoms occupying all the octahedral positions and X atoms at the tetrahedral positions. If one were to calculate effective atoms in the unit cell, there are 4 Z atoms (fcc), 4 Y atoms (1/4*12 edge centres + 1 body centre) and 8 X atoms (tetrahedral positions), which is illustrated in Figure 1.1. This makes an effective unit cell stoichiometry of $X_8Y_4Z_4$, simplified as X_2YZ.

So far, we have only discussed the ideally ordered structure, where each atom is at its Wyckoff position. This is denoted by $L2_1$ as per the *Strukturbericht* designation. The associated space group and Pearson symbol are $Fm\bar{3}m$ and *cF16* respectively, as mentioned earlier. However, it is possible, and in reality often found, that some atoms exchange their atomic positions. Such a structural defect is known as anti-site disorder.

There are different types of anti-site disorder depending on the atomic positions being exchanged. One possible scenario is that Y and Z atoms exchange positions. For ease of understanding, complete disorder shall be assumed, i.e., all Y and Z atoms are completely mixed and there is an equal probability for Y and Z to be found at both $4a$ and $4b$ Wyckoff positions. In other words, either of

$4b$ and $4a$ positions are occupied by 50% Y and 50% Z atoms, distributed randomly in the structure. The resulting structure is denoted as *B2* in the *Strukturbericht* designation, and is illustrated in Figure 1.2. Since the Y and Z positions become equivalent, the effective composition is now $X_2Y'_2$, or rather XY', simply. The unit cell can also be more uniquely defined by one of the sub-cells of the $L2_1$ structure and the effective lattice constant is halved. The resulting space group is $Pm\bar{3}m$ (221) with $cP2$ as the Pearson symbol. The prototype for this structure is CsCl. *B2*-type disorder is one of the more common disorders found in Heusler compounds [38, Chapter 4].
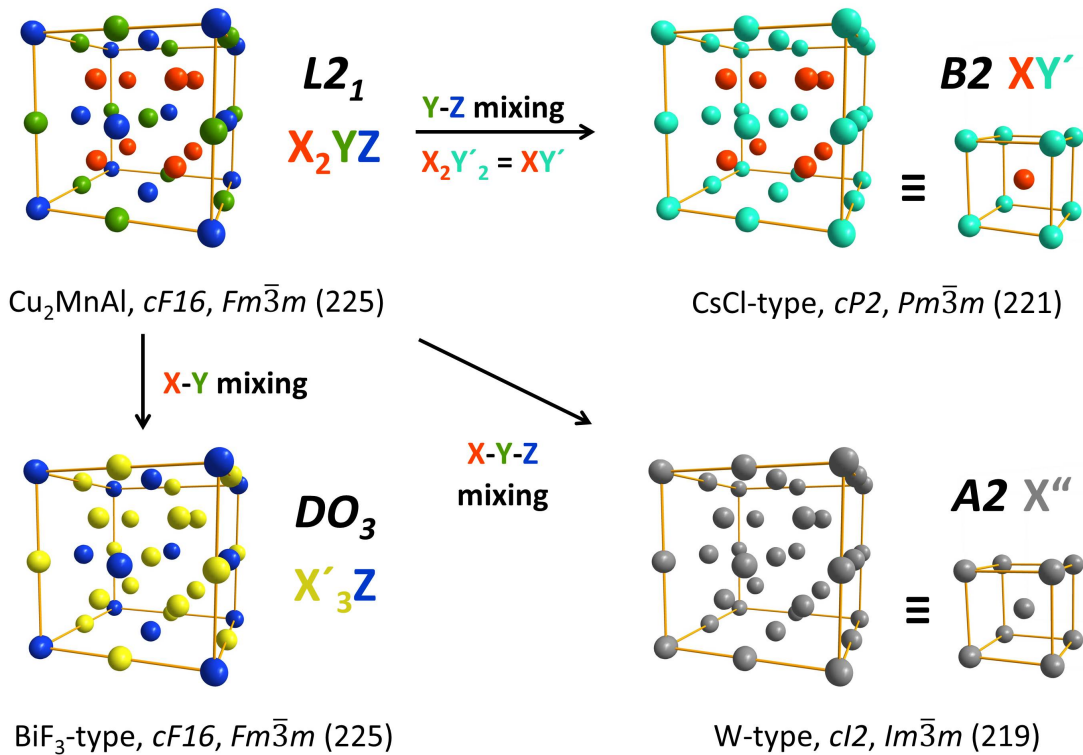
Figure 1.2: Heusler compound X_2YZ with the fully ordered $L2_1$ structure as well as the *B2* (Y-Z mixing), DO_3 (X-Y mixing) and *A2* (X-Y-Z mixing) type disordered structures. The equivalent unit cell as well as the space group and the Pearson symbol are also mentioned for each.

Another possible structure due to an alternate disorder in the Heusler compounds is called DO_3 as per the *Strukturbericht* designation. In this case, the X and Y sites are mixed. Both X and Y atoms are randomly distributed equally on $8c$ and $4b$ positions, which become equivalent. The space group for such a scenario is $Fm\bar{3}m$ (225), with BiF_3 as the prototype. As can be seen in Figure 1.2, the effective lattice constant remains the same.

It is also possible that all the three atoms X, Y and Z mix completely and all positions become equivalent, leading to a basic body-centered cubic (bcc) W structure. This is known as the *A2*

disorder. The space group is $Im\bar{3}m$ (229) with Pearson symbol as *cI2*. As in the case of *B2* disorder, the effective lattice parameter is also half of the $L2_1$ ($Fm\bar{3}m$) structure. The structure is shown is Figure 1.2. A few other exotic types of disorder have also been reported in literature, which are not so common. The reader is guided to the work of Graf et al. [39] for an overview of the same.

Order-disorder transitions

An important aspect arises due to the existence of possible disorders. Since the various disorders, as introduced above, are in general entropy-driven, a specific disorder may become stable at elevated temperatures. It is also possible that a disordered structure may be thermodynamically more stable than the ordered structure at room temperature itself. For example, Miura et al. calculated that a partially disordered structure is more stable than the $L2_1$ ordered structure in the ground state for a series of cobalt-based Heusler compounds [40].

The stability of different type of disorders leads to distributed regimes in temperature, along with associated order-disorder transitions [41]. Annealing experiments for improving order have to be designed keeping the specific ordering regimes in mind, for both bulk as well thin films. Hence, an optimized annealing profile is needed to achieve the highest possible ordering in the shortest time. Annealing temperature and time also play a more important role in the case of thin films, as one has to keep in mind the kinetics of interdiffusion at the various interfaces (For example, [42]). Therefore, in order to obtain a highly ordered sample, it is important to know the temperatures associated with the corresponding order-disorder transitions of the respective material.

As mentioned before, the above scenarios are discussed assuming that complete order or disorder is present. However, in practical scenarios, a fraction of the lattice is disordered while the rest of the lattice is ordered. Many a times, a mixture of multiple disorders may be present. In order to better understand the origin of disorder, we shall now present a brief discussion on what drives disorder.

1.2.1 What drives defects and disorder?

There are various types of defects present in a material, such as point defects, dislocations, stacking faults etc. [43]. Defects in any material are mainly determined by entropy [44], and there is an energy barrier associated with the creation of any defect. In any condition, say in a solid, there is a small fraction of particles with higher energy, which manifests as thermal vibrations. The higher energy of these particles may be sufficient to cross the energy barrier for the formation of a defect. Due to this, there is an equilibrium defect concentration at a given temperature for any material, ideally going to zero at 0 K. Therefore, we must not forget that there is an equilibrium defect concentration associated with room temperature as well. This does not mean that the same amount of defects are always present in material at room temperature, as kinetics come into play, and thus, the amount of defects also depends on the processing route.

There are various intrinsic factors which may lead to defects and disorder in a material, such as electronegativity, atomic radii, valence etc. of the constituent elements. Some elements prefer to occupy certain sites and local environments based on their electronegativity as well as valency, leading to disorder. In the case of Heusler compounds, strong site preferences lead to disorder and the structure may have to be alternatively defined [39]. Site preference has been well studied in perovskites; e.g., a recent study on a double perovskite found that both Al and Fe prefer to occupy the octahedral sites where as Ga prefers the tetrahedral site [45]. Such a scenario may also be possible in Heusler compounds. Apart from electronegativity, the relative size of the species involved can also be a possible reason for disorder. If the size of an element is sufficiently small with respect to the other constituents, the energy required to move to an interstitial site may be fulfilled by entropy itself. Furthermore, such site and vacancy defects may be more pronounced depending on the type of bonding. Ionic, metallic and covalent bonds have quite different bond strengths depending on the species involved, and may suffer from defect generation under sufficient conditions. Thus, the attributes of species forming the material play an important role towards the possibilities of defects and disorder.

Apart from the fact that considerable defects are generated in a material during synthesis, it is likely that additional defects are induced during further processing. For an ideal cooling at equilibrium, a material should be cooled infinitely slowly to room temperature, which is unrealistic. The finite cooling rate involved in real-world scenarios leads to defects being created in the material because of thermal shock due to contraction/expansion during the temperature change. The higher the quenching rate, the higher is the likelihood of defect generation in the material. In addition to that, other processes such as pulverization, cutting and polishing during sample preparation for characterization also induce defects and strains through stress. Defects are also introduced in a material upon irradiation with high energy electrons, neutrons or ions, e.g., during sample preparation for transmission electron microscopy using focused ion beam (FIB) [46]. Therefore, it is imperative that the possibilities of defect generation and possible material degradation must be taken into consideration during any processing, preparation and experimentation.

As is discussed later in the chapter, the presence of specific type of disorder may or may not affect the physical properties. This necessitates the identification and accurate quantification of the various disorders present in a material. This aspect, with regards to Heusler compounds is discussed next.

1.2.2 Characterizing disorder: Methods and challenges

The straightforward effect of atomic disorder can be easily seen in X-ray diffraction. Figure 1.3 shows the simulated X-ray diffraction patterns of Co_2FeSi for various conditions of order and disorder using PowderCell software [47], for Mo K_α radiation. The ordered $L2_1$ structure has superlattice

reflections (111) and (200), which are the hallmark of an fcc system. In the complete *B2* disorder, the structure reduces to an ordered bcc. Due to this, (111) reflection becomes extinct, and is not seen. On the other hand, the *DO₃*-type disorder still has a fcc structure. Both (111) and (200) are observed albeit the relative intensities are very different. When all the positions are mixed, i.e., the *A2* disorder, no superlattice reflections are observed and only the (220) reflection for the primitive bcc is seen.
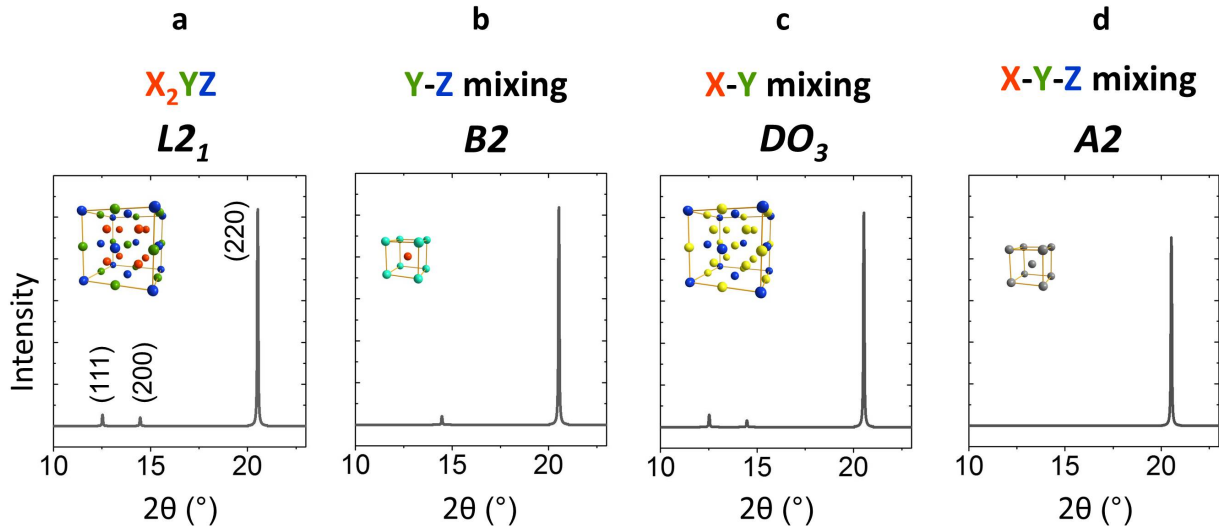
Figure 1.3: Simulated X-ray diffraction patterns with Mo K_α for Co₂FeSi for different conditions (a) fully ordered *L2*₁ (b) *B2* disorder (c) *DO₃* disorder (d) *A2* disorder.

However, there are various challenges associated with analysis of disorder using X-ray diffraction. Firstly, the relative intensities of the superlattice reflections with respect to the main (220) reflection are in general quite small. The simulated relative intensities (using PowderCell software [47] for Mo K_α radiation) for Co₂FeSi under different conditions of disorder are summarized in Table 1.1. As can be seen, the (111) and (200) reflections are below 6 %, in an ideal case.

Another problem in practical situations is that a sample may contain more than one type of disorder, with varying ratio, depending on the sample preparation and post-processing. Since the defects are entropy-driven, statistically, there is a finite probability of finding each type of disorder. In many cases, selected disorder scenarios may be ignored as they may be highly unlikely energetically, and the data may be analysed accordingly. One may still analyse the X-ray diffraction (XRD) data using Rietveld refinement [48], but the information obtained from such an analysis with regards to multiple disorders, offers a more qualitative look, rather than a quantitative one.

The problem is further compounded in the laboratory setups, as there is significant background and noise associated. Fluorescence of different elements with different X-ray sources poses an additional challenge for XRD. Some elements, e.g., manganese, gives higher fluorescence with both Co and Cu

Table 1.1: Relative intensities for the superlattice reflections (111) and (200), with respect to the main bcc reflection at (220) for Co_2FeSi calculated for diffraction with Mo K_α.

Structure/Disorder	(111)	(200)	(220)
$L2_1$ fully ordered	5.1	3.9	100
$B2$ disorder	0	3.9	100
DO_3 disorder	5.7	3.0	100
$A2$ disorder	0	0	100

K_α sources, as compared to Mo K_α source. What that means is that the data is significantly more noisy for Co and Cu sources measured for the same amount of time.

An additional problem may also arise for compounds containing specific elements. Depending on X-ray source, the scattering coefficients of the constituent elements may lead to extinction of superlattice reflections. As an example, atomic scattering factors for Co, Fe, Mn and Cr with Cu K_α, which is one of most commonly used laboratory X-ray sources, are almost the same. Due to this, the analysis of any disorder between these atoms may be quite difficult. Even if the superlattice reflections are not extinct, the intensity may be strongly affected. For example, the intensity of the (111) reflection for Co_2MnSi is 0.8 % of the main (220) reflection in complete DO_3 disorder (calculated using PowderCell software [47] for Mo K_α radiation). In addition to that, higher order reflections follow an inverse θ-dependence and their intensities are much lower. Therefore, in order to avoid the issues of fluorescence and similar scattering factors, a judicious choice of X-ray source is necessary.

Notwithstanding the issue of low intensities of superlattice reflections and noise, a quantification procedure using XRD for multiple disorders in samples has been given by Takamura et al. [49]. They have used multiple X-rays sources to quantify the fraction of $B2$, DO_3 and $A2$ disorder in Co_2FeSi thin films. Nevertheless, it is tedious and difficult to do for each and every sample, as well as requires access to multiple X-ray sources which might not always be possible. In a recent report, Li et al. [50] have developed a generalized form of the site-specific formula unit (SSFU) composition model for the amount of disorder in a material, but it pertains specifically to non-stoichiometric samples, where a deliberate disorder is induced.

Apart from the issues mentioned already, size and strain-effects intrinsic to the sample are known to affect peak intensities [51]. It thus becomes difficult to analyse the disorder, specially in real-world scenarios, where multiple disorders are present. Anomalous X-ray diffraction at synchrotron has been used to study atomic disorder in thin films in a few reports [52, 53]. Synchrotron XRD does give good data and avoids many issues associated with laboratory measurements, but does not have

ease of access and time. Thus, quantitative analysis of multiple disorders with synchrotron XRD is not possible on a regular, day-to-day basis.

Another possibility to study the disorder is through neutron diffraction. Neutrons offer certain advantages over X-rays. The intensities of superlattice reflections in neutron diffraction may be considerably higher for certain compositions, as the scattering factors are quite different than X-rays, which would allow us to better quantify the disorder. However, neutron diffraction also has limitations similar to XRD, e.g., analysis of systems containing elements with similar or low scattering coefficients. Furthermore, neutron diffraction requires a much longer time as compared to synchrotrons since the flux is considerably lower, and thus, also needs a much larger amount of sample. Nevertheless, neutron diffraction has been used since the early days to characterize the disorder in Heusler compounds [54–56]. Neutron diffraction in conjunction with extended X-ray-absorption fine structure (EXAFS) has also been used to study the atomic disorder in Co_2MnSi [57].

Apart from diffraction studies, various other techniques exist which can probe the local chemical environments such as nuclear magnetic resonance (NMR) and Mössbauer spectroscopy. These techniques, specially NMR, provide significantly reliable quantitative information on the presence and extent of various disorder. Zero-field NMR has garnered much attention recently as a definitive tool to quantify disorder in Co-based Heusler compounds [58–70]. Although, both NMR and Mössbauer spectroscopy are relatively time consuming techniques and need specialized equipment and expertise, they are available on a rather daily basis to some extent.

The details of order-disorder transitions, which were discussed earlier, are quite important with regards to processing as well as in order to obtain a specific ordering in a sample through annealing. In literature, quite a bit of work on order-disorder transitions in binary alloys has been done through the analysis of order in samples quenched after annealing at different temperatures (For example, [71–74]), using various techniques discussed above. However, depending on the system, it might not be possible to avoid ordering reactions during quenching [71, 75], or the quenching rate might not be fast enough to avoid any low temperature transformations. Hence, in addition to characterizing disorder at room temperature, it is also important to find out the order-disorder transitions at higher temperatures, *in situ*. Ideally, one would perform NMR or Mössbauer spectroscopy, but it is highly complicated to do these measurements at high temperatures, as the signals are reduced. In principle, high temperature diffraction experiments can be done. Although XRD has been used to study the order-disorder transition in Heusler compounds [41], the challenges and limitations of XRD or even neutron diffraction with regards to characterizing disorder still remain.

In literature, calorimetric techniques such as differential scanning calorimetry (DSC) have been extensively used to study the order-disorder transition [76–79]. Calorimetric measurements have also been used to study the different ordering phenomena as well as magnetic transitions in Heusler compounds [11, 12, 80–84]. However, one must be careful with calorimetric measurements as it

is a rather indirect technique. Furthermore, being a non-equilibrium technique, the heating and cooling rate may affect the signal strongly, e.g., a higher-order transition may get smeared out, if the heating/cooling rate is too fast. A well-calibrated equipment with high sensitivity, along with an understanding of the kinetics of the various changes that may involved, are mandatory for calorimetric experiments as it may lead to anomalous data otherwise.

There are various methods to characterize disorder in Heusler compounds, and as is always the case, none being perfect. A combination of different techniques is a must, in order to best characterize and understand properties of a homogeneous sample in the light of its order. We shall now discuss the physics of Heusler compounds which makes them so interesting, and have a look at some relevant physical properties and magnetism.
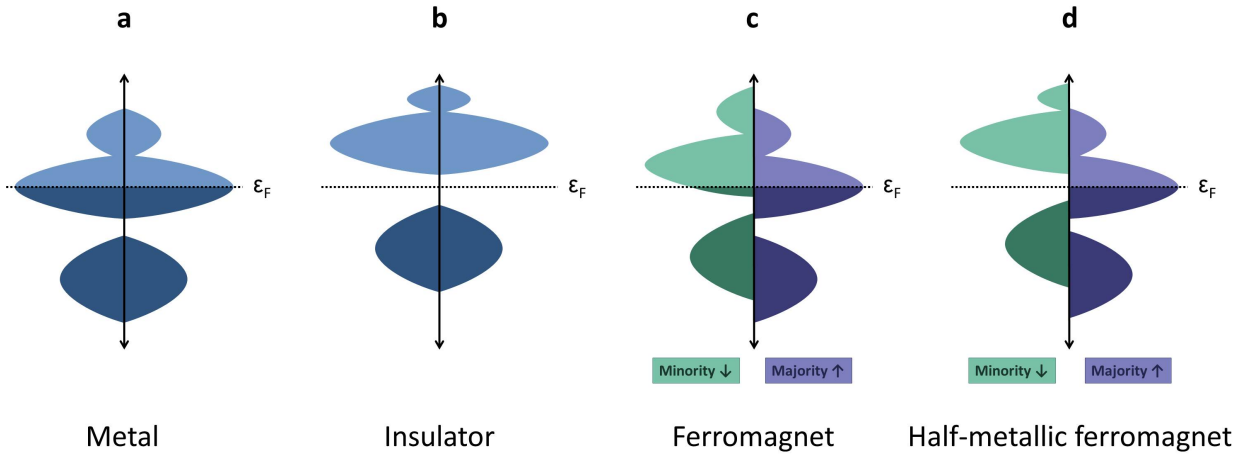
1.3 Magnetism of Heusler compounds

Historically, as was recounted earlier, the idea of Heusler compounds began with Cu_2MnAl, with its unprecedented magnetic properties, which in turn were closely related to the structure. Since then, a variety of properties have been discovered in the class of Heusler compound, all of which arise out of the same cubic structure. The interaction among the atomic species plays a crucial role in the magnetism of Heusler compounds, and depending on the constituent elements, various magnetic phenomena can be observed such as ferromagnetism, antiferromagnetism, ferrimagnetism etc.

The inherent magnetism of a material can be understood from its electronic structure. For the uninitiated, electronic band structure pertains to the range of allowed and not-allowed energies of an electron that it may have within a large periodic lattice. Presently, electronic structure can be calculated using various methods such density-functional theory, *ab initio* calculations etc. although under various constraints in addition to the assumptions of the band structure theory. For example, they give the ground state at 0 K, where one can neglect various interactions and effects. Nevertheless, it does give us strong hints towards many physical properties and helps us to understand the underlying physics of a given material. We shall now discuss a distinctive aspect of the electronic structure in some materials, and its importance for properties, with respect to Heusler compounds.

1.3.1 Half-metallic ferromagnetism

Some ferromagnetic materials have a unique electronic structure, where at the Fermi edge, there is a finite density of states (DOS) along one spin direction and a band gap in the other. Such a property is called half-metallic ferromagnetism. In Figure 1.4, the density of states for a metal, insulator, ferromagnet and a half-metallic ferromagnet are shown.

Figure 1.4: Spin-resolved density of states for (a) metal (b) insulator (c) ferromagnet (d) half-metallic ferromagnet.

The concept of half-metallic ferromagnets was first given in 1983 by de Groot et al. [85] for $C1_b$-type half-Heusler compounds and a similar feature was also calculated for $L2_1$-type Co_2MnAl by Kübler et al. [86] in the same year. Since then, such a feature has been predicted in many other materials, from oxides to even metal-filled carbon nanotubes [87], although almost all of them have not been experimentally verified so far. Different types of half-metallic ferromagnets have been classified and discussed in detail in a comprehensive review by Katsnelson et al. [88] and the reader is referred to that for further reading (for classification, also see Coey et al. [89]).

1.3.1.1 Spin polarization and its measurement

Normally, for a non-ferromagnetic material, the spin states ($\uparrow$ and $\downarrow$) are degenerate. In a ferromagnet, the situation is no longer degenerate and the density of states (DOS) at the Fermi level is higher along one spin direction than the other, yielding minority and majority states. The spin polarization (P) is then defined as [90]:

$$P = (n_\uparrow \epsilon_F - n_\downarrow \epsilon_F)/(n_\uparrow \epsilon_F + n_\downarrow \epsilon_F) \tag{1.1}$$

where $n_\uparrow \epsilon_F$ or $n_\downarrow \epsilon_F$ are the density of states along the respective directions at the Fermi energy. The $\uparrow$ and $\downarrow$ indicate the majority and minority spin directions, respectively, purely as a convention. In the case of a half-metallic ferromagnet, either of $n_\uparrow \epsilon_F$ or $n_\downarrow \epsilon_F$ is zero, which results in P being 100 %, and is fully spin polarized. With regards to experiments, the term *spin polarization* is not unique, and depends on how it is measured [89].

In order to confirm the half-metallic ferromagnetism, it is necessary to measure the spin polarization of a material. As of now, there is no technique which gives an absolute indication of

the half-metallicity. There are various experiments from which it is deduced, the most reliable so far being spin-resolved positron annihilation [91], which gives Fermi surfaces along different spin directions. Furthermore, in most systems, the expected 100 % spin-polarization of charge carriers is only predicted near 0 K as well as assuming no spin-orbit interactions [88]. NiMnSb is the only Heusler compound so far confirmed to be half-metallic, that too at low temperatures, as no Fermi surface was observed along one spin direction by Hanssen and Mijnarends [92]. We shall briefly mention the various techniques as well as the main drawback(s) of each.

One of the most common and simple way to deduce the spin polarization is from magnetoresistance of a point contact or a magnetic tunnel junction. It is calculated from the Jullière's model [93], where the tunnel magnetoresistance ($TMR = \Delta R/R$) of a multilayer stack is a function of spin polarization of two electrodes, P_1 and P_2.

$$TMR = 2P_1P_2/(1 + P_1P_2) \tag{1.2}$$

The spin polarization can be easily calculated if the polarization of one of the electrodes in known or if they are identical ($P = P'$) [89]. Unfortunately, the interfaces between the layers and their quality may have a strong effect on the measured spin polarization. Powder magnetoresistance (PMR) is another variant where powder of the half-metallic material is compacted for measurement and the point contacts are established between the grains of the powder. The main disadvantage with this technique is that the Heusler compounds are prone to oxidation. The oxidation is more likely in powdered samples due to increased surface area, and therefore the respective PMR measurements are specifically affected.

Several surface sensitive techniques are quite popular as well, which in theory can measure spin polarization. One such technique is point contact Andreev reflection (PCAR) [94, 95], and is widely used to probe spin polarization of ferromagnetic materials. Another technique is spin-polarized photoemission (SP-PES) which measures the spin polarization of the photoelectrons that are ejected yielding the spin-polarized density of states near ϵ_F. Recently, high spin polarization ($\sim$96 %) has been reported using ultraviolet photoemission (UPS) in the Heusler compound Co_2MnSi [96]. X-ray magnetic circular dichroism (XMCD) is another technique which is used to obtain spin-resolved density of states, and the spin polarization can be deduced from that.

The main drawback of such surface sensitive measurements is that the surfaces have different energies than the bulk, and may lead to different properties. For example, manganese segregation on the surface has been observed in NiMnSb leading to a loss of half-metallicity [97, 98]. To make matters worse, Heusler compounds are prone to oxygen-capture and extreme care must be taken to avoid oxidation at the surface during measurement, specially for compounds containing specific elements such as Cr and Mn.

In addition to already mentioned issues, some techniques also involve complex mathematical

formulations to extract the spin polarization, whose reliability is still a matter of discussion. Due to various factors mentioned, there is no smoking-gun technique for measurement of spin polarization. Apart from the issue of 'reliability', most of the above mentioned techniques are, unfortunately, laborious and require very specialized experiments. Nevertheless, they do give us an idea about the trend of half-metallicity, which in principle, can be utilized to optimize a material.

1.3.1.2 Properties and applications of half-metallic ferromagnetism

Scientific research in most fields, is driven by the novel physical properties and their potential applications. Many a times, it is the basis to begin with, e.g., unusual magneto-optical properties observed in NiMnSb, was the starting point for developing the concept of half-metallic ferromagnetism (HMF) [85]. Since then, as possibilities of materials and experiments have evolved, the interest in HMF towards potential applications has been further propelled.

In the modern age, research that is promising for the field of advanced electronics and computing is given additional impetus. Complete spin polarization as a material property has been extensively sought after in the field of spintronics [99], or spin transport electronics which utilizes the spin of the electrons. Spintronics emerged in 1980s, based on the historic work by Grünberg et al. [100] and Fert et al. [101], who independently discovered giant magnetoresistance (GMR). The GMR effect is the observation of a large change in resistance by switching the magnetic ordering of a layer in a multilayer stack. It was a significant breakthrough, as the change in resistance just by switching the magnetic exchange in multilayers, could be used as the basis for electronics. The GMR along with the corresponding TMR (tunnel magnetoresistance) effects, are widely used today as the underlying mechanism of read-heads in hard disk drives and magnetic sensors.

Realization of high room-temperature TMR effect [102, 103] has further propelled the interest to new heights, as it has paved the way for novel MRAM (magnetic random access memory) devices, such as 3D racetrack memory as well as spin valves and filters [104, 105]. All these technologies and devices utilize the spin polarization, and thus, a half-metallic material is sort of a holy grail, since as per the simple Jullière's model (equation 1.2), highest magnetoresistance is possible for completely spin polarized systems.

Heusler compounds are one of the more promising systems for achieving half-metallicity, as many such compounds have been predicted. Although, they have not yet been experimentally verified, many show high TMR ratio, e.g., $Co_2FeAl_{0.5}Si_{0.5}$, where a TMR ratio of 386% at room temperature has been observed [106]. Another important aspect with regards to applications is the Gilbert damping constant which defines the switching speed of magnetization. Heusler compounds, in general, have weak spin-orbit interactions. In addition, low spin DOS at ϵ_F in some compounds (For example, $Co_2FeAl_{0.5}Si_{0.5}$), lead to a small Gilbert damping constant, which is also independent of atomic ordering. A small Gilbert damping constant implies that the relaxation timescales are of the order

of nanoseconds, which is crucial for fast operation of devices [104].

As a side note, although most technological applications with regards to spintronics pertain to thin films, there are additional complications which have not been completely understood. The effect of surface layer as well as the interfaces in thin films have not been well understood, although they are known to have strong effect on the properties, leading to a loss of half-metallicity in specific cases. As an example, half-metallicity is only expected for manganese-terminated (001) films of Co_2MnSi [107]. Therefore, an understanding of the interactions at the interfaces and surfaces along with reliable experiment techniques to measure half-metallic properties is essential, in order to develop new Heusler-based systems for applications.

We have seen that realization of half-metallicity holds immense potential for applications. The next section discusses Co-based Heusler compounds towards their growing popularity as promising half-metallic ferromagnets.

1.3.2 Cobalt-based Heusler compounds

Co-based Heusler compounds in the $L2_1$ structure have found much prominence recently in the scientific community. They have remarkably high Curie temperatures as compared to other systems which show half-metallic ferromagnetism. A high Curie temperature is important for half-metallic ferromagnets as the band gap shrinks with increasing temperature, and the depolarization effects are relative to the Curie temperature (T/T_C) [88]. $Co_2FeAl_{1-x}Si_x$ system displays Curie temperatures in the range of 1100-1200 K, which is the highest for any material where half-metallicity has been predicted [108]. Such high Curie temperatures can make it possible to preserve 100 % spin polarization even at room temperatures, which makes these compounds very promising for applications.

The Co-based Heusler compounds are unique in the sense that the Co-Co interaction plays an important role in the half-metallic ferromagnetism, unlike half-Heusler compounds where there is no magnetic interaction at the X ($4c$) sublattice. In some of the Co-based Heusler compounds, there exist a van-Hove singularity at the Fermi edge along one spin direction and thus a high density of states in that direction. A high density of states at ϵ_F could be essential for spectroscopic methods such as spin resolved photoemission to detect the 100% spin polarization [109]. Also, in case there is a loss of band gap in the other direction due to various effects such as high temperature, disorder, interface etc., the effective spin polarization may still remain quite high which makes it desirable for applications.

Half-metallicity has so far been predicted in various Co-based Heusler compounds, although initially it was not so. Around the same time when half-metallic ferromagnetism was found in half-Heusler compounds [85], Kübler had showed that the density of states nearly vanishes in the minority spin direction for selected Co-based Heusler compounds [86]. Another work also reported a

minimum in the density of states at the Fermi level for Co_2MnSn [110]. Only around a decade later, as the electronic structure calculations improved, half-metallic ferromagnetism was first reported for Co_2MnX (X=Si,Ge) by Ishida et al. [111]. They also suggested a possible correlation between the valence electrons and the band-gap in the minority states as well as hinted towards tunable half-metallic properties in quaternary Co-based Heusler compounds. Such a correlation was later well established, and is discussed next.

1.3.3 Magnetic moments and Slater-Pauling rule

Slater [112] and Pauling [113] independently and somewhat simultaneously discovered that it is possible to estimate magnetic moments (m) of $3d$ transition elements and their binary alloys from the average number of valence electrons (n_V) which was called the Slater-Pauling curve [114].

As per the Slater-Pauling rule, magnetic moment ($m = n_\uparrow - n_\downarrow$, in units of Bohr magneton μ_B) can be related to number of valence electrons $n_V = n_\uparrow + n_\downarrow$ per atom, where $n_\uparrow$ and $n_\downarrow$ are spin electrons per atom in the majority and minority states, respectively. The magnetic moment can be rearranged as:

$$m = n_V - 2n_\downarrow \tag{1.3}$$

or it can be rewritten as:

$$m = 2n_\uparrow - n_V = 2(n_{d\uparrow} + n_{sp\downarrow}) - n_V \tag{1.4}$$

where, $n_{d\uparrow}$ and $n_{sp\downarrow}$ are the majority d and sp states. Later on, Williams et al. [115] and Kübler [116] expanded and described the Generalized Slater-Pauling curve, based on the works of Friedel [117] and Tanakura et al. [118]. The Generalized Slater-Pauling curve is a plot of magnetic moment (m) versus *magnetic valence* (n_M) defined as:

$$n_M = 2(n_{d\uparrow}) - n_V \tag{1.5}$$

Hence, m can be further rewritten as:

$$m = n_M + 2n_{sp\downarrow} \tag{1.6}$$

Slater-Pauling rule also divides the dependence of m on n_V into two regions [119]. One half of the curve corresponds to mainly materials with close-packed structures (face-centered cubic (fcc) and hexagonal close-packed (hcp), e.g., Co and Ni) which have high valence-electron concentrations ($n_V \geq 8$) and is defined by itinerant magnetism. The second part corresponds to region of localized moments having low concentration of valence electrons ($n_V \leq 8$). Materials with body-centered cubic (bcc) or bcc-derived structures are found in this region, iron being a borderline case. Depending on

which type of system one is dealing with, equation 1.3 or 1.6 can be used to estimate the magnetic moment.

In the case of the itinerant systems, equation 1.6 is preferred. It was noted that the $n_{sp\downarrow} \approx 0.3$ in general [114], and any deviations are either due to magnetic weakness or sp contributions to $n_{\uparrow}$ that differ from 0.3 [115]. The magnetic moment is then given by:

$$m = n_M + 0.6 \tag{1.7}$$

For the elements to the right of Fe in the periodic table, as per the Hund's rule, the majority d-band is filled and thus $n_{d\uparrow} = 5$ and as per equation 1.3 the magnetic valence is then calculated as:

$$n_M = 10 - n_V \tag{1.8}$$

This well explains the itinerant half of the Slater-Pauling curve, e.g., for elements Ni and Co. Malozemoff et al. [120] also showed that the rule can be generalized for alloys such as Co-Cr and Ni-Cr, as well as can be extended to alloys containing metalloids.

We shall now discuss the other half of the Slater-Pauling curve, which pertains to localized magnetism. In this case, the Fermi energy is pinned in the minimum of the minority density of states, which is exhibited by such materials. This constrains the number of occupied electrons in the minority band ($n_{d\downarrow}$ to be approximately 3 [119, 121]). Hence equation 1.3 is thus reduced to:

$$m \approx n_V - 6 \tag{1.9}$$

In the case of half-magnetic ferromagnets, there exists a real gap rather than a minimum, which requires that the number of occupied minority states is an integer [114]. Thus, the Slater-Pauling rule $m_{HMF} = n_V - 6$ is strictly fulfilled for half-metallic ferromagnets.

However, depending on the composition, the average number of valence electrons might be a non-integer, leading to a non-integral moment, e.g., for quaternary compounds. For alloys containing different atoms, it is often more convenient to use the whole unit cell. In order to do that, the total number of valence electrons per formula unit N_V is used instead of the average number of valence electrons n_V.

With regards to Heusler compounds, Kübler first noted that fulfilment of the Slater-Pauling rule for $C1_b$ Heusler NiMnSb [116], which was later confirmed to be a half metallic ferromagnet [92]. Although initially quite a few of the Heusler compounds were reported to deviate from the Slater-Pauling curve, many of the Co-based Heusler compounds with the $L2_1$ structure follow the Slater-Pauling rule well [122]. For the $L2_1$ structure, the effective atoms are 4, so one has to subtract 24 (six times the number of atoms), and the moment per formula unit is given by:

$$M_{X_2YZ} = N_V - 24 \tag{1.10}$$

whereas for the half-Heusler compounds (XYZ), since there are 3 effective atoms, the moment per formula unit is given by:

$$M_{XYZ} = N_V - 18 \tag{1.11}$$

Figure 1.5 shows the Slater-Pauling curve, with the two regions for materials having localized moments and itinerant systems. As can be seen, Co-based Heusler compounds follow the Slater-Pauling rule quite well. A much detailed discussion on historical development and underlying theory of the Slater-Pauling rule can be found in the book by Kübler [114].
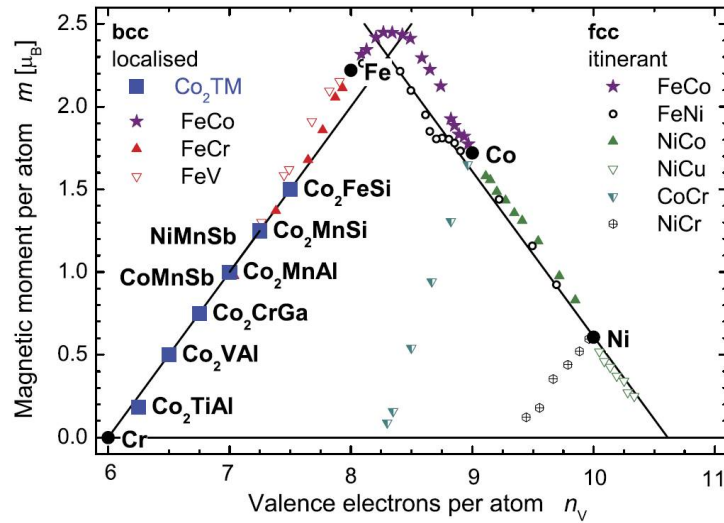
Figure 1.5: Slater-Pauling curve for $3d$ transition metals and alloys (reproduced from Felser et al. [90]).

Based on the constituent elements, Heusler compounds may have a wide range of magnetic moments, from high saturation magnetization in Co_2FeSi (6 μ_B, as N_V=30), to Fe_2VAl which should ideally have zero net magnetization as per the Slater-Pauling rule since it has 24 valence electrons in the unit cell. The possibility to design materials with magnetic moments as required, is always sought for. It also leads to interesting physics, from half-metallic Heusler materials where the net magnetization is really small (ferrimagnetic), to a compensated antiferromagnetic compound which have also been predicted to be superconducting [123]. The discussion on these materials is beyond the scope of this work, and the reader is directed to various review articles [37, 124] for details.

'Curie temperature Slater-Pauling curve': Ferromagnetic Heusler compounds exhibit a whole range of Curie temperatures, from as low to as ~125 K for Co_2TiGa [125] to as high as 1100 K for Co_2FeSi [126]. Interest has always been there to try and understand the underlying physics and what leads to such broad distribution. Co-based Heusler compounds are again very interesting in

that respect, as they seem to follow a 'Curie temperature Slater-Pauling curve' [127], i.e., the Curie temperature varies linearly with the number of valence electrons [122]. Kübler [128] developed a theoretical basis to calculate the Curie temperature for magnetic materials, which was later used for Co-based Heusler compounds and the linearity was found to fit well to the experiments [129]. This not only has led to a better understanding of the relation between the electronic structure and Curie temperature, but also made it possible to predict and possibly design materials accordingly.

Magnetic moments, specially in the case of Co-based Heusler compounds, are an important physical parameter. It must be kept in mind that the fulfillment of the Slater-Pauling rule is not the criterion for a half-metallic ferromagnetism, as many Co-based Heusler compounds which are even metallic or semiconducting follow the Slater-Pauling rule. Any deviations from Slater-Pauling rule, may hint towards an inherent physical phenomenon in the material, e.g., a change in the exchange interactions (j) between the various atoms [130]. However, it need not always be the case. One must keep in mind that magnetic moments are also affected by atomic disorder and chemical inhomogeneity and one must always do a thorough characterization to account for that, if present. Let us have a closer look at the possible effects of structural defects and disorders on physical properties, and how they may even be utilized.

## 1.4 Understanding the structure-property relationship

So far, we have discussed some very interesting properties of Heusler compounds, both in terms of physics as well as applications. Nevertheless, various properties and possibilities that have been mentioned so far, have been discussed for the fully ordered $L2_1$ structure, but in practice, there are always structural defects present in any Heusler compound, such as anti-site disorder, vacancies etc. In addition, majority of the predicted Heusler compounds suffer from issue of thermodynamic instability, which is also sometimes referred to as chemical disorder. This section pertains to a brief discussion on the effect of such disorder on physical properties and whether that can be utilized in any way.

First we shall discuss the effects of anti-site disorder. The details of the common types of disorder that may be possible have already given in Section 1.2. Anti-site disorder may strongly affect the respective properties depending on the elements and type of disorder. Webster and Ramadan [131] first reported on the effect of $B2$ disorder in $Pd_2MnIn_{1-x}Sn_x$ and $Pd_2MnIn_{1-y}b_y$, that although it does not affect the Mn moments, disorder leads to an antiferromagnetic exchange, due to the change in the sublattice. First band structure calculations incorporating the lattice imperfections was done by Ebert and Schütz [132] for PtMnSb and found it to have a drastic effect on spin polarization, which was supported by X-ray absorption experiments. Similar band structure calculations were also performed for NiMnSb and it was shown to reduce spin polarization [133] as well as affect magnetic moments [134]. There have been various studies regarding the effects of disorder on physical

properties, both theoretically and experimentally, for quite a few Heusler compounds.

Since the present work pertains to Co-based Heusler compounds, it is pertinent to understand how disorder may affect their properties. As has been mentioned, the Co-sublattice plays an important role in the magnetism of Co-based Heusler compounds. Disorders such as DO_3 (between X an Y positions) and $A2$ disorder(between all X,Y and Z positions) strongly affect magnetic moments and in turn spin polarization, as compared to $B2$ disorder (between Y and Z positions) [10]. Gercsi and Hono also calculated the energy of systems with various disorders and showed that for some specific cases, fully ordered $L2_1$ system is less stable than the disordered ones, and thus, are difficult to synthesize [10].

We take $Co_2(Cr_{1-x}Fe_x)Al$ as a specific example, for which a detailed systematic band structure calculations for various disorders have been done by Miura et al. [40], where strong reduction in saturation moments as well as the loss of half-metallicity has been calculated. Complete $B2$ disorder still has high spin-polarization, although band-gap was lost at 10% $B2$ disorder [40] (Figure 1.6). On the other hand, even a small amount of DO_3 disorder strongly reduces both the magnetic moments and spin polarization. Similar results have been obtained for other Co-based Heusler compounds [135, 136]. An experimental work on the effects of disorder in Co_2CrAl thin films report a reduction in T_{Curie} as the disorder increases $L2_1 \rightarrow B2 \rightarrow A2 \rightarrow$ amorphous [137]. Atomic disorder can also account for anomalous behaviour in magnetization and response in ferromagnetic resonance at low temperatures in Co_2CrAl films [138].
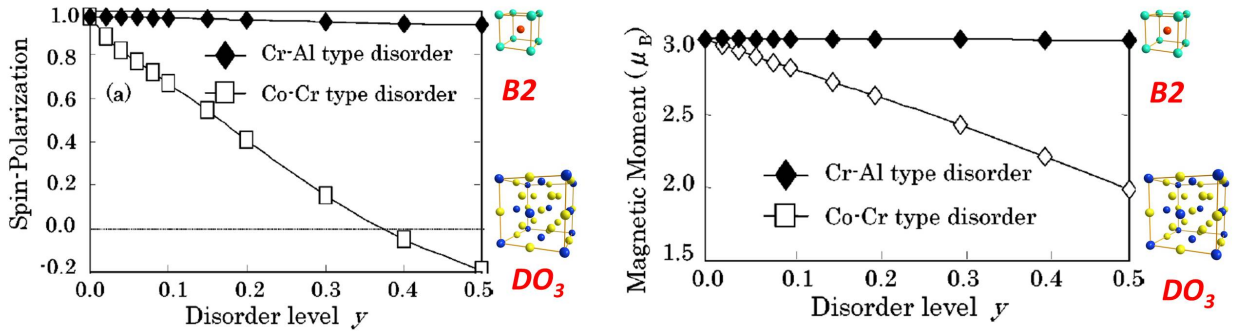
Figure 1.6: Effect of $B2$ and DO_3 disorder on magnetic moment and spin polarization in Co_2CrAl (adapted from Miura et al. [40]).

Disorder effects also depend on the materials and the elemental species involved. Ti-Al $B2$ disorder reduces half-metallicity in Co_2TiAl [139], unlike $Co_2Cr_{1-x}Fe_xAl$. Co-Mn disorder in Co_2MnSi and Co_2MnGe both strongly affects half-metallicity [140]. Incidentally, it was also calculated that in Co_2MnSi, the half-metallic nature is preserved for small amounts of 8 % Co-Mn off-stoichiometry and the gap is also slightly increased [141], whereas in Co_2MnGe, the half-metallicity is locally destroyed, but screened within 2 atomic shells [142]. In some systems, DO_3-type disorder may even lead to an increase in the saturation magnetization [143].

Effect of disorder can also be seen in other physical properties. For example, transport measurements provide an indirect way to look at the structure and crystallinity. Residual resistivity ratio, RRR (R_{300K}/R_{5K}), gives an indication of the quality of the crystal [144]. The nature of the resistivity-change with temperature is known to be strongly affected due to disorder in double perovskite polycrystals [145] and the same may also be expected for Heusler compounds. A study of effect of disorder on the anomalous Hall effect in $Co_2FeSi_{0.6}Al_{0.4}$ and $Co_2FeGa_{0.5}Ge_{0.5}$ films show very distinct influence of the type of disorder [146]. Vidal et al. also showed that *B2* disorder leads to an improvement in the anomalous Hall effect whereas *DO$_3$* disorder contributions affect it negatively [146].

Such effects of disorder are not specific to Co-based materials. Similar calculations have been done for Fe_2VAl, where it was calculated that the introduction of any type of disorder leads to enhanced spin moments and makes the material magnetically active [147], even though the composition has 24 valence electrons and as per Slater-Pauling rule (equation 1.10), should have zero net magnetization. Since the zero net magnetization has not been experimentally realized for Fe_2VAl, the existence of atomic disorder has also been put forth as the likely reason. Furthermore, superparamagnetic clusters, formed possibly due to the anti-site disorder, have been found to affect the relaxation rate in nuclear magnetic resonance on Fe_2VAl [148]. Similarly, effects of anti-site disorder on physical properties has been studied in various other Heusler compounds as well [149–151].

In addition to the anti-site disorder, chemical homogeneity of the samples is also a challenge for quite a few of the Heusler compounds. Many Heusler compounds are stable at room temperature, but cannot be synthesized directly from the melt, and specialized techniques must be employed to synthesize these so-called incongruent melting compounds (refer Section 2.1.1.1 on page 28 for details). Even then, still quite a few of the predicted compositions are not thermodynamically stable at all, leading to multi-phase mixture during synthesis and processing. Non-equilibrium techniques such as melt-spinning may be utilized to synthesize such compounds [152]. Thin films, at times, also allow to stabilize a metastable system, and many compounds have been explored via that route. Still, issues pertaining to chemical disorder are frequently encountered in bulk samples and thin films, which are many a times neglected for want of fitting theory to data. A detailed discussion on this aspect has been done later with regards to $Co_2Cr_{1-x}Fe_xAl$.

Chemical segregation may also be driven due to surface and interfaces. Segregation of manganese at the surface of NiMnSb films has been reported, and is also found to affect spin polarization [97]. Si segregation on Co_2MnSi thin film surface has also been recently reported [153] and is likely the cause of reduced tunnel magnetoresistance in the respective films. A similar situation could very well be possible in other systems.

Apart from atomic disorder and chemical inhomogeneity, defects such as vacancies, also have an effect on electronic structure and properties. An equilibrium concentration of such defects is likely at any given temperature. The defect concentrations may even be significantly higher than the

equilibrium concentration depending on the synthesis technique and processing conditions [154].

Research has so far been focused mainly on probing the effect of vacancies through theoretical calculations due to the ease of study as compared to experiments where very specialized equipment is needed to quantify vacancies. It has been shown that vacancies shrink the minority gap and may even lead to generation of spin states at the Fermi energy in the minority direction [155, 156]. Various other works also report a similar effect on electronic structure in several Heusler compounds [157–159], but the presence of vacancies does not destroy half-metallicity in all cases. Band structure calculations for Co_2CrAl [160], Co_2VSn [161] and Fe_2MnSi [162] Heusler compounds show that even though vacancies are likely to be formed, the half-metallicity is retained, although the minority band-gap has shrunk. Vacancies also seem to play a role in other physical properties as well, as reported for FeVSb half-Heusler compound [163]. The possible extent of such defect-driven effects should be kept in mind during the experimentation as well as during the process of designing and developing materials for applications.

Defects do seem to have a strong negative impact on the properties, but ways have been found to utilize the disorder-effects so as to better understand the material and even possibly tune the properties. Anti-site disorder may be introduced by partially substituting one site by other, e.g., $X_{2-\delta}Y_{1+\delta}Z$, in order to study the effect of disorder on electronic structure and properties [136, 164, 165].

Partial substitution of one of the transition elements, can also be used to 'dope' with holes or electrons. The position of the Fermi energy inside the minority spin-gap can thus be tuned. Galanakis et al. [166] have shown that the ternary Co-based Heusler compounds, which do not have 100 % spin polarization but do have the Fermi level at the edge of the band gap, can be tuned by quaternary additions so that half-metallicity is attained. In the same work, they have also calculated that using such a scheme, defect-driven half-metallic antiferromagnetism, or a so-called compensated half-metal can be obtained [166].

Vacancies can also be used to induce half-metallicity in semiconducting half-Heusler compounds [167]. Also, coherency strains due to inherent point-defects such as vacancies reduce the thermal conductivity leading to an increased figure of merit for thermoelectric applications [168].

Recently, first-order magnetic transition leading to large exchange bias was reported and was understood to be disorder-induced [169]. In another report, the anti-site disorder was explained as the reason for ferrimagnetic clusters leading to a large exchange bias effect seen in Mn-Pt-Ga Heusler compound [170]. It remains to be confirmed whether such an effect is due to structural defects like anti-site disorder, or an outcome of chemical inhomogeneity in the material, although the latter is a more likely culprit. A large exchange bias effect due to anti-site disorder has also been reported in multiferrroics [171] and is not limited to Heusler compounds only.

Presence of chemical inhomogeneity is specially utilized in the field of thermoelectrics. Evolution of secondary phase due to a phase transformation or immiscibility is used to nano-structure the

material as desired, which leads to improved thermoelectric performance [172, 173]. Presence of multiple phases has been successfully utilized in select half-Heusler compounds, which has emerged as a promising new class of high temperature thermoelectrics [174, 175].

Anti-site disorder is also known to induce martensitic and metamagnetic transitions in a material. Magnetocaloric effect in Mn_2NiX Heusler compounds has been predicted to evolve due to anti-site disorder between one of the Mn and the Ni sublattice [176]. Another work on Ni-Co-Mn-In Heusler system also found that atomic disorder significantly increases the peak magnetic entropy change which is desired for magnetocaloric applications [177].

Chemical inhomogeneities may also change the nature of magnetism, e.g., from soft to hard magnetic in manganese-based Heusler compounds. This may have potential applications towards development of hard magnets, such as Mn-Co-Ga system [178]. First principle calculations have recently shown that the chemical disorder can also be a possible design tool to engineer high spin polarization in Mn_3Ga Heusler system [179].

As we have seen, the structure and changes in structure have a strong relationship with the physical properties of Heusler compounds. Moreover, additional aspect of chemical inhomogeneities has a large effect on the properties as well. Therefore, a better understanding of the correlation between the intrinsic material attributes and the physical properties that evolve extrinsically, is a must, and is the underlying theme of this doctoral work. It has already been mentioned in the Introduction how this interplay between the changes in intrinsic attributes and the physical properties is addressed is this work.

Before moving on to the results and discussion, the details of the sample preparation and experimental techniques used in the present work are outlined in the next chapter.

Chapter 2

Sample Preparation
and Experimental Techniques

The present chapter deals with the methods of sample preparation. We shall focus on the Floating Zone growth as it is the most relevant synthesis technique for the present work. The principle and specific advantages shall also be briefly discussed. In the end, additional experimental techniques used for characterization and physical property measurements are briefly described. Before we get into the details, it is important to revisit some basics of material science to assist the reader in better understanding.

2.1 Thermodynamics and phase diagrams

At first glance, synthesis of samples may seem rather straightforward. However, there is no 'magic pot' where you melt the constituents together and solidify, such that the atoms always occupy the right atomic sites in the lattice site and everything is homogeneous, which may only require a bit of annealing. Nature, although beautifully simple in its essence, is not so straightforward.

Quite frequently, sample may become unstable under specific conditions, or the desired structure and composition might not even be stable at all, depending on the thermodynamics. Figure 2.1 shows a few scanning electron microscopy images from the author's work, for samples prepared using a standard melting procedure. The contrast in backscattered images represents chemical contrast, and the presence of 2-4 phases can be clearly seen. Such scenario of multiple phases is common, and in most cases, it may not be possible to obtain a phase-pure material even with further processing (For example, annealing).

If for some reason, samples are prepared without considering stability or homogeneity, one may run into problems. The subsequent measurements of physical properties would likely be anomalous, and since the material aspects are disregarded, they end up being attributed to alternate mechanisms and the properties may never be optimized on that basis.

Therefore, the important questions, from the scientific point-of-view, are that the properties that we measure are due to which phase and how do the phases interact with each other as well as how that affect the overall properties, i.e., how the intrinsic attributes and extrinsic properties are entangled. As has already been discussed earlier with examples, even a few nanometers thick interfaces in films may affect the properties. The interactions between phases would differ on a case to case basis, and would also be dependent on their volume fraction and distribution. It is possible that the secondary phase is too small and does not have any affect, but it cannot and should not be assumed so.
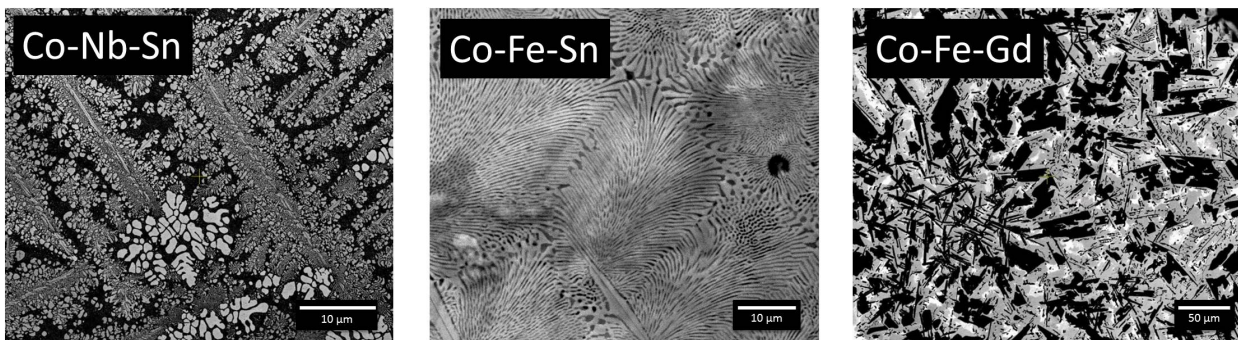
Figure 2.1: Back-scattered electron (BSE) images from scanning electron microscopy show the presence of multiple phases in arc-melted samples of ternary systems.

There is another important issue that should be kept in mind with regards to the additional phases, howsoever small in fraction. As a 'gedanken experiment', we prepare a sample with an intended stoichiometry but a small fraction of a secondary phase is present, which has a composition different from that of the intended stoichiometry. Even though the secondary phase might be negligible, but since we started with stoichiometric amount of each element, the actual composition of the main phase is not exactly as it was intended, as the secondary phase would be at least richer in one of the elements. The scenario is illustrated in Figure 2.2.
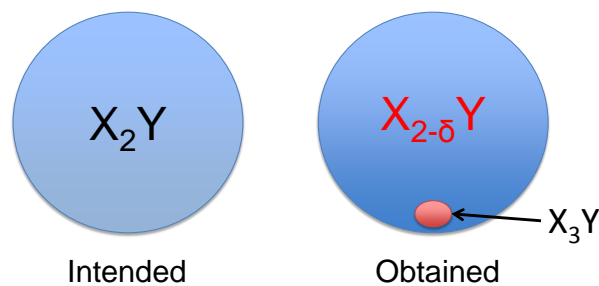
Figure 2.2: Diagram shows an example of effect of phase separation, even though the secondary phase may be deemed negligible in volume fraction.

It is thus paramount to be able to convincingly answer the question "How to get what I want?". For that purpose, the significance of thermodynamics associated with the system cannot be overemphasized. Thermodynamics basically defines whether something is stable under the given conditions or not, and how the stability is affected during certain processing. The change in free energy (ΔG) determines whether a process is energetically favourable. If the ΔG is negative, the change can happen spontaneously, as the system gains energy. If the ΔG is positive, a reaction or a transformation may proceed once sufficient energy requirements are met, so that the energy barrier can be crossed.

However, ideally, thermodynamics only defines things at equilibrium. The rate of change or kinetics of a process is as fundamental towards any transformation as thermodynamics, and as influential with regards to how a state may be described or established. For example, sodalime glass, which is understood as a solid in normal life, may be defined as a liquid, given the timescale one is looking at is large enough. Kinetics, therefore, goes hand-in-hand with thermodynamics in determining any change in a system under given conditions.

Equilibrium itself is defined when a material is kept at a given condition for an infinite time. Hence, any real world transformative process is essentially, non-equilibrium. Therefore, in principle, nothing is ever, truly stable, and any change is dependent on kinetics. Utilizing the kinetics can allow us to overcome thermodynamics, specially in the case where things are energetically unfavourable, which is the case more often than not. Metastable phases can be synthesized, with the use of the right technique and conditions, e.g., in the case of thin films. Having said that, understanding of the thermodynamics of a process is essential, and foremost, since in order to realize materials for applications, it is important to know the stability as well as information about any possible transformation and its kinetics, under conditions of synthesis, processing, characterization or measurement and application. A very important tool for that purpose are thermodynamic phase diagrams. For further discussion in this text, 'phase diagram' would mean a thermodynamic phase diagram, unless otherwise stated.

2.1.1 Phase diagrams

A phase diagram is essentially a plot or a map of the state of a system, under the variables of temperature, pressure and composition. By definition, phase diagrams give a state under the condition of equilibrium, corresponding to the minimum free energy of the system. The Gibbs's phase rule [180] is central towards understanding phase diagrams and defines the relationship between variables, components and phases, given as:

$$P + F = C + 2 \tag{2.1}$$

where P is the number of phases in thermodynamic equilibrium, C is the number of chemically independent constituents in the system and F is the number of independent intensive variables, also

called as degrees of freedom. A phase here is defined as homogeneous, bounded by a surface and is typically solid, liquid or gas. Temperature (T), pressure (p) and composition (x_i) are the typical intensive variables (Figure 2.3a). If pressure is excluded as a variable, then the phase rule reduces to $P + F = C + 1$. By and large, phase diagrams are a graphical representation of Gibb's phase rule [181].

The most common classification of phase diagrams is based on the number of components involved. Phase diagrams with 1, 2 and 3 components are called as unary, binary and ternary phase diagrams, respectively. We shall now familiarize ourselves with some terms pertaining to phase diagrams, as they will be used during further discussion.
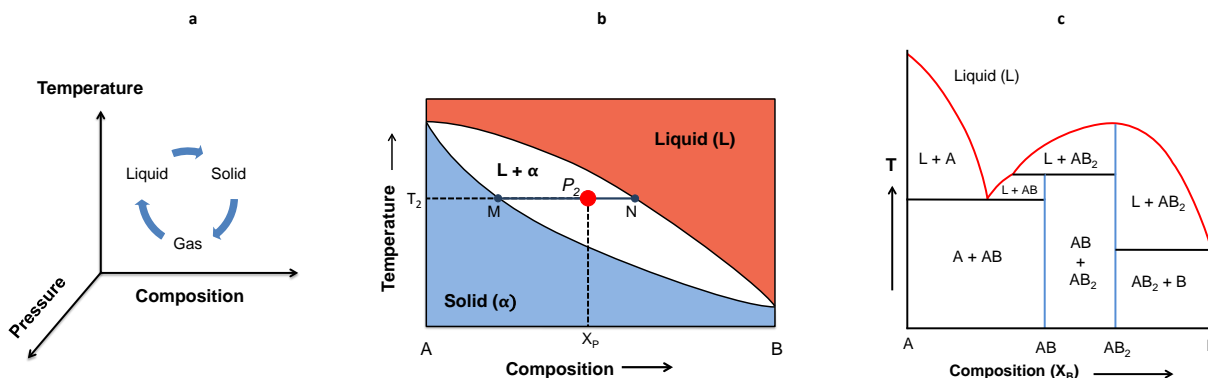
Figure 2.3: Illustrations regarding phase diagrams (a) The variables and phases in equilibrium for a standard phase diagram (b) Binary phase diagram for A-B having a binary solid solution (b) Binary phase diagram for A-B with various two-phase fields; line compounds (AB and AB$_2$) are marked with blue whereas the liquidus is marked in red colour.

As per the phase rule, any point on a boundary between two fields is the point of equilibrium between the two regions it bounds. Figure 2.3b shows the schematic of the simplest binary phase diagram, with a solid solution between A and B components, x-axis being composition (in terms of mole fraction of B, X_B) and temperature on the y-axis. A region in the phase diagram where a single phase is stable, is referred to as a single-phase field. Region L and α are single-phase fields of liquid and solid respectively. In Figure 2.3b, a point P_1, is stable as a solid of composition X_P at any temperature T_2, if it lies inside the single-phase field α. The limiting case of single-phase field is a single composition, which is referred to as a line compound or element (For example, compositions AB, AB$_2$ in Figure 2.3c, marked with blue color).

A multi-phase field is one where more than one phase is stable at each point, and are called two-phase field, three-phase field and so on. For example, region marked as L+α in Figure 2.3b is a two-phase field. A composition X_P at any temperature T_2, is stable as a mixture of solid and liquid,

if it is inside the two-phase field L+α. The composition and fraction of the corresponding solid and liquid are given by the intersection of a horizontal line at that temperature with the phase-field boundaries, also known as the tie line (compositional line MN in Figure 2.3b). Within a unique multi-phase field, the same phases coexist albeit in different ratios at different points, depending on the position of the composition on the tie line. Furthermore, a N-phase field, is always bounded, along the direction of temperature axis, by N number of (N−1)-phase fields i.e. a two-phase field is always bounded by two single-phase field or line compositions. The phases in a N-phase field are all the phases in the (N−1)-phase fields bounding it. This can be seen for the two-phase field, AB+AB$_2$ in Figure 2.3c, which is bounded by line compounds AB and AB$_2$ at any given temperature.

Figure 2.3c shows a schematic of a slightly more complex binary phase diagram, with multiple phase fields. All the vertical lines, A, AB, AB$_2$ and B, are line compounds of single phases, and bound different two-phase fields among themselves or with the single phase field of liquid (L). A curve above which all everything is completely liquid, is referred to as the liquidus. For example, the liquidus is marked by red colour in Figure 2.3c.

All the concepts and terminologies mentioned above extend for a three-phase field similarly. All the aspects of the phase diagram, e.g., how many regions bound another, the angles at which phase boundaries connect, can be understood from the phase rule.
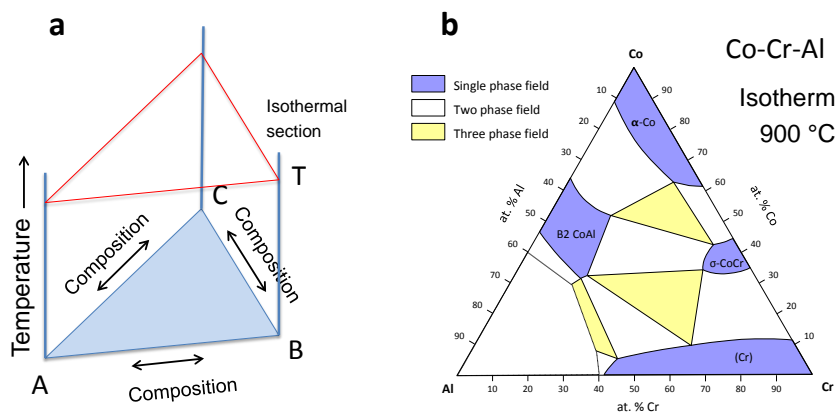
Figure 2.4: (a) Schematic showing the axes for a ternary phase diagram along with lines for an isothermal section (b) Isothermal section at 900 °C for Co-Cr-Al system showing the various multi-phase fields in different colours (adapted from Bondar [182]).

For phase diagrams involving 3 components, there are 4 variables involved, one each for the compositions and one for temperature. A 3-dimensional figure is needed to completely draw the phase diagram as shown in Figure 2.4a. In order to simplify them for the purpose of printing and visualization, isothermal sections are normally drawn. Figure 2.4c shows an exemplary isothermal section of Co-Cr-Al at 900 °C (redrawn based on [182]).

The complexity of phase diagrams is compounded for more components and it becomes difficult for representation even in three dimensions. Pseudo-binary or pseudo-ternary phase diagrams can also be drawn to simplify them, which are technically not between two or three components, but rather compositions. There are various other nuances of understanding and extracting information from phase diagrams, specially as the phase diagrams become more complex with increasing constituents. Since the focus of this text is not on phase diagrams per se, the description is, therefore, limited. For an in-depth discussion on phase diagrams, a comprehensive book on phase diagrams by West and Saunders [183] is recommended.

The concept of phase diagrams at equilibrium is precarious, particularly if they are experimental, as no technique is absolutely at equilibrium. Specialized experiments have been developed for phase diagram determination, e.g., diffusion couples [184] as well as the recently developed multiples [185], where a combination of two phases is kept together for extended duration of time, so that the interface can attain equilibrium through diffusion, which is them studied to develop the phase stability. The interested reader is referred to the book by Zhao on phase diagram determination [186].

2.1.1.1 Congruent and incongruent melting

An important aspect, with respect to sample preparation, is the melting and/or solidification characteristics of a phase. Naturally, single components such as A and B in Figure 2.5 directly melt at T_1 and T_2 respectively.
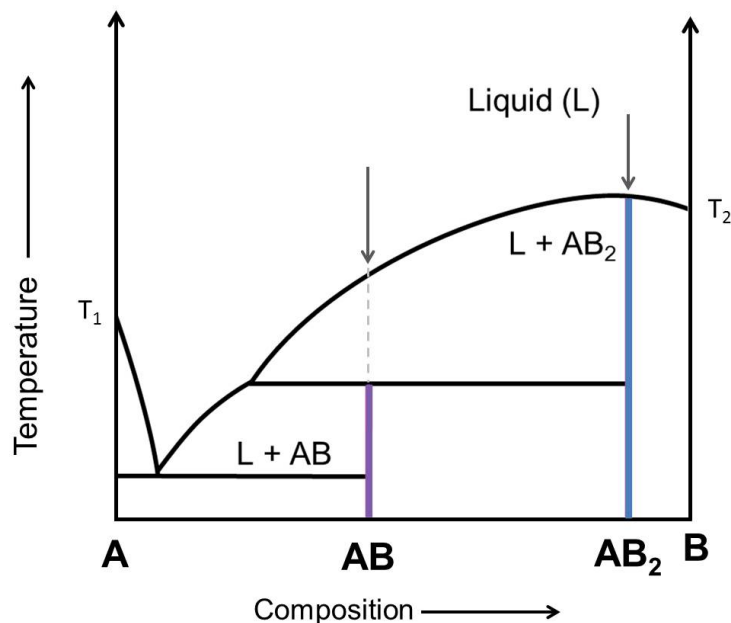
Figure 2.5: Schematic of a phase diagram showing congruent and incongruent melting scenarios.

If a multi-component phase of a specific composition is directly in equilibrium with the liquid of same composition, e.g., AB_2 in Figure 2.5 (blue line), it is called as congruent melting. In other words, the solid of that composition can always be formed by cooling the liquid of that composition.

On the other hand, when the solid is not in equilibrium with the liquid of same composition, e.g., AB (Figure 2.5), it cannot be obtained by cooling directly from the melt. Such a scenario is an example of incongruent melting. It is important to be aware of the melting behaviour of a material, as standard synthesis methods such as arc-melting as well as quite a few crystal growth techniques, such as Bridgman and Czochralski technique can only be used to synthesize phase-pure sample in systems with congruent melting. Specialized techniques such as Floating Zone technique are needed to have a possibility at synthesizing phase-pure incongruently melting compounds. We shall now discuss the details of different types of sample preparation employed in this work, with a special focus on the Floating Zone technique.

2.2 Methods of sample preparation

As mentioned in the last section, understanding the thermodynamics and controlling the kinetics makes it possible to develop materials with desired crystal structure and microstructure. Since intrinsic features and physical properties are closely interlinked, ability to form appropriate samples is a boon for applications, in addition to the understanding of the underlying physics. Having said that, sample preparation is not easy, specially for multi-component systems. The phase diagrams can get highly complicated even for a binary system (see Figure 2.4 for example), and there is no single synthesis technique that can do it all. Each method has its own advantages and disadvantages. Therefore, one must understand the preparation route well before it is used.

The choice of the technique also depends on the quality and type of sample that is needed. For various scientific purposes, a polycrystalline sample might be sufficient. In general, polycrystalline sample are relatively easier to make as compared to single crystals, under the assumption that the phase can be stabilized or metastabilized, as per the conditions of the process. On the other hand, depending on the properties that one intends to study, a single crystal might be a necessity, e.g., crystalline anisotropy. In addition to that, different synthesis routes are preferred for oxides, ceramics, organic compounds etc., specially since the required conditions of environments and processing, e.g., melting, are significantly different. For example, one must be careful of oxidation issues during the processing of intermetallic and organic compounds at high temperatures. The discussion in this work shall be limited to intermetallics, since the present work only deals with these compounds. First, we shall discuss the preparation of the polycrystalline intermetallic compounds.

2.2.1 Synthesis of polycrystalline samples

In the present work, in order to prepare polycrystalline samples, arc-melting setup has been used, which is the most commonly used method of sample preparation for intermetallic compounds. It is reminiscent of the 'magic pot' mentioned earlier, as basically it involves melting everything together and solidifying. Figure 2.6 shows the schematic of an arc-melting along with a photograph of our setup at IFW Dresden.

1. Cu crucible
2. W electrode
3. Sample material
4. Getter material
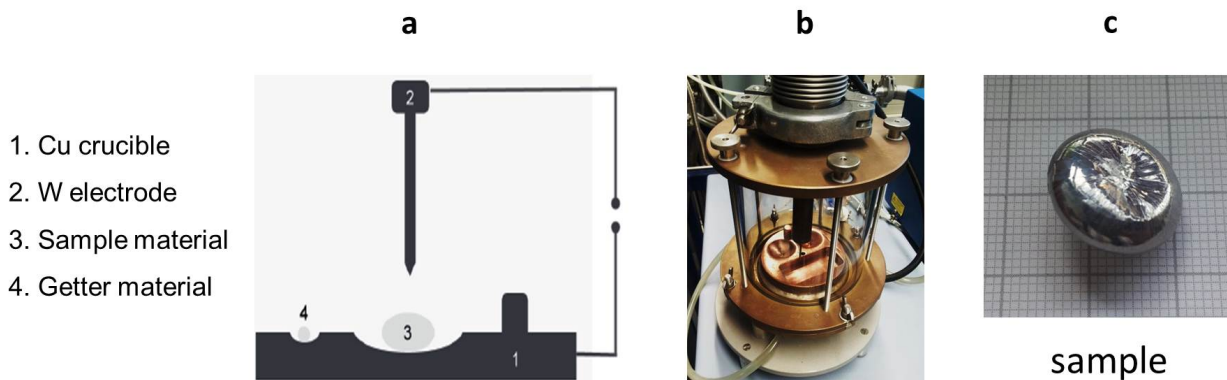
Figure 2.6: Arc-melting setup (a) Schematic (b) Photograph of setup at IFW Dresden, (c) A typical sample obtained from arc-melting.

Our setup has a water-cooled copper block with multiple depressions which act as crucibles. The top part has a water-cooled tungsten electrode tip connected to a bellow for easy manoeuvrability. A high voltage generator is connected across the electrode and the copper block, to generate and sustain the arc. The chamber has quartz window all across, and is connected to a turbo-molecular pump for evacuation in addition to a connection to the argon-supply for back-filling post-evacuation. For the experiment, the sample constituents are placed in one of the crucibles and a Ti or Zr piece is placed in the other one, which is used as oxygen getter. The chamber is then closed and evacuated to at least 10^{-5} mbar pressure, and is back-filled with argon. The chamber is kept at a slightly lower pressure than ambient pressure to allow easy movement with the bellow. Once the cooling water is switched on, the arc is struck and first the Ti or Zr getter is melted to absorb oxygen and the process is repeated 2-3 times to remove remnant oxygen in the chamber. The sample is then melted at least 3 times, flipping the solid sample after each melting to achieve a better mixing. In most cases, the final sample has a shiny surface free of oxidation, such as shown in Figure 2.6c.

The resulting sample, if one is able to obtain a chemically homogeneous sample, is generally strongly polycrystalline in nature, as there are multiple nucleation sites due to the crystalline copper crucible. Also, the samples undergoes a cooling rate several 100 K/sec during solidification, because of the water-cooled copper crucible. The fast cooling rate must be kept in mind during analysis as

a quench process is involved. Since the sample is heated from the top, and the water-cooled Cu crucible containing the sample is at the bottom, there is a strong thermal gradient vertically, which may also have an affect on the sample. If the sample is not phase-pure, a compositional gradient along the same direction may be additionally present due to the thermal gradient.

In principle, the arc-melting technique should work quite well for congruent melting compounds or compositions. However, synthesis of incongruent melting materials is tricky. As the sample is quickly brought from the molten region to room temperature, some instabilities may be avoided if the region of instability is small in temperature. Unfortunately in most cases of the incongruently melting compositions, the cooling rate is not fast enough to avoid phase separation or transformations and this leads to the formation of a sample containing multiple phases. Thus, an alternate technique such as Floating Zone growth is required in order to have a possibility of synthesizing incongruent melting compositions, and will be discussed later on.

Care must also be taken when working with volatile materials such as manganese, or with elements which may react with the crucible, such as tin. Weight loss in the sample after preparation should always be measured. In our case, if the material loss was higher than 0.5 $wt.\%$, the sample was discarded. An important aspect one should be careful about is whether all the constituent elements have melted during the arc-melting. Sometimes it can happen that when the melting points of the components are very different, the sample may seem to be melted during the arc-melting, but a small part of higher melting element might still remain inside as such. This incomplete mixing can be checked macroscopically after cutting the sample. However, sometimes it is not so easy to distinguish as the length scales might be small. Such an incomplete mixing can be minimized with an induction heating source. A casting setup using induction heating is discussed next.

2.2.1.1 Preparation of feed and seed rod for Floating Zone growth

Floating Zone (FZ) technique requires polycrystalline rods of intended stoichiometry, as a starting material. The preparation of the rods shall be first briefly outlined before describing the FZ technique itself. Also, the meaning of the terms feed and seed rod shall be explained in that part, as it is not so relevant here.

A Hukin-type cold-crucible setup with radio-frequency (RF) heating was used for casting the required rods. A schematic of the crucible and the setup is shown in Figure 2.7. the crucible consists of two parts. The outer part has arms made of copper, which are water cooled (Figure 2.7b). An additional crucible made of two pieces fits inside this crucible. It is also made of copper and determines the thickness and maximum length of the cast rod.

The constituent pieces of the intended stoichiometry are placed in the top part of the water-cooled Cu crucible after fixing the setup. The crucible is then raised to an optimal position inside the water cooled coils, so that the coupling in the sample is good enough to heat the sample with minimal

power. The crucible is surrounded by a quartz tube which is evacuated to at least 10^{-5} mbar pressure, and back filled with argon before the experimentation. The sample is then melted 2-3 times in the top part of the crucible to have a good mixing, and is also flipped after each melting to facilitate the homogenization. In the final melting, once the sample is completely molten, the copper finger is quickly moved down, pulling the molten material in the crucible. As in arc-melting, high heat dissipation by the cold copper crucible acts as a quenching process and must be kept in mind. The steps along with the initial setup is shown in Figure 2.7a-d. An example of the final rod sample that is obtained is also shown.
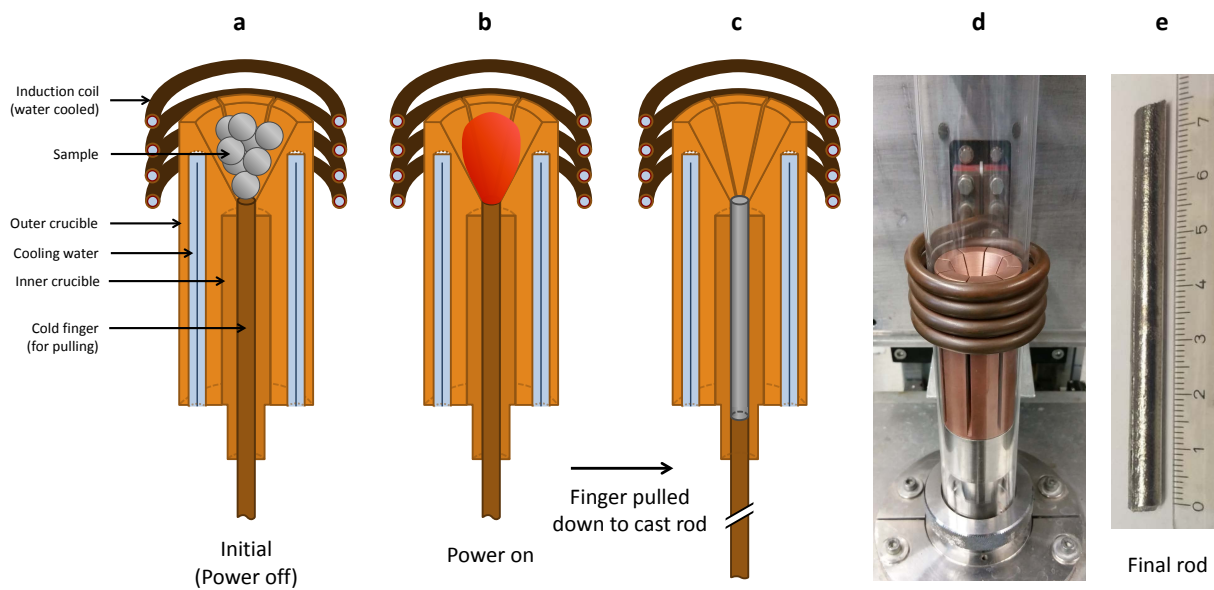
Figure 2.7: Induction melting setup (a)-(c) The cross-section of the crucible show the stages of the casting process. (d) Photograph of the setup at IFW Dresden (e) A typical cast rod of 6 mm diameter.

The main advantage of the induction melting is that it allows for a more uniform heating and a much better mixing as compared to the arc-melting. The disadvantage with this setup is that there is no oxygen getter material and the chamber volume is also large. Due to this, the evacuation needs to be done for extended time, or must be repeated multiple times while flushing with Ar in between the evacuations. The final rod sample might even be slightly oxidized at surface, which can affect the growth process and therefore one must be careful during preparation to keep the oxygen contamination to a bare minimum.

As already mentioned, compositions that melt incongruently, in most cases cannot be synthesized as a phase-pure sample using conventional techniques such as the arc-melting. It is also not possible to do so using many popular crystal growth techniques, and specialized method such as Floating Zone (FZ) growth is needed to obtain a homogeneous sample.

2.2.2 Optical Floating Zone technique

2.2.2.1 Principle, phase dynamics and grain selection

As a starting point, two dense rods of intended stoichiometry are first prepared and fixed vertically. Floating Zone (FZ) technique gets its name from the fact that a molten region is suspended between those two vertical coaxial rods. The steps involved in the formation of the molten zone are shown in Figure 2.8a-d. The two rods are first brought closer in a hot zone from opposite directions coaxially and the tips are melted by slowly increasing the heating power. Once the tips have melted sufficiently, the two rods are brought closer so that the molten tips join each other, thereby forming the molten zone. The molten zone is suspended purely by surface tension. This molten region or zone is then translated along the rods such that one rod melts and the solid interface grows in the other rod simultaneously. The translation can be done by either moving the heating source for the hot zone along the rods, or keeping the source fixed while the rods are moved at the same speed.
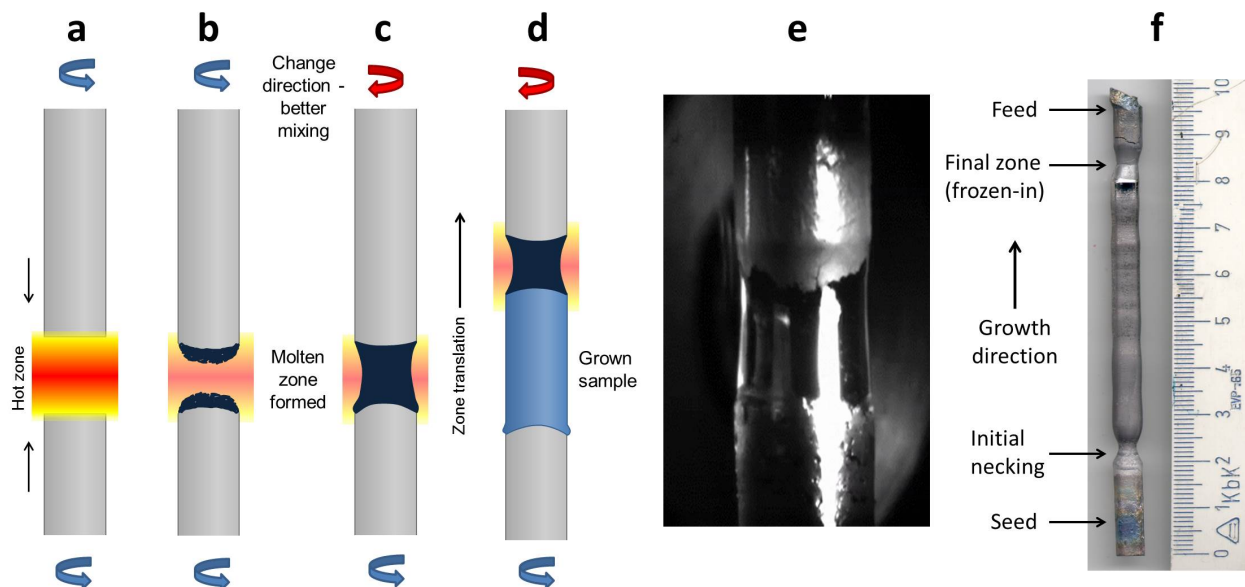
Figure 2.8: Floating Zone technique (a)-(d) show the zone formation and translation (e) Snapshot of the zone during growth (courtesy of Franziska Seifert, IFW Dresden) (f) A final grown sample; the different regions are marked.

The rod which melts during translation, i.e., one that feeds the molten zone, is called the feed rod and the rod with the solidification interface is called as seed rod or even just seed. In Figure 2.8a-d, the lower rod would be the seed, and the upper rod would be the feed rod. As the seed rod solidifies, the various grains grow, if the seed rod is polycrystalline. In general, the seed rod is polycrystalline like the feed rod, although a single crystal may be used as a seed as well in order to fix the growth direction. Figure 2.8e shows the snapshot of the molten zone from the live-stream of

the high temperature camera mounted next to the mirror in our setup at IFW Dresden.

Since the zone is freely suspended, the need for a crucible is eliminated. Hence there is no worry of contamination or reaction with a crucible, which can be very advantageous for specific systems. The length of the feed rod determines how long the experiment can go on, depending on the growth rate or speed of translation of the zone. The growth rate can vary from 0.1 mm/hour to 10 mm/hour or even higher, and the choice of growth speed for an experiment would depend on the material and phase dynamics involved.

During the translation, the rods are also rotated along their axes, to homogeneously heat the sample as well as obtain an optimal solid-liquid interface at the solidification front. In addition, once the zone is formed, the direction of rotation of the feed rod is reversed to facilitate better mixing in the zone.

A flow of Ar gas is maintained in the sample chamber in the case of intermetallics, to minimize oxidation. Nevertheless, oxidation can never be completely avoided, e.g., for materials containing Al, and many-a-times a thin oxide layer forms on top of the zone, which may also affect the growth. A careful choice of the growth parameters is therefore needed during the experiment.

We have already mentioned that FZ technique can be used to grow the incongruently melting compounds. We shall now explain how this is achieved in the phase diagram, and how FZ is different from other techniques. It is deemed necessary to mention that the scenario presented here is an approximate one, although it succinctly illustrates the important aspects. A detailed outline and explanation of the process is beyond the scope of this work.

Figure 2.9a shows a simplified schematic of an incongruent melting scenario for compound AB. To start with, the feed and seed rods are made of the intended stoichiometry, AB. The rods are melted to form a zone, which has a composition AB as well. Once the zone translation is started, AB_2 solidifies initially since it is stable at that temperature (Point P_{t1} in Figure 2.9a). The solid that grows out of zone is richer in B as compared to the zone, and the zone get richer in A. As the growth progresses, stoichiometry of AB is being fed to the zone by melting of the feed rod. Since the amount of AB being fed to the zone is same as the amount of AB_2 solidifying out, it is insufficient to compensate for the decreasing concentration of B in the zone, and therefore, the zone keeps becoming richer in A (Point P_{t2} in Figure 2.9a). This is also reflected in the zone temperature which follows the phase boundary of the two-phase field $L+AB_2$.

When the zone composition reaches the phase boundary of L+AB two-phase field, the desired phase AB becomes stable at the temperature and starts solidifying at the interface (Point P_{t3} in Figure 2.9a). When such a condition is achieved, the zone reaches an equilibrium since the composition being fed into the zone by melting is same as what is solidifying out, even though the zone composition is completely different. The corresponding FZ-grown samples at different stages of the growth are illustrated in Figure 2.9b. Once the zone reaches the end of the feed rod, the translation is stopped, and the zone is frozen by closing the heat source. An example of the final
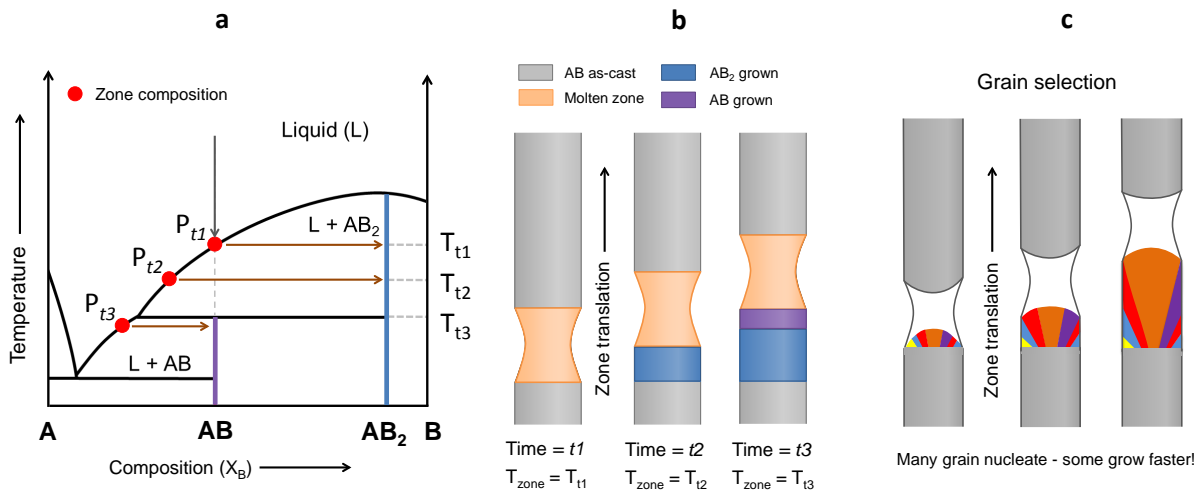
Figure 2.9: Phase dynamics during Floating Zone (FZ) experiment (a) Phase diagram with incongruent melting condition for a compound AB is shown. The zone composition at different times during growth (time t1<t2<t3) is marked along with the respective zone temperatures. The corresponding growth of sample during FZ growth of AB is shown in (b). (c) Nucleation and grain selection during growth; Each color represents a grain along a different orientation.

grown sample is shown in Figure 2.8.

The situation continues as long as the feed rod lasts, or unless the system is perturbed, e.g., by impurities or imperfections in the feed rod. Thus a large single crystal of an incongruently melting compound can be grown under optimal conditions. It must be stressed that the complexity of phase reactions involved can be very different for different compositions. It is possible that a incongruent melting composition may not be synthesized at all by FZ growth. Nevertheless, the fact that it may be possible to grow a composition which melts incongruently is a definitive advantage.

Grain selection: We would also like to briefly explain how it is possible to obtain a large single crystal by using the FZ growth. At the solidification interface, multiple grains nucleate in the beginning. Depending on the crystal structure, some grains grow faster than the others, as atomic stacking along different planes is associated with different energies. With time, as grains grow bigger, the faster growing grains squeeze out the slower ones. This is termed as grain selection and is illustrated in Figure 2.9c. It need not be the grain that is in the middle grows fastest, as the nucleation is at random unless using a single crystalline seed. If after a growth experiment, the grains are not big enough, the final part of the grown rod itself can be used as seed for the next growth experiment to optimize the grain selection and obtain a single crystal. If the growth parameters have been optimized, a single crystal may also be used as the seed, in order to grow large single crystals along a preferred orientation.

2.2.2.2 Phase diagram information from Floating Zone growth

An important step after the growth process is the analysis of the composition and structure of the quenched zone and other portions of the FZ-grown sample, which may give information on the phase fields and boundaries in the vicinity of the composition, specifically for compositions that do not melt congruently. Analysis of the composition of the grown sample during different parts of the growth gives information about the phase dynamics and reactions that may be taking place at different temperatures.

Such an analysis is particularly useful for systems where phase diagram data is not available, which is commonly the case for quaternary and further multi-component systems. For example, in a typical growth of composition AB in Figure 2.9a, the information about the existence of a single line compound in the vicinity in addition to its composition can be obtained from the initial regions of the growth experiment, since it solidifies out first. It can also distinguished whether the composition is a line compound or a phase-field on the basis of the changes in the composition fo the grown sample, if any.

The composition of the sample that solidifies initially, also gives information of the trend of the liquidus line. In the example of composition AB in Figure 2.9a, since AB_2 solidifies out, it tells us that the liquidus is at a higher temperature at the B-rich side of the composition. Furthermore, tracking the grown compositions can give us an idea of the evolution of the zone composition during the growth. For example, in the scenario illustrated in Figure 2.9a, the information about the solidification of a B-rich composition in the initial stages of the growth, tell us that the molten zone got correspondingly richer in A. An additional advantage of some FZ setups is that the temperature can be monitored *in situ* using a pyrometer. Furthermore, the exact composition at the liquidus once the zone has stabilized can be obtained from the frozen final zone. Based on all the above information, an approximate liquidus line as well the phase fields in the vicinity of the grown composition can be obtained.

Such an analysis of the FZ experiment for a composition which may not even exist would give significant information of the phase reactions and the stable phases involved. Hence, FZ technique allows us to gain a better understanding of the thermodynamics of a given system, even if the growth experiment does not prove successful, and this information may be quite useful in subsequent growth experiments.

We shall now briefly describe the setup of an optical FZ growth equipment.

FZ setup

A couple of different setups are possible for the FZ technique, each with its own advantages and disadvantages. Different heating sources can be used in a FZ experiment. Most common is optical heating, where a light from a high energy lamp is focussed using mirrors, and is thus called optical

FZ technique. Other heat sources include RF heating [187] and laser heating [188], although they are not as widely used.

For an optical FZ equipment, there are 2 different types of possible setups. In a conventional setup, 2-4 ellipsoidal mirrors with halogen lamps at their foci are placed horizontally around the sample chamber, which together act as heating source [189]. The higher the number of mirrors used in a horizontal setup, the more homogeneous is the heating all around. In contrast, the vertical FZ setup developed at MPEI Moscow by Balbashov et al. [190] involves two ellipsoidal mirrors placed vertically above and below the sample chamber such that the sample lies in the focus of the upper mirror, and a xenon arc lamp is at the focus of the lower mirror. A schematic of the setup is shown in Figure 2.10a (reproduced from [191], also see [192]). The 3-7 kW lamp may be used in such a setup, and thus depending upon the absorption characteristic of a sample, the temperature may reach up to 3000 °C. Furthermore, since all the light is focussed on the sample using one mirror, the heating is axially homogeneous. For the present work, a similar vertical FZ setup developed at IFW Dresden [193] was used, in addition to a URN-2ZM furnace from MPEI Moscow [190] for certain experiments.
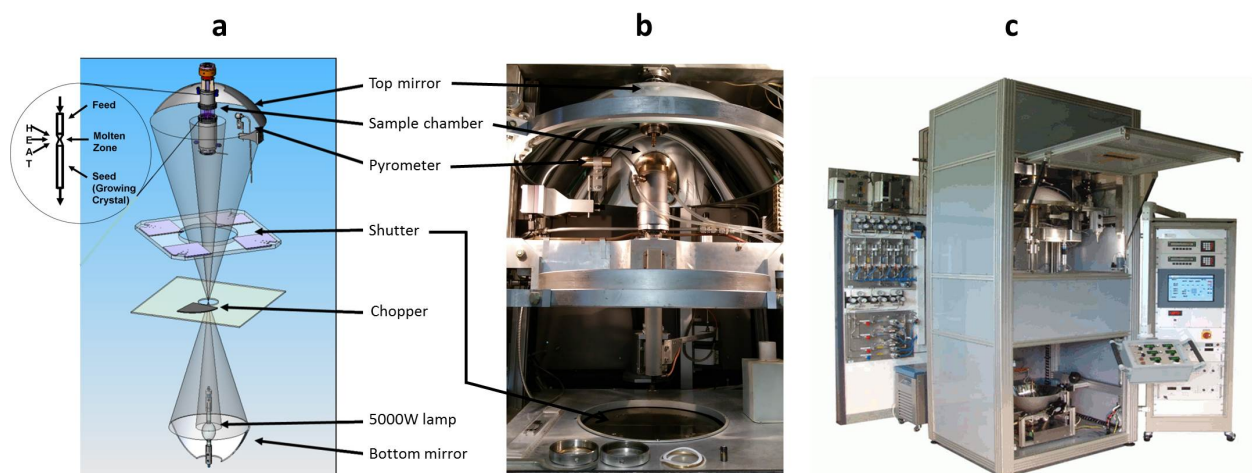
Figure 2.10: Floating Zone setup (a) Schematic of a vertical two-mirror setup (reproduced from [191]) (b) Photograph of the top-half of the furnace (b) Photograph of vertical FZ setup at IFW Dresden (reproduced from [194]).

The vertical setup has a couple of additional advantages. A rotating chopper is used to cut the light for a millisecond, as shown in the schematic, and the temperature is measured *in situ* using a two-colour pyrometer. There is no perceptible change in the heating profile and the sample as well as the zone do not feel the stopping of light for such a short time, which is done once or twice in a minute. The temperature measurement allows for 'almost' real time data on the temperature of zone, which is helpful to understand the thermodynamics, as already mentioned. The pyrometer

can also be moved to a certain extent and the thermal profile along the zone can be measured. The temperature profile along the zone determines the viscosity and surface tension of the molten liquid, which affects the zone shape. The zone shape and the thermal profile across the solidification front in particular, affects the shape of the solid-liquid interface, which is also an important factor towards grain selection and a bad interface may even lead to unwanted nucleation [192].

Another advantage of the vertical FZ setup is that the optical window that is required at the sample chamber is much smaller as compared to the horizontal mirror setup. It is therefore possible to go up to 50 bar pressure during the growth experiment while using a normal quartz window. The quartz can be replaced with a sapphire single crystal window, which allows for up to 150 bar pressure during the growth experiment [195]. Such high pressures are specially helpful during the growth of volatile or high-pressure stabilized materials [196]. Moreover, pressure being a thermodynamic variable, can also be used to possibly alter the phase instability as well as to suppress the phase transformations [195, 197].

It is important to mention that there are some disadvantages to the FZ process as well. It is not ideal to work with volatile materials, although as has been mentioned, can be overcome or minimized by using high pressure, depending on the material. There is also a quite high technical difficulty associated with the technique. Moreover, quite a large amount of sample material is required even for a trial growth, in order to make the feed and seed rods. It is therefore not optimal to work with compositions with costlier constituents such as Ir or Rh, for example.

In spite of the certain disadvantages mentioned above, FZ technique is most suited to grow incongruently melting Heusler compounds, and therefore has been utilized in this work. We shall now give brief information on the different experimental techniques for characterization and physical property measurements.

2.3 Techniques for characterization and measurement of physical properties

We have utilized various experimental techniques to characterize the samples structurally as well to measure their physical properties. First, the various techniques of sample characterization are briefly discussed, and in the end, the various experimental techniques used in the present work are mentioned.

Scanning electron microscopy (SEM) and electron backscattered diffraction (EBSD)

Electron microscopy allows us to study the intrinsic microstructure of the material at different length-scales. Various matter interactions occur upon exposure to electrons, which are probed by different detectors. The corresponding modes of operation give complementary information about the material, such as topography from secondary electrons (SE mode), chemical contrast from back-scattered electrons (BSE mode) as well as spectroscopic analysis using the emitted X-rays (EDX). In order to study the microstructure, the samples were first embedded in a non-conducting resin and then subsequently wet polished. Microscopy for all the samples was done using a NOVA-NANOSEM (FEI) high resolution scanning electron microscope (SEM) with an energy-dispersive X-ray (EDX) analyser. Additiona landscape images of the frozen zones from FZ experiments were taken using Philips XL30 electron microscope by Mrs. Sabine Müller-Litvanyi at IFW Dresden.

Electron Backscattered Diffraction (EBSD) technique was used for higher resolution images as well to characterize the structure of secondary phases at small length scales. The EBSD measurements were carried out using a FEG-SEM Ultra 55 Plus (Zeiss) with a Nordlys F detector and Oxford Instruments HKL Channel 5 data acquisition software package. The EBSD measurements are courtesy of Dr. Horst Wendrock at IFW Dresden.

Transmission electron microscopy (TEM)

In order to confirm the homogeneity of a sample, Transmission electron microscopy (TEM) was performed which allowed us to probe the atomic length-scales. As the name implies, TEM is done in transmission mode, and therefore extremely thin samples are needed for measurements, which were prepared by focused ion beam (FIB) milling by means of a Crossbeam SEM/FIB 1450 XB (Zeiss) with Ga ion-beam for milling at 5-30 kV. In addition to the microstructural and spectroscopic analysis of the material using TEM, precise structural analysis can also be done in a very local area using electron diffraction. The sample preparation for the TEM measurements were by Mrs. Dina Lohse and Ms. Tina Sturm at IFW Dresden. The TEM measurements were performed on two different setups, a CM-20 field emission gun (FEG) TEM operating at 200 kV equipped with an energy-dispersive X-ray (EDX) analyzer and a FEI Titan 80–300 fitted with a CEOS CETCOR

third order spherical aberration corrector operated at an electron acceleration voltage of 80 kV. The TEM measurements were courtesy of Dr. Maria Dimitrakopoulou, Dr. Felix Börrnert and Marcel Haft at IFW Dresden, for different samples respectively.

X-ray diffraction (XRD)

Analysis of X-ray diffraction (XRD) is an important tool to study the structure of a material. Since various features such as disorders affect the specific intensities of superlattice reflections, a precise analysis can give a lot of information on the material. The diffraction data is also affected by various microstructural features such as defects and strain in the material, and the respective information can be extracted as well using a detailed analysis. XRD on powdered samples was performed using a STOE STADI diffractometer in transmission geometry with Mo K_α radiation from Germanium monochromator and DECTRIS MYTHEN 1K detector. In order to perform the powder investigations, the samples were crushed by hand using a stainless steel mortar and pestle. For the purpose of Rietveld refinement of the XRD data, FullProf software package was used [198].

Differential thermal analysis (DTA)

Differential thermal analysis (DTA) is a form of calorimetric technique where a sample and an inert reference are subjected to a heating or cooling profile under identical conditions and the temperature difference between them is measured. Any change in the sample, such as phase transitions, melting etc which occur through an endothermic or exothermic process can be detected relative to the reference. The associated enthalpy change can be calculated from the measurement as well. In many setups, it is also possible to measure the mass change in the sample with temperature against the reference, and this is known as thermogravimetric analysis (TGA). For our measurements, a Setaram TAG High Performance Symmetrical TGA System was used which is a high precision DTA setup for high temperature measurements in controlled environments. The DTA measurements were performed by Mr. Jochen Werner at IFW Dresden.

Nuclear magnetic resonance (NMR)

Electronic structure of an atom is affected by the local hyperfine fields which can be probed using radio frequency (RF)-pulses in the presence of a high external field. Nuclear Magnetic Resonance (NMR) probes the local environments of an NMR-active species, e.g., Co. For a ferromagnet, the local crystal fields are sufficiently large and an external field is not needed. In such a case, the local fields around an atom in a lattice are determined by the nearest and next-nearest neighbours which can be analysed (refer to [64, 66] for further details). Thus, NMR is much more sensitive to defects and disorders, as compared to X-rays for example, and allows us to quantify the extent of disorder. Since we are dealing with Co-based Heusler compounds, which are strongly ferromagnetic, zero-field

NMR has been performed to calculate the disorder in our samples. The NMR measurements are courtesy of Dr. Alexey Alfonsov at IFW Dresden.

Measurement of physical properties

The magnetic properties were investigated by a Quantum Design MPMS-XL-5 superconducting quantum interference device (SQUID). Magnetization up to 1200 °C was measured using a high temperature setup of a standard Vibrating Sample Magnetometer (VSM). Specific heat measurements were performed using Quantum Design physical property measurement system (PPMS). The specific heat measurements are courtesy of Steven Rodan at IFW Dresden. The thermal and electrical transport measurements were performed using a 4-point probe. These measurements are courtesy of Frank Steckel at IFW Dresden.

Annealing experiments

In addition to the various techniques of sample preparation and experimentation mentioned in this chapter, annealing experiments were performed as well. In order to perform annealing procedures, samples were sealed in quartz ampoules, after evacuation to at least 2.10^{-5} mbar pressure. Each ampoule was also back filled with argon, but kept at a slightly lower pressure than ambient pressure. The annealing was carried out in calibrated box furnaces and the sample was cooled down to room temperature subsequently. If a high cooling rate was needed, the sample was quickly taken out of the furnace and quenched in water.

So far, we have discussed the various aspects of Heusler compounds and its properties. In addition, the sample preparation and experimental techniques used in the present work have been described. Apart from that, the details of relevant aspects of thermodynamics and material science have been given, in order to aid the reader in better understanding of the complete text. Some specific details have not been mentioned so far, as they are only application to specific parts of the thesis, and shall be introduced or described in the respective sections. We shall now move on to the results and discussion. As mentioned earlier, two different aspects of material-property correlation have been studied in this work, each on a different Heusler system. Observations and results related to the quaternary $Co_2Cr_{1-x}Fe_xAl$ series are first discussed.

Chapter 3

$Co_2Cr_{1-x}Fe_xAl$: Towards a Novel Half-Metallic Ferromagnet

3.1 Introduction and motivation

$Co_2Cr_{1-x}Fe_xAl$ quaternary Heusler system, a substitution series between Cr and Fe at the Y ($4a$) sublattice, has been well studied in literature. It has been predicted to be a half-metallic ferromagnet along the whole series [5–7] and as a result, has attracted much attention in the research community. In addition, unlike most other Co-based Heusler compounds, a van-Hove singularity has been calculated in the majority spin direction which is beneficial for applications as well as for the detection of high spin polarization [109] (see Section 1.3.1.1).

There is an additional aspect of $Co_2Cr_{1-x}Fe_xAl$ which makes it even more interesting. As has been already discussed, electronic structure can be strongly affected by disorder, which is always present to some extent in a material. In most cases, disorder leads to a reduction in spin polarization which can be considerably large for specific types of disorder. In the $Co_2Cr_{1-x}Fe_xAl$ series, the composition $Co_2Cr_{0.6}Fe_{0.4}Al$ is predicted to be 100 % spin polarized where the Fermi energy lies in the middle of a wide band gap [6] (Figure 3.1). Due to this, it is expected to be much less susceptible to disorder effects, making $Co_2Cr_{0.6}Fe_{0.4}Al$ the composition of main interest. The wide band gap in the density of states (DOS) for $Co_2Cr_{0.6}Fe_{0.4}Al$ gives a possibility to retain 100 % spin polarization at higher temperatures, as the depolarization effects scale with temperature leading to shrinkage of the band gap at higher temperatures [88]. Furthermore, being a Co-based Heusler system, it also boasts of high Curie temperatures, which is advantageous towards realization of half-metallicity at elevated temperatures. Therefore, $Co_2Cr_{0.6}Fe_{0.4}Al$ has the most robust half-metallic ferromagnetism in the whole $Co_2Cr_{1-x}Fe_xAl$ series [109] and possibly one of the most robust in the whole class of Heusler compounds. Thus, $Co_2Cr_{1-x}Fe_xAl$ is a highly promising system towards realization of half-metallic ferromagnetism at elevated temperatures as well as for applications.
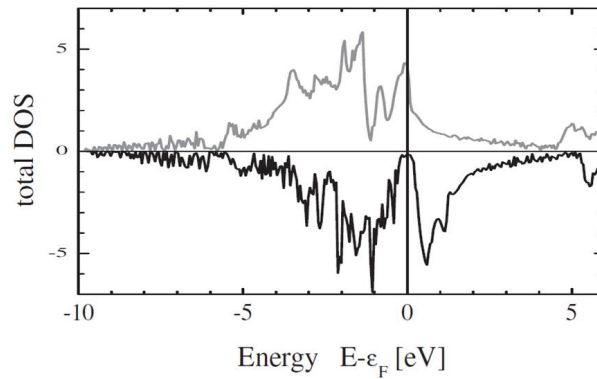
Figure 3.1: Spin-resolved density of states (DOS) for Co$_2$Cr$_{0.6}$Fe$_{0.4}$Al Heusler compound (reproduced from Felser et al. [6]).

Unfortunately, numerous difficulties and inconsistencies have been reported with respect to the different physical properties. A maximum powder magnetoresistance of 88 % at 295 K [199], as well as a maximum tunnel magnetoresistance of 101% at 4 K [200] has been observed. Furthermore, only a maximum of 81% spin polarization is calculated from magnetoresistance [201]. Large deviations between the band structure calculations and the electronic structure of bulk Co$_2$Cr$_{1-x}$Fe$_x$Al samples as well as the measured magnetic properties are found and until now, have been attributed to anti-site disorder [202, 203]. However, the large difference cannot be fully accounted for by such defects, even by assuming complete disordered structure, e.g., as has been calculated by Miura et al. [40]. Formation of paramagnetic clusters observed in Mößbauer spectroscopy for annealed and subsequently quenched polycrystalline Co$_2$Cr$_{0.6}$Fe$_{0.4}$Al samples [204] have been suggested as an alternative explanation for the reduction of the magnetic moments, but the reason for their formation has so far not been clarified.

Element-specific magnetic moments from X-ray magnetic circular dichroism (XMCD) measurements on annealed polycrystalline Co$_2$Cr$_{0.6}$Fe$_{0.4}$Al samples show a considerable difference from theoretical values which has also been attributed to anti-site disorder [205]. Similar mismatch in the magnetic data, especially at the Cr-rich side, has also been observed for films of Co$_2$Cr$_{1-x}$Fe$_x$Al [206, 207]. An even further reduction of magnetic moment was observed in annealed bulk samples which were slowly cooled rather than quenched after annealing, which were attributed to secondary phases observed by neutron diffraction in those samples [204]. Furthermore, thermal transport measurements on both bulk as well as thin films show that the compositions on the Cr-rich side of Co$_2$Cr$_{1-x}$Fe$_x$Al are semiconducting in nature where as the Fe-rich side is metallic [208–210]. No clear understanding exists towards the reason for this change in resistivity. So far, the above mentioned issues have neither been specifically addressed, nor completely accounted for. Some theories related to inherent magnetism of the system have been put forth, but are not coherent in explaining all the problems reported in literature.

Apart from the aforementioned inconsistencies with the measured physical properties, there have been other issues related to the material properties and synthesis of $Co_2Cr_{1-x}Fe_xAl$ as well. Bulk polycrystalline $Co_2Cr_{1-x}Fe_xAl$ samples have been reported to be phase-segregated, and increase in the Fe content leads to reduction in the inhomogeneity [202]. The segregated samples contained two cubic phases, although additional non-cubic impurity peaks have been reported on the Cr-rich side after annealing [202]. A transmission electron microscopy (TEM) study of polycrystalline $Co_2Cr_{1-x}Fe_xAl$ samples also shows phase segregation even at the nanoscale [211, 212].

Element selective X-ray absorption spectroscopy photoelectron emission microscopy (XAS-PEEM) imaging of the $Co_2Cr_{0.6}Fe_{0.4}Al$ surface shows a similar Cr-rich inhomogeneity [213]. On the other hand, a hexagonal closed packed (hcp) phase has been observed in $Co_2Cr_{1-x}Fe_xAl$ thin films [214], and a phase segregation is likewise observed through TEM [215]. Unidentified reflections or shoulders on certain reflections have also been observed by X-ray diffractometry in thin films with similar stoichiometry [206, 216, 217], although they have not been addressed.

It seems that the discrepancies with physical property measurements on $Co_2Cr_{1-x}Fe_xAl$ are most likely related to the phase stability and chemical segregation in the system. However, so far no detailed study has been done in this regard and the different investigators observe very different phases, in terms of both structure and morphology. The present work focuses on the intrinsic material attributes of the $Co_2Cr_{1-x}Fe_xAl$ system, and attempts to develop a better understanding of the material-property correlation, as a step towards realization of a half-metallic ferromagnet. We begin by presenting our work pertaining to Floating Zone (FZ) growth of selected compositions in the $Co_2Cr_{1-x}Fe_xAl$ series, towards a better understanding of the thermodynamics in the system.

3.2 Phase dynamics in Co$_2$Cr$_{1-x}$Fe$_x$Al: Understanding the anomalous properties

To summarize what we have seen in the literature, there is possibly a chemical instability in the sample that leads to inhomogeneity, which in turn is likely responsible for the anomalous physical properties (see previous section). In order to understand the fundamental evolution of a measured physical property as well as experimental realization of theoretical calculations, a phase-pure homogeneous sample is mandatory. Therefore, first and foremost, any issues with the Co$_2$Cr$_{1-x}$Fe$_x$Al system must be addressed, before the measurements can be compared to theory.

In order to obtain a phase-pure sample as well as study the phase dynamics in the system, samples have been synthesized and studied using different techniques. Three compositions in the Co$_2$Cr$_{1-x}$Fe$_x$Al series were chosen: the ternary end members Co$_2$CrAl and Co$_2$FeAl, along with the main composition of interest, Co$_2$Cr$_{0.6}$Fe$_{0.4}$Al. We first present the results on polycrystalline samples, and confirm that the material suffers from chemical segregation due to incongruent melting. As discussed in Chapter 2, the Floating Zone (FZ) technique is the technique of choice to grow such incongruently melting intermetallic compounds. We have grown the selected compositions using the FZ technique, and as we shall see later in this section, significant progress has been made towards understanding the phase reactions in the Co$_2$Cr$_{1-x}$Fe$_x$Al system [218].

3.2.1 Polycrystalline as-cast samples

Polycrystalline samples of Co$_2$CrAl, Co$_2$FeAl and Co$_2$Cr$_{0.6}$Fe$_{0.4}$Al were prepared using the arc-melting setup (for details, refer to Section 2.2.1), with at least 4N pure constituents. Figure 3.2 shows the back-scattered (BSE) images from the scanning electron microscopy (SEM) for the three compositions. All the samples showed phase segregation similar to that reported in literature [202].
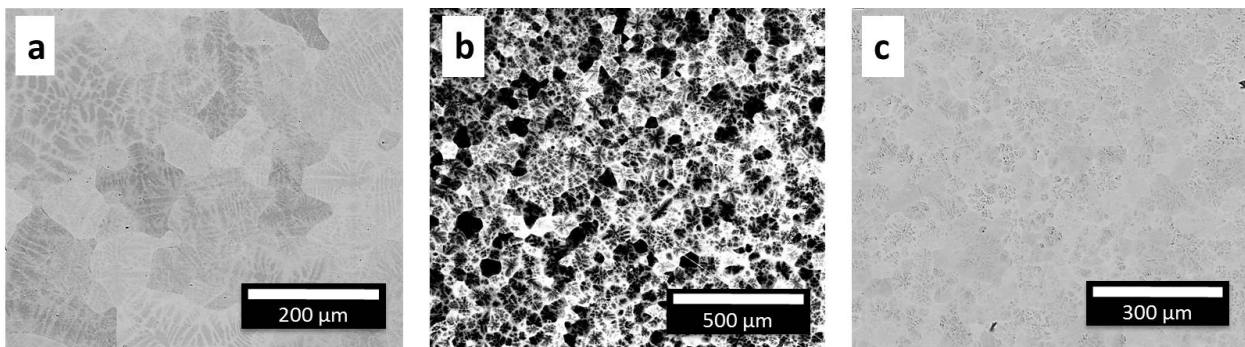
Figure 3.2: Backscattered electron (BSE) images from scanning electron microscopy (SEM) for as-cast polycrystalline samples showing phase segregation (a) Co$_2$FeAl, (b) Co$_2$CrAl and (c) Co$_2$Cr$_{1-x}$Fe$_x$Al.

The energy dispersive X-ray spectroscopy (EDX) measurements from SEM for all the phases are given in Table 3.1. As-cast Co$_2$FeAl sample solidifies into Fe-rich dendrites surrounded by an Al-rich phase with only a small difference in composition ($\sim$5 atomic %). On the other hand, in Co$_2$CrAl, dendritic phase segregation is into a Cr-rich phase and an Al-rich phase. The two phases are significantly different in composition ($\sim$15 atomic %), which can also be seen in the strong chemical contrast in the BSE image (Figure 3.2). Co$_2$Cr$_{0.6}$Fe$_{0.4}$Al also segregates into a Cr-rich phase and an Al-rich phase although the difference in the composition of the two phases is smaller than in Co$_2$CrAl, which is reflected in the BSE image as well.

Table 3.1: Energy dispersive X-ray spectroscopy (EDX) data (atomic %) from SEM for polycrystalline Co$_2$FeAl, Co$_2$CrAl and Co$_2$Cr$_{1-x}$Fe$_x$Al samples.

	Sample	Co	Cr	Fe	Al
Co$_2$FeAl	Nominal	50	–	25	25
	Al-rich phase (dark)	47±0.1	–	21±0.1	32±0.5
	Fe-rich phase (light)	49±0.6	–	26±0.2	25±0.4
	Overall	48	–	24	28
Co$_2$CrAl	Nominal	50	25	–	25
	Cr-rich phase (light)	48±0.2	31±0.3	–	21±0.2
	Al-rich phase (dark)	49±0.7	17±0.4	–	34±0.6
	Overall	48	24	–	28
Co$_2$Cr$_{0.6}$Fe$_{0.4}$Al	Nominal	50	15	10	25
	Cr-rich phase (light)	48±0.3	19±0.5	12±0.4	21±1.1
	Al-rich phase (dark)	48±0.3	13±1.0	10±0.3	29±1.5
	Overall	48	16	11	25

An error of $\sim$2 atomic % is associated with the EDX measurement.

The X-ray diffraction (XRD) data for the as-cast samples is shown in Figure 3.3a. All three compositions have cubic structure with complete *B2*-type disorder ($Pm\bar{3}m$) and therefore no (111) reflection is seen. Although, two phases are present in all the samples, additional reflections or satellites are not observed. It seems that both phases have very similar lattice constants leading to overlapped reflections in the XRD pattern. If we only look at the XRD data, the sample can easily be misunderstood as consisting of a single phase. It is therefore important to observe the microstructure at micro- and nanoscale, in different regions, in order to confirm the phase purity of a material.

Since the reflections overlap, it is also not possible to accurately deconvolve the individual lattice constants during refinement. Hence, the XRD data were refined with a single $Pm\bar{3}m$ phase, and thus only an average lattice constant could be determined which is summarized in Table 3.2. The XRD data with refinement along with the details of the refinement are given in Appendix A (Page 145-146).
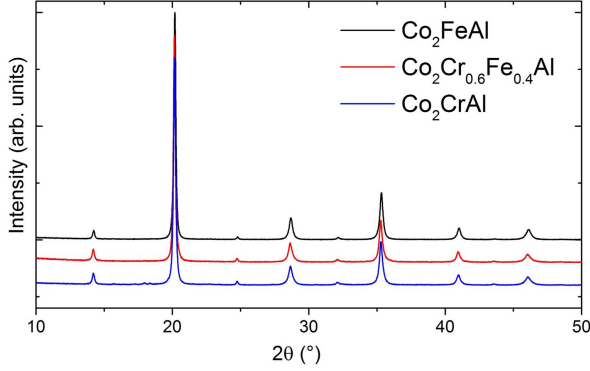
Sample	Space group	Lattice (Å)
Co$_2$FeAl	$Pm\bar{3}m$	2.863(2)
Co$_2$Cr$_{0.6}$Fe$_{0.4}$Al	$Pm\bar{3}m$	2.867(2)
Co$_2$CrAl	$Pm\bar{3}m$	2.866(2)

Figure 3.3: X-ray diffraction data for as-cast Co$_2$FeAl, Co$_2$Cr$_{0.6}$Fe$_{0.4}$Al and Co$_2$CrAl samples.

Table 3.2: Refinement of X-ray diffraction for as-cast Co$_2$FeAl, Co$_2$Cr$_{1-x}$Fe$_x$Al and Co$_2$CrAl samples.

The morphology and composition of the two phases in all three samples confirm the scenario of incongruent melting (refer to Section 2.1.1.1 for details). In order to overcome the issue of incongruent melting, Floating Zone (FZ) growth was undertaken for the three compositions.

3.2.2 Growth via Floating Zone technique

FZ growth experiment requires seed and feed rods of the intended stoichiometry as precursor, as was detailed in Section 2.2.2. Polycrystalline seed and feed rods of Co$_2$FeAl, Co$_2$CrAl and Co$_2$Cr$_{1-x}$Fe$_x$Al were cast (refer Section 2.2.1.1 for details) with at least 4N pure constituents. The subsequent FZ experiments were performed in an Ar atmosphere. The growth speeds employed were 2-5 mm/hr along with a counter-rotation of seed and feed rod of the order of ∼0.3 Hz. The final zone was quenched in order to study the zone composition. Multiple experiments were performed for each composition for reproducibility. Final growth rods for one set of such experiments are shown in Figure 3.4.

Despite the high purity atmosphere during the growth, a thin layer of surface oxidation is observed which can be seen in Figure 3.4. A shiny surface was observed in the final part of the growth rod. Samples were studied from different positions of the grown rods but no traces of oxygen are observed in any sample, beyond the resolution of the SEM.

Upon inspection of the quenched final zones, the growth interface is found to be convex in all
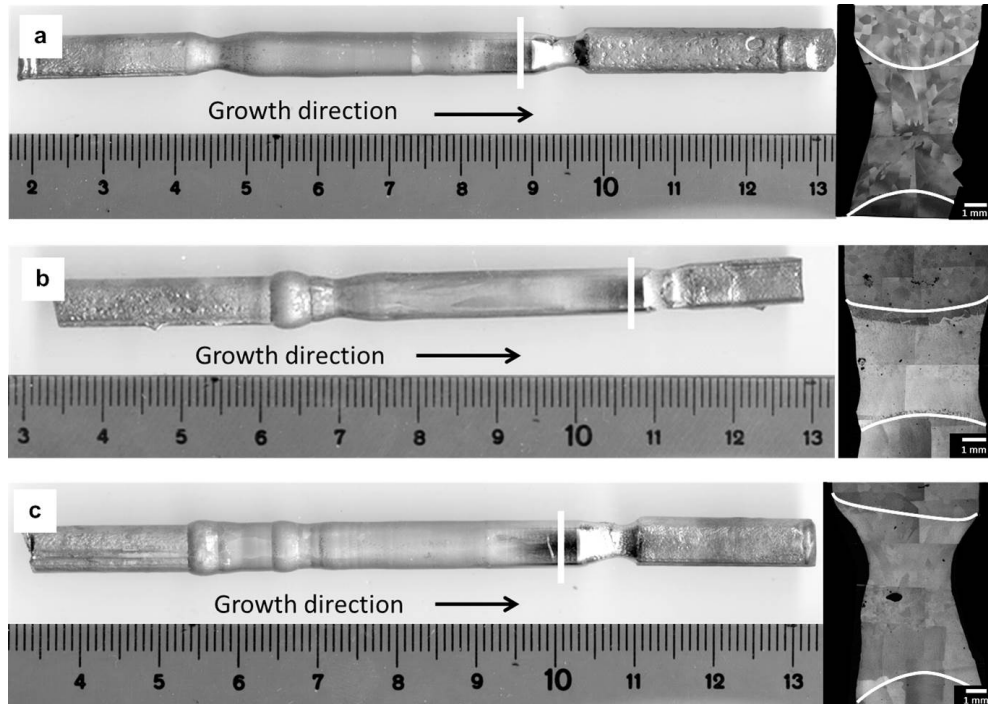
Figure 3.4: Floating Zone (FZ)-grown samples (a) Co_2FeAl (b) Co_2CrAl, and (c) $Co_2Cr_{0.6}Fe_{0.4}Al$ along with the corresponding frozen zones. Vertical white lines on the grown sample mark the area from where samples were taken for the study. The interfaces in the zone cross-sections have been marked with white lines for clarity.

three cases, as indicated by white lines in Figure 3.4. A convex interface is preferable over a concave interface, since a concave interface enhances the defects in the growing sample and may lead to additional nucleation during growth [192]. Behr et al. also recommend a less-curved interface for an optimal growth [192]. The feed and seed rod rotation speeds employed in our FZ experiments, has been based on their work, and as a result shallow interfaces have been obtained (Figure 3.4).

Detailed compositional analysis was performed on the frozen zones for all three compositions. For Co_2FeAl, the final zone has no substantial enrichment of elements. The average melt temperature of the stabilized zone during growth of Co_2FeAl was ~1510 °C. On the other hand, the overall composition in the frozen zone for Co_2CrAl growth is found to have excess Cr (~5 atomic %, at the cost of Al), whereas samples from the beginning of the growth are found to be enriched in Al to the same extent, which is in agreement with the liquidus projection [182]. This is easily understood from the similar chemical inhomogeneity due to element segregation seen in the case of polycrystalline as-cast samples (page 46). The average melt temperature of the stabilized zone during growth of Co_2CrAl was ~1540 °C. The zone for $Co_2Cr_{0.6}Fe_{0.4}Al$ is also enriched in Cr but to a lesser extent (excess of ~2 atomic % at the cost of Al) and samples from the beginning of the growth have an excess of Al overall. Samples from the later part of the growth have an overall nominal composition

confirming a stable growth. The average melt temperature of the stabilized zone during growth of $Co_2Cr_{0.6}Fe_{0.4}Al$ was also ~1540 °C similar to that of Co_2CrAl.

As has been described already in Section 2.2.2.2, tracking the zone temperature along with the composition in the zone as well as different parts of the grown sample, can give us information about the different boundaries in the phase diagrams and their extent. We shall demonstrate this briefly for the case of Co_2CrAl. The following discussion will be along the lines of a CoAl-CoCr pseudo-binary phase diagram, as changes in composition was only observed for Al versus Cr along the grown rod and in the zone, whereas the Co concentration remained the same throughout. Please note that this view is certainly oversimplified, but nevertheless adds to the understanding.
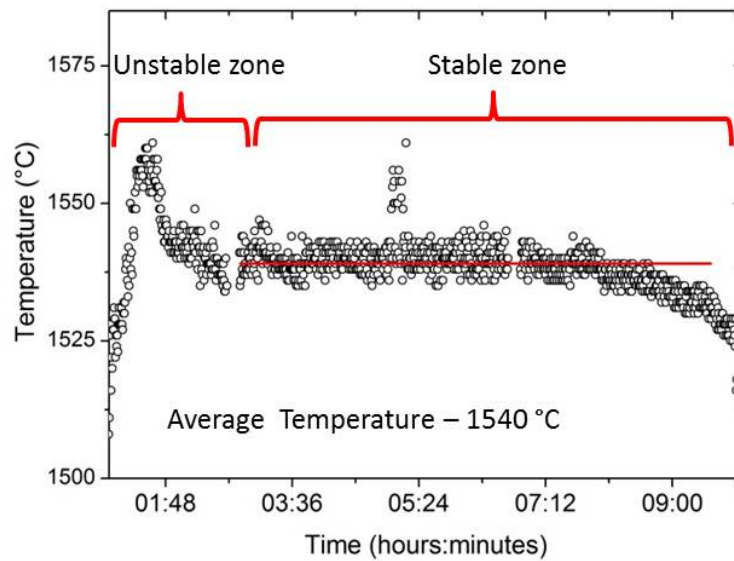
Figure 3.5: Temperature of the molten zone measured *in situ* during Floating Zone growth of Co_2CrAl. Average temperature of the zone during the experiment was found to be ~1540 °C.

Figure 3.5 shows the *in situ* measurement of zone temperature for FZ growth of Co_2CrAl. In the figure, initial increase in the zone temperature is due to the melting and zone formation stage. Even after the zone was formed, it was unstable, since the nominal composition melts incongruently, as was confirmed in polycrystalline samples. The sample that solidified first had higher Al concentration and the zone was found to be rich in Cr. Also, the zone temperature went down as time progressed. This means the liquidus temperature is high at the Al-rich side and reduces as the Cr content increases. Also, a likely peritectic reaction ($Liquid + Solid_1 \rightarrow Solid_2$) is present at the Cr-rich composition in the phase diagram with reference to the nominal Co_2CrAl. After about two hours, the zone had stabilized which could be clearly seen in the corresponding zone temperature measured during the growth. The average temperature of the zone during most part of the stable growth was approximately 1540 °C. The temperature slightly dropped in the last hour possibly due to

evaporation of impurities or volatile oxides and subsequent deposition on the quartz window of the growth chamber. However, no substantial effect of the evaporation was seen in the grown sample and the overall composition was nominal within the error of EDX measurements.

As we have demonstrated, FZ growth can give us more insight into the phase diagram specially near the liquidus, as compared to most of the sample preparation techniques, which can help us in further experiments as well as in understanding of the system as a whole. We shall move on to a detailed characterization of grown samples of each composition. For the discussion on the material, samples were taken from the end of the growth process marked by vertical white lines on the grown rods in Figure 3.4. All data from here onwards would refer to those samples unless otherwise stated.

3.2.2.1 Floating Zone growth of Co_2FeAl

The FZ-grown Co_2FeAl sample was found to be homogeneous and phase-pure and the composition was nominal within the acceptable error (<2 atomic %) of the SEM-EDX measurement as shown in Figure 3.6a. We did not obtain a single crystal, although mm-sized coarse grains were observed in the final cross-section. The grain selection during growth was clearly not optimal.

EDX data	Co	Fe	Al
Nominal	50	25	25
Average	50±0.5	26±0.6	24±0.4
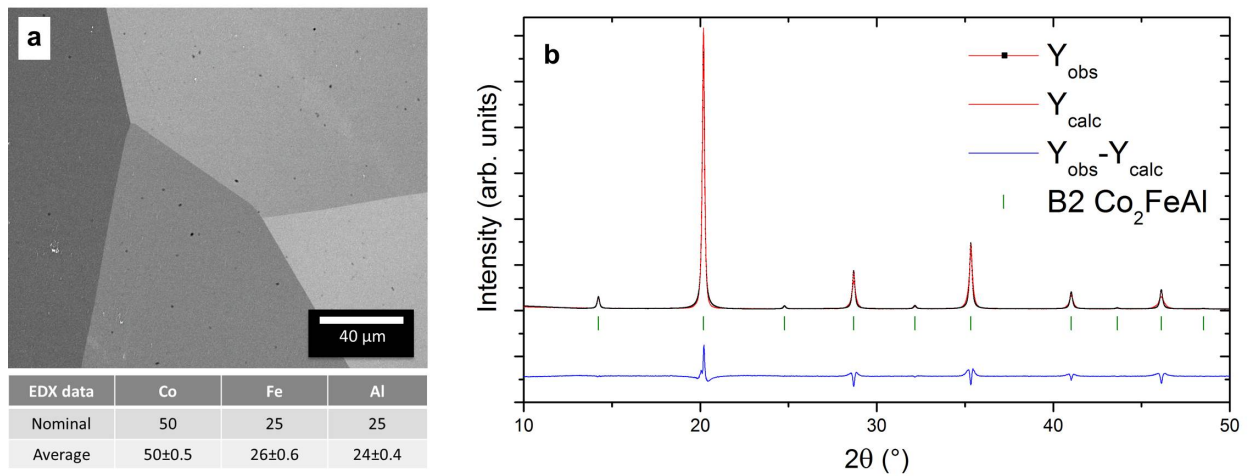
Figure 3.6: Floating Zone (FZ)-grown Co_2FeAl (a) BSE image along with the average EDX data (b) X-ray diffraction pattern with refinement.

The sample had a cubic crystal structure, same as that observed for as-cast sample, as seen in the XRD data (Figure 3.6b). Since (111) superlattice reflection unique to $L2_1$ order was not observed, the sample had complete $B2$-type order (refer section 1.2.2). The XRD data was analysed for $Pm\bar{3}m$ space group and the lattice constant was found to be 2.863(4) Å using Rietveld refinement, details of which are summarized in Appendix A (Page 147).
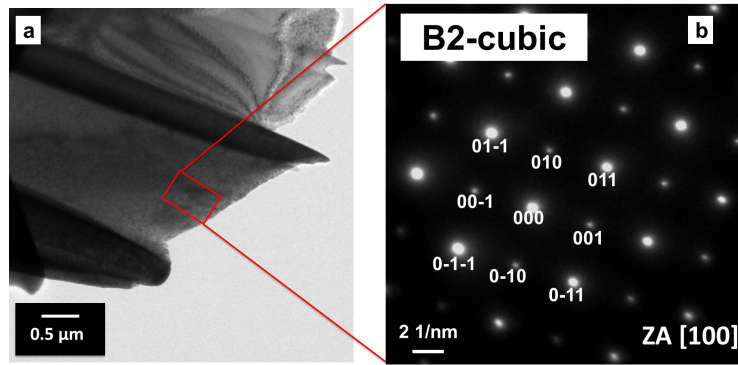
Figure 3.7: Floating Zone (FZ)-grown Co$_2$FeAl (a) High resolution transmission electron microscopy (HRTEM) image (b) Selected area (electron) diffraction (SAED) pattern of a small region marked with red square. (TEM data courtesy of Dr. Maria Dimitrakopoulou)

The sample homogeneity and the *B2*-type structure were further confirmed by TEM (Figure 3.7). Thus, using FZ growth, it was possible to grow phase-pure Co$_2$FeAl which was earlier found to be incongruent melting.

3.2.2.2 Floating Zone growth of Co$_2$CrAl

The FZ-grown Co$_2$CrAl sample was found to have an unexpected microstructure containing two-phases, as shown in Figure 3.8a. It consists of an interconnected basket-weave pattern of a secondary phase in the matrix of the primary phase. The feature size of the corresponding phases was too small (∼100-200 nm) to accurately measure individual composition using SEM-EDX without signal getting mixed from the other phase. Only an average measurement could be done, and was found to be nominal within the error of the equipment.
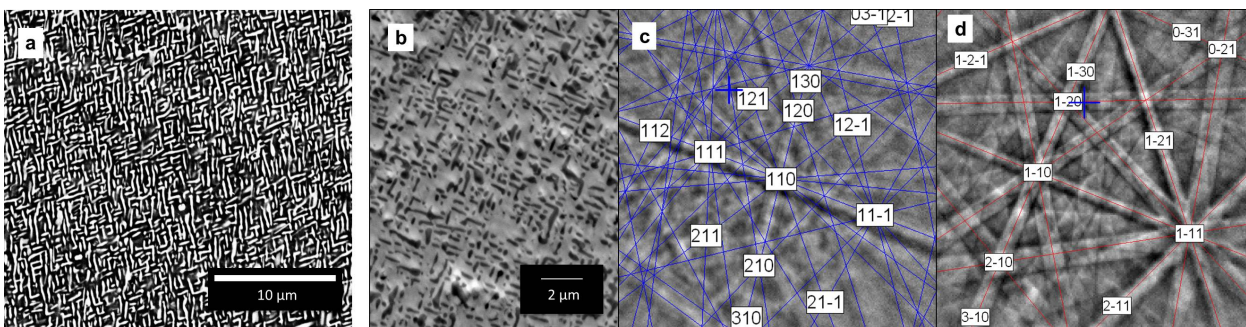
Figure 3.8: Floating Zone (FZ)-grown Co$_2$CrAl (a) BSE image (b) BSE image in tilted position for electron back-scatter diffraction (EBSD) (c) EBSD pattern of the matrix consistent with cubic symmetry (d) EBSD pattern of the secondary phase consistent with tetragonal symmetry. (EBSD data courtesy of Dr. Horst Wendrock)

The corresponding XRD pattern (Figure 3.9) indicates a tetragonal splitting of the main reflection (220) which fits well to a σ-CoCr phase. A similar tetragonal splitting was observed earlier by de Teresa et al. [202], albeit in an annealed polycrystalline sample.
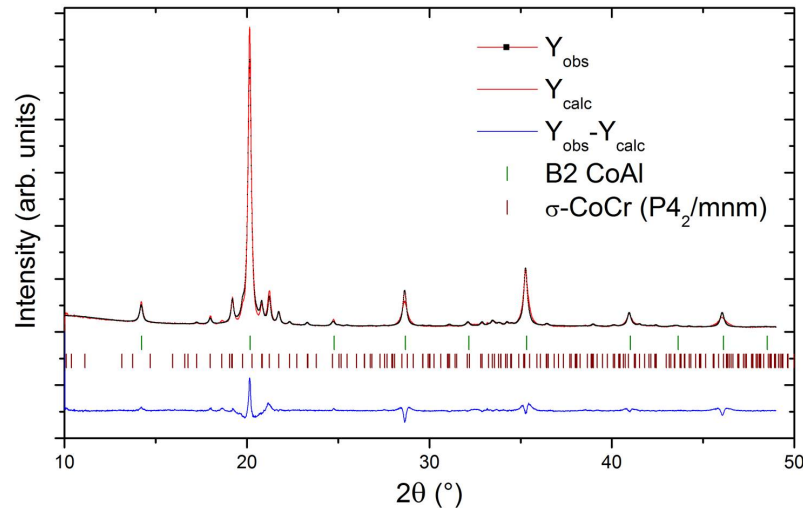
Figure 3.9: X-ray diffraction pattern with refinement for Floating Zone (FZ)-grown Co_2CrAl.

We performed EBSD measurements to shed further light on the structure and orientation of those phases (Figure 3.8(b-d)). The data were consistent with a tetragonal σ-CoCr secondary phase in a CoAl-type *B2* matrix. The matrix was single crystalline, oriented along [-6 -2 1] direction whereas the secondary phase also has one orientation throughout, along [1 0 4] direction. This suggests that a homogeneous single phase was obtained using FZ, which subsequently underwent a solid-state phase transformation at lower temperatures leading to formation of the secondary phase.
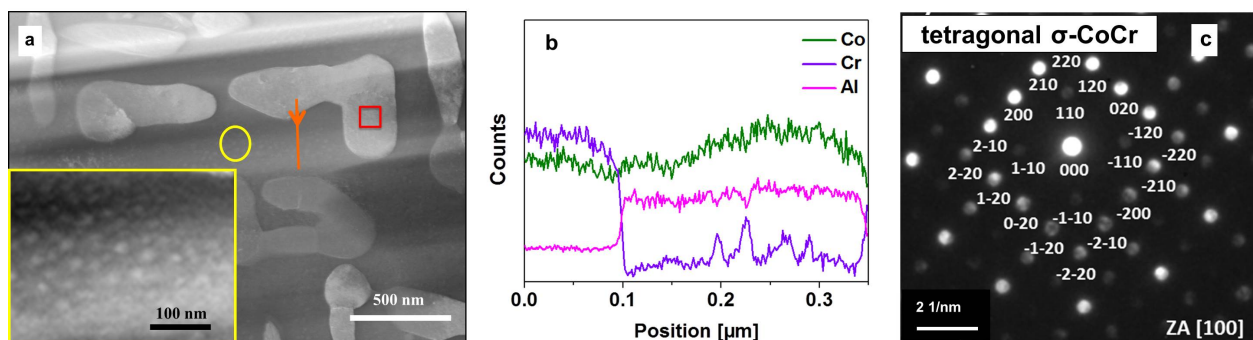
Figure 3.10: Floating Zone (FZ)-grown Co_2CrAl (a) high angle annular dark field (HAADF) scanning transmission electron microscopy (STEM) image; inset: nanoscale segregation (b) EDX-linescan (marked with orange line in (a)) across phase boundary of the secondary phase (c) Nanobeam diffraction for the secondary phase in the region marked in (a) by red square. (TEM data courtesy of Dr. Maria Dimitrakopoulou)

Transmission electron microscopy (TEM) was performed to find out the phase compositions as well as to confirm the structures of the matrix phase and the secondary phase (Figure 3.10). The corresponding phase compositions from TEM are listed ahead in Table 3.3. The average overall composition from SEM is also given for comparison. The secondary phase had a composition of Co$_{46}$Cr$_{53}$, and the structure was tetragonal σ-CoCr phase, confirming the XRD and EBSD data analysis (Figure 3.8d and 3.9). As expected, the matrix was deficient in Cr, since a Cr-rich phase separated out. Even though the composition was not nominal to Co$_2$CrAl, the matrix was CoAl-type *B2* phase.

Table 3.3: EDX data (from transmission electron microscopy (TEM) and scanning electron microscopy (SEM)) along with standard deviation for Floating Zone (FZ)-grown Co$_2$Cr$_{0.6}$Fe$_{0.4}$Al (atomic %). (TEM data courtesy of Dr. Maria Dimitrakopoulou)

Phase	Co	Cr	Al
Nominal	50	25	25
CoAl type *B2*(TEM)	55±0.7	17±0.7	28±0.7
σ-CoCr type (TEM)	46±0.7	53±0.7	01±0.7
Overall average (SEM)	49±0.3	25±0.7	26±1.0

Furthermore, additional chemical segregation in the matrix at a much smaller length-scale than the secondary phase was also observed in TEM, as shown in the inset of Figure 3.10a. In the EDX-linescan across phase boundary of the secondary phase (Figure 3.10b), modulations in the matrix especially for the Cr content, are observed, corresponding to an additional segregation. This segregation was of the order of 10-20 nm especially with respect to the Cr content, and is an order of magnitude smaller than the larger secondary phase. The nanoscale segregation was similar to that observed in an earlier work on annealed polycrystalline samples [211]. Similar modulations in composition, specially Cr, were also noticed in the past for annealed Co$_2$Cr$_{0.6}$Fe$_{0.4}$Al films [219]. We think that this nanoscale segregation may be the starting point of the σ-phase precipitation.

The lattice parameters and the phase fractions of the two phases were analysed by Rietveld refinement of the XRD data and is summarized in Appendix A (Page 147). The cubic matrix ($Pm\bar{3}m$, *B2* type structure) had a lattice constant of 2.867(4) Å while the secondary phase was tetragonal (P4$_2$/mnm, a=b=8.765(4) Å, c=4.536(4) Å). The phase fraction of the secondary phase from the refinement was 21.7±0.5 vol%, which was similar to that obtained from analysis of SEM-BSE images (24±3 vol%) within experimental uncertainty.

The morphology of the secondary phase in FZ-grown Co$_2$CrAl did not appear to have the solidification characteristics of a directional-growth process. The microstructure and the spatially ordered

nature of secondary phase also lacked the characteristics of a conventional phase transformation involving nucleation and growth, which might have taken place in the solid state. Our analysis supports the idea of a *spinodal decomposition* taking place in the material. Before we comment further, it would be pertinent to explain the thermodynamics of spinodal decomposition, which is a very specific type of phase transformation involving localized diffusion.

3.2.2.3 Spinodal decomposition

The spinodal decomposition is a characteristic feature of a miscibility gap in a system. A miscibility gap is a region inside a single-phase field in a phase diagram, where the constituent becomes immiscible due to a thermodynamic instability. Figure 3.11 shows an approximate schematic of a phase diagram with a miscibility gap. The single phase is initially stable at higher temperatures for a large range of compositions. Below a certain temperature, this phase becomes thermodynamically unstable for a given range leading to a region of immiscibility. When a composition in this specific range is cooled and reaches the miscibility gap, quasi-periodic perturbations in the chemical composition, which may be due to, e.g., thermal motion, become stable and grow with time. The compositional variation is dependent on the most stable structure type, based on the constituents. Illustration of the composition evolution along a line for different times ($t_3 > t_2 > t_1$) is also shown in Figure 3.11. The phase separation is very localized as it is diffusion controlled, as well as happens simultaneously throughout the material as opposed to a nucleation and growth mechanism. Such a phenomenon is known as spinodal decomposition.
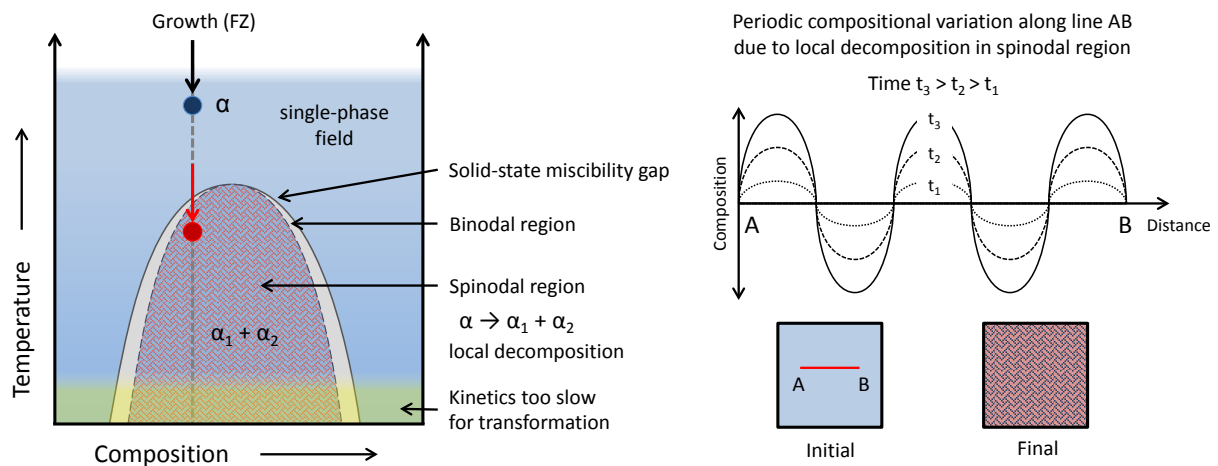
Figure 3.11: Schematic of a phase diagram with a miscibility gap showing the spinodal and binodal regions. Using FZ growth, a single phase is obtained at high temperatures, which undergoes decomposition as it is cooled down. A sketch of compositional evolution along a line during the decomposition process at different times is also shown.

Due to the spinodal decomposition, the system develops an overall periodic-like microstructure, similar to what was observed in the case of FZ-grown Co$_2$CrAl. Initially the evolving secondary phase has the same structure as the matrix and may undergo a structural transformation later to a more stable structure. Moreover, since the atoms need to diffuse very locally, the timescales associated with the such a transformation is very small. It is possible that even if a sample is quenched, there is phase separation at the nano-scale which must be confirmed using TEM.

With regards to our sample, we understand that initially a pure cubic phase solidified from the melt, thanks to the FZ technique, as confirmed by the EBSD data shown in Figure 3.8. As the temperature was lowered and the solid-state miscibility gap was reached, the single phase underwent spinodal decomposition leading to a secondary phase which, at lower temperatures, transformed into a tetragonal CoCr-type phase in a CoAl-type *B2* matrix. The periodic-like nature of the composition variation, which is a feature of a phase transformation via spinodal decomposition (Figure 3.11), was confirmed by the linescan in TEM as shown in Figure 3.10. The orientation-relationship between the matrix and the evolving secondary phase led to the phase having the same orientation everywhere.

We shall now look at the FZ growth of our main composition of interest, Co$_2$Cr$_{0.6}$Fe$_{0.4}$Al, and show that such a scenario is present there as well.

3.2.2.4 Floating Zone growth of Co$_2$Cr$_{0.6}$Fe$_{0.4}$Al

Similar to the Co$_2$CrAl sample, the FZ-grown Co$_2$Cr$_{0.6}$Fe$_{0.4}$Al appeared to be phase-pure at low magnifications, but was also found to be phase segregated upon close examination (Figure 3.12a). The secondary phase was more globular and not interconnected as was in the case of Co$_2$CrAl.

The feature size of the secondary phase is of the order of 50-100 nm, smaller than in the case of Co$_2$CrAl. The structure and composition of this phase could not be accurately determined using SEM or EBSD, although the matrix was found to be a CoAl-type *B2* phase (Figure 3.12a-b). The phase fraction of the secondary phase was determined to be 9±2 vol% by an analysis of the corresponding BSE images, which is also smaller than the secondary phase fraction in FZ-grown Co$_2$CrAl.

XRD showed a *B2* phase with additional reflections which were indexed with a hcp ϵ-Co phase (Figure 3.12c). A two-phase Rietveld refinement could be successfully performed. The cubic matrix had a lattice constant of 2.866(4) Å ($Pm\bar{3}m$) while the lattice parameters for the hexagonal secondary phase were a=b=2.529(4) Å, c=4.072(4) Å for a P6$_3$/mmc space group. The secondary phase volume fraction from refinement was calculated to be 7.4(5) vol%. The phase fraction value from XRD data should be more accurate as it is a bulk measurement unlike analysis of image from SEM or EBSD as was calculated above. Details of the refinement parameters are in Appendix A (Page 147).
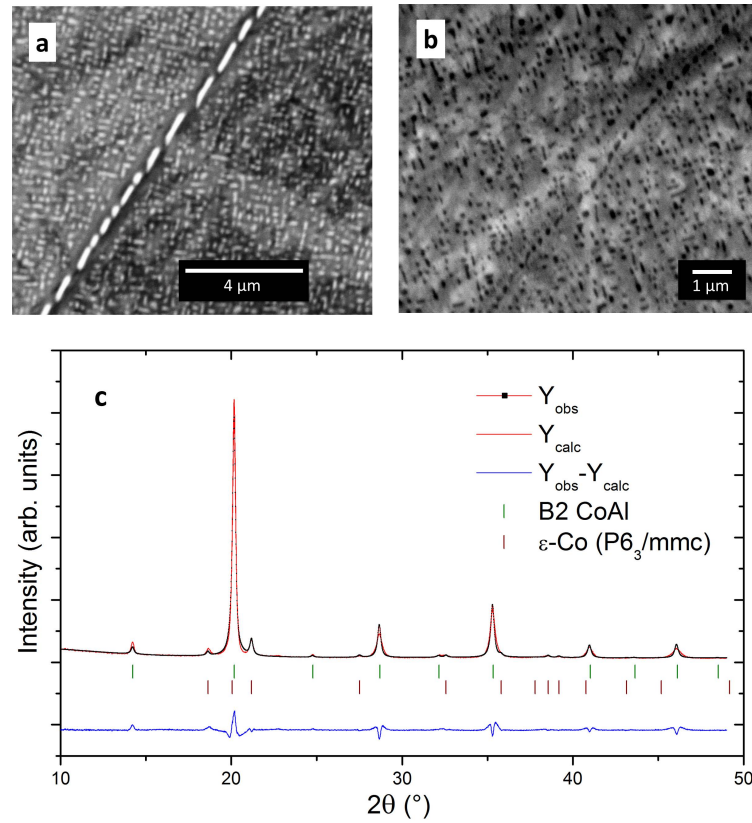
Figure 3.12: Floating Zone (FZ)-grown $Co_2Cr_{0.6}Fe_{0.4}Al$ (a) BSE image (b) BSE image in tilted position for EBSD (c) X-ray diffraction with refinement. (EBSD data courtesy of Dr. Horst Wendrock)
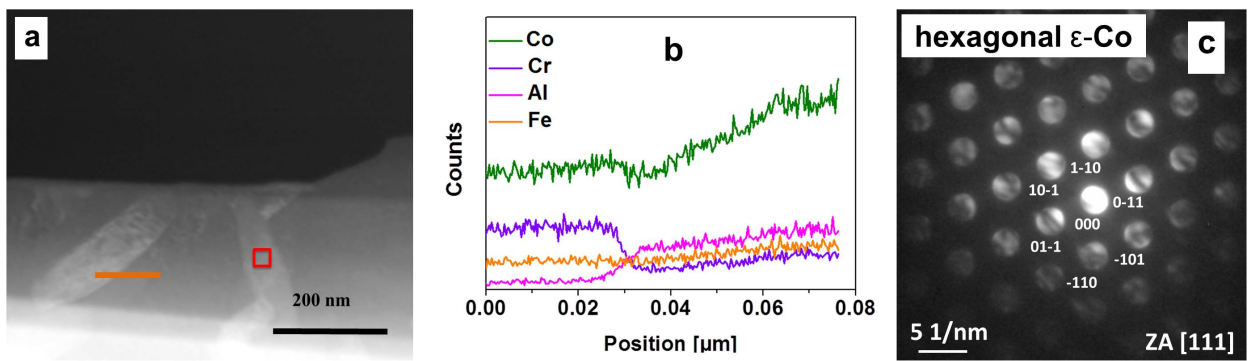
Figure 3.13: Floating Zone (FZ)-grown $Co_2Cr_{0.6}Fe_{0.4}Al$ (a) High angle annular dark field (HAADF) scanning transmission electron microscopy (STEM) image (b) EDX-linescan (marked with orange line in (a)) across phase boundary of the secondary phase (c) Nanobeam diffraction for the secondary phase in the region marked in (a) by red square. (TEM data courtesy of Dr. Maria Dimitrakopoulou)

The structure of the secondary phase in Co$_2$Cr$_{0.6}$Fe$_{0.4}$Al was confirmed to be hexagonal ϵ-Co-type through TEM (Figure 3.13), unlike the tetragonal σ-CoCr phase in FZ-grown Co$_2$CrAl (Figure 3.10). The composition was found to consist of mainly Co with dissolution of small amounts of Cr and Al. The compositions of the secondary phase and matrix from TEM-EDX are listed in Table 3.4. The average overall composition from SEM is also given, which matches well to the nominal composition.

Table 3.4: EDX data (from transmission electron microscopy (TEM) and scanning electron microscopy (SEM)) along with standard deviation for Floating Zone (FZ)-grown Co$_2$Cr$_{0.6}$Fe$_{0.4}$Al (atomic %). (TEM data courtesy of Dr. Maria Dimitrakopoulou)

Phase	Co	Cr	Fe	Al
Nominal	50	15	10	25
CoAl type *B2* (TEM)	55±0.7	09±0.7	10±0.7	26±0.7
ϵ-Co type (TEM)	55±0.7	32±0.7	12±0.7	01±0.7
Overall average (SEM)	47±0.4	15±0.3	11±0.2	27±0.1

FZ-grown Co$_2$Cr$_{0.6}$Fe$_{0.4}$Al seems to have undergone a phase transformation via spinodal decomposition as well. The secondary phase in FZ-grown Co$_2$Cr$_{0.6}$Fe$_{0.4}$Al is smaller as compared to that of Co$_2$CrAl, which signifies that the extent of decomposition is less in Co$_2$Cr$_{0.6}$Fe$_{0.4}$Al. No further nanoscale segregation in the matrix was observed in the EDX-linescan in TEM (Figure 3.13b), further corroborating the smaller extent of decomposition. The observed microstructure was also similar to one simulated for the early stages of spinodal decomposition [220].

We have thus confirmed the presence of a solid-state miscibility gap in both the ternary Co-Cr-Al and the quaternary Co-Cr-Fe-Al system, which has not been reported so far in literature. However, it needs to be mentioned that there is no 'smoking-gun' feature/method to confirm that the phase transformation is indeed a spinodal decomposition. Nevertheless, we shall present a few more arguments supporting our interpretation.

The presence of a solid-state miscibility gap in the Fe-Cr binary system has been well documented. So far, there are no reports of spinodal decomposition in the Co-Cr-Al system, mostly due to the fact that it has not been well studied. However, spinodal decomposition in Co-Fe-Al system in the Fe-rich side has been documented [221–223]. The phase separation in that composition range is into an ordered *B2* phase and a disordered *A2* phase [224] and the microstructure observed through TEM is also quite similar to that in our case. It must be noted that the samples in the above studies were prepared either by arc-melting or melt-spinning. Both of the techniques have very different kinetics as compared to FZ technique, which involves directional growth and slow cooling of the

sample. Even though there is a lack of experimental work in the system, such an aspect can be modelled theoretically. The microstructure for FZ-grown Co_2CrAl is also in very good agreement with the simulations of spinodal decomposition in thin films done by Seol et al. [220].

The simulation is based on an elastically anisotropic film with a cubic structure, and the film is also elastically constrained by the substrate [220]. Conditions at the crystallization front during the FZ process can be assumed to be similar to a thin film growth. During the growth, the crystallization front moves unidirectionally at a very slow speed ($\sim$ 2-5 mm/hr), similar to a layer-by-layer growth process. In addition, during the FZ experiment, a uniform thermal gradient is present. When a part of the sample is in the temperature regime of spinodal decomposition, the lower part is already at a significantly lower temperatures, where kinetics are slow. Thus, the sample undergoing decomposition is elastically constrained, similar to the constraints of the modelling by Seol et al. [220]. Hence the FZ growth process can be approximated and understood to be locally similar to the growth of thin films. This further corroborates the concept of phase transformation via spinodal decomposition in the $Co_2Cr_{1-x}Fe_xAl$ series, as the microstructures in the simulations on spinodal decomposition in thin films match well with those of our samples.

Since we have described the phase transformation for the first time in $Co_2Cr_{1-x}Fe_xAl$ series, let us consider it from the point of view of the overall phase diagram, and try to build a coherent picture.

3.2.3 Phase dynamics and the effect on physical properties

Analysis of the available phase diagram data is necessary to understand the phase transformations. However, it is not feasible to plot an isotherm for the phase diagram for a quaternary system such as Co-Cr-Fe-Al as one would need 4 axes, one for each element. Nevertheless, it is possible to gain an understanding through available binary and ternary phase diagrams between the various elements, although it would purely be suggestive in nature.

Calculated phase diagram data are available for Co-Fe-Al, and the projection of the $Co_2Cr_{0.6}Fe_{0.4}Al$ composition (approx. $Co_{59}Fe_{12}Al_{29}$) lies in the large solid solubility region of CoAl and FeAl cubic phases until room temperature [225], and can account for the large solid solubility of CoAl. However, since the spinodal decomposition is observed in the Cr-rich side of $Co_2Cr_{1-x}Fe_xAl$ whereas Co_2FeAl could be grown phase-pure, we shall focus on the Co-Cr-Fe and Co-Cr-Al system.

Detailed phase diagram data for Co-Cr-Fe is available and phase separation by spinodal decomposition has been well documented in the Fe-rich compositions with a bcc structure [221–223]. However, no immiscibility is reported so far in Co-rich compositions. Any composition in the $Co_2Cr_{1-x}Fe_xAl$ system would correspond to a much small fraction of Cr and Fe, compared to Co and Al.

Regarding the Co-Cr-Al system, ternary phase diagram data is available only for 900 °C and above [182, 226, 227]. In the available isotherm at 1250 °C [182], the Co_2CrAl composition lies in the three-phase field of a *B2* type CoAl (cubic), σ-CoCr (tetragonal) and α-Co (ht, cubic) phases

but very close to the two-phase field of *B2* CoAl (cubic) phase and σ-CoCr (tetragonal) phase. Also, since Co-Cr-Al is an incongruently melting system, phase segregation in Co_2CrAl into Al-rich and Cr-rich phases during a fast solidification process, such as arc-melting, can be explained easily. As the temperature is lowered from 1250 °C, the three-phase field becomes smaller, and at 900 °C, the Co_2CrAl composition is at the boundary between the three-phase field and the two-phase field (Figure 3.14).
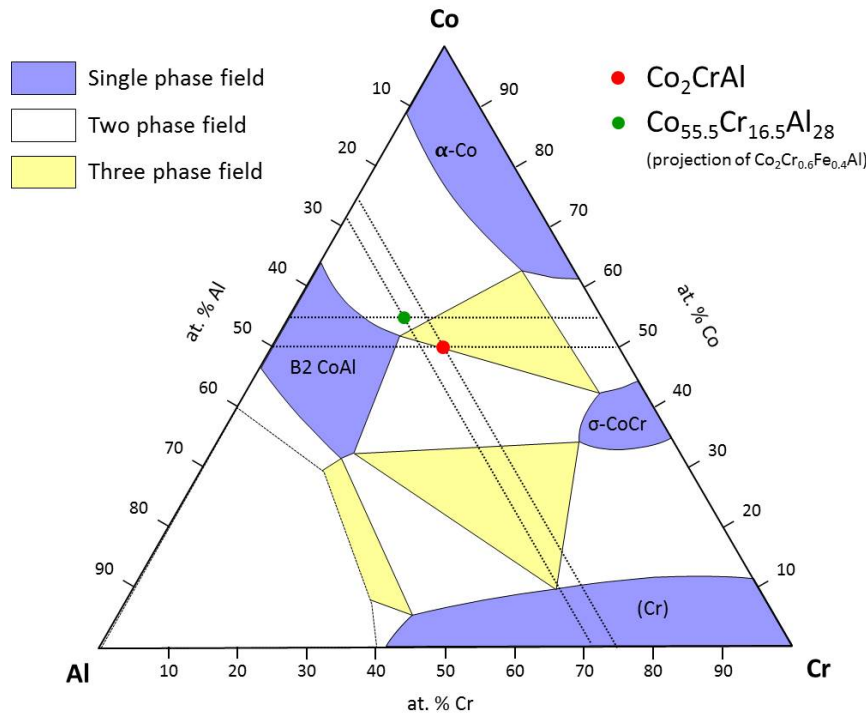
Figure 3.14: Isothermal section for Co-Cr-Al system at 1000 °C (adapted from Bondar [182]).

However, we believe that phase diagram maybe a bit more complicated than reported. We know from our analysis that using the FZ technique we are able to obtain a phase-pure Co_2CrAl at higher temperatures which undergoes spinodal decomposition at lower temperatures due to the presence of a solid-state miscibility gap. Therefore, below a given temperature, either the Co_2CrAl is stable as a compound or the composition lies in the region of *B2* CoAl solid solubility and at further lower temperatures, the composition becomes unstable.

The Co_2CrAl composition lies in the vicinity of the two-phase regime of CoAl (cubic) phase and σ-CoCr (tetragonal) phase at higher temperatures (Figure 3.14), and the stability of the two compounds could possibly be the reason for the existence of a immiscibility at lower temperatures. Spinodal decomposition in the material leads to phase separation into a CoAl- and CoCr-type phases which are initially have the same cubic structure, but the CoCr-type phase later undergoes phase transformation to tetragonal structure, as it is more stable.

In the case of the Co$_2$Cr$_{0.6}$Fe$_{0.4}$Al composition, a similar scenario may be expected. However, the main point of difference in the quaternary composition with the Co$_2$CrAl is the structure and composition of the secondary phase that evolves. In Co$_2$Cr$_{0.6}$Fe$_{0.4}$Al, the secondary phase is a hexagonal ϵ-Co type phase. In order to correlate with the available phase diagram data, the projection of the Co$_2$Cr$_{0.6}$Fe$_{0.4}$Al composition, approx. Co$_{55.5}$Cr$_{16.5}$Al$_{28}$, is plotted in the Co-Cr-Al isotherm at 900 °C, marked by green dot in Figure 3.14. The projection lies in the two-phase field of CoAl (cubic) and Co (ht, cubic), unlike the case of Co$_2$CrAl (marked by red dot) which may explain the phase separation of the Co$_2$Cr$_{0.6}$Fe$_{0.4}$Al composition in the respective phases. Furthermore, pure Co is known to undergo a transformation from α-Co (cubic) to ϵ-Co (hexagonal) at ~430 °C under ambient pressure [228, 229]. Therefore, it is likely that in Co$_2$Cr$_{0.6}$Fe$_{0.4}$Al due to the immiscibility, the α-Co evolves from the cubic CoAl, and subsequently transforms to ϵ-Co at lower temperatures. The stability of ϵ-Co until only ~430 °C could limit the extent of the miscibility gap, which may in turn account for the lesser extent of the spinodal decomposition observed.

This scenario gives a coherent picture of the solidification and transformation in both as-cast and FZ-grown samples, and therefore the available phase diagram data needs be amended to add to information on the immiscibility gap. Some of the phase boundaries at higher temperatures must be revisited as our data from FZ experiments suggest a slightly different scenario.

We shall now shift our attention to the magnetic properties of these FZ-grown samples and try to understand the effect of spinodal decomposition, specially on saturation magnetization.

Magnetic properties

Magnetic measurements were performed on as-cast and FZ-grown samples for all the three compositions. All the samples were found to be ferromagnetic at room temperature and no phase transformations were observed for any sample between 5 K and 300 K. The saturation moments at 5 K are summarized in Figure 3.15. All the samples show soft magnetic behaviour along with high saturation moments characteristic for Heusler compounds as shown in the representative M(H) curve in the inset of Figure 3.15. For all the as-cast samples, the saturation moments do not match with the Slater-Pauling values, most likely due to the phase segregated nature of the samples. The observed trend is similar to an earlier work on annealed polycrystalline samples [203].

In the case of Co$_2$FeAl, the as-cast sample had a slightly higher saturation moment than the Slater-Pauling value and this discrepancy is most probably due to the phase segregated nature of the sample. However, although the FZ-grown Co$_2$FeAl sample was phase-pure, it had a slightly higher saturation moment than the Slater-Pauling value. This is most likely a result of anti-site disorder, as has been calculated for some specific cases [143, 203].

In the cases of as-cast Co$_2$CrAl and Co$_2$Cr$_{0.6}$Fe$_{0.4}$Al as well, the saturation moments were found to be lower than the Slater-Pauling value. Moreover, FZ-grown Co$_2$CrAl and Co$_2$Cr$_{0.6}$Fe$_{0.4}$Al, unlike
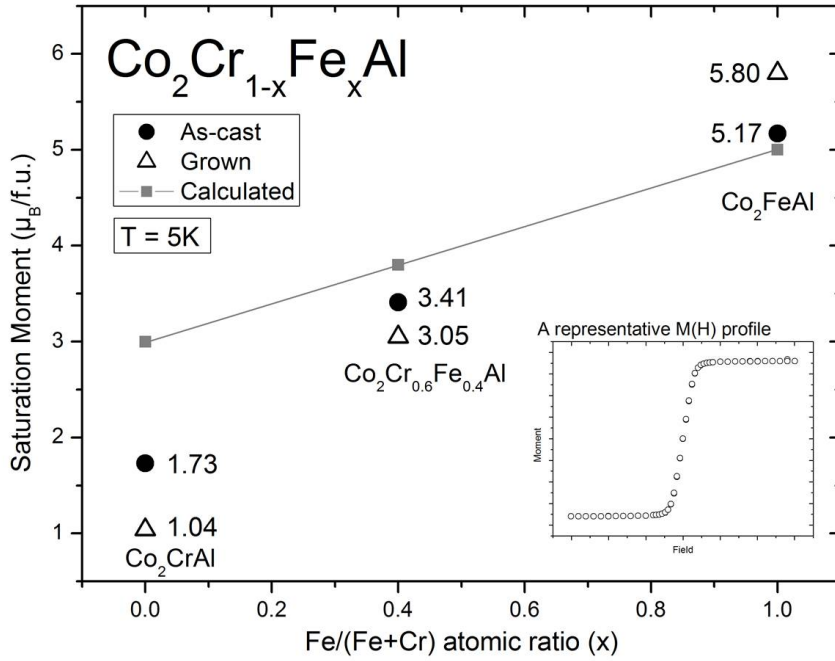
Figure 3.15: Saturation magnetization data for as-cast and Floating Zone (FZ)-grown $Co_2Cr_{1-x}Fe_xAl$ samples with calculated magnetic moments (Slater-Pauling value); inset: Magnetization versus field curve at 5 K for as-cast Co_2FeAl is shown as an example.

Co_2FeAl, showed a further lowering in the saturation moment as compared to the corresponding as-cast sample. The effect was much stronger in the case of Co_2CrAl, where the spinodal decomposition is much more pronounced as compared to $Co_2Cr_{0.6}Fe_{0.4}Al$, suggesting that the saturation moment is closely related to the degree of spinodal decomposition.

An earlier work on Co-Cr thin films [230] asserts that the deviations from the theoretical saturation moment arises due to the existence of two non-magnetic phases, specifically hexagonal ϵ-Co phase and tetragonal σ-CoCr phase which become stable at lower temperatures [231]. This is reported to lower the saturation moments and is consistent with our results and analysis. The further lowering of the saturation moments for FZ-grown Co_2CrAl and $Co_2Cr_{0.6}Fe_{0.4}Al$ as compared to respective as-cast samples is most likely due to the secondary phases that evolve, which have complete different structure and morphology, as well as due to their interaction with the matrix.

The secondary phase seems to considerably affect the magnetic properties, even when the extent of decomposition is much less, as in the case in $Co_2Cr_{0.6}Fe_{0.4}Al$ where the secondary phase fraction is only ∼8 %. The lowering of saturation moments is directly related to the extent of the secondary phase.

We shall now revisit the literature, in light of the understanding of the phase dynamics in the $Co_2Cr_{1-x}Fe_xAl$ system.

3.2.4 Understanding the discrepancies in bulk samples as well as thin films

We have shown that the as-cast samples prepared using arc-melting are phase segregated due to incongruent melting which affect the magnetic properties (Section 3.2.1), and our results are in agreement with what has been reported earlier [202]. The phase segregation in as-cast samples affects the magnetic properties, and the reduction in saturation moments matches well with earlier work on as-cast samples [203].

Furthermore, we have been able to confirm the presence of a low temperature solid-state miscibility gap in Cr-rich side of the $Co_2Cr_{1-x}Fe_xAl$ series, which leads to formation of non-cubic secondary phases via spinodal decomposition, as seen for our bulk FZ-grown samples. Although this phase separation is not seen in our as-cast samples, Teresa et al. observed a evolution of a secondary non-cubic phase upon annealing of as-cast $Co_2Cr_{1-x}Fe_xAl$ samples [202]. This similar to what has been observed in our FZ-grown Co_2CrAl and $Co_2Cr_{0.6}Fe_{0.4}Al$ sample, suggesting that there is indeed a possibility that the decomposition may take place upon annealing of the as-cast sample itself. A Cr-rich inhomogeneity seen in X-ray absorption spectroscopy photoelectron emission microscopy (XAS-PEEM) for bulk $Co_2Cr_{1-x}Fe_xAl$ samples [213]is likely due to the same reason. Since the spinodal decomposition is possible in as-cast sample, a phase segregation at the nanoscale is expected, and has been seen in literature as well [211, 212]. Since the evolving secondary phases after spinodal decomposition are non-magnetic, it would explain the paramagnetic clusters seen in Mößbauer spectroscopy for sample slowly cooled after annealing [204]. We have shown that the secondary phases strongly affect the properties, and thus the anomalous data for various physical proerties in literature for bulk samples [199, 205, 209] can be accounted for.

In general, issues of material instability as seen in bulk samples are not expected in the case of thin films, as metastable phase-pure phases can be synthesized. Incidentally, a TEM study on $Co_2Cr_{0.6}Fe_{0.4}Al$ films [214] showed a similar cross-type pattern as the microstructure observed in our FZ-grown samples. Another TEM work on $Co_2Cr_{0.6}Fe_{0.4}Al$ films reported a Co-rich segregation in films annealed at temperatures higher than 500 °C [219]. A similar evolution of hexagonal and tetragonal phases on sequential annealing has been reported for $Co_2Cr_{1-x}Fe_xAl$ films [232]. Furthermore, the saturation moments obtained for FZ-grown Co_2CrAl and $Co_2Cr_{0.6}Fe_{0.4}Al$ matched very well with those in thin films of the same composition [207]. This further hints towards a similar phase separation in films.

Since the chemical segregation due to a spinodal decomposition process is very localized, time-scales for phase separation to occur are much shorter as compared to other diffusion-based processes. Even a short annealing process as in the case of thin films is sufficient to cause the decomposition reaction. Most films are annealed at slightly elevated temperatures post deposition, for phase formation, homogenization and ordering. Therefore, we believe it is quite likely that a solid-state phase transformation via spinodal decomposition, as seen in our bulk data, occurs in thin films of respective

compositions as well. Since the low temperature phase dynamics leads to formation of non-cubic phases, the additional reflections in the XRD pattern, seen in some reports mentioned earlier [206, 216, 217], can also be accounted for. The phase transformation via spinodal decomposition would also very well explain the various anomalous data in physical properties reported in literature for thin films [200, 201, 207, 208, 210].

To summarize, we have been able to identify the underlying phenomenon of solid-state transformation via spinodal decomposition in the Co$_2$Cr$_{1-x}$Fe$_x$Al system. This previously unnoticed inherent phenomenon plaguing the system, leads to drastic changes in the intrinsic material attributes, which has an intricate correlation with the physical properties of these Heusler compounds. This knowledge has allowed us coherently account for almost all the anomalous data reported in literature for both bulk samples and thin films [218].

The next logical step would be to develop a recipe to avoid the decomposition and synthesize a phase-pure material. In order to do that, it is important to develop an understanding of the extent of the phase transformations. The following section discusses the various experiments performed in order to explore the relevant phase-space.

3.3 Annealing and off-stoichiometry in Co$_2$CrAl: Exploring the immiscibility

Existence of a miscibility gap in the Co-Cr-Fe-Al system has been demonstrated in the last section, where the secondary phase increases with Cr concentration in the sample. We have consistently shown that the phase transformation via spinodal decomposition strongly affects the properties, and is responsible for the large discrepancies documented in literature. It is therefore necessary to either develop a processing route to obtain a phase-pure sample from the as-grown one or work towards avoiding the spinodal decomposition all together during synthesis.

There is no clear guideline in literature as to how a spinodal decomposition can be avoided. As already mentioned, the decomposition process involves a highly localized diffusion and does not need much time to take place. This makes it quite difficult to avoid the decomposition, e.g., phase separation has been observed in films grown at 500 °C, even without annealing [214].

The first approach involves a fast cooling rate to avoid the spinodal decomposition. A possible scenario is to quench the sample rapidly from sufficiently high temperatures during the sample preparation itself, thereby forming a metastable phase. Unfortunately, it is not possible to do so during the FZ experiment, as a shallow temperature gradient at the solidification front is needed for an optimal interface [192], which is essential for zone stability and grain selection. Due to this, the time during which the already grown sample cools down in a FZ experiment is sufficient to cause the phase transformation via spinodal decomposition. Alternate synthesis techniques where such a cooling rate can be applied, do not allow growth of such an incongruent melting system. Another possibility along similar lines is that the two-phase sample after phase transformation is annealed at sufficiently high temperatures, above the solid-state miscibility gap. The secondary phase would dissolve with sufficiently long annealing time and the sample is then quenched as fast as possible to minimize time in the region of immiscibility, thus metastabilizing the high-temperature phase. The concept is illustrated in Figure 3.16a.

Second approach in order to avoid the phase transformation, may be to optimize the composition so that we are outside the miscibility gap, as shown in Figure 3.16b. An optimized composition would allow us to obtain a single phase during the FZ experiment itself. It is not necessary that we should be outside the miscibility gap till room temperature, but just until considerably lower temperatures where the kinetics are slow enough, that the decomposition is arrested.

Regarding the annealing experiments, it should be kept in mind that this is not a sure-shot way. The stability of the secondary phase at high temperatures and the cooling rate required to avoid any decomposition during quenching are very material-specific. Furthermore, with the other approach of moving around in the phase diagram, there is a possibility of strongly affecting the physical properties. Nevertheless, It is important to try both the approaches in order to better understand the phase diagram and thereby develop a possible route to achieve a phase-pure sample while
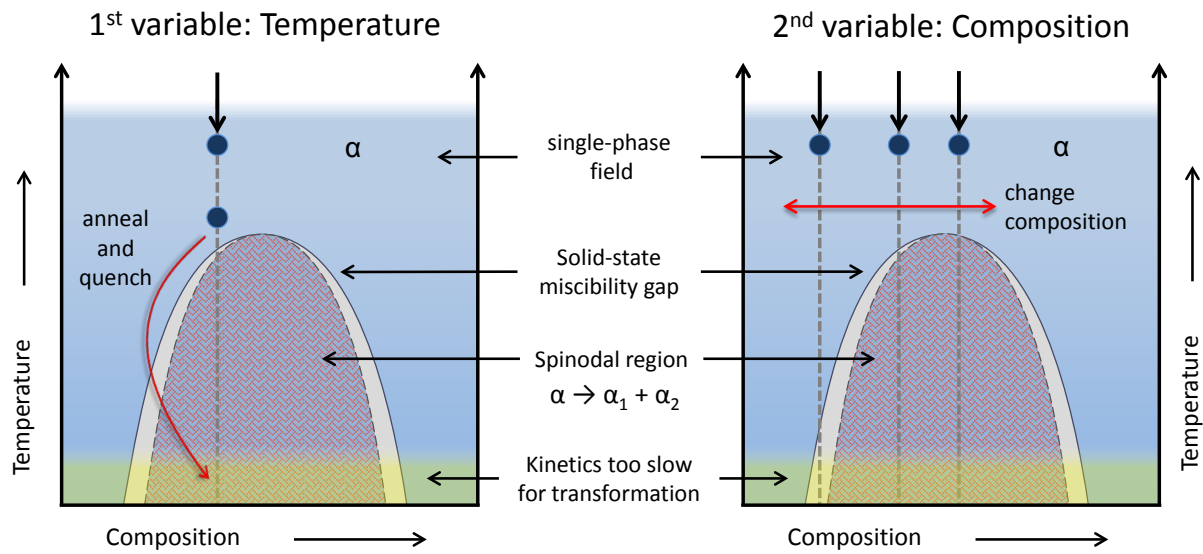
Figure 3.16: Schematic for avoiding spinodal decomposition in a phase diagram (a) annealing followed by quenching (b) optimize the composition.

retaining the interesting properties.

We have performed both the annealing experiments as well as the off-stoichiometry approach which are detailed in this section. We selected Co_2CrAl for this study as its secondary phase after the spinodal decomposition is more pronounced and hence it is easier to track the changes and to compare different experiments. Also, with regards to the off-stoichiometric study, the higher the number of elements present, e.g., $Co_2Cr_{0.6}Fe_{0.4}Al$, the more are the parameters to optimize in the phase-space. Hence, the ternary Co_2CrAl composition makes it easier to test the approach, as compared to the quaternary sample.

The effect of annealing on the spinodally decomposed FZ-grown Co_2CrAl sample has been studied [233], and is discussed next.

3.3.1 Annealing experiments on Floating Zone (FZ)-grown Co₂CrAl

FZ-grown Co₂CrAl samples containing σ-CoCr secondary phase in a *B2*-CoAl matrix (Figure 3.17a, also see Section 3.2.2.2), were annealed for 3 weeks at 750 °C, 1000 °C and 1250 °C, respectively. Normally, the samples are sealed in evacuated quartz ampoules, but quartz cannot be used for annealing beyond 1100 °C as it becomes porous to oxygen and may even crystallize. Hence, the third sample was sealed in a niobium crucible for annealing at 1250 °C and the experiment was done in a constant argon flow to avoid oxidation of niobium. All samples were quenched in water after annealing.
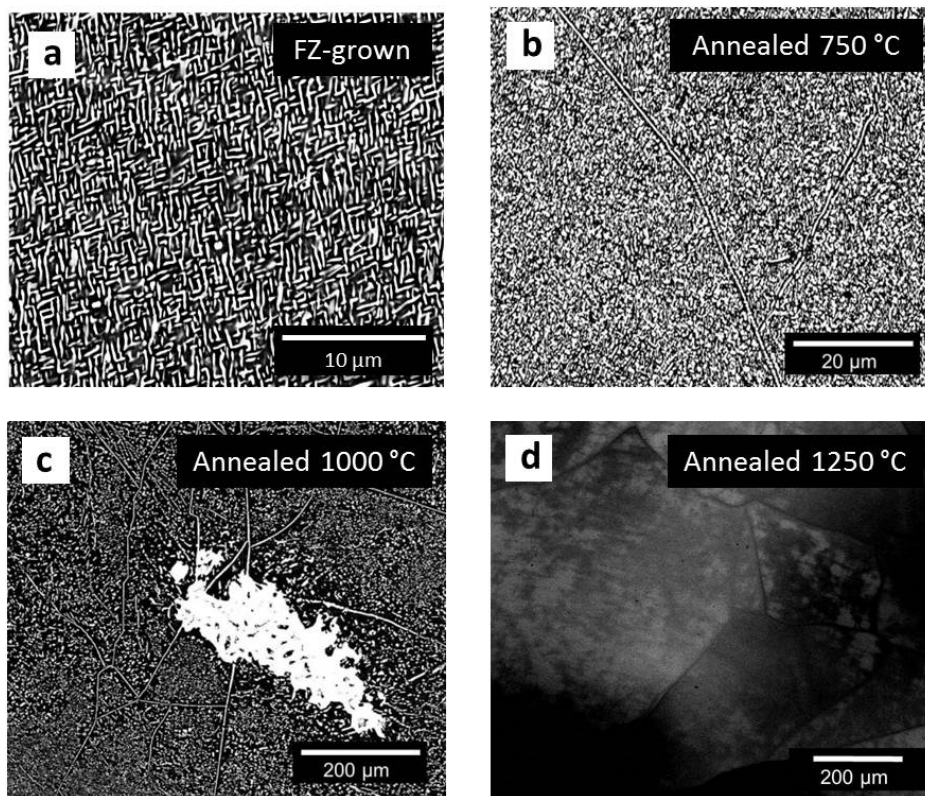
Figure 3.17: BSE images for Floating Zone (FZ)-grown Co₂CrAl annealed for 3 weeks at (a) as-grown Co₂CrAl (b) 750 °C, showing increased secondary σ-phase fraction (c) 1000 °C, showing lower secondary σ-phase fraction with agglomeration (d) 1250 °C, showing weak contrast between two cubic phases.

The sample annealed at 750 °C exhibits a more pronounced secondary phase which is clearly apparent in the BSE image in Figure 3.17b. The secondary phase seems to be more pronounced and interconnected as compared to the as-grown sample (Figure 3.17a). Since the secondary phase fraction increased at 750 °C, the sample was still inside in the immiscibility gap. This is further reflected in the increase of the relative intensities for the σ-phase reflections in the XRD data, as

shown in Figure 3.18.

In the sample annealed at 1000 °C, the overall secondary phase fraction was reduced, although agglomeration was also observed in the grains to some extent as seen in the BSE image (Figure k3.17c). XRD data in Figure 3.18 shows a reduction in the relative intensities of the tetragonal splitting of the main reflection which is consistent with the lower phase fraction of the σ-phase.
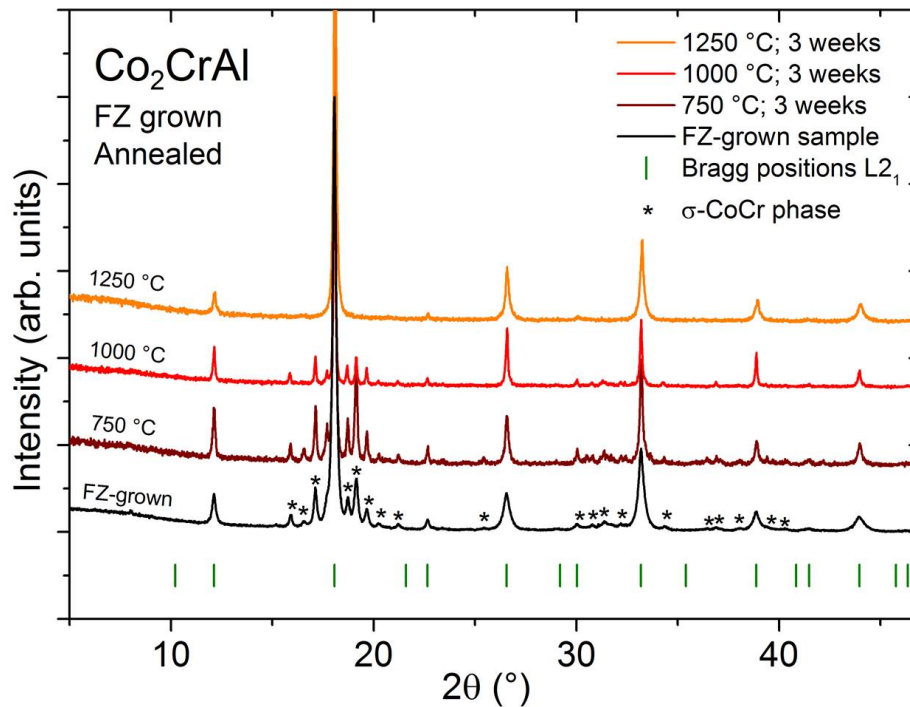
Figure 3.18: X-ray diffraction data for Floating Zone (FZ)-grown and annealed Co_2CrAl samples. The secondary σ-phase reflections have been marked. The Bragg positions for ordered $L2_1$-type cubic structure are also shown.

The sample annealed at 1250 °C was found much different from the other samples. There was no strong contrast for the σ-CoCr phase in the BSE image (Figure 3.17d) although some variation in composition (chemical contrast) was surely visible. However, the boundaries between regions with different compositions were rather diffuse. Also, XRD data did not show any tetragonal splitting of the main reflection and the sample was pure $B2$-cubic as seen in Figure 3.18. The contrast seen in BSE image corresponds to two cubic $B2$-type phases with similar lattice constants, which were thus difficult to distinguish in XRD. The sample looked quite similar to that observed in arc-melted samples. It seems that at 1250 °C, the sample was in the two-phase field below liquidus. Due to this, broadening of the reflections for the 1250 °C annealed sample was also perceptible, as compared to samples annealed at lower temperatures.

The samples annealed at different temperatures, were found to be quite different in terms of

phases, morphology and microstructure, from the FZ-grown Co_2CrAl sample. The magnetization data provided further information on the effect of these changes and are discussed next.

3.3.1.1 Magnetic properties

Magnetization measurements were performed on all the annealed samples, and were found to be ferromagnetic at room temperature. No phase transitions were observed between 5 K and 300 K. However, the saturation moments differed considerably from the Slater-Pauling value (3 μ_B/f.u.) and are summarized in Figure 3.19. All the samples showed soft-magnetic behaviour at 5 K (Refer to the inset in Figure 3.19).
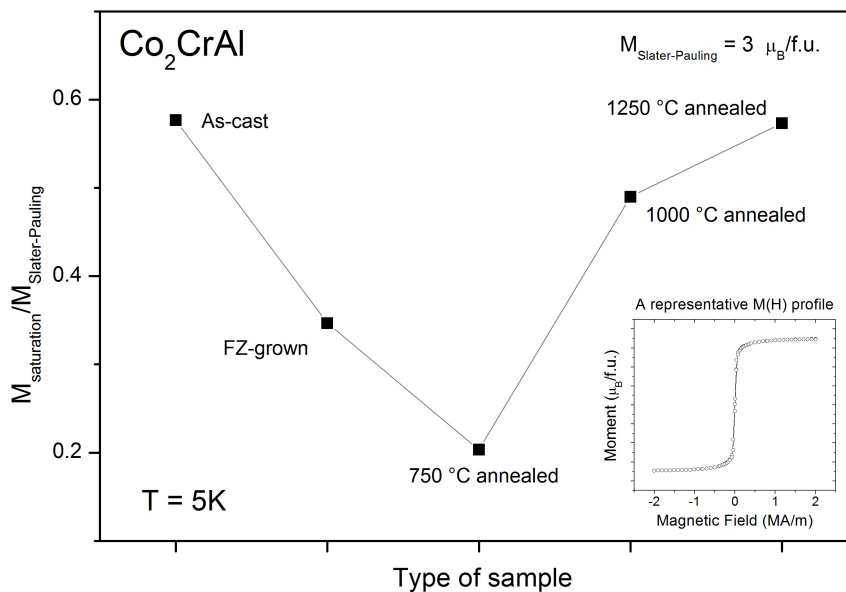
Figure 3.19: Relative saturation magnetization data for the various Co_2CrAl samples. Annealed samples were kept at respective temperatures for 3 weeks and then quenched. Inset: Magnetization versus field curve at 5 K for as-cast Co_2CrAl sample.

We have already seen that the saturation moment for both as-cast and FZ-grown Co_2CrAl showed marked deviations due to phase segregation. The magnetic moment of the FZ-grown sample was considerably smaller than that of the as-cast sample due to the well developed secondary σ-phase which is reported to be non-magnetic [230]. Saturation moment was further reduced after annealing at 750 °C which could be attributed to the increased fraction of σ-phase, as seen in XRD and SEM. Furthermore, the reduction in the σ-phase fraction for sample annealed at 1000 °C, as seen in XRD and SEM, was also reflected in the magnetization as the saturation moment increased relatively. The saturation moment for sample annealed at 1250 °C was similar to that observed for the as-cast sample, and further supported the fact that they are similar intrinsically. Thus annealing did not really offer any improvements in the saturations moments as the phase separation could not be

avoided.

As discussed earlier, phase diagram data for the Co-Cr-Al system are limited and isothermal sections are only available for 900 °C and above [182, 226, 227]. We have already discussed that existing phase diagram information is incomplete and even the available data need corrections. Based on our annealing experiments, we have further improved our analysis of the phase diagram.

It appears that, at 750 °C in the phase diagram, the sample is still inside the two-phase regime of the miscibility gap, as the extent of decomposition is increased due to annealing. This is further reflected in the relative intensities in XRD. Also, the saturation moment is further lowered which is understandable as the secondary σ-CoCr phase has a strong effect on the magnetic properties in bulk (our data) as well as in thin films [230].

After annealing at 1000 °C, the overall fraction of the secondary phase was less and visible in the lower intensities for the tetragonal splitting of the main reflection as seen in Figure 3.18. However, the secondary phase segregated and did not fully dissolve even after annealing for 3 weeks, as can be seen in the BSE image (Figure 3.17c). Most likely, at 1000 °C, the phase boundary of the two-phase regime of the miscibility gap is quite close. Due to the lower amount of the secondary phase, the saturation moment of the annealed sample increased (1.47 μ_B/f.u.) as compared to the FZ-grown sample (1.04 μ_B/f.u.) although it was still considerably below the Slater-Pauling value (3 μ_B/f.u.) as seen in Figure 3.19.

The sample annealed at 1250 °C was considerably different from the other annealed samples. The tetragonal secondary phase was dissolved completely and the sample exhibited two segregated cubic phases. The SEM, XRD and magnetization data confirmed that the intrinsic attributes as well as magnetic properties of the 1250 °C annealed sample was quite similar to that obtained through arc-melting. However, the formation route was completely different in both the cases. The two-phase field below liquidus extends till 1250 °C at least, which led to a phase separated sample upon annealing.

Clearly, annealing did not help to get rid of the phase separation. The secondary phase was stable till high temperatures, even possibly above the miscibility gap. The secondary phase did reduce a bit in volume fraction, but did not dissolve completely. The solid-state miscibility gap even extends close to the two-phase field near melting point which makes it difficult to avoid the spinodal decomposition. In addition to that, the stability of the secondary phase at high temperature further makes it highly unlikely to achieve a phase-pure sample through annealing [233].

Since temperature variable was found to be unsuccessful, we further explored the composition variable illustrated in Figure 3.16, in order to try and avoid the solid-state miscibility gap.

3.3.2 Off-stoichiometric Co$_2$Cr$_{0.8}$Al$_{1.2}$, Co$_2$Cr$_{0.6}$Al$_{1.4}$ and Co$_2$Cr$_{0.4}$Al$_{1.6}$

As mentioned earlier, moving around in the phase diagram through off-stoichiometry is another possibility to avoid the region of immiscibility. In order to study the effect of off-stoichiometry, one must be careful in choosing the elements to be optimized. For the ternary Co$_2$CrAl, it was decided not to affect the Co sublattice since affecting the atom at $8c$ Wyckoff position strongly affects the electronic structure and various physical properties as has been shown by Miura et al. [40]. In order to decide between Cr and Al, we refer to our earlier data on FZ-grown Co$_2$Cr$_{1-x}$Fe$_x$Al (Section 3.2.2). As we have seen, the extent of spinodal decomposition is lower in the case of Co$_2$Cr$_{0.6}$Fe$_{0.4}$Al as compared to Co$_2$CrAl, and finally for Co$_2$FeAl no phase separation was observed. The reduction in Cr content seems to move the composition away from the solid sate miscibility gap in the phase diagram. Keeping this in mind, three off-stoichiometric Co$_2$CrAl compositions, Co$_2$Cr$_{0.8}$Al$_{1.2}$, Co$_2$Cr$_{0.6}$Al$_{1.4}$ and Co$_2$Cr$_{0.4}$Al$_{1.6}$ have been studied, in order to explore the extent of immiscibility.

3.3.2.1 Polycrystalline samples

As-cast polycrystalline samples of Co$_2$Cr$_{0.8}$Al$_{1.2}$, Co$_2$Cr$_{0.6}$Al$_{1.4}$ and Co$_2$Cr$_{0.4}$Al$_{1.6}$ were prepared by arc-melting, from at least 4N pure constituents. The BSE images are shown in Figure 3.20. All three compositions showed phase separation with a dendritic morphology due to incongruent melting, similar to the case of Co$_2$CrAl. The nominal composition as well as the compositions of the two phases are summarized in Table 3.5.
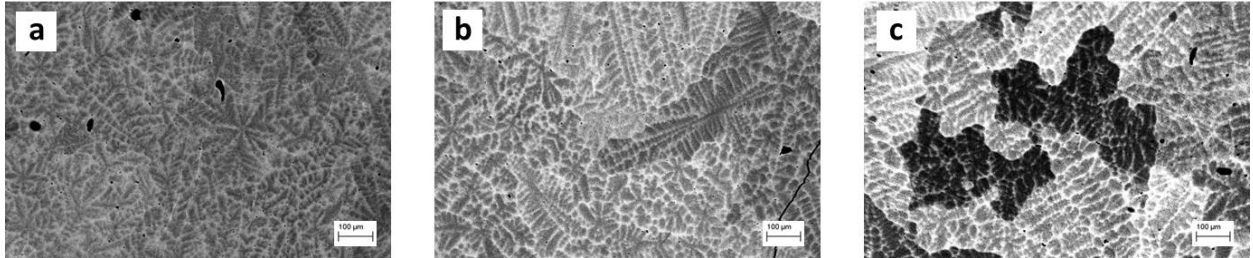
Figure 3.20: Backscattered electron images (BSE) for as-cast samples showing phase segregation (a) Co$_2$Cr$_{0.8}$Al$_{1.2}$ (b) Co$_2$Cr$_{0.6}$Al$_{1.4}$ (c) Co$_2$Cr$_{0.4}$Al$_{1.6}$.

The observed XRD data for all three compositions are plotted in Figure 3.21. All of them are cubic with *B2* type order, as no (111) superlattice reflection was observed. As in the case of Co$_2$CrAl, the two-phases had similar lattice such that the reflections overlapped. Refinement was only possible using a single $Pm\bar{3}m$ phase and the average lattice constants are listed in Table 3.5. The XRD data with refinement along with the details of the refinement are summarized in Appendix A (Page 148-149). No clear trend was observed in the lattice constants, although the main reflection of Co$_2$Cr$_{0.8}$Al$_{1.2}$ appeared broad as compared to others, as can be noticed in the inset of Figure 3.21.

Table 3.5: EDX data for as-cast $Co_2Cr_{0.8}Al_{1.2}$, $Co_2Cr_{0.6}Al_{1.4}$ and $Co_2Cr_{0.4}Al_{1.6}$ samples.

EDX (atomic %)	$Co_2Cr_{0.8}Al_{1.2}$			$Co_2Cr_{0.6}Al_{1.4}$			$Co_2Cr_{0.4}Al_{1.6}$		
Phase	Co	Cr	Al	Co	Cr	Al	Co	Cr	Al
Nominal	50	20	30	50	15	35	50	10	40
Al-rich (dark)	51.7	13.1	35.2	50.9	9.6	39.5	51	6.4	42.6
Cr-rich (light)	49.2	30.0	20.8	48.5	29.0	22.5	47.8	25.1	27.1
Overall	50.4	21.5	28.1	50.6	14.4	35	50.1	10.7	39.2
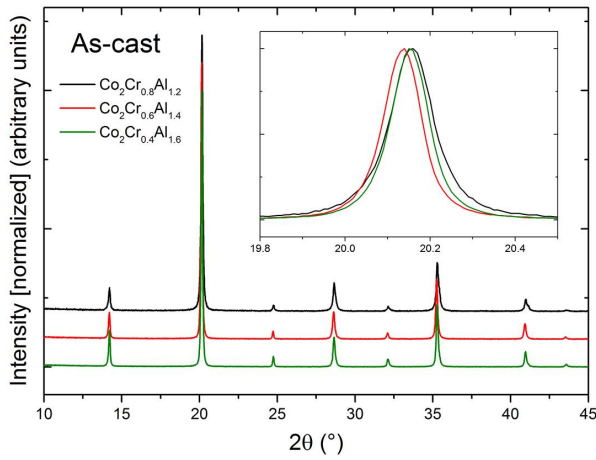
Figure 3.21: X-ray diffraction data for as-cast $Co_2Cr_{0.8}Al_{1.2}$, $Co_2Cr_{0.6}Al_{1.4}$ and $Co_2Cr_{0.4}Al_{1.6}$ samples.

Table 3.6: Refinement of XRD for as-cast $Co_2Cr_{0.8}Al_{1.2}$, $Co_2Cr_{0.6}Al_{1.4}$ and $Co_2Cr_{0.4}Al_{1.6}$ samples.

Sample	Structure	Lattice (Å)
$Co_2Cr_{0.8}Al_{1.2}$	$Pm\bar{3}m$	2.864(2)
$Co_2Cr_{0.6}Al_{1.4}$	$Pm\bar{3}m$	2.865(2)
$Co_2Cr_{0.4}Al_{1.6}$	$Pm\bar{3}m$	2.868(2)

Since all the compositions melt incongruently, it was required to grow them using FZ technique.

3.3.2.2 Floating Zone growth

Polycrystalline seed and feed rods of $Co_2Cr_{0.8}Al_{1.2}$, $Co_2Cr_{0.6}Al_{1.4}$ and $Co_2Cr_{0.4}Al_{1.6}$ were cast (refer Section 2.2.1.1 for details) with at least 4N pure constituents. The subsequent FZ growths were performed in an Ar atmosphere. The growth speed employed was 5 mm/hr along with counter-rotation of seed and feed rod of the order of ∼0.3 Hz, for all experiments. The final zone was quenched in the end. Figure 3.22 shows the final grown samples. All the samples showed a thin layer of oxidation at the surface. The growth for $Co_2Cr_{0.4}Al_{1.6}$ was not as stable as compared to the other two compositions, and therefore, a long sample could not be grown, even after multiple attempts.
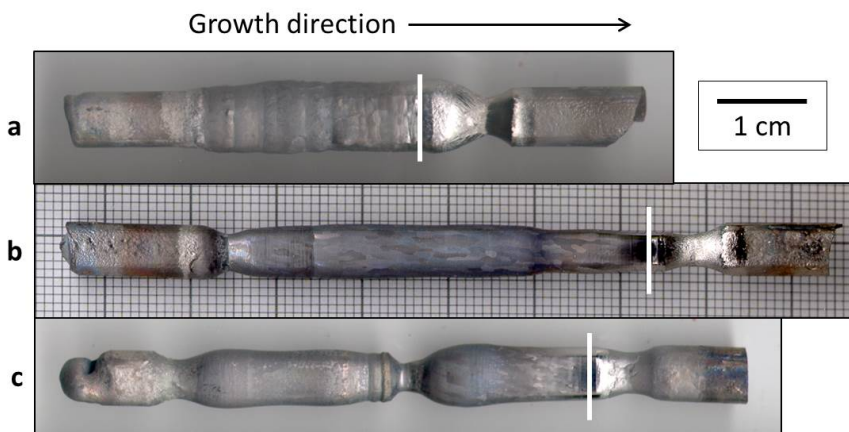
Figure 3.22: Final samples from the Floating Zone growth for (a) Co$_2$Cr$_{0.8}$Al$_{1.2}$ (b) Co$_2$Cr$_{0.6}$Al$_{1.4}$ (c) Co$_2$Cr$_{0.4}$Al$_{1.6}$ off-stoichiometric compositions.
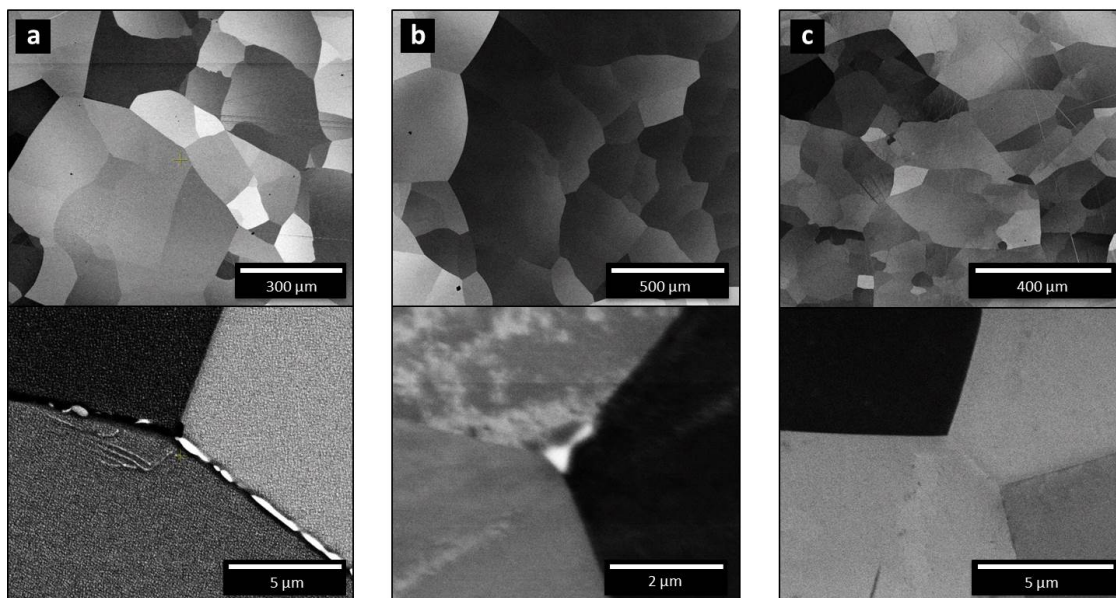
Figure 3.23: Backscattered electron images for Floating Zone (FZ)-grown samples (a) Co$_2$Cr$_{0.8}$Al$_{1.2}$ (b) Co$_2$Cr$_{0.6}$Al$_{1.4}$ (c) Co$_2$Cr$_{0.4}$Al$_{1.6}$.

Samples were studied from different positions of the grown rods but only the data from the final part of the grown sample marked by white lines (Figure 3.22) are presented here. The Figure 3.23 shows the observed microstructures for the three compositions at different magnifications. At low magnifications, all the three compositions seem phase-pure, with multiple grains. Since we now know from the Co$_2$CrAl growth experiments, that the secondary phase is at the nanoscale,the sample was carefully analysed at significantly higher magnifications.

At higher magnifications, the secondary phase segregation at the grain boundaries could be

clearly seen for $Co_2Cr_{0.8}Al_{1.2}$. Due to spinodal decomposition, the secondary phase was also finely distributed in the grains, as was in the case of Co_2CrAl and $Co_2Cr_{0.6}Fe_{0.4}Al$. Comparing to the stoichiometric Co_2CrAl, the extent of phase separation had gone down, as the secondary phase features were smaller. With regards to $Co_2Cr_{0.6}Al_{1.4}$, no spinodal-like features were observed within the grains, although the secondary phase was perceptible at some grain boundaries, mainly at the triple grain boundaries as shown in Figure 3.23b. Finally coming to the $Co_2Cr_{0.4}Al_{1.6}$ composition, no secondary phase was observed even at the grain boundaries as can be seen in Figure 3.23c.

Since the secondary phase observed for $Co_2Cr_{0.8}Al_{1.2}$ and $Co_2Cr_{0.6}Al_{1.4}$ was significantly small, individual EDX measurements could not be performed. Overall EDX data for $Co_2Cr_{0.8}Al_{1.2}$ and $Co_2Cr_{0.6}Al_{1.4}$ along with the data for $Co_2Cr_{0.4}Al_{1.6}$ is listed in Table 3.7.

Table 3.7: EDX data for Floating Zone (FZ)-grown $Co_2Cr_{0.8}Al_{1.2}$, $Co_2Cr_{0.6}Al_{1.4}$ and $Co_2Cr_{0.4}Al_{1.6}$ samples.

EDX (atomic %)	$Co_2Cr_{0.8}Al_{1.2}$			$Co_2Cr_{0.6}Al_{1.4}$			$Co_2Cr_{0.4}Al_{1.6}$		
Phase	Co	Cr	Al	Co	Cr	Al	Co	Cr	Al
Nominal	50	20	30	50	15	35	50	10	40
Overall	50.1	20.8	29.1	50.6	14.3	35.1	51.7	9.2	39.6

Figure 3.24 shows the XRD data for all the three compositions. No strong secondary reflections were observed for FZ-grown $Co_2Cr_{0.8}Al_{1.2}$ in the XRD data, even though spinodal decomposition was seen in the BSE images. The main reflection was broader for $Co_2Cr_{0.8}Al_{1.2}$ as compared to $Co_2Cr_{0.6}Al_{1.4}$ and $Co_2Cr_{0.4}Al_{1.6}$ but no perceptible tetragonal splitting as in the case of stoichiometric Co_2CrAl was seen (inset of Figure 3.24). XRD data could not be refined using the σ-CoCr tetragonal phase from the stoichiometric Co_2CrAl. It is quite possible that the secondary phase had a different structure, as was observed in the case of $Co_2Cr_{0.6}Fe_{0.4}Al$. The refinement could only be done using a single $Pm\bar{3}m$ cubic phase and the lattice constant is listed in Table 3.8. The obtained lattice constant was smaller for $Co_2Cr_{0.8}Al_{1.2}$ as compared to $Co_2Cr_{0.6}Al_{1.4}$ and $Co_2Cr_{0.4}Al_{1.6}$, although all three had similar lattice parameters, suggesting that the lattice was strained due to the presence of the secondary phase, even when it was less than that of Co_2CrAl. Nevertheless, the secondary phase is indeed less, as compared to Co_2CrAl. Even though the $Co_2Cr_{0.8}Al_{1.2}$ composition still lies in the spinodal regime, but as we had speculated, we have moved towards the edge of the miscibility gap.
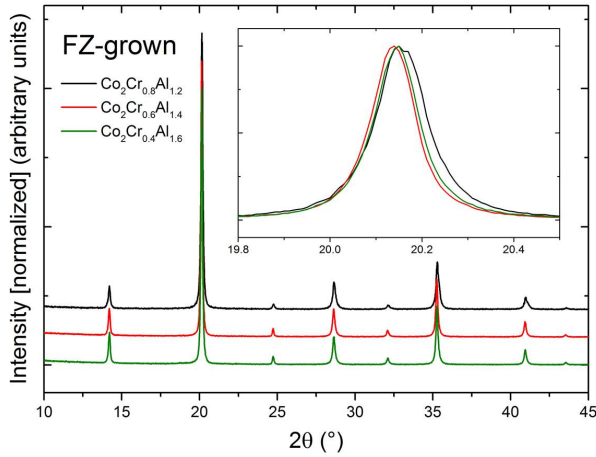
Figure 3.24: X-ray diffraction data for Floating Zone (FZ)-grown Co$_2$Cr$_{0.8}$Al$_{1.2}$, Co$_2$Cr$_{0.6}$Al$_{1.4}$ and Co$_2$Cr$_{0.4}$Al$_{1.6}$ samples.

Sample	Structure	Lattice (Å)
Co$_2$Cr$_{0.8}$Al$_{1.2}$	$Pm\bar{3}m$	2.865(2)
Co$_2$Cr$_{0.6}$Al$_{1.4}$	$Pm\bar{3}m$	2.870(2)
Co$_2$Cr$_{0.4}$Al$_{1.6}$	$Pm\bar{3}m$	2.869(2)

Table 3.8: Refinement for Floating Zone (FZ)-grown Co$_2$Cr$_{0.8}$Al$_{1.2}$, Co$_2$Cr$_{0.6}$Al$_{1.4}$ and Co$_2$Cr$_{0.4}$Al$_{1.6}$ samples.

No additional reflections or perceptible shoulders were observed in XRD data of FZ-grown Co$_2$Cr$_{0.6}$Al$_{1.4}$. Refinement of the XRD data was attempted using the CoAl-type cubic and CoCr-type tetragonal phases, as in the case for Co$_2$Cr$_{0.8}$Al$_{1.2}$, but the secondary phase fraction converged to zero. The secondary phase fraction was considerably smaller as seen in SEM, and the peaks overlapped as well, which made it difficult to do a two phase refinement. The data was refined using a single $Pm\bar{3}m$ cubic phase, as in the case of as-cast samples (Table 3.8).

Since a periodic well-distributed nano-structure in the grains due to spinodal decomposition is not seen, the Co$_2$Cr$_{0.6}$Al$_{1.4}$ composition is out of the spinodal region. In the phase diagram, the Co$_2$Cr$_{0.6}$Al$_{1.4}$ composition possibly falls in the nucleation region (binodal) of the miscibility gap till room temperature, as small amounts of secondary phase was observed at the grain boundaries. Even if the spinodal region is encountered at sufficiently low temperatures, the kinetics are likely too slow for the decomposition to take place.

In the case of Co$_2$Cr$_{0.4}$Al$_{1.6}$, phase separation was not observed the SEM. No additional features were observed in XRD (Figure 3.24) as well, and the data could be well refined using a single $Pm\bar{3}m$ cubic phase (Table 3.8). The XRD data with refinement along with the details of the various refinement parameters for all the three compositions are given in Appendix A (Page 148-149).
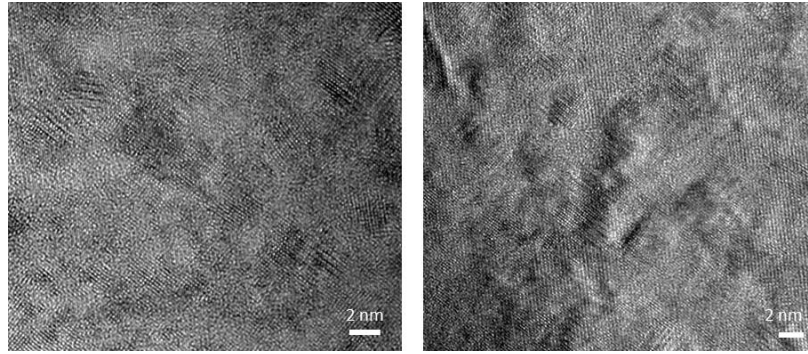
Figure 3.25: High resolution TEM data for Floating Zone (FZ)-grown Co$_2$Cr$_{0.4}$Al$_{1.6}$ sample at different positions. (TEM data courtesy of Dr. Felix Börrnert)

It seems that a phase-pure sample has been obtained. However, as mentioned earlier, the secondary phase is sometimes on the order of a few nanometers only, and therefore, might not be seen in SEM. Therefore, the sample homogeneity and structure were confirmed by using TEM, as shown in Figure 3.25 and no secondary phase was observed even at the nanoscale for Co$_2$Cr$_{0.4}$Al$_{1.6}$ (the contrast seen in the image is due to uneven thickness of the sample and atomic corrugation). We can thus confidently say that the spinodal decomposition and the solid-state phase transformation has been successfully avoided.

Magnetic properties

Magnetization measurements were performed for all three compositions. All the samples were found to be ferromagnetic at room temperature and no transition was observed between 5 K and 300 K. Figure 3.26 shows the summary of the saturation magnetization for both as-cast and FZ-grown samples. All the samples were found to be soft-magnetic and a representative M(H) curve is shown on the side as well. As the extent of spinodal decomposition reduced in Co$_2$Cr$_{0.8}$Al$_{1.2}$, the saturation moment improved relative to the Slater-Pauling value. The ratio improved further in Co$_2$Cr$_{0.6}$Al$_{1.4}$, where a well distributed secondary phase due to spinodal decomposition was not observed. The saturation moment did not match the Slater-Pauling value, possibly due to the small amount of secondary phase being still present.

However, Co$_2$Cr$_{0.4}$Al$_{1.6}$ although phase-pure, the magnetization did not show expected improvements. It should be kept in mind that the Slater-Pauling rule need not fit so well to the off-stoichiometric samples, as we are quite far away from the ideal ordered Heusler structure. In addition to this, off-stoichiometry is a form of deliberate disorder where Al atoms occupy the Cr sites. As has been already discussed with the various examples in Chapter 1, anti-site disorder may strongly affect the saturation moment. This may be the reason for the lower saturation moment for Co$_2$Cr$_{0.4}$Al$_{1.6}$, even though the sample was chemically homogeneous.
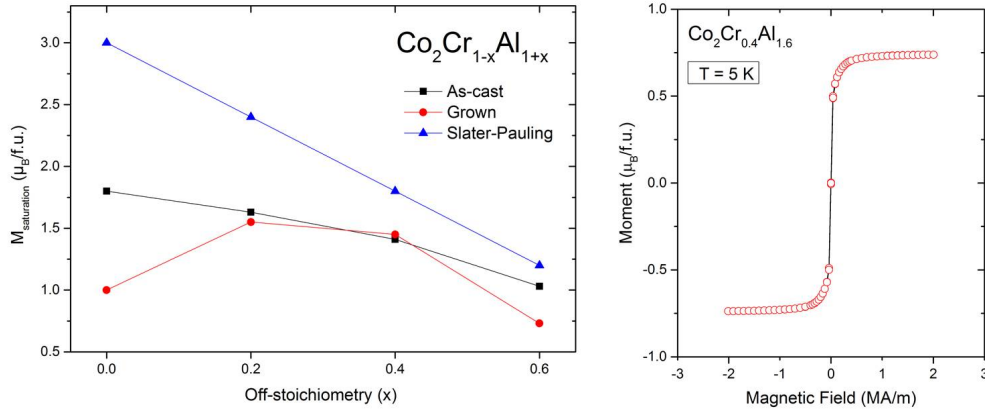
Figure 3.26: Magnetization data for as-cast and Floating Zone (FZ)-grown Co$_2$CrAl, Co$_2$Cr$_{0.8}$Al$_{1.2}$, Co$_2$Cr$_{0.6}$Al$_{1.4}$ and Co$_2$Cr$_{0.4}$Al$_{1.6}$ samples along with the Slater-Pauling values for comparison. The magnetization-field curve for Co$_2$Cr$_{0.4}$Al$_{1.6}$ is shown as representative of the soft-magnetic behaviour of all the samples.

Thus the magnetization data also gives a possibility to track the extent of spinodal decomposition in the system. We have utilized the various data from the annealing and off-stoichiometry experiments to plot an approximate picture of the miscibility gap which is discussed next.

3.3.3 Extent of immiscibility

The available data from both the annealing of Co$_2$CrAl and the off-stoichiometric samples were combined to develop the phase-space for the extent of the miscibility gap. So far nothing is reported in this regards for Co-Cr-Al in the available literature, to the best of our knowledge.

Firstly, based on our data of Co$_2$CrAl FZ-grown samples annealed at different temperatures, we conclude that the solid-state miscibility gap exists at least until 1250 °C in the phase diagram. The spinodal regime of the miscibility gap in the phase diagram is up to the vicinity of 1000 °C. At 750 °C, we are well within the two-phase regime as a pronounced secondary phase is seen in sample annealed at that temperature. The high stability of the secondary phase which is observed, is even seen for annealed polycrystalline samples by de Teresa et al. [202].

In the next step, as Cr was substituted with Al, the extent of the spinodal decomposition was reduced. At the Co$_2$Cr$_{0.8}$Al$_{1.2}$ composition, the miscibility gap is still encountered. When the composition was further changed to Co$_2$Cr$_{0.6}$Al$_{1.4}$, no spinodal decomposition features were observed. A small amount of secondary phase was seen at the grain boundaries. The two-phase binodal region (shaded grey in Figure 3.11) around the spinodal region led to nucleation of the secondary phase. The secondary phase nucleates preferentially at the grain boundaries as they are sites of higher energy, what was precisely observed in our case as well.

Finally for Co$_2$Cr$_{0.4}$Al$_{1.6}$, in the phase diagram, either the composition is completely out of the

miscibility gap, or the immiscibility exists at considerably low temperatures where kinetics are too slow for phase separation or nucleation. Either way, we did not observe any nanoscale secondary phase in the TEM as well. Thus, we were able to successfully synthesize a phase-pure off-stoichiometric composition for Co$_2$CrAl, where the miscibility gap was avoided.

We used the available data to a plot a tentative pseudo-binary phase diagram which is shown in Figure 3.27. An estimate of the melting points of the different compositions was obtained from the zone temperature during the FZ experiment. Normally, the molten material is superheated to have an optimal viscosity for the zone formation, and therefore, the temperature of the molten zone is ~50 K above the melting point and depending on the composition may even be higher [196]. The melting points are extracted accordingly from the *in situ* temperature measurements during the growth and plotted. The error for the pyrometer measurement and thermal fluctuations at the zone add up to a considerable error in the melting point values, and hence should be considered qualitatively. A rough linear liquidus is drawn to highlight the trend. The trend fits to the existing phase diagram data as Co$_{50}$Al$_{50}$ has a melting point of approximately 1645 °C [234].
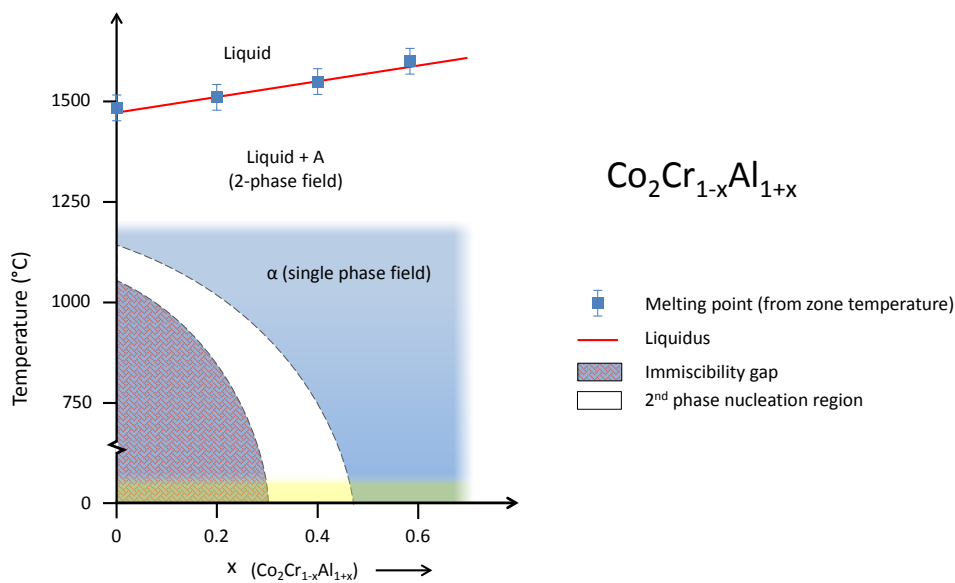
Figure 3.27: Schematic of a tentative pseudo-binary phase diagram for Co$_2$Cr$_{1-x}$Al$_{1+x}$.

The maximum of the miscibility gap is not plotted at the stoichiometric Co$_2$CrAl as we do not have information on the Cr-rich side of the stoichiometric composition, and it is quite possible that the miscibility gap is even higher in these compositions.

We have seen that the annealing experiments were not successful in obtaining a phase-pure sample. Nevertheless, annealing the different off-stoichiometric compositions at various temperatures further revealed the extent of spinodal region. As the miscibility gap became smaller with off-stoichiometry, it allowed us to find an optimal annealing temperature in order to avoid the secondary phase through

annealing and subsequent quenching. This would make it possible to avoid the secondary phase formation, even at smaller off-stoichiometry. However, as mentioned earlier, annealing experiments do not always work. It may be possible that the secondary phase is highly stable and may not dissolve fully. Such a phenomenon has been observed in annealing at 1000 °C, that the secondary phase decreased in volume fraction but did not completely go away even after 3 weeks. Desirable additional experiments at different temperatures and for prolonged time for further analysis may be tried, but are tedious. More importantly, the focus in the present work was on the quaternary Co-Cr-Fe-Al system, and the study of annealing and off-stoichiometry in Co$_2$CrAl was only taken as a test case.

Thus, we have been able to gain a better understanding of the thermodynamics in the Co-Cr-Al system. More importantly, the concept of substituting Cr with Al, in order to move away from the spinodal region has been successfully demonstrated. This approach was extended to the Co$_2$Cr$_{0.6}$Fe$_{0.4}$Al compound, which was our main composition of interest, and the results are discussed in the following section.

3.4 Off-stoichiometric Co$_2$Cr$_{0.4}$Fe$_{0.4}$Al$_{1.2}$: A new half-metallic ferromagnet

So far, we have confirmed the presence of the hitherto unknown solid-state miscibility gap in the Co-Cr-Fe-Al system and have been able to account for almost all of the issues/anomalous data reported in the literature. We also explored the strategy to get rid of the inhomogeneity in as-grown Co$_2$CrAl sample by annealing the sample at high temperatures but we did not succeed in obtaining a homogeneous sample. On the other hand, we were able to demonstrate that the region of instability can be successfully avoided through off-stoichiometry.

The composition-variable strategy can be extended to the Co$_2$Cr$_{0.6}$Fe$_{0.4}$Al composition, which is most interesting in terms of properties and applications as outlined earlier. Co$_2$Cr$_{0.6}$Fe$_{0.4}$Al being a quaternary system, there are 4 elements which may be varied among themselves in order to optimize the composition. At the same time, it should be kept in mind that we do not want to affect the electronic structure so strongly that all the interesting features are lost. For this reason, interfering with the Co sublattice was avoided since it plays the most important role in the inherent magnetism of Co-based Heusler compounds as has been discussed earlier in Chapter 1. Taking the cue from the off-stoichiometric Co$_2$CrAl, substituting Cr with Al, without affecting the Fe atoms seemed to be best choice.

Since the extent of spinodal decomposition was found to be much smaller in Co$_2$Cr$_{0.6}$Fe$_{0.4}$Al as compared to Co$_2$CrAl, a small off-stoichiometry was speculated to be sufficient to avoid the miscibility gap. Therefore, an off-stoichiometric composition Co$_2$Cr$_{0.4}$Fe$_{0.4}$Al$_{1.2}$ was chosen for the experimentation.

3.4.1 Synthesis and characterization

First, the Co$_2$Cr$_{0.4}$Fe$_{0.4}$Al$_{1.2}$ composition was prepared by arc-melting using at least 4N pure constituents. Figure 3.28a shows the BSE image for the as-cast sample. As in the case of all samples studied in the series so far, the as-cast Co$_2$Cr$_{0.4}$Fe$_{0.4}$Al$_{1.2}$sample was found to be phase-separated due to incongruent melting. The phase segregation resulted in two phases - an Al-rich phase and a Cr-rich phase, Co being more or less same throughout. Table 3.9 shows the EDX data for the two phases.

Similar to the rest of the series, the two cubic phases in the as-cast sample had similar lattice constants and thus the XRD data (Figure 3.28b) could only be refined with a single $Pm\bar{3}m$ phase with a lattice constant of 2.860(2) Å. The details of the refinement for the XRD data are listed in Appendix A (Page 150).
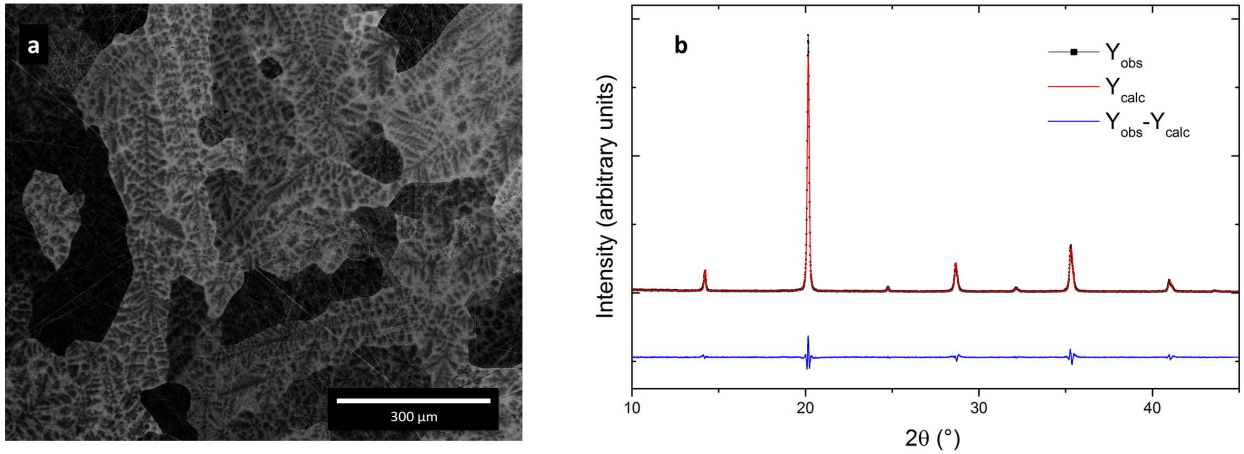
Figure 3.28: As-cast Co$_2$Cr$_{0.4}$Fe$_{0.4}$Al$_{1.2}$ sample (a) BSE image shows the two phases (b) X-ray diffraction data with Rietveld refinement.

Table 3.9: EDX data for as-cast Co$_2$Cr$_{0.4}$Fe$_{0.4}$Al$_{1.2}$ sample.

Phase	Co	Cr	Fe	Al
Nominal	50	10	10	30
Al-rich (dark)	48.5	6	6.8	38.7
Cr/Fe-rich (light)	48.6	14.4	12.9	24.1
Overall	49.6	9.3	9.2	31.9

Due to the phase segregated nature, FZ experiment was performed subsequently in order to avoid the two-phase field below liquidus. Seed and feed rods for the FZ growth were prepared from at least 4N pure constituents. The conditions for the FZ growth experiment was same as that for the other samples; a growth speed of 5 mm/hr along with counter-rotation of the seed and feed rod at ~0.3 Hz were used. The final zone was quenched at the end of the experiment.

The final grown sample is shown in Figure 3.29a. Slight surface oxidation was observed in this case as well. The grown sample along with the zone were cut and analysed. Figure 3.29b shows the cross-section of the zone. The melting and solidification interface profiles are marked with white lines. The solid-liquid interface at the solidification front was convex, and additionally, the interface curvature was very shallow, as desired. The final part of the grown rod, marked by a vertical white line in the Figure 3.29a, was used for further characterization and measurements.
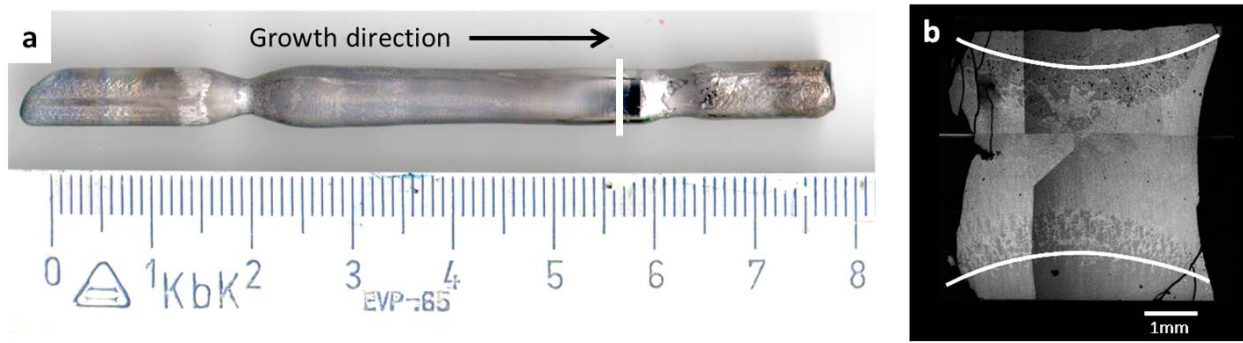
Figure 3.29: Floating Zone growth of $Co_2Cr_{0.4}Fe_{0.4}Al_{1.2}$ (a) Grown rod (vertical white line marks the final part of the sample for study) (b) zone cross-section (white lines highlight the interfaces).

Figure 3.30a shows the microstructure of FZ-grown $Co_2Cr_{0.4}Fe_{0.4}Al_{1.2}$, at different magnifications. The final part of the as-grown sample was found to be phase-pure with multiple grains as per the BSE data. No segregation was observed at the grain boundaries even at higher magnifications (inset of Figure 3.30a). The overall composition from EDX is also listed in Figure 3.30a and matches with the nominal composition within the margin of error of the measurement (The slightly higher Al composition (~ 2 %) is an overestimation due to a technical issue in the EDX measurement).

EDX (at. %)	Co	Cr	Fe	Al
Nominal	50	10	10	30
Overall	47.3	10	10	32.7
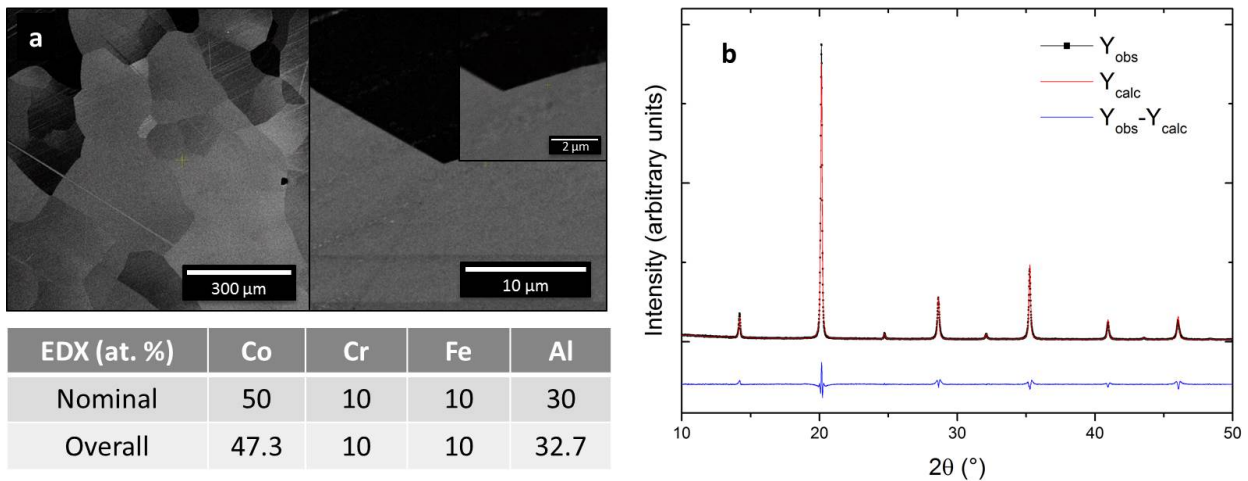
Figure 3.30: Floating Zone (FZ)-grown $Co_2Cr_{0.4}Fe_{0.4}Al_{1.2}$ sample (a) BSE image along with EDX data (b) X-ray diffraction data with Rietveld refinement.

The XRD data for the sample is shown in Figure 3.30b. The crystal structure is cubic ($Pm\bar{3}m$) with B2-type order as no (111) superlattice reflection is seen. No additional reflections for any impurity phase are observed as well. The lattice constant from Rietveld refinement is found to be 2.867(4) Å. The details of the refinement are mentioned in Appendix A (Page 150).
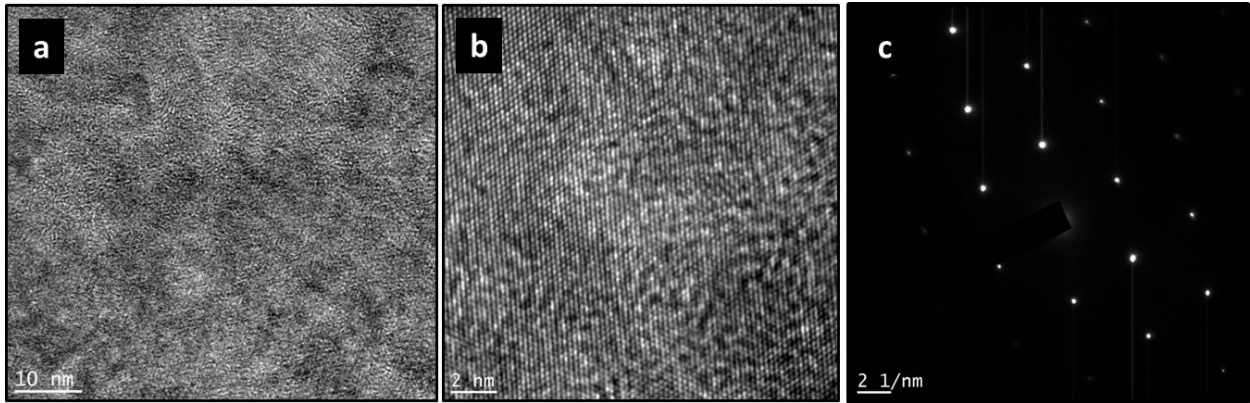
Figure 3.31: TEM data on Floating Zone (FZ)-grown $Co_2Cr_{0.4}Fe_{0.4}Al_{1.2}$ sample (a) bright field image (b) high resolution image showing nanoscale homogeneity (b) SAED pattern. (TEM data courtesy of Dr. Felix Börrnert and Marcel Haft)

As already discussed for the FZ growth of $Co_2Cr_{0.4}Al_{1.6}$, an important thing that must be kept in mind is that in the phase diagram, as one moves towards the edge of the miscibility gap, the composition may undergo only early stages of the spinodal decomposition. In such cases, the secondary phase would be of the order of only a few nanometers, and thus, would not be seen in SEM. Such a small phase fraction would also not reflect any changes in XRD as well. Therefore, a careful analysis with high resolution TEM was deemed necessary to be able to confirm whether the sample is really phase-pure.

Figure 3.31 shows the TEM data for FZ-grown $Co_2Cr_{0.4}Fe_{0.4}Al_{1.2}$. No secondary phase is observed even at the nanoscale. The contrast seen in the image is due to uneven thickness of the sample and atomic corrugation. The sample is single crystalline in the field of view. The structure and chemical homogeneity is thus confirmed as the sample was chemically homogeneous even at the nanoscale.

Notwithstanding the phase-purity, the biggest challenge of changing the composition of a system is that it may affect the electronic structure of the material, and therefore it is essential to clarify the extent of change in the band structure. In order to check whether the half-metallicity and the associated features of $Co_2Cr_{0.6}Fe_{0.4}Al$ are still retained in the off-stoichiometric sample, band structure calculations were performed for the $Co_2Cr_{0.4}Fe_{0.4}Al_{1.2}$ composition.

3.4.2 Band structure calculations

The density functional theory (DFT) calculations have been performed using the SPR-KKR (spin polarized relativistic Korringa-Kohn-Rostoker) code [235] version 5.4. The local density approximation (LDA) exchange correlation functional parametrization by Vosko, Wilk and Nusair [236] was used to converge the total energy to an accuracy of better than 10^{-5}Ry. The full shape of the potential was taken into account with the constraint of spherical symmetry. The disorder on

Wyckoff position $4b$ was treated within the coherent potential approximation (CPA) [237], assuming a mixture of 40% Fe, 40% Cr and 20% Al while assuming integer occupation of the Wyckoff positions $4a$ and $8c$. The band structure calculations are courtesy of Dr. Jan Trinckauf at IFW Dresden.

Figure 3.32 shows the comparison of the density of states for the stoichiometric Co$_2$Cr$_{0.6}$Fe$_{0.4}$Al which was similar to that reported earlier [6], along with the density of states for off-stoichiometric Co$_2$Cr$_{0.4}$Fe$_{0.4}$Al$_{1.2}$ sample. There was no significant change in the band structure and half-metallicity is maintained. The density of states at the Fermi level does not go to zero, which is purely an issue of the type of code used for calculations, as the integrals get rounded off, leading to only a minimum, as reported in the case of Co$_2$Cr$_{0.6}$Fe$_{0.4}$Al [6]. For the same reason, the density of states at Fermi level in our calculations for both the stoichiometric Co$_2$Cr$_{0.6}$Fe$_{0.4}$Al and the off-stoichiometric Co$_2$Cr$_{0.4}$Fe$_{0.4}$Al$_{1.2}$ composition did not go to zero as well.
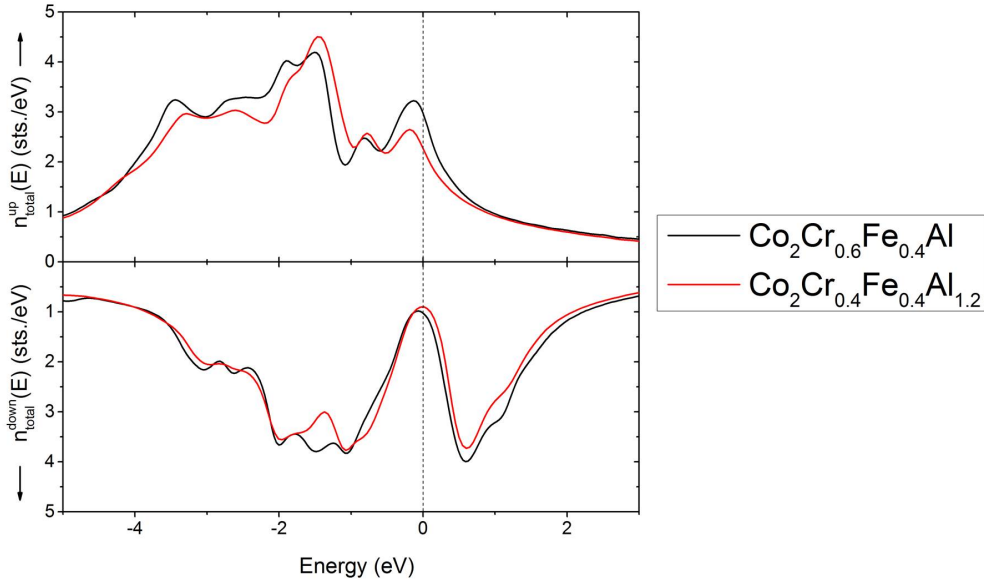
Figure 3.32: Comparison of density of states for the stoichiometric Co$_2$Cr$_{0.6}$Fe$_{0.4}$Al and the off-stoichiometric Co$_2$Cr$_{0.4}$Fe$_{0.4}$Al$_{1.2}$ sample using SPR-KKR calculation. (Calculations courtesy of Dr. Jan Trinckauf at IFW Dresden)

The new off-stoichiometric composition Co$_2$Cr$_{0.4}$Fe$_{0.4}$Al$_{1.2}$ is found to be a half-metallic ferromagnet, as evident from the gap in the minority states (Figure 3.32). The additional salient features such as the van-Hove singularity at the Fermi level are also not affected by the change in stoichiometry. There is also no shift in the Fermi edge and ϵ_F still remains in the middle of the band gap (Figure 3.32). All the interesting features of the stoichiometric composition are retained and there is no significant shrinking or shifting of the band gap.

Thus, we have the prospect of realizing a new half-metallic ferromagnet in the Co$_2$Cr$_{1-x}$Fe$_x$Al series. However, it is deemed important to check whether the various physical properties such as

saturation magnetization finally fit to the theory, as this discrepancy has been a common problem in the series [203, 207].

3.4.3 Physical properties

Various physical properties were measured on the FZ-grown $Co_2Cr_{0.4}Fe_{0.4}Al_{1.2}$. The magnetization data is shown in Figure 3.33. The sample is soft magnetic as can be seen in Figure 3.33a. The saturation magnetization is found to be 3.11 μ_B/f.u. which matches well with the Slater-Pauling value of 3.2 μ_B/f.u. as calculated from equation 1.10. This is very promising as such a good match of the saturation magnetization with the Slater-Pauling value has so far not been reported for $Co_2Cr_{0.6}Fe_{0.4}Al$ (compare, e.g., [203]). Moreover, no transitions were observed in the temperature dependence of magnetization till 5 K (Figure 3.33b), as expected.

High temperature magnetization was also measured and is shown in Figure 3.33c and the Curie temperature is found to be 790 K using a Curie-Weiss fit for $1/\chi$. The heating and cooling curve were slightly different due to surface oxidation of the sample during the measurement. Due to the high Curie temperature, the saturation field and susceptibility had a negligible temperature dependence till room temperature.
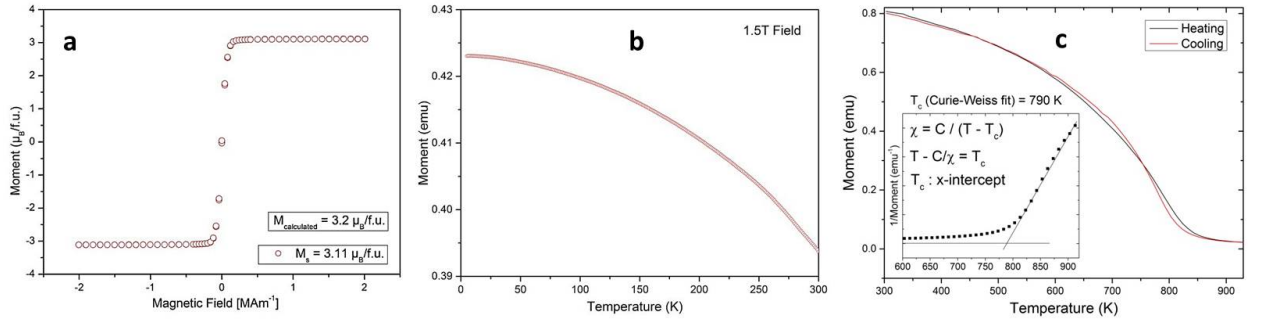
Figure 3.33: Magnetization data for Floating Zone (FZ)-grown $Co_2Cr_{0.4}Fe_{0.4}Al_{1.2}$ sample (a) Magnetization vs. field curve at 5 K (b) Magnetization as a function of temperature (M(T)) in 1.5 MAm^{-1} field till 5 K (c) High temperature M(T) at 1 MAm^{-1} field.

Resistivity was measured using a standard four-probe alternating current technique. A 1x1x10 mm sample was used for the measurement. Figure 3.34a shows the resistivity ρ as a function of temperature in zero magnetic field. Resistivity showed a clear metallic temperature dependence from 50 K till 300 K with an almost linear increase with increasing temperature. There is a resistivity minimum observed below 50 K with a logarithmic upturn in resistivity at lower temperatures. The residual resistivity was 0.189 $m\Omega cm$ with a residual resistivity ratio (RRR) of $\rho(300K)/\rho_R = 1.05$. It was difficult to compare the RRR values to the stoichiometric $Co_2Cr_{0.6}Fe_{0.4}Al$ as it is reported to have a semiconducting behaviour both in bulk as well as films [208–210], possibly due to the phase segregation. Nevertheless, higher values of RRR have been reported in literature for other Heusler

compounds, e.g., Co$_2$MnSi [144] and Co$_2$FeSi [238]. The rather low RRR value is likely due to the *B2*-type disorder present in the material. In addition, the sample was not annealed and was thus expected to contain larger amount of stresses and defects which cause scattering on these defects at low temperatures.
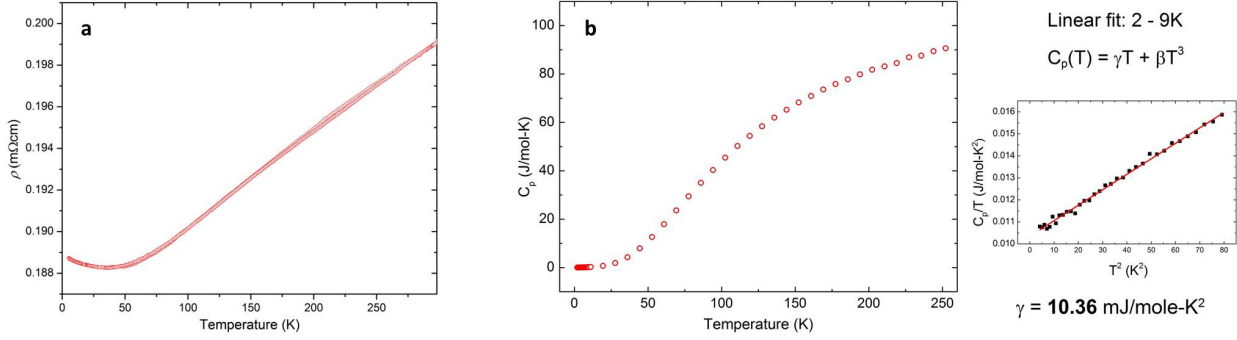
Figure 3.34: Floating Zone (FZ)-grown Co$_2$Cr$_{0.4}$Fe$_{0.4}$Al$_{1.2}$ sample (a) Resistivity data (b) Specific heat data with the low temperature fit (2-9 K). (Transport data courtesy of Frank Steckel; Specific heat data courtesy of Steven Rodan)

Normally, a logarithmic upturn at low temperatures is characteristic of classical Kondo effect, due to the spin-flip scattering of conduction electrons at the dilute magnetic impurities [239, 240]. It has been discussed that a resistance minimum in Heusler systems is unlikely to be due to Kondo effect, specially due to a lack of field dependence. It has been understood that such a low temperature resistivity minimum is due to scattering at localized moments or a manifestation of electron scattering at the low-lying excitations of the disordered lattice [152], although an exact mechanism is still not known. One may speculate of a similar scenario in the present material.

Figure 3.34b shows the specific heat measurement on FZ-grown Co$_2$Cr$_{0.4}$Fe$_{0.4}$Al$_{1.2}$. The specific heat was measured till 2 K. Heat capacity increased monotonically with increasing temperature and no transitions were observed. The low temperature regime (2-9 K) was fitted with $C = \gamma T + \beta T^3$ as shown in Figure 3.34b as well. Specific heat coefficient γ was found to be 10.36 $mJmol^{-1}K^{-2}$ whereas the coefficient of phononic contribution, β, was found to be 0.070 $mJmol^{-1}K^{-4}$. Only a few reports exist on specific heat data on Heusler compounds [241, 242], although the phase homogeneity of the measured compositions has not yet been addressed. A recent work on specific heat measurements on select Heusler compositions has been done keeping the same in mind [243], where it was shown that the specific heat coefficient γ for the spinodally decomposed Co$_2$Cr$_{0.6}$Fe$_{0.4}$Al is higher than the phase-pure Co$_2$Cr$_{0.4}$Fe$_{0.4}$Al$_{1.2}$. The higher γ value for the Co$_2$Cr$_{0.6}$Fe$_{0.4}$Al composition is possibly due to contributions from the hexagonal ϵ-Co phase that separates out. The hexagonal ϵ-Co has been reported to have a high density of states (DOS) at the Fermi level [244, 245] and hence, its presence is expected to lead to a high γ. A recent work also reported similar high DOS for the

hexagonal cobalt but it was incorrectly labelled as the α phase [246].

Furthermore, the γ value in $Co_2Cr_{0.4}Fe_{0.4}Al_{1.2}$ was higher than those observed for, e.g., Co_2FeSi and Co_2FeAl (FZ-grown) which were phase-pure. In the $Co_2Cr_{1-x}Fe_xAl$ system, a high γ value is expected because of the van-Hove singularity in the majority spin direction. Therefore, the observed higher γ for the off-stoichiometric composition further supports our calculations of the electronic structure.

In addition to the chemical homogeneity of the sample, the saturation magnetization also matched nicely with Slater-Pauling value which is unprecedented for $Co_2Cr_{1-x}Fe_xAl$ samples in the Cr-rich side, as was described in the beginning of the chapter. Other physical property measurements, such as resistivity and specific heat measurements, also did not show any anomalies. The goal of the present work has been to progress towards a half-metallic ferromagnet, and the physical properties measured have been found very promising.

We can thus confidently say, that we have discovered a new potential half-metallic ferromagnetic material, which does not suffer from intrinsic material issues. The physical properties specially magnetization makes the composition very encouraging towards realizing 100 % spin polarization, hopefully even at elevated temperatures. Our results are encouraging towards measurement of spin polarization as a final proof of the half-metallicity and we believe that our results would generate sufficient interest in the thin film community to prepare adequate samples with the off-stoichiometric composition for measurements of magnetoresistance and spin polarization.

3.5 Conclusion

In the first part of this work (Section 3.2), we have performed FZ growth on selected compositions in the series in order to overcome the incongruent melting behaviour. Based on our results, we have confirmed the presence of a solid-state miscibility gap in the Co-Cr-Fe-Al system, which leads to a phase separation at low temperatures via spinodal decomposition [218]. The secondary phase strongly affects magnetic properties and since the transformation occurs at low temperature, it is likely to occur in thin films as well. We have thus been able to coherently explain almost all the anomalous data in literature pertaining to physical properties as well as material issues, for both bulk samples as well as thin films.

The second part of the work (Section 3.3) focused on understanding the region of immiscibility in Co$_2$CrAl under the variables of temperature and composition. We showed that annealing treatments on Co$_2$CrAl are not successful in getting rid of the secondary phase, as the miscibility gap exist at least till 1000 °C [233]. On the other hand, the spinodal decomposition in Co$_2$CrAl could be completely avoided through changing the composition. Reducing the Cr content in the material worked well, and a phase-pure Co$_2$Cr$_{0.4}$Al$_{1.6}$ was synthesized by FZ technique. Based on the analysis of the annealing and off-stoichiometry experiments, we have also been able to develop a pseudo-binary phase diagram for Co$_2$CrAl highlighting the extent of immiscibility.

In the final section (3.4), we have demonstrated that the recipe of off-stoichiometry through reducing Cr content is successful for quaternary Co$_2$Cr$_{0.6}$Fe$_{0.4}$Al composition. We describe a new composition Co$_2$Cr$_{0.4}$Fe$_{0.4}$Al$_{1.2}$, which can be synthesized as a phase-pure sample using the FZ technique. The band structure calculations show that the half-metallicity as well as the other interesting features of Co$_2$Cr$_{0.6}$Fe$_{0.4}$Al should be retained in the off-stoichiometric composition, specifically the Fermi edge being in the middle of the band gap in the minority spin direction as well the van-Hove singularity at Fermi level along majority spin direction. The magnetization data fit quite well to the Slater-Pauling value, which has so far not been seen in the quaternary Co$_2$Cr$_{1-x}$Fe$_x$Al system. Additional measurements such as specific heat support the band structure calculations. We thus present the prospect of new potential half-metallic ferromagnet in the Co$_2$Cr$_{1-x}$Fe$_x$Al Heusler system, which is highly promising towards experimental realization.

Chapter 4

Ordering Phenomena in $Co_2FeAl_{0.5}Si_{0.5}$ Explored via *In Situ* Neutron Diffraction

4.1 Introduction and motivation

$Co_2FeAl_{1-x}Si_x$ is another quite interesting quaternary Heusler system, like $Co_2Cr_{1-x}Fe_xAl$. Electronic structure calculations predict half-metallic ferromagnetism along the whole series [8–10], as in the case of $Co_2Cr_{1-x}Fe_xAl$. In fact, the band gap in $Co_2FeAl_{1-x}Si_x$ is slightly wider than in $Co_2Cr_{1-x}Fe_xAl$, although it does not have a van-Hove singularity in the density of states at Fermi energy for the majority spin direction. In addition, being a substitution series between Co_2FeAl and Co_2FeSi, it has one of the highest Curie temperatures in the Heusler family, varying between 1100-1200 K, as measured by differential scanning calorimetry (DSC) [12]. In stark contrast to the $Co_2Cr_{1-x}Fe_xAl$ system, the $Co_2FeAl_{1-x}Si_x$ series is thermodynamically stable, and the whole composition range is reported to exist as a solid solution between Co_2FeAl and Co_2FeSi.
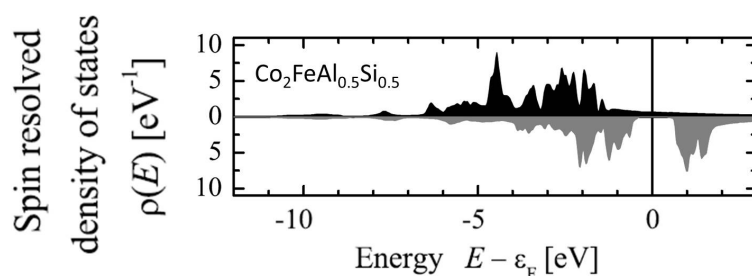
Figure 4.1: Spin resolved density of states for $Co_2FeAl_{0.5}Si_{0.5}$ showing the Fermi edge in the middle of band gap (reproduced from Fecher et al. [9]).

As was discussed in the last chapter, one of salient advantages of a quaternary system is that its various features can be tuned. In the case of $Co_2FeAl_{1-x}Si_x$ with $x = 0.5$, the Fermi level lies in the middle of a wide band gap. Figure 4.1 shows the spin resolved density of states for $Co_2FeAl_{0.5}Si_{0.5}$.

Therefore, the half-metallicity in Co$_2$FeAl$_{0.5}$Si$_{0.5}$ is supposed to be robust against small amounts of disorder and temperature effects, similar to Co$_2$Cr$_{0.6}$Fe$_{0.4}$Al. This is advantageous for applications, as it can be quite difficult to remove disorder completely since partial disorder ($B2$ or DO_3) has been calculated to be thermodynamically more stable in various Co-based quaternary Heusler compounds [10].

Efforts have been made to experimentally realize a potential half-metallic ferromagnet in the Co$_2$FeAl$_{1-x}$Si$_x$ system, as well as the ensuing high tunnel magnetoresistance (TMR) ratio. In one of the early works, magnetic tunnel junctions (MTJs) of Co$_2$FeAl$_{0.5}$Si$_{0.5}$ on a MgO substrate were reported to have TMR ratio of ∼175 % at room temperature with an estimated spin polarization of 68 % [247, 248], and the MTJs were also reported to have high temperature stability. A similar TMR ratio of about 196 % at 7 K (125 % at 300 K) was also reported using oxidized Si substrates [249]. The TMR ratios could further be improved to 390 % at 5 K (220 % at 300 K) [250]. Although Fermi level tuning was demonstrated in Co$_2$FeAl$_{0.5}$Si$_{0.5}$ MTJs, the TMR ratios obtained were lower than that reported earlier [251]. A study on bulk samples annealed at 873 K for 7 days reported a spin-polarization of only $P = 0.6$ measured by Point-Contact Adreev Reflection (PCAR) [8]. A TMR ratio of 832 % at 9 K (386 % at 300 K) has been reported recently for Co$_2$FeAl$_{0.5}$Si$_{0.5}$ junction with CoFe$_2$O$_4$ ferrite barrier, resulting in a spin polarization of 90 % at 9 K (81 % at 300 K) [252]. The various issues with measurement techniques for spin polarization have been discussed in Section 1.3.1.1, specially their reliability. However, the bottom line is that in spite of being stable and robust to disorder, along with a high Curie temperature, half-metallicity has not yet been experimentally confirmed in Co$_2$FeAl$_{0.5}$Si$_{0.5}$, and the TMR ratios reported so far, even though quite high, are considerably lower than what is expected for a half-metallic ferromagnet.

The imperfect spin-polarization and the eluding half-metallic ferromagnetism in Co$_2$FeAl$_{0.5}$Si$_{0.5}$ has been attributed to the presence of large amount of anti-site disorder, as it is difficult to obtain a pure $L2_1$ order even in films [8, 247, 251]. As has been discussed in Section 1.4, anti-site disorder may move the Fermi level out of the band gap, leading to loss of the half-metallic ferromagnetism. Furthermore, the depolarization effects scale with increasing temperature and the band gap shrinks. For the ternary end members Co$_2$FeAl and Co$_2$FeSi, the Fermi edge lies at the edge of the band gap [9], and therefore it has been difficult to obtain high spin polarization and TMR ratios in those materials. In Co$_2$FeAl$_{0.5}$Si$_{0.5}$, although the Fermi level lies in the middle of the band gap [9], different disorder concentrations have been found to be energetically more stable [8, 10], and therefore, this material may be specifically prone to partial $B2$ disorder. It was also reported that the TMR values in Co$_2$FeAl$_{0.5}$Si$_{0.5}$ are sensitive to the amount of $B2$ order present in a sample [253]. Therefore, a thrust has been there to understand and improve the ordering in this material.

Conventional synthesis routes for bulk samples of such stable compounds, e.g., arc-melting, are quite non-equilibrium in nature. Therefore, it is difficult to control the ordering process during synthesis and the main way to improve the $L2_1$ order in a sample is via an annealing procedure. In

general, it is understood that there are regimes in temperature, where each type of order or disorder is stable. The annealing profiles in literature for bulk samples are based on the order-disorder transition temperatures followed by a quenching procedure so that the corresponding order can be frozen-in.

However, there has been quite a bit of debate over temperature regime of the order-disorder transitions in the $Co_2FeAl_{1-x}Si_x$ series, specially $Co_2FeAl_{0.5}Si_{0.5}$ as the $L2_1$-$B2$ transition and the paramagnetic-ferromagnetic transition are quite close to each other. Initially, Balke et al. studied the order-disorder transitions using differential scanning calorimetry (DSC) [11], and based on the DSC signal, the $L2_1$-$B2$ transition was attributed to an average transition temperature, although the signal observed in the representative data was relatively broad. The $L2_1$-$B2$ transition temperature for $Co_2FeAl_{0.5}Si_{0.5}$ was reported as ∼1125 K [11]. The supposed $T_{L2_1/B2}$ transition temperatures were later assumed to be Curie temperatures in a detailed structural and magnetic study done by Umetsu et al. [12]. Umetsu et al. further observed an overlap of the structural and magnetic transitions in the DSC data for $Co_2FeAl_{0.5}Si_{0.5}$, and the $T_{L2_1/B2}$ was identified as ∼1150 K. Furthermore, in order to differentiate the magnetic and structural ordering temperatures, thermo-magnetization was used in conjunction with DSC. In particular, for $Co_2FeAl_{0.5}Si_{0.5}$, low temperature saturation moment was in accordance with the Slater-Pauling value, and a Curie temperature of ∼1100 K was reported [12]. Contrary to the above mentioned reports, a very different $L2_1$-$B2$ transition temperature of 851 K has also been reported for $Co_2FeAl_{0.5}Si_{0.5}$ in a rather recent work using DSC data [84]. It shall suffice to say, that the issue of order-disorder transitions in $Co_2FeAl_{0.5}Si_{0.5}$ is far from resolved.

The annealing temperature for films post-growth also plays an important role, as they have been found to strongly affect the TMR properties [253]. A study of the effect of annealing temperature in $Co_2FeAl_{0.5}Si_{0.5}$ thin films was done using a combination of X-ray absorption spectroscopy, X-ray magnetic circular dichroism (XMCD), magneto-optical Kerr effect (MOKE) magnetometry, and Brillouin light scattering (BLS) [254]. Magnetic anisotropy and Kerr amplitude were found to have an anti-relation with annealing temperature. On the other hand, saturation moments extracted from BLS do not follow either trend but rather has a maximum for annealing at 575 °C. Moreover, in the same work of Trudel et al. [254], the saturations moments at all annealing temperatures except at 475 °C are higher than the Slater-Pauling value. The orbital-to-spin-moment ratio remained unchanged for different annealing temperatures. No specific conclusions were drawn with respect to an optimal annealing profile to be followed, although the MOKE signal was taken to be indicative of $L2_1$ ordering [254].

As we have seen, an optimal annealing profile either for bulk or films, has so far not been agreed upon in literature. In order to optimize the annealing process towards high quality $Co_2FeAl_{0.5}Si_{0.5}$, an understanding of the phase stability and order-disorder transitions is pertinent, which itself is under contention. Since analysing the order-disorder transitions through DSC is a rather indirect way, the present study attempts to put the discussion to rest through *in situ* measurements at

high temperatures. For that purpose, *in situ* neutron diffraction were performed on powdered as-cast $Co_2FeAl_{0.5}Si_{0.5}$ samples till 1400 K. In order to probe the ordering in the system, we tracked the superlattice reflections in diffraction, which helped us to better understand the order-disorder transition. We were also able to highlight the presence and evolution of antiphase domains and their interplay with the ordering. Complementary XRD analysis allowed us to better quantify the ordering and thus optimize the annealing procedure. We shall first briefly explain why neutron diffraction was chosen for *in situ* measurements as opposed to X-ray diffraction.

4.1.1 Why neutron diffraction?

Neutrons, being quantum particles, also undergo coherent scattering as per the Bragg's law, which is used to describe X-ray diffraction. However, the interaction of neutrons with matter is quite different than X-rays. X-ray diffraction is due to the electron cloud of the atom and therefore the scattering factor is larger for higher atomic number, whereas neutrons interact with the nucleus, and the scattering factor depends on the nuclear potential [255]. Due to this, there is no systematic variation with the atomic number and scattering by neutrons can even be significantly different for isotopes. As an example, vanadium, being a transition metal, is almost invisible to neutrons as the scattering amplitude is approximately zero and therefore, is the material of choice for sample holders and containers for neutron experiments. Another advantage with neutrons is that the atomic nuclei act as point-like scatterers compared to the wavelengths involved. Hence, the neutron scattering factors are independent of the scattering angle, unlike X-rays which interact with the relatively larger electron cloud. This enables a higher precision in structure determination from high angle reflections [255].

As already discussed in Section 1.2.2, quantitative determination of atomic disorder through X-ray diffraction is relatively difficult in Heusler compounds due to the small relative intensities of superlattice reflections which may be further reduced depending on composition as well as disorder. On the other hand, due to the different scattering cross-sections in neutrons, the superlattice reflections can have considerably higher relative intensity depending upon the composition, which would allow for a more accurate determination of disorder.

Neutrons also have spin in contrast to X-rays, and therefore interact with the magnetic moments of the electrons. Since neutron diffraction probes the magnetic structure of the material as well, *in situ* measurements may also allow us to track the ferromagnetic ordering in $Co_2FeAl_{0.5}Si_{0.5}$. In addition, the microscopic magnetic structure is very sensitive to the structural ordering in the material, specially in the case of Heusler compounds and therefore, may act as an additional parameter to study the order-disorder transitions.

Moreover, in $Co_2FeAl_{0.5}Si_{0.5}$ the *L2₁-B2* ordering and the ferromagnetic ordering regimes seem to overlap [12]. The interplay between the magnetic and structural ordering, as to whether they

drive each other or they are independent, still remains an open question. So far, magnetic ordering was reported to increase the chemical interchange energy for *B2* disorder, thereby stabilizing the *L2₁* structure whereas, on the other hand, chemical ordering from *B2* to *L2₁* was found to have no perceivable effect on the T_c [12]. These conclusions are based on indirect DSC measurements along with a simplified numerical analysis, and thus needs better scientific evidence. In additional to that, the origin of a possible magnetic contribution to interchange energy, which has been reported in Co-Fe and Fe-Al binary systems, is still unknown [256, 257]. Neutron diffraction may also be able to shed light on these issues.

Neutron diffraction was, therefore, the technique of choice for this study as it offered all those significant advantages.

4.1.2 Experimental details

For the purpose of the study, polycrystalline samples of $Co_2FeAl_{0.5}Si_{0.5}$ were prepared using the arc-melting setup (see Section 2.2.1). Two batches of samples were sealed in quartz ampoules and annealed at 1000 K and 1273 K respectively for 7 days and subsequently quenched in water. The choice of annealing temperature was based on the literature [11]. The annealed samples were subsequently milled to a powder using a motorized mortar and pestle. An additional as-cast sample was pulverized for *in situ* annealing experiment. All the samples were extensively characterized at every stage. Later in the thesis, we shall discuss measurements on additional samples annealed after the neutron diffraction experiments, and therefore, we shall henceforth refer to both the samples annealed for the neutron diffraction together as 'prior-annealed' samples.

The neutron diffraction was performed with Dr. Matthias Frontzek at the Cold Neutron Powder Diffractometer (DMC) station in the Swiss Spallation Neutron Source (SINQ) at the Paul-Scherrer Institute (PSI) in Villigen, Switzerland. A neutron wavelength of 2.4576 Å was used for the measurements. Two different setups were used in the experiment; a simple sample holder for the room temperature measurements and a high temperature furnace setup for the *in situ* measurement. In principle, the high temperature furnace itself could be used for room temperature measurements. However, a separate sample holder was used to measure as-cast and prior-annealed samples as it was simpler and faster to change the samples.

First, the as-cast and the prior-annealed samples were sealed in vanadium sample holders for room temperature neutron diffraction measurement as shown in Figure 4.2a. After the room temperature measurements, the as-cast sample was sealed in a quartz ampoule to avoid oxidation during the *in situ* measurements at high temperatures. The quartz ampoule was placed inside a vanadium crucible with thermocouple which was placed inside a furnace with vanadium windows to allow for neutron transmission. The schematic is shown in Figure 4.2b. The thermocouple was directly attached to the sample holder to get as accurate measurement as possible.

a   **b**
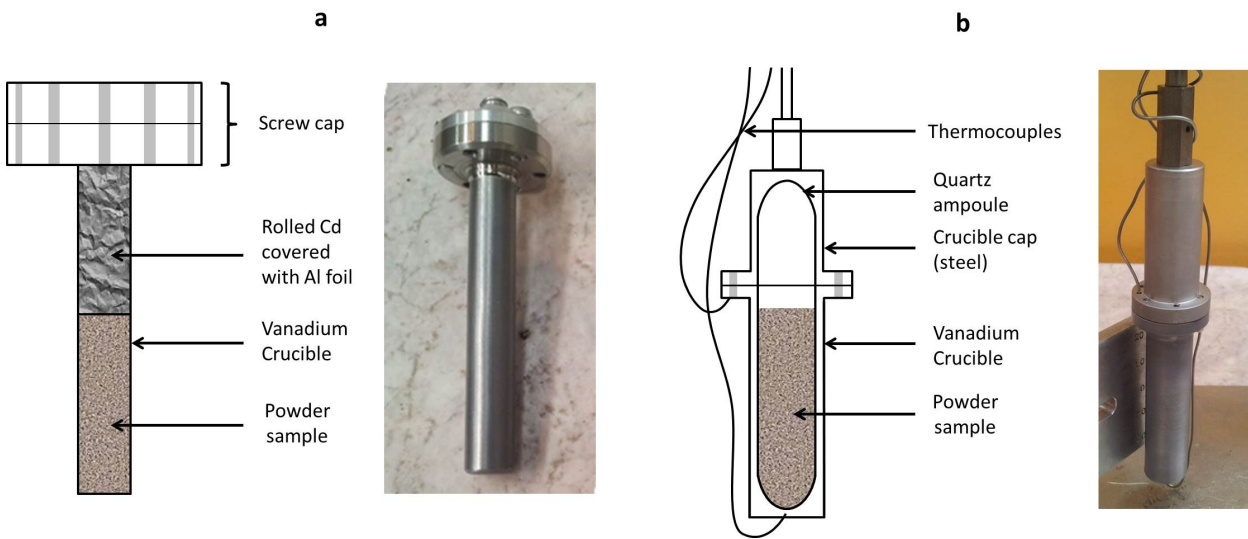
Figure 4.2: Sample holders for powder neutron diffraction (a) room temperature measurement (b) *in situ* measurement (fixed inside furnace).

Different measurement profiles were set up in the high temperature *in situ* diffraction measurements which is shown in Figure 4.3a-c. The sample was monitored for changes during the heating/cooling as well. After the experiment, high temperature measurements were done on an empty furnace according to the profile shown in Figure 4.3d, so that the background contributions may be identified.
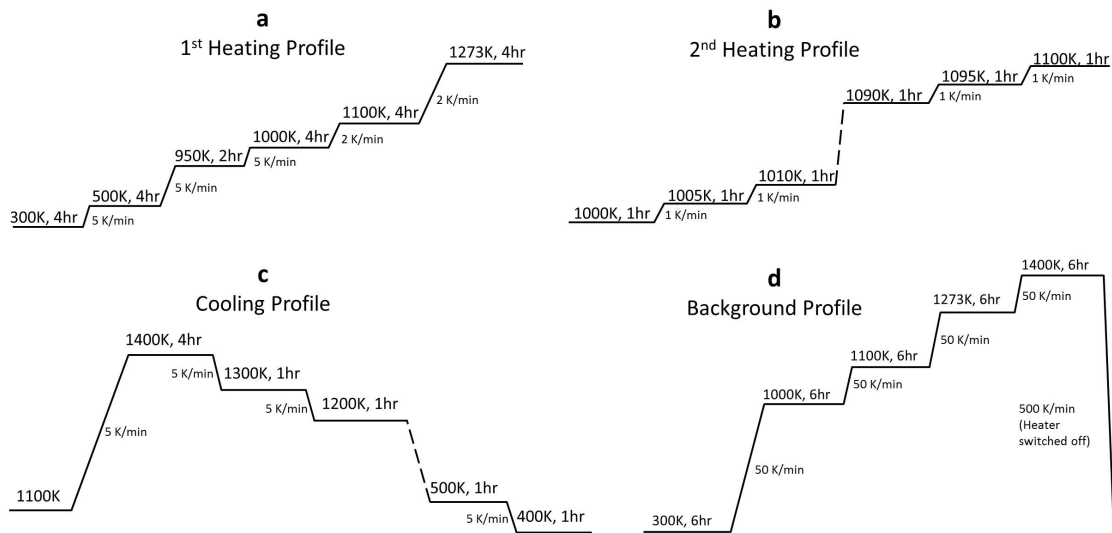
Figure 4.3: Measurement profiles for the *in situ* experiment on Co$_2$FeAl$_{0.5}$Si$_{0.5}$ (a) 1st heating profile (b) 2nd heating profile (c) cooling profile (d) profile for background measurements with empty furnace.

An important thing to keep in mind is that in our experimental setup, the neutron flux is constantly monitored just before the sample position. In the output data, the intensities from the detector are automatically normalized to the neutron flux. Thanks to that, the diffraction patterns can be directly compared for any changes and need not be further normalized. This is particularly helpful for observing changes in the main reflection. Otherwise, as in the case of laboratory X-rays, the patterns have to be normalized with respect to the maximum intensity in order to compare changes in the superlattice reflections.

A rather unfortunate aspect of the high temperature setup at the experimental station was that the furnace is not calibrated after purchase, and the calibration of the manufacturer is used for all subsequent measurements. Due to this, an error of up to ∼2 % is expected in the temperature value, specially at higher temperatures. Due to this, an accurate comment on the various temperatures may not be possible.

The samples for the neutron diffraction experiments were well characterized, and the data is presented next, before we discuss the data from neutron diffraction.

4.1.3 Characterization of samples for neutron diffraction

The as-cast sample and both the samples annealed at 1000 K and 1273 K, respectively, were found to be homogeneous and phase-pure. All the three samples were polycrystalline in nature, as expected from the arc-melting synthesis. An exemplary backscattered electron (BSE) image for the as-cast sample is shown in Figure 4.4a. The composition was found to be approximately nominal from the energy dispersive X-ray spectroscopy (EDX) data, within the marginal error of the equipment, given in Figure 4.4a as well.

Figure 4.4b shows the X-ray diffraction patterns for the as-cast and prior-annealed samples. All the three samples had same crystal structure ($Fm\bar{3}m$). Intensity ratio of the (111) superlattice reflection was quite smaller than that for the ideal $L2_1$ order (as obtained from PowderCell software [47]). Both the as-cast and prior-annealed samples had similar lattice constants, as calculated from Rietveld refinement, and are summarized in Table 4.1. The XRD data with refinement along with the details of the refinement are given in Appendix A (Page 151-152). No substantial correlation could be made between the lattice constants and the annealing temperatures.

It is known that Co$_2$FeSi prefers to order in $L2_1$ whereas Co$_2$FeAl almost always orders as $B2$. Therefore in order to take into account the $B2$ disorder, Rietveld refinement of the XRD data was done with the assumption that the mixing between Y ($4a$) and Z ($4b$) sublattice was only between Fe and Al for the sake of simplicity. A good refinement could be obtained using this scheme and the values for all three samples are also listed in Table 4.1. The amount of $B2$-type disorder for the as-cast sample was quite high (∼55 %). As calculated from Rietveld refinement, an improvement of about ∼17 % in the $L2_1$ order was observed for the sample annealed at 1000 K, whereas the sample

a

	Co	Fe	Al	Si
Nominal	50	25	12.5	12.5
Actual	48±0.5	24±0.5	14±0.5	14±0.5

b
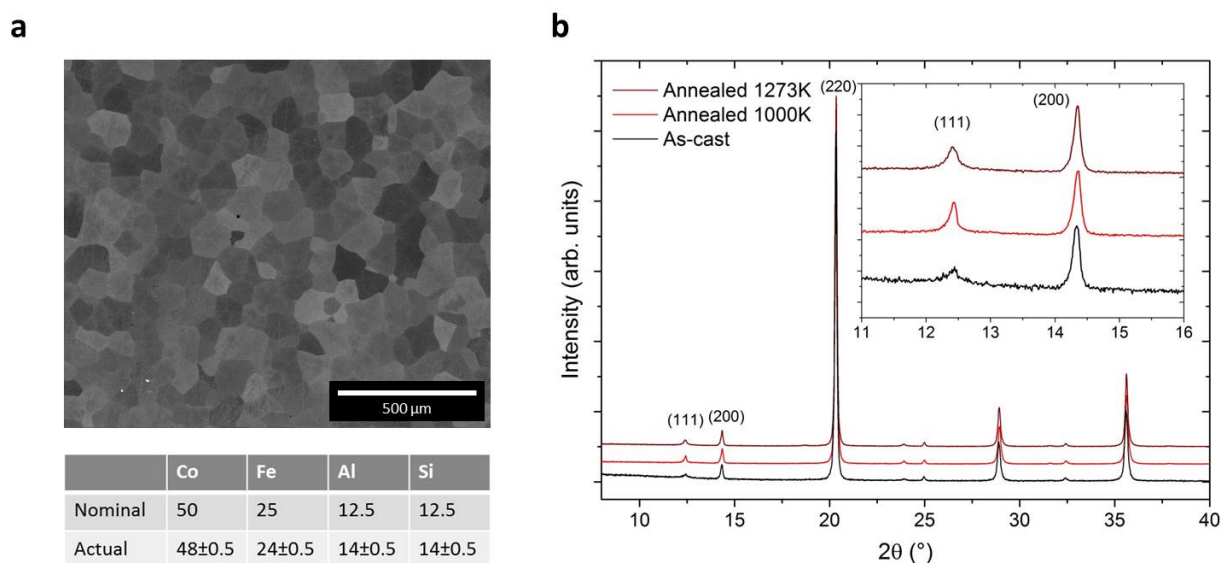
Figure 4.4: Characterization of the as-cast and prior-annealed Co$_2$FeAl$_{0.5}$Si$_{0.5}$ samples for room temperature neutron diffraction (a) exemplary BSE image for the as-cast sample showing the grains and the EDX data below (b) X-ray diffraction patterns for all three samples plotted with a y-axis offset (inset shows the (111) and (200) peaks).

annealed at 1273 K only improved by about ∼13 % in the $L2_1$ order. The annealing experiments indeed lead to a reduction in the disorder although the change was not as considerable as expected or widely understood.

Table 4.1: Rietveld refinement of the X-ray diffraction data for the as-cast and prior-annealed Co$_2$FeAl$_{0.5}$Si$_{0.5}$ samples.

Sample	Space group	Lattice constant (Å)	B2 disorder (%)
As-cast	$Fm\bar{3}m$	5.683(4)	55.1
Annealed-1000K-WQ	$Fm\bar{3}m$	5.681(4)	37.7
Annealed-1273K-WQ	$Fm\bar{3}m$	5.682(4)	41.8

Although, *B2*-type anti-site disorder was taken into account during refinement, the relative intensities of the superlattice reflections were quite small. The effect of anti-site disorder on the reflections in XRD has already been discussed in Section 1.2. Due to the diminished intensities, in addition to the noise associated in standard laboratory XRD measurement, the values for anti-site disorder obtained from refinement have a large error. Therefore, the values for the phase fractions listed in Table 4.1 should be taken as purely indicative of a general trend of improvement of $L2_1$ order

rather than quantitatively. It is also possible that small amounts of other types of disorder such as DO_3-type might be present in the samples but it was rather difficult to address multiple disorders in the XRD analysis. Nonetheless, annealing did help to improve ordering, although the improvement was not so much. Additionally, the (111) superlattice reflection seemed to be a bit broad as compared to the (220) or (200) reflection, both in as-cast as well as in the annealed samples. Unfortunately, the intensities were too small to make any detailed analysis.

Magnetization measurements were performed on all three samples and the saturation magnetization is plotted in Figure 4.5a. The saturation moments at 5 K matched with the Slater-Pauling value, within the error of the measurement, which is mostly due to the error in the measurement of the sample weight. It is of note that the sample annealed at 1000 K had a slightly lower saturation than that of the as-cast sample, whereas the 1273 K annealed sample had a slightly higher value. This is likely due to the extents of different disorders in the samples. A saturation moment higher than the Slater-Pauling value due to small amounts of DO_3-type of disorder has been discussed earlier [109], that might have led to such an effect in the as-cast sample as well as for the sample annealed at 1273 K.
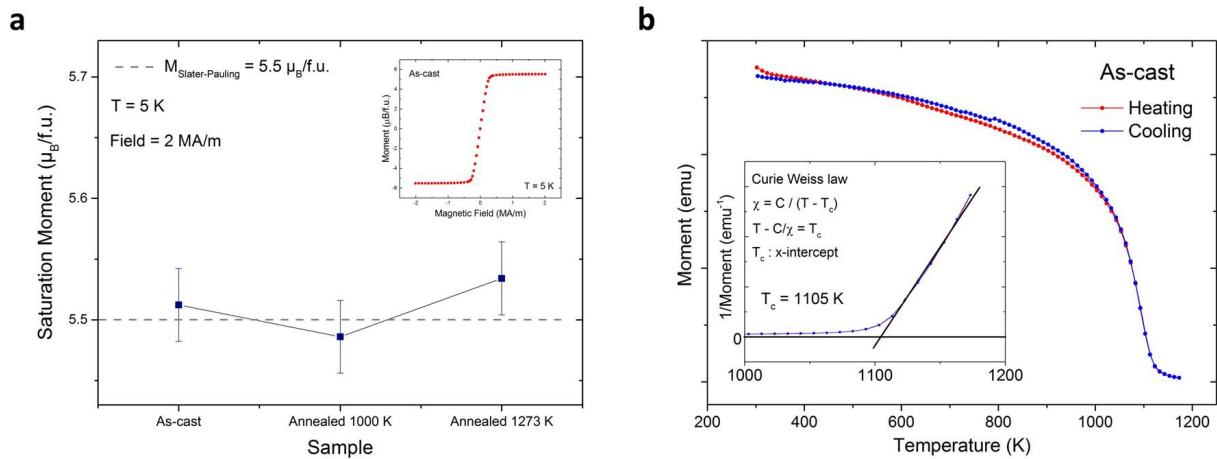
Figure 4.5: (a) Saturation magnetization for the as-cast and prior-annealed $Co_2FeAl_{0.5}Si_{0.5}$ samples (inset shows the M(H) curve at 5 K for as-cast sample) (b) High temperature M(T) data for as-cast $Co_2FeAl_{0.5}Si_{0.5}$ sample with an inset showing the Curie-Weiss fit.

All the samples were soft-magnetic and the M(H) at 5 K is shown in the inset of Figure 4.5a as an example. Curie temperature was calculated from Curie-Weiss fit of high temperature magnetization data and was found to be 1105 K (Figure 4.5b). This is accordance with what has been deduced from the DSC measurements [12, 84]. No other transitions were observed in the measurement. The small difference in the heating and cooling curves of the high temperature magnetization is likely due to surface oxidation of the sample.

After the structural and magnetic characterization, the samples were subsequently taken for the

neutron diffraction measurements, which are discussed next.

4.2 Neutron diffraction experiments

4.2.1 Measurements on as-cast and prior-annealed samples

Samples annealed at 1000 K and 1273 K were measured in the room temperature setup along with the as-cast sample for comparison. Each measurement was done for 4 hours. To begin with, the relative intensity of the superlattice reflections were considerably higher than that in XRD, the reason for which has been discussed in Section 4.1.1. This can be clearly seen in Figure 4.6 where the superlattice reflections are much intense than for XRD in Figure 4.4, and is thus expected to allow for a much reliable determination of the lattice parameters and ordering. Also, since a much larger wavelength was used in the neutron diffraction ($\lambda = 2.4576$ Å) as compared to laboratory X-rays used in our study ($\lambda_{Mo-K_\alpha} = 0.70926$ Å), quite a fewer number of reflections were seen in the same 2θ range, and only the reflections corresponding to (111), (200) (220) and (311) planes were observed. Small background reflections from the Al foil used in the sample holder were also observed (marked by asterisk '$*$' in Figure 4.6).
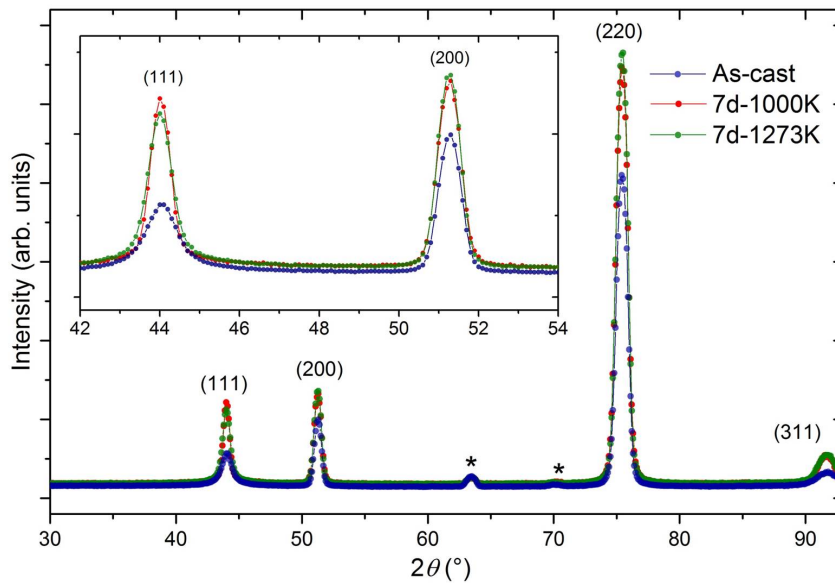
Figure 4.6: Room temperature neutron diffraction for as-cast and prior-annealed Co$_2$FeAl$_{0.5}$Si$_{0.5}$ samples (asterisk '$*$' marks the background reflections from the Al foil).

As observed in the XRD data, the relative intensities of (111) are higher for both the annealed samples than for the as-cast sample, as is expected for higher ordering due to annealing. The 1000 K annealed sample also has a slightly higher intensity at the (111) reflection as compared to the 1273 K annealed sample which would normally signify higher $L2_1$ ordering. This is accordance with the

XRD data as the sample annealed at 1000 K had a relatively higher $L2_1$ order (refer Table 4.1). The relative intensities of the (111) reflection cannot be directly used to calculate $L2_1$ order as depending on the magnetic structure, there is an unequal magnetic contribution to all the reflections.

A change in the intensity of the (220) reflection after annealing is also seen. There was a significant increase in the (220) intensity for the annealed samples. It is likely due to the changes in magnetic structure upon improved structural order. The difference in the extent of disorder for the two annealed samples could lead to difference in the intensity of the (220) and (111) reflections. It may be possible that the magnetic contribution was transferred from the (220) reflection to the (111) reflection.

An additional noticeable feature in the diffraction data is the relative broadening of the (111) and (311) reflections for as-cast sample as compared to the (200) and (220) reflections, and this selective peak broadening still remains after the annealing. Various microstructural features affect the peak shape in diffraction and in order to analyse the selective peak broadening, line profile analysis was performed.

4.2.1.1 Line profile analysis of neutron diffraction at room temperature

In order to quantify the peak broadening, peak fitting was done on the neutron diffraction data for the three samples. The fitting was done with a Pseudo-Voigt function using Xpert Highscore Plus software [258]. The background was fitted with a polynomial function. Pseudo-Voigt function P, is a linear combination of a Gaussian (G) and a Lorentzian function (L) [259] as given in the equation 4.1:

$$P = \eta L + (1 - \eta)G \qquad (0 \leq \eta \leq 1) \tag{4.1}$$

η is known as the shape factor, and gives the fraction of the Lorentzian contribution to the peak shape on top of the basic Gaussian function. Various microstructural features manifest as predominantly either Gaussian or Lorentzian contribution to a Bragg reflection. For example, crystallite shape is mostly a Gaussian contribution whereas crystallite or domain size features are mostly Lorentzian [259]. Therefore, comparing the shape factor for samples with different processing routes would allow us to compare them which may give us an idea of the underlying differences between the annealing processes. Another parameter that can be obtained from fitting is the integral breadth. This is the ratio of the peak area to the peak height. Integral breadth gives information about the broadness of the peak in general, and thus, can be used to check if the peaks are getting sharper upon annealing.

The shape factor and integral breadths for (111), (200) and (220) reflections obtained from peak fitting as discussed above are plotted in Figure 4.7. The (200) and (220) reflections did not undergo much change upon annealing, both in terms of the shape factor and the integral breadth. However,

the observation was different for the (111) reflection. For the (111) reflection in the as-cast sample, both the shape factor and the integral breadth had a considerably higher value than the (200) and (220), implying significant peak broadening. There was a reduction in shape factor as well as the integral breadth for both the annealed samples. A slightly higher reduction in both parameters was observed for the sample annealed at 1000 K.

As per the diffraction theory, the integral breadth has a θ-dependence [260]. For a standard sample, the integral breadth should be higher for reflections at higher angles. However, (111) reflection in our data does not follow this trend for both the as-cast and the prior-annealed samples. In all the three samples, the integral breadth of (111) reflection was higher than that of (200) reflection. For the as-cast sample, integral breadth of (111) reflection was ever higher than that of the (220) reflection, which is at a much higher 2θ. The strong deviation from the trend in our sample suggests a large density of defect/disorder/deformation which was most likely not healed fully with either of the two annealing procedures, although annealing at 1000 K seems to be comparatively more efficient in reducing the defects.
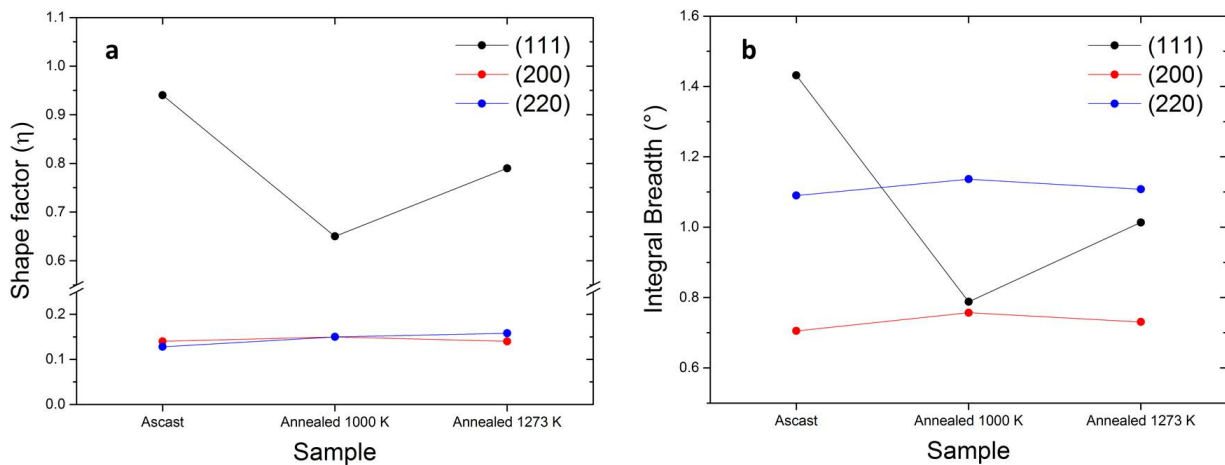
Figure 4.7: Line profile analysis of room-temperature neutron diffraction data for as-cast and prior-annealed Co₂FeAl₀.₅Si₀.₅ samples at room temperature (a) Shape factor and (b) integral breadth for (111), (200) and (220) reflections.

The selective peak broadening at (111) reflection, as reflected in a large integral breadth and shape factor, could be due to various reasons. A high shape factor means a large Lorentzian contribution which is generally due to crystallite or domain size features. A possible scenario in materials which are prone to disorder is the presence of regions of different types of order/disorder, distributed randomly in the material. These regions of either ordered or disordered structure are known as antiphase domains. The interface between two regions with different order/disorder is a type of stacking fault defect, and is referred to as antiphase domain boundary. Antiphase domains have been extensively studied in binary ordered alloys, and TEM is normally used for a direct observation

[261–264]. Figure 4.8a shows the well-formed antiphase domains in Fe-Al binary alloys as seen in TEM [265].

Since, in principle, antiphase domains of the disorder structure as well as the antiphase domain boundaries are types of defect, the presence of antiphase domains and domain boundaries may also affect the diffraction data, but the type of effect depends on the structure of the ordered and disordered systems of a material. As an example, the presence of antiphase domains may affect the peak intensities, e.g., in hexagonal closed packed ordered structure, but the integrated intensities are not affected [266]. The antiphase domain boundaries are only stable along certain crystallographic planes depending on the structure, due to energy considerations [267]. Thus, any associated effects due to the presence of antiphase domains and domain boundaries will manifest on the superlattice reflections [268]. If the domains size is sufficiently small, it may lead to size effects in diffraction such as peaks broadening. Since the antiphase domain boundaries affect only superlattice reflections, presence of antiphase domains may lead to selective peak broadening [268].
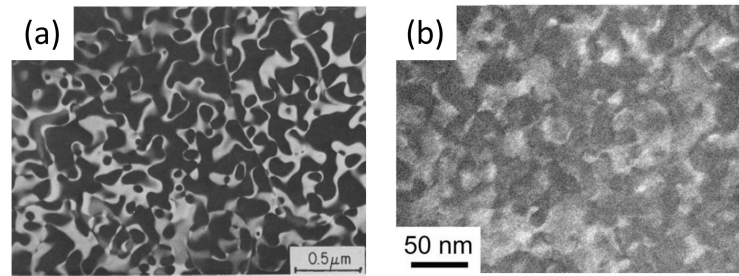
Figure 4.8: Antiphase domains as seen in TEM (a) well-formed distinct antiphase domains in Fe-25.5%Al (reproduced from Swann et al. [265]) (a) Nanoscale, diffused antiphase domains in annealed bulk $Co_2FeAl_{0.5}Si_{0.5}$ sample (reproduced from Nakatani et al. [8]).

Such selective peak broadening in diffraction data due to antiphase domains have been reported for different materials [198, 269–271]. Formation of antiphase domains upon deformation confirmed via TEM has been shown to lead to selective peak broadening of superlattice reflections in Pd_2MnSn Heusler compound [272]. We believe that a similar scenario is valid for our samples as well, since there was a significant amount of disorder present for both as-cast and prior-annealed samples. Nakatani et al. [8] have showed through TEM that the antiphase domains in $Co_2FeAl_{0.5}Si_{0.5}$ were less than 50 nm in size for annealed polycrystalline samples (Figure 4.8b). They also commented on the peak broadening at (111) reflection in XRD data as resulting from antiphase domains but the intensities were too low to clearly perceive the peak broadening. A similar situation was seen in our XRD data as well (Figure 4.4b). Due to the increased relative intensities of the superlattice reflections in neutron diffraction, the selective peak broadening at (111) could be clearly observed. Furthermore, as the Lorentzian contribution was high only for the (111) reflection, this confirms

that the effect in our case was indeed selective, and was most likely due to the antiphase domains. Furthermore, antiphase domain boundaries are technically stacking faults, and are formed along specific crystallographic directions depending on the type of the disorder. Antiphase domain boundaries in intermetallic systems containing $L2_1/B2$ antiphase domains have been calculated to be only stable along displacement vector $\mathbf{f}=\langle 111\rangle$ [267], and thus only (111) and corresponding higher-order peaks are expected to be affected by broadening. A similar scenario is observed in our data for both as-cast and annealed samples.

We believe that due to sample preparation by casting, large amount of disorder exists. We also expect that the resulting antiphase domains are quite small as they lead to selective peak broadening. Nanoscale antiphase domains in Co$_2$FeAl$_{0.5}$Si$_{0.5}$ have been reported and were also understood to be the cause of apparent selective peak broadening in XRD [8]. Upon annealing, as the volume fraction of disorder goes down, these antiphase domains should also reduce. However, since the annealing treatment does not lead to a large increase in $L2_1$ (Table 4.1), significant antiphase domains are possibly still present afterwards. In addition, it seems that although both the annealing procedures do lead to an increase in the volume fraction of $L2_1$ regions, the supposedly nano-sized antiphase domains containing $B2$ disorder, do not grow or coalesce as one would expect. In principle, the domain evolution during annealing should be analogous to grain-growth. In addition to the time and temperature parameters, grain-growth is also dependent on the cooling rate. It could be possible that quenching the sample from high temperatures might have an effect on the antiphase domain and domain boundary evolution.

Furthermore, on comparing the prior-annealed samples, the sample annealed at 1000 K had a higher $L2_1$ order than the sample annealed at 1273 K which is above the reported order-disorder transition. Along similar lines, the selective peak broadening was also less for the 1000 K annealed sample as seen from the line profile analysis. Clearly, the evolution of antiphase domains is different in the samples annealed above and below the $L2_1$-$B2$ order-disorder transition. It is possible that there is a correlation between the ordering phenomenon and the morphology and distribution of antiphase domains.

However, in both the prior-annealed samples, there is considerable selective peak broadening, even though the (111) superlattice reflection is sharper for the sample annealed at 1000 K. More importantly, it is known from the XRD data that either of the annealing procedures was not able to significantly reduce the disorder. In order to obtain a higher $L2_1$ order, it is important to better understand the order-disorder regimes, so that the annealing procedure may be optimized. For this purpose, high temperature *in situ* measurements were performed on the as-cast sample and are discussed next. The effect of the annealing temperature and the subsequent cooling rate on the antiphase domain evolution, as well as a possible convolution with the ordering phenomena were studied as well.

4.2.2 High temperature *in situ* measurement

For the *in situ* measurement, the furnace was installed and the as-cast sample was transferred to the high-temperature sample holder (Figure 4.2b). Figure 4.9 shows the measurement of the as-cast sample at 300 K in the high temperature setup. As it was mentioned earlier, due to a longer neutron wavelength as compared to Mo Kα or even Co Kα, only (111), (200), (220) and (311) reflections were seen till 95°. Since the initial measurement at 300 K was on the same sample as that in the room-temperature setup, it allowed us clearly assign/distinguish the background (marked by an asterisk '*' in Figure 4.9). This was further confirmed from the background measurements done at various temperatures once the *in situ* experiment was over and the data for all the measurements are given in Appendix B (Page 153). The background measurement at 300 K are also plotted in Figure 4.9 for reference. The background data are plotted with a small offset along y-axis in order to better distinguish the background reflections.
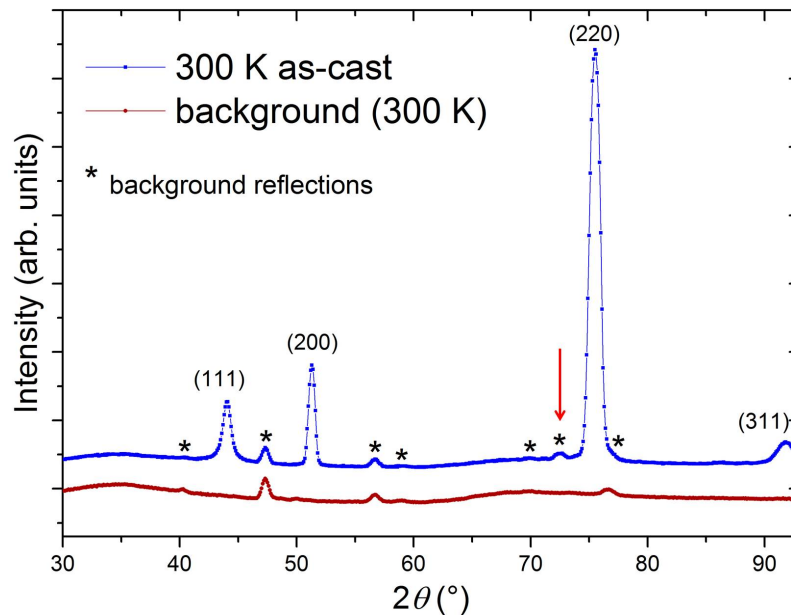
Figure 4.9: Neutron diffraction on as-cast $Co_2FeAl_{0.5}Si_{0.5}$ sample at 300 K in the *in situ* setup along with background measurement on empty furnace at 300 K, plotted with a small y-axis offset for better visualization (red arrow marks the peak from furnace contamination).

All the background features observed during the *in situ* measurements have been accounted for, except the peak at $\sim 72°$ (Marked with red arrow in Figure 4.9). The peak was observed for the heating profiles of the *in situ* measurement and was absent during cooling (Figure 4.12a, *vide infra*) and the subsequent background measurements (see Appendix B on page 153). This feature is not from the sample, as the peak was not seen in measurement done on the as-cast sample in the room temperature setup. Most likely, there was some contamination on the furnace, e.g., from earlier

measurements, which evaporated or decomposed when the furnace was heated till 1400 K and was thus not seen in measurements afterwards. Moreover, the background measurements were performed after the annealing experiment, it was not observed there possibly for the same reasons.

In the first heating profile, as shown in Figure 4.3a, measurements were performed at 300 K, 950 K, 1000 K, 1100 K and 1273 K with a 5 K/min heating rate in-between. Each measurement was done for 4 hours except 950 K where the measurement was done for 2 hours, just to be sure of the start of the order-disorder transition.

Figure 4.10a shows a stack-plot for the diffraction data obtained for the 1st heating profile where the (111) (200) (220) and (311) reflections have been labelled. A small systematic decrease of the intensity for all reflections with increase in temperature is expected due to the Debye-Waller factor (thermal vibrations) [273], in the absence of any transitions. This can in clearly seen for the (220) reflection as it is not affected by the order-disorder or magnetic transitions. Nevertheless, the intensity of the (111) superlattice reflection is strongly affected at 1100 K, and at 1273 K no intensity is perceptible in the same 2θ range. On the other hand the (200) superlattice reflection seem to undergo a gradual change as well, like the (220) reflection. The drastic change in the intensity of (111) reflection above 1000 K is due to the *L2$_1$-B2* order-disorder transition, as the (111) intensity becomes zero for a sample with complete *B2* disorder.
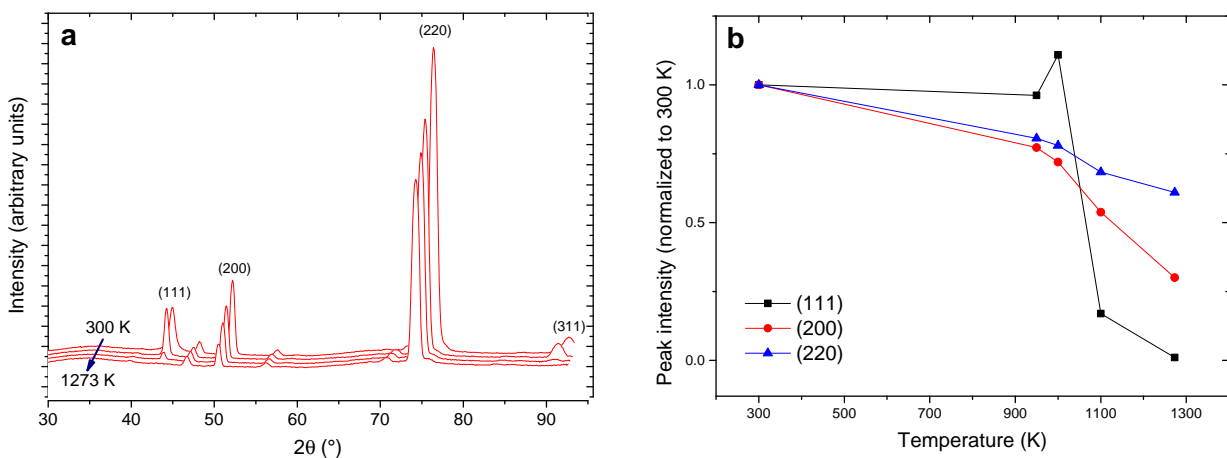
Figure 4.10: Neutron diffraction performed *in situ* on Co$_2$FeAl$_{0.5}$Si$_{0.5}$ (a) 3D stack-plot (small x- and y-axis offset) for the measurements in 1st heating profile (b) Intensities for 1st heating profile as obtained from peak fitting.

In order to better visualize the changes with temperature, peak fitting was done using the Pseudo-Voigt function (Equation 4.1), as discussed earlier. Figure 4.10b shows the intensities of (111) and (200) and (220) reflections for the 1st heating profile, as obtained from peak fitting.

During the first heating profile, the intensities for (111), (200) and (220) did not change considerably till 1000 K due to the absence of any transition. However, unlike the (200) and (220) reflections, a

small increase is seen in the (111) intensity going from 950 K to 1000 K (Figure 4.10b). The increase in (111) intensity may be understood as coming from an increase in $L2_1$ order in the sample due to an effective short-term annealing, during the time spent for diffraction measurements at 950 K and 1000 K, as well as during the heating in-between. At 1100 K, the (111) superlattice reflection was significantly reduced due to $L2_1$-$B2$ transition and was absent at 1273 K.

In principle, the (200) superlattice reflection intensity should not be affected by the $L2_1$-$B2$ ordering, although the rate of decrease in the (200) intensity is higher above 1000 K, as is visible from the slope in Figure 4.10b. This is likely because of two reasons. Firstly, the Curie temperature for the material is also around 1100 K, as was seen in high temperature magnetization data (Figure 4.5b), and the magnetic contribution are expected to be reduced in the paramagnetic regime. A small change of slope for the (220) intensity between 1000-1100 K is likely due to the same reason. In addition to the change in magnetic contribution, $A2$ disorder is also likely to become prominent at higher temperatures, which would lead to an decrease in the intensity of (200) reflection, specially above the $L2_1$-$B2$ transition.

As the next logical step, it was decided to closely examine the tentative $L2_1$-$B2$ transition. Based on calorimetry measurements, the transition temperature is reported to be ∼1125 K [11, 12]. However, in our measurements at 1100 K, the (111) superlattice reflection was quite small, which suggests that at 1100 K, majority of the $L2_1$-$B2$ transition is already over, in contrast to that reported in the literature. However, it must be kept in mind that the difference in the value of the transition temperature with literature may be partly due to the issue with calibration of the furnace mentioned earlier in Section 4.1.2. Moreover, it is also possible that there is an offset in the calorimetry measurement due to the cooling rate of 10 K/min which makes it non-equilibrium, as opposed to our *in situ* experiment where the sample is kept 1000 K and 1100 K for 4 hours in the 1st heating cycle, along with a heating rate of 1 K/min in-between, resulting in a relatively near-equilibrium measurement. Nonetheless, since as per the 1st heating profile in the setup, the majority of the $L2_1$-$B2$ transition was observed between 1000 K and 1100 K, it was decided to focus more on that temperature range in the subsequent measurements.

In order to have a closer look at the $L2_1$-$B2$ transition, the second heating profile was set up (Figure 4.3b). Sample was first cooled to 1000 K and 2nd heating profile was set up. One hour long measurements were performed at every 5 K between 1000 K and 1100 K, with a 1 K/min heating rate in-between (Figure 4.3b).

Figure 4.11a shows 3D stack-plot for the diffraction measurements. First thing to note is that the sharp transition as expected from the literature based on DSC measurements was not observed [11, 12, 84]. The changes in peak intensities around the transition, and the gradual reduction in the (111) reflection due to increasing $B2$ disorder can be seen in the inset Figure 4.11a. Moreover, the complete $L2_1$-$B2$ transition is expected to be larger than 100 K as the transition is not complete at 1100 K, since there is a finite intensity of the (111) superlattice reflection. Needless to say, indirect

measurements such as DSC, which is popular in literature to study such order-disorder transitions, see e.g., [79–83], do not provide complete information about the nature of the transition.

Peak intensities obtained from peak fitting are shown in Figure 4.11b. The intensities for all three (111), (200) and (220) reduce almost linearly with temperature. The (111) superlattice reflection reduced at a greater rate than the other reflections due to the *L2$_1$-B2* transition, as expected. The changes in the magnetic contributions due to the ferromagnetic-paramagnetic transition are also expected in the same temperature regime, but no distinction could be made between the two transitions.
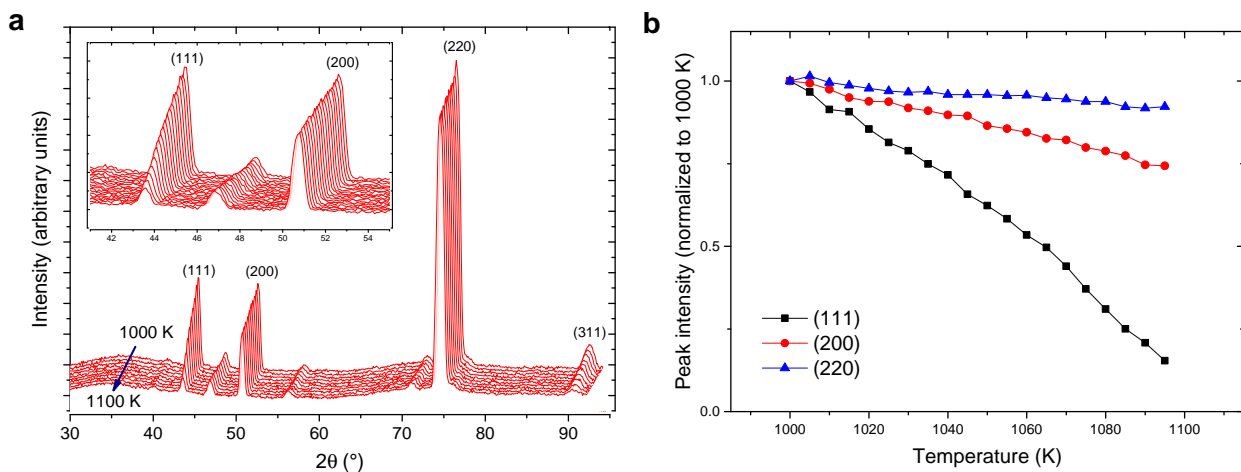
Figure 4.11: Neutron diffraction performed *in situ* on Co$_2$FeAl$_{0.5}$Si$_{0.5}$ (a) 3D stack-plot (small x- and y-axis offset) of the measurements around the *L2$_1$-B2* transition showing a gradual change (inset) (b) Intensities for 2nd heating profile as obtained from peak fitting.

The overall changes in the (200) and (220) intensities over the temperature range were small (see Figure 4.11a). The change here was mainly due to the Debye-Waller factor since both peaks should not be affected by *L2$_1$-B2* transformation. The Debye-Waller factor is a function of the scattering factor, q, which in turn is a function of θ [273]. The θ-dependence of Debye-Waller factor leads to a slight difference in the rate of change of intensities at (200) and (220) [274], which was observed in our data as well. As mentioned earlier, the change in the magnetic contributions as the Curie temperature is quite close, as well the changes due to *A2* disorder are also likely to be convoluted with the Debye-Waller factor.

Following the 2nd heating profile, the sample was heated to 1400 K (the maximum temperature of the furnace) with 5 K/min, and a 4 hour measurement was performed. At 1400 K, the (200) reflection is also quite small, which is mostly due to a predominant *A2*-type disorder (mixing of all the three X, Y and Z sublattices) at such high temperatures, since the intensity of (200) reflection is zero for a complete *A2* disorder.

Finally, a cooling profile was set (Figure 4.3c), where 1 hour long measurements were performed at every 100 K between 1400 K and 400 K with a cooling rate of 5 K/min in-between. As cooling of the furnace from 400 K to 300 K took a lot of time, it was not measured. No changes were observed earlier during the heating from 300-400 K in the 1st heating profile, and no transition has also been reported in literature in that temperature range. Regarding the thermodynamic changes, the kinetics are known to be too slow in that specific temperature regime. Hence, it can be safely assumed that the sample is same at both the temperatures, and the diffraction data at 400 K is therefore, equivalent to those at room temperature.

Figure 4.12a shows the stack-plot for all the measurements during the cooling profile. The sharp increase in the (111) reflection below 1100 K due to the *B2-L2*$_1$ transition can be clearly seen. The intensities of the (111), (200) and (311) reflections as obtained from peak fitting are plotted in Figure 4.12b. The temperature scale is plotted from 1400 K to 300 K so that the changes can be better visualized.
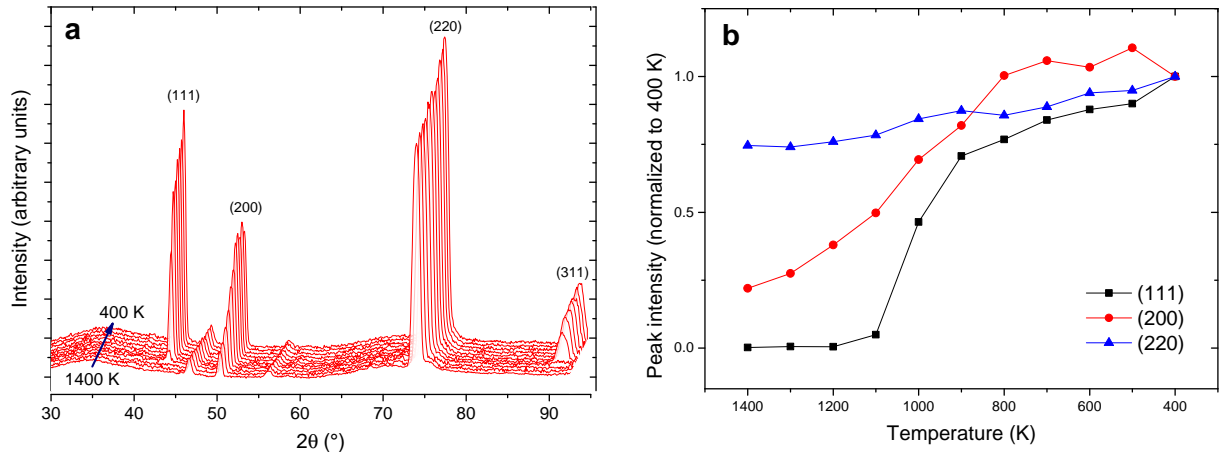
Figure 4.12: Neutron diffraction performed *in situ* on Co$_2$FeAl$_{0.5}$Si$_{0.5}$ (a) 3D stack-plot (small x- and y-axis offset) of measurements during the cooling profile (b) Intensities for cooling profile as obtained from peak fitting (plotted with decreasing temperature along x-axis for better visualization).

As expected, the (111) reflection underwent a sharp increase below 1100 K because of the *B2-L2*$_1$ transition as well as the magnetic contribution due to ferromagnetic ordering. However, the sharp increase in the (111) intensity is observed till 900 K, in contrast to the 1st heating profile where the decrease was seen only after 1000 K. The large increase in the (111) intensity from 1000 K to 900 K could also be due to a similar short-term annealing effect, as discussed for heating between 950 K and 1000 K, during the measurement time at 1000 K and 900 K as well as during the slow cooling of the sample in-between. The effective annealing below the *B2-L2*$_1$ transition would result in a higher *L2*$_1$ order thereby leading to a sharp increase in the intensity of the (111) superlattice

reflection. Nevertheless, the change in (111) intensity around the *B2-L2$_1$* transition is observed over a temperature range of 100-150 K. Both the structural and magnetic transitions seem to overlap as only a broad change is seen, similar to what was observed during the 2nd heating profile.

On the other hand, the main cubic (220) reflection did not undergo any significant changes upon cooling except due to the Debye-Waller factor (Figure 4.12a), although there does seem to be a small increase in the intensity of (220) reflection for the measurements at 1000 K and 900 K, which may also be from increased magnetic contributions due to higher *L2$_1$* order, as a result of short-term annealing discussed above.

The (200) reflection increased gradually on cooling from 1400 K to 800 K. The increase is likely due to a combination of *A2-B2* transformation and *B2-L2$_1$* transition in addition to the magnetic structure due to paramagnetic to ferromagnetic transition. The change in the (200) intensity is gradual from 1400 K and no regime of *B2-A2* transition is observed. It could be that the transition regime is at a higher temperature but it is rather unlikely as the (200) at 1400 K is already quite small, suggesting that the *A2* disorder is predominant. At 800 K and below, the trend of the change in (111) intensity was the same as (220) reflection.

In order to compare the changes at 1400 K, the diffraction pattern for the measurement done at 1400 K is plotted against the initial 300 K measurement in Figure 4.13a. The shift in the peak positions is expected and is mostly due to the lattice expansion with temperature. Regarding the intensities, the (220) reflection was considerably smaller in intensity at 1400 K as compared to 300 K, primarily due to the Debye-Waller factor [273]. Furthermore, no (111) superlattice reflection is seen as the sample is considerably above the *L2$_1$* regime. At such high temperatures, complete *A2* disorder is expected, which would lead to extinction of the (200) reflection as well. However, there is a small intensity for (200) superlattice reflection, which suggests that a small amount of *B2* disorder is still present.

Since the whole *in situ* experiment involved extended measurements over 3 profiles, and took approximately 3 days to finish, the sample can be considered to have undergone an alternate annealing procedure, with a relatively slow cooling as compared to the conventional quenching approach. It is thus important to compare the final data after the *in situ* experiment to that of the as-cast sample. For the sake of differentiation with the prior-annealed samples which were quenched, the final sample after *in situ* experiment shall be hereafter referred to as the '*in situ* annealed' sample in further discussion.

In order to better visualize the changes after the *in situ* experiment, the comparison of the room temperature measurement on the *in situ* annealed sample (400 K) versus the initial 300 K measurement representative of the as-cast sample is shown in Figure 4.13b. Firstly, the relative intensity of the (111) reflection was significantly higher for the post-annealed sample which is suggestive of a higher *L2$_1$* fraction in the sample. Moreover, a significant change can be seen in

the peak shape before and after the *in situ* experiment. As discussed earlier, the (111) reflection is significantly broad for the as-cast sample due to the presence of antiphase domains. In contrast, the final sample after *in situ* annealing clearly has a much sharper (111) peak (Figure 4.13b). The selective peak broadening seems to be minimal after the *in situ* annealing. In order to better understand the evolution of antiphase domains, a detailed line profile analysis is done for the whole experiment, and is discussed later in Section 4.2.2.1.
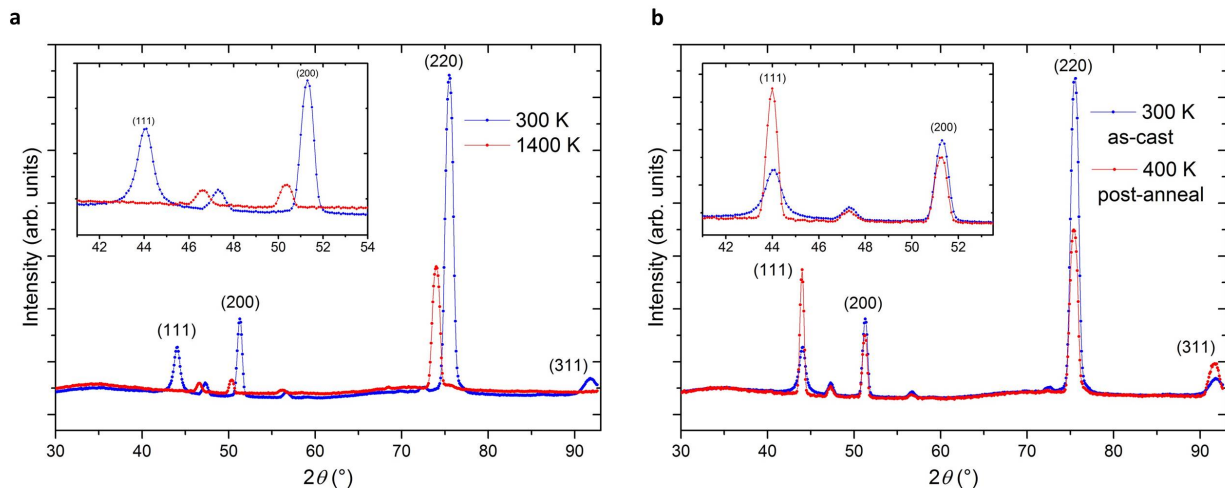
Figure 4.13: Neutron diffraction performed *in situ* on $Co_2FeAl_{0.5}Si_{0.5}$ (a) 300 K and 1400 K measurements (b) 300 K and post-anneal 400 K measurements.

The *in situ* annealed sample also had another contrasting aspect as compared to the one before the *in situ* experiment. The intensity at the (220) reflection was considerably reduced after *in situ* annealing (Figure 4.13b). The (220) peak corresponds to the primitive body-centred cubic (bcc) structure of the material and should not be affected even by complete mixing of all the sublattices. Normally, small changes may be expected in neutron diffraction as the magnetic contribution may shift to other reflections depending on the ordering of the material, which has been observed for the two prior-annealed samples (Figure 4.6). However, magnetic contributions are a small fraction of the structural intensity and cannot account for such strong changes.

In addition, the relative intensity of (111) reflection was considerably higher than the (220) reflection ($\sim 0.7*I(220)$) after the *in situ* experiment as can be seen clearly in Figure 4.13b. The relative intensity is much higher than the calculated value for a fully $L2_1$ ordered sample. Although DO_3 disorder may lead to an higher (111) relative intensity compared to the ideal $L2_1$ order, such a large relative intensity of (111) superlattice reflection cannot be obtained with DO_3 disorder or with any other type of disorder. Another explanation could be that there is crystallographic texture in the sample: The annealing at rather high temperatures ($\leqslant 1400$ K), even though for a relatively shorter time, may have led to preferred grain growth in the powdered sample. However, this must

be confirmed through detailed characterization of the sample using microscopy and diffraction. Unfortunately, as sample was activated upon exposure to neutrons[1], it was not possible to perform further experiments and analysis on the annealed sample, and the status quo is maintained presently. Therefore, corresponding laboratory experiments under similar conditions were performed in order to shed more light on the possible texture which might have developed in the sample. A detailed analysis of the subsequent experiment and characterization is presented later in Section 4.3.

So far, any Rietveld refinement of the neutron diffraction data has not been shown. As was seen in the measurements, the magnetic structure is such that it manifests as contributions to the structural reflections. In addition to that, significant fraction of *B2* disorder is present at all temperatures. Also, there is clearly a mixture of *A2* and *B2* disorder present at temperatures above the *B2-L2$_1$* transition region. On top of that, significant microstructural effects such as peak broadening in the initial stages and crystallographic texture in the later part of the annealing as well as for the final sample are present, as reflected in our observed data. Since only 4 reflections are observed in the measured 2θ, it makes the analysis and refinement quite challenging. Due to all these factors, it was not possible to successfully perform Rietveld refinement on the diffraction data. Nevertheless, the diffraction data has been further analysed through line profile analysis. Based on this, the order-disorder transition as well as the antiphase domains and related aspects are discussed next.

4.2.2.1 Evolution of *L2*$_1$ order and the order-disorder transition

We have already discussed the trends of the peak intensities during the annealing process. However, relative intensity of the (111) and (200) superlattice reflections with respect to the main cubic (220) reflection, is a better parameter for order than comparing the peak intensities, as it allows us to assess the change in (111) and (200) together as the order evolves, and it may even be possible to do so quantitatively [49]. Therefore, the relative intensities (I$_{hkl}$/I$_{220}$) were calculated from the peak fitting for all measurements during the *in situ* experiment. The relative intensities were further normalized to the I$_{hkl}$/I$_{220}$ value at 300 K (for the as-cast sample) to highlight the changes during the *in situ* experiment, and the data for different profiles are plotted in Figure 4.14.

Figure 4.14a shows the relative intensities for the measurements done during the 1st heating profile along with the cooling profile. The reduction in the relative intensity of (111) points towards the reduction in *L2$_1$* order. The changes in the relative intensities during the 1st heating profile are similar to the plot of peak intensities (Figure 4.10b). The sharp reduction in (111) relative intensity between 1000 K and 1100 K due to the *L2$_1$-B2* transition observed in the peak intensity of (111) reflection, as well as the small increase in the peak intensity going from 950 K to 1000 K is

---

[1]An atom nucleus, which may be stable, may absorb free neutrons, leading to a heavier nucleus, thereby entering an excited state. The radioactive atom decays over time by emission of gamma rays, and depending on scenario, along with particles such as beta rays (electrons), alpha particles etc. The half-life may range from fraction of seconds to many years, depending on the activated entity, e.g., ^{60}Co has a half-life of over 5 years.

correspondingly observed in the relative intensities as well (Figure 4.14a).
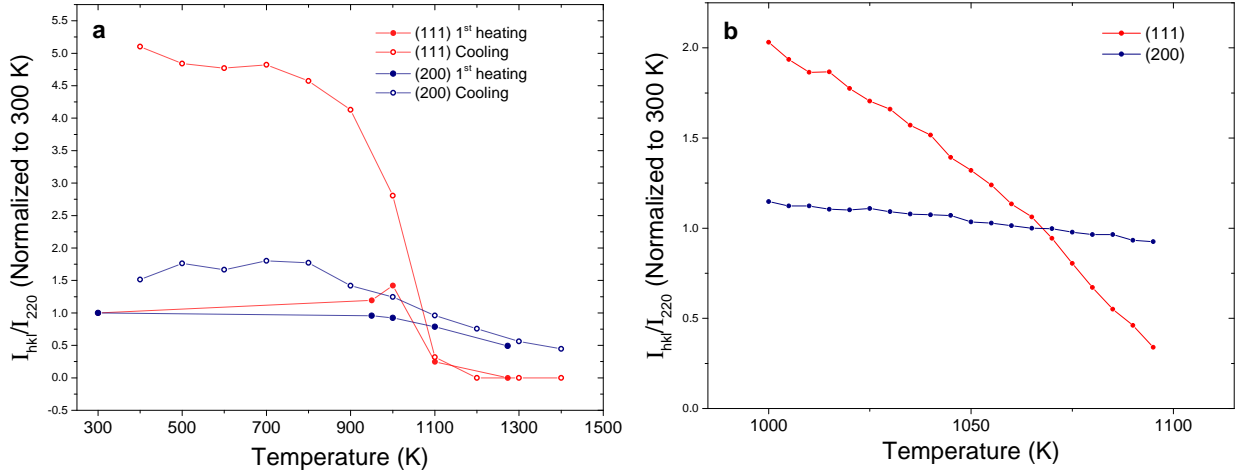
Figure 4.14: Intensities of (111) and (200) superlattice reflections, relative to (220) for the *in situ* neutron diffraction on $Co_2FeAl_{0.5}Si_{0.5}$ during (a) 1st heating profile and the cooling profile (b) 2nd heating profile close to the transition

The reduction in the relative intensity of (200) reflection is small till 1100 K, as compared to corresponding change in peak intensity (Figure 4.10b), suggesting that the till 1100 K, *L2₁-B2* ordering phenomenon is predominant. Moreover, the relative intensity of the (200) reflection is still considerably large at 1400 K ($\sim 0.5*[I(200)/I(220)]_{300K}$), implying that there is still a significant amount of *B2* disorder present. This is in contrast to what was observed when only the peak intensities are considered (Figure 4.12b), which gave the impression that the sample is predominantly *A2* ordered at 1400 K, as discussed earlier. This highlights the advantage of relative intensities as a parameter for order as compared to just peak intensities. Therefore is it possible that a *B2-A2* transition may exist above 1400 K.

The general trend in relative intensities of (111) and (200) superlattice reflections during cooling (Figure 4.14a) was similar to that observed for peak intensities (Figure 4.12b). The various features such as the sharp increase of (111) intensity till 900 K in contrast to heating as discussed earlier, are further enhanced. However, improvement in the relative intensities for both the (111) and (200) reflection during cooling as compared to that during heating, due to the *in situ* annealing, is clearly seen. The relative intensity of the (111) superlattice reflection after cooling is higher by a factor of 5 as compared to the initial 300 K (as-cast sample). This may seem to suggest a large improvement in *L2₁* order, but it must be kept in the mind that the intensities after the *in situ* experiment are quite anomalous (Figure 4.13b) which cannot be explained by any particular type of order/disorder alone, and is likely due to the presence of crystallographic texture in the sample. It is therefore important to address the data from different points of view, in order to get a complete picture.

An additional odd feature is perceptible in the relative intensities, as the sample was cooled from 500 K to 400 K (Figure 4.14a); an increase in the relative intensity for (111) superlattice reflection was observed as the sample was cooled from 500 K to 400 K, along with a corresponding equal reduction in the relative intensity of the (200) reflection. This was rather unexpected as ordering kinetics are significantly reduced at such low temperatures and there are no known transitions in the material in that temperature regime as yet reported in the literature.

The relative intensities for the measurements in 2nd heating profile between 1000 K and 1100 K are plotted in Figure 4.14b. As was also observed in the plot of peak intensities, the (111) reflection decreased at a much higher rate as compared to (200) reflection due to the *L2$_1$-B2* transition. Although both the order-disorder transition and the ferromagnetic-paramagnetic ordering is expected in this range, no distinction could be made between the two in the relative intensities (Figure 4.14b), and a broad transition was observed, similar to the plot of peak intensities (Figure 4.11b). Moreover, any sudden change in the slope of relative intensity marking the onset of a transition was not observed as well.

The relative intensity of (111) at 1095 K was significantly small as compared to the relative intensity at 1000 K ($\sim$0.1*$[I(111)/I(220)]_{1000K}$). Since the relative intensity of the (111) superlattice reflection is directly related to the amount of *L2$_1$* order, such a small (111) relative intensity means that the sample was predominantly *B2* ordered at 1095 K. At 1095, we should be below the magnetic transition as per the high temperature magnetization data (Figure 4.5b), and a similar value has also been reported in the literature for the Curie temperature [12, 84]. Thus, the structural contribution to the (111) reflection at 1095 K is even lower, if the magnetic contributions are taken into account. This suggests that at 1095 K, we are quite close to the end of the *L2$_1$-B2* transition or maybe even above it, with a small fraction of remnant *L2$_1$* order.

As we have already mentioned, in literature the transition is understood to be rather sharp since a T$_{L2_1-B2}$ is assigned based on peak position in calorimetry data [11, 12, 84]. Contrary to that, it has been clearly shown that the *L2$_1$-B2* transition is indeed quite broad, spreading over $\sim$100 K. Since the change is gradual over $\sim$100 K, the ordering phenomenon is a higher order transition. Moreover, the change in the intensity of the (111) reflection between 1000-1100 K is more or less linear. Similar linear trends in the order parameter for (111) superlattice reflection have been observed below the transition temperature by Soltys for the ordering phenomena in B$_2$MnAl Heusler compounds (B = Cu, Ni, Co, Pd, Pt) [41]. More importantly, the fact that the transition is broad, spreading over 100-150 K, has an impact on the annealing profile, since there is no sharp transition temperature such that one is on the safer side below a few 10s of K. Therefore, annealing profile to obtain higher order in a material has to be carefully designed, keeping in mind the nature of the order-disorder transition while deciding the annealing temperature.

With regarding to the magnetic ordering, the T$_C$ at $\sim$1105 K as seen for the high temperature

magnetization data is not perceptible in the changes in relative intensities. Due to the quite broad nature of the ordering phenomenon, the magnetic contribution is overlapped and no separate hint of the magnetic transition is observed. It seems that the transitions are convoluted, i.e., one drives the other, thereby leading to a broad transition. It is also possible that such a relatively slower measurement overall, involving 1 hour measurements at each temperatures in addition to a slow 1 K/min heating rate in-between, smears out both the transitions and therefore only a broad transition is observed. Since neutron diffraction also probes the magnetic structure, we had hoped that this would allow us to shed light on the convolution between the structural and magnetic ordering. To be able to make any scientific commentary on the inter-dependence between the two transitions, a good Rietveld refinement incorporating both the magnetic and crystallographic structure is needed at least, which unfortunately, has not been possible so far.

4.2.2.2 Evolution of antiphase domains and selective peak broadening

In addition to the peak intensities, line profile analysis also gives us integral breadth and shape factor (Section 4.2.1.1). Integral breadth gives an idea about the broadness of a peak, whereas shape factor can tell us about possible microstructural contributions to the peak shape. We have used both the parameters to discuss the selective peak broadening observed in the neutron diffraction of as-cast and prior-annealed samples as a result of the nanoscale antiphase domains. Annealing the sample followed by quenching does not seen to have much effect on the size of such domains, as the selective peak broadening still remained. It could be possible that the antiphase domains are affected by the cooling rate after annealing. In order to better understand the evolution of antiphase domains we have done a detailed analysis of the *in situ* measurements with respect to integral breadth and shape factor.

The integral breadths of (111), (200) and (220) reflections from the peak fitting of all the *in situ* measurements are plotted in Figure 4.15a. Firstly, there were no significant changes in the integral breadths for the (220) and (200) reflections during or after annealing. Since integral breadth has a θ-dependence [260], the observed value of integral breadth of the (220) reflection ($2\theta = 75.5°$ at 300 K) was found higher than that of the (200) reflection, which is at a lower 2θ ($2\theta = 51.3°$ at 300 K) (see Figure 4.9).

On the other hand, the integral breadth values for (111) reflection reduced significantly during the 1st heating profile itself. As the temperature was increased to 1000 K from room temperature, the integral breadth reduced to half. At temperatures above the tentative *L2₁-B2* transition, the (111) superlattice reflection becomes extinct and therefore the integral breadth values are zero. During cooling, (111) reflection reappeared at 1100 K due to structural and magnetic ordering. The integral breadth during subsequent cooling below 1000 K were significantly lower than that before annealing. In the final sample after *in situ* measurement, the integral breadth of (111) reflection was of the

order of the (200) reflection, suggesting that the peak broadening has considerably reduced.
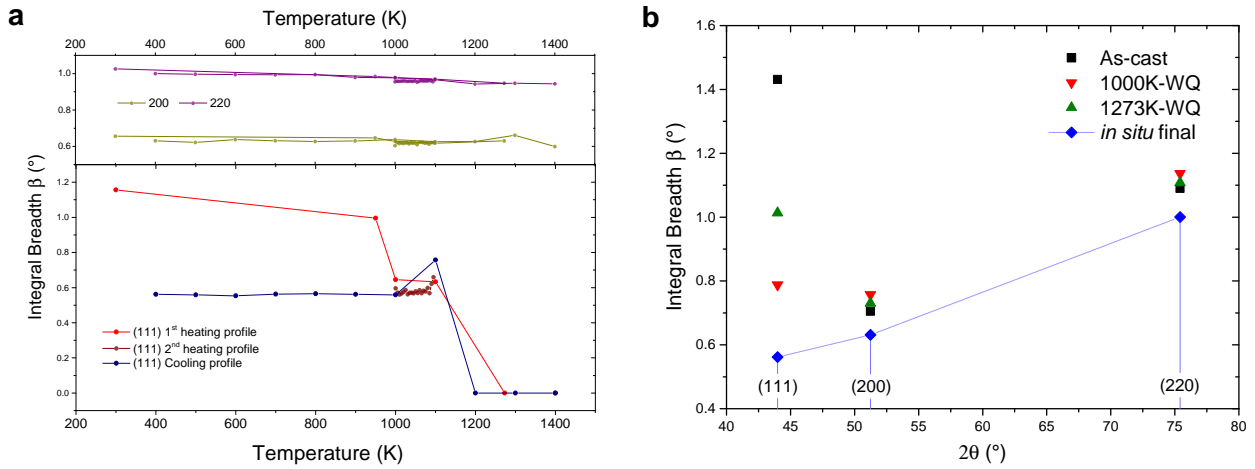
Figure 4.15: Line profile analysis of Co$_2$FeAl$_{0.5}$Si$_{0.5}$ using Pseudo-Voigt function (a) Integral breadths for (111) (200) and (220) reflections during the *in situ* neutron diffraction (b) Comparison of the integral breadths for the final sample after *in situ* annealing with the as-cast and the prior-annealed samples which were quenched.

Figure 4.15b compares the integral breadths of the (111), (200) and (220) reflections for final sample after *in situ* annealing against the as-cast and prior-annealed samples which were quenched. It should be mentioned again that the both the as-cast and quenched samples have high integral breadths for the (111) superlattice reflection specifically (refer Section 4.2.1). Based on the angular dependence of integral breadth, the value for (111) reflection should be lower than that of both the (200) and (220) reflections, since it is at a lower 2θ. After the *in situ* annealing, the observed trend fits to theory and the selective peak broadening in (111) reflection has either disappeared or is minimal. Since the selective peak broadening is understood to be due to size of the antiphase domains, the reduction/absence of peak broadening after the *in situ* experiment implies that the antiphase domains are no longer nano-sized.

As already mentioned in Section 4.2.1.1, the shape factor η gives the fraction of the Lorentzian contribution to the peak shape which is due to certain microstructural effects such as finite crystallite or domain size. Figure 4.16a shows the shape factor variation for the *in situ* measurements till 1100 K for both the heating and cooling profile. the shape factor of (111) and (200) reflections at higher temperatures are not shown, as due to low intensities the error in the fitting is significantly high, and in particular, the (111) reflection is absent above 1200 K. Firstly, both the (200) and (220) reflections had zero shape factor at all stages of the *in situ* annealing experiment, signifying a purely Gaussian peak profile. In contrast, (111) superlattice reflection was predominantly Lorentzian in profile at 300 K before the experiment as the shape factor was ∼0.8. Similar to integral breadth, the shape factor reduced significantly during the initial heating itself. As the sample was cooled

below 1000 K, the shape factor was approximately zero. Thus, the (111) reflection had little or no Lorentzian contribution after the *in situ* annealing, implying a minimal amount of antiphase domain boundaries.

The shape factors of the (111), (200) and (220) reflections for final sample after *in situ* annealing as compared to the as-cast and prior-annealed samples which were quenched, are shown in Figure 4.16b. The improvement in the sharpness of the peaks with the *in situ* annealing as compared to the quenched samples can be clearly seen in the reduction of the shape factor for the *in situ* annealed sample, particularly of the (111) reflection.
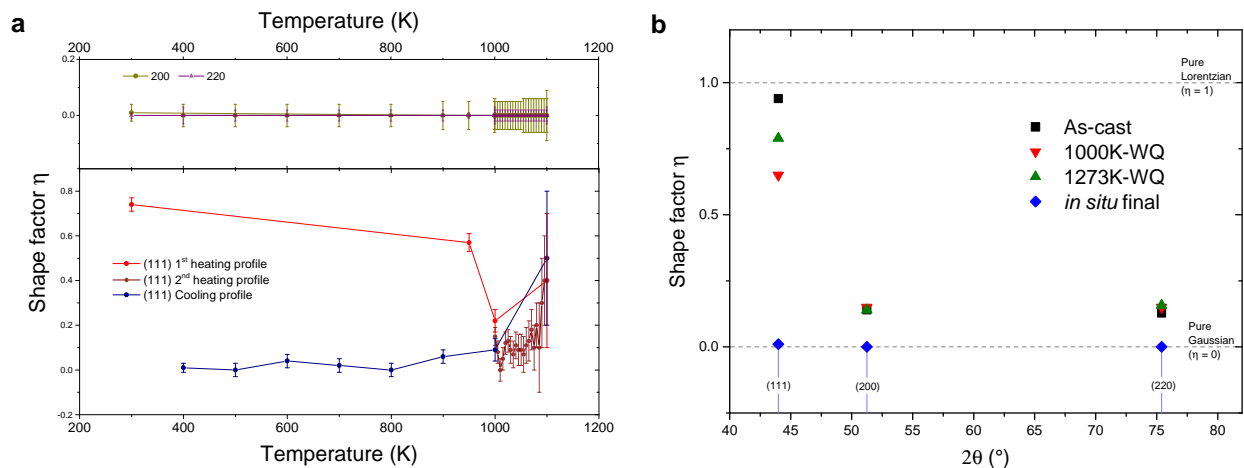
Figure 4.16: Line profile analysis of $Co_2FeAl_{0.5}Si_{0.5}$ using Pseudo-Voigt function (a) Shape factor for (111) (200) and (220) reflections during the *in situ* neutron diffraction (b) Comparison of the shape factors for the final sample after *in situ* annealing with the as-cast and the prior-annealed samples which were quenched.

We would like to briefly comment on the growth of the antiphase domains in general. Substantial theoretical work about antiphase boundary motion and structural domain coarsening has been done by Allen and Cahn [275, 276]. Since the order-disorder is, in general, thermally-driven, antiphase domain growth is also directly related to the temperature [277–279]. So, the higher the annealing temperature, the faster is the domain coarsening. Therefore, in principle, the annealing temperature should be as close to the order-disorder transformation as possible. However, one must be careful, as just below the transition temperature, the atom movement is much more rapid and the sense of ordering may be reversed with few interchanges [280]. It has been shown through TEM that the resulting antiphase domain fluctuations are found to be quenched-in in addition to rugged antiphase domains boundaries in a sample annealed really close to the ordering temperature and subsequently quenched, whereas homogeneous antiphase domains along with smooth domain boundaries were observed in a sample annealed at 80 K below the transition temperature [276]. Similar homogeneous disordering along with thickening of domain boundaries has been seen for samples heated close to the

temperature regime of the order-disorder transition using *in situ* TEM [72, 265]. The quenching-in of the critical fluctuations in $AuAgZn_2$ Heusler compounds was shown by high temperature X-ray diffraction as the sample was quenched from near as well as from above the transition temperature [281]. The quenching-in of the critical fluctuations, is the likely reason behind the observation of selective peak broadening due to nanoscale domains in our sample annealed at 1000 K and subsequently quenched, since at 1000 K, we are already in the order-disorder transition regime. During the *in situ* experiment, the sample is in the order-disorder regime for relatively shorter time during cooling. Even if a small amount of such new domains nucleated during that time, they would have healed out during the slow cooling at lower temperatures since slow cooling allows for additional annealing, and therefore nanoscale domains and selective peak broadening is not observed.

Thus, we conclude that the antiphase domains are no longer of the order of nanoscale after the *in situ* annealing as domains coarsening has taken place due to the slow cooling. At the same time, the volume fraction of the *B2* antiphase domains has gone down, as the ordering has improved in the material. The higher development of the $L2_1$ order after the *in situ* experiments as compared to samples quenched after annealing, seems to be connected to the evolution of the antiphase domains and domain boundaries. We shall now briefly discuss how the ordering phenomena and the growth of antiphase domains may be convoluted.

4.2.2.3 Antiphase domains and ordering phenomena

The ordering phenomena and the antiphase domains are closely related. A higher order in a material would mean that the volume fraction of the domains of the ordered structure is higher. Therefore, for a system with a given amount of order, the antiphase domains of the respective ordering must grow during the ordering process or new antiphase domains may nucleate. Clegg and Buckley [73] described the growth and coalescence of antiphase domains during ordering as a three step process: for a system coming from the a disordered state, initially a network of antiphase domain boundaries develops through nucleation although the overall order remains low; this is followed by a domains consolidation stage, where the domains become distinct and the degree of order reaches an equilibrium; the final stage is the coalescence of the ordered domains and depending on the material system and temperature, the three stages may even occur concurrently. Abromeit and Matsumara [282] also observed similar ordering kinetics involving nucleation and growth of ordered domains followed by migration and annihilation of antiphase domain boundaries, in the case of a $L1_2$ order-disorder transition using Monte Carlo simulations. The mobility of the antiphase domains was also found to be inversely proportional to the long range order parameter in Cu_3Au [283]. The above mentioned literature highlights the close relationship between the evolution of order and the antiphase domains and domain boundaries. For a detailed overview of the state-of-the-art of various aspects of ordering phenomena as well as antiphase domains, the works of Cahn et al. are

recommended [284, 285].

Most of the work on order-disorder transition has been done on binary alloys, and the ordering phenomena in ternary systems such as Heusler compounds has not been extensively studied. Gilles et al. recently demonstrated that a small amount of a ternary alloying addition can have a strong influence on the ordering phenomenon [286]. Similar to the multi-stage growth of antiphase domains mentioned above, Livet et al. [281] also observed an incubation period for the well-defined antiphase domains to form before the antiphase domain growth, in the case of $AuAgZn_2$ Heusler compound through high temperature X-ray diffraction, although only in the case when the sample is quite close to the transformation temperature.Moreover, recent simulations by Zhang et al. show that the occurrence of ordering phenomena is dependent on the type of the stacking fault at the antiphase domain boundaries [287], which in turn is dependent on the type of order/disorder structures feasible in a system. Clearly, the growth of ordering in the material is mediated via the growth of antiphase domains and domain boundaries, although further higher temperature studies focussing on the kinetics of order-disorder transformation need to be done on different Heusler compounds.

Since we have mentioned the current understanding of the stages of antiphase growth during ordering, we would also like to briefly mention the mechanism of the domain growth. Antiphase domains differ from grains as the crystallographic lattice is coherent across an antiphase domain boundary and the orientation is maintained, unlike grain boundaries which are incoherent. The antiphase domain boundary motion is therefore governed by bulk diffusion, which is mediated via vacancy mechanism whereas grain growth is governed via the much faster surface diffusion, since the atoms at the grain boundaries are less strongly bound as compared to an atom in the lattice, due to the incoherency [280]. The vacancy-driven order-disorder transition has been treated computationally [288, 289] and has been confirmed for other binary systems [282, 290, 291]. Regarding Heusler compounds, some theoretical treatments of the order-disorder transition has been done using various approximations and computational methods [292–295], and the interaction and ordering between the nearest- and next-nearest-neighbours were found to play a significant role in the kinetics of ordering. Furthermore, the interaction of atoms with vacancies between the 1st and the 2nd nearest neighbours was also deemed to be important in the kinetic behaviour of ordering in $AuAgZn_2$ Heusler compound [296]. Due to the defect-driven nature of the order-disorder transition, it may be easier to obtain higher order in a polycrystalline as-cast sample as compared to a single crystal.

Clearly, the evolution of the antiphase domains and domain boundaries is closely entangled to the evolution of order, which in turn is related to the point defects in the material. Thus, tracking the evolution of antiphase domains can further give us an idea about the amount of order in a sample. Nevertheless, detailed study of the kinetics of the order-disorder transition in different Heusler compounds is still missing, and no related work has been done on quaternary systems to the best of our knowledge; and therefore, there is much to be verified and understood in this regards in this vast family of Heusler compounds.

So far, we have shown that the *in situ* annealing involving slow cooling is far more beneficial than quenching towards obtaining a higher $L2_1$ order as well as small fraction of defects. However, there is a strong possibility that sample after *in situ* experiment suffers from crystallographic texture, and the peak intensities for the final 400 K data are anomalous. Due to this, it has not possible to calculate the amount of $L2_1$ order, even though the ordering in the sample seems to have improved after the *in situ* experiment. In principle, the sample can be analysed in the laboratory and can even be milled to remove the texture if present. Unfortunately, since the sample had become activated due to extended exposure to neutrons, it has so far not been possible to study and further characterize the sample post-annealing. Therefore, corresponding laboratory annealing experiments have been performed as per the *in situ* measurements and the details are discussed next.

4.3 Laboratory annealing experiments with subsequent slow cooling

$Co_2FeAl_{0.5}Si_{0.5}$ sample from the same as-cast batch as the one for neutron measurements was taken and powdered using a steel mortar and pestle. The resulting powder was then sealed in an evacuated quartz ampoule backfilled with Ar. During the *in situ* neutron diffraction, a complicated annealing procedure was followed, which involved a lot of steps along multiple profiles (see Figure 4.3). In order to simplify things, the sample was annealed for 3 days at 1400 K followed by subsequent slow cooling at the rate of 2 K/min to room temperature.
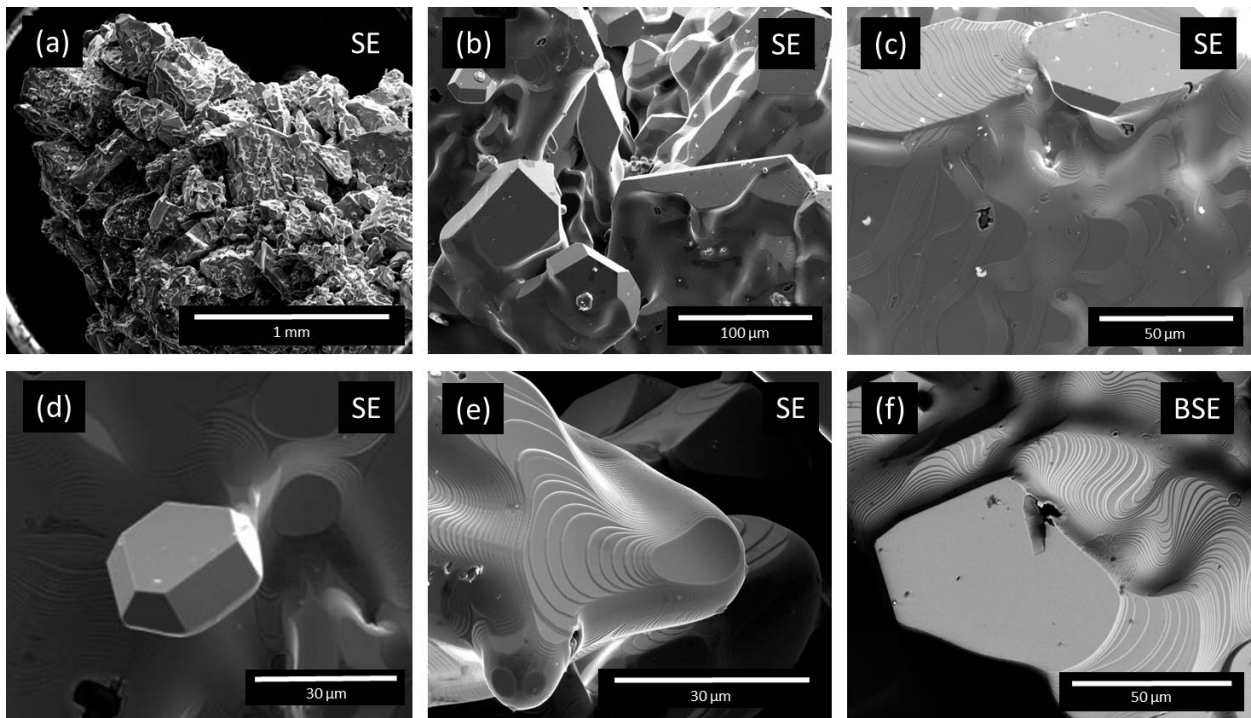
Figure 4.17: Annealed and subsequently slow-cooled $Co_2FeAl_{0.5}Si_{0.5}$ powder sample (a)-(e) Secondary electron (SE) images showing faceted growth morphology at different magnifications (f) Back-scattered electron (BSE) image showing growth of single-crystalline planes.

Figure 4.17 shows the secondary electron (SE) and back-scattered electron (BSE) images for a piece of the annealed sample at different magnifications. The morphology of the annealed powder was found to be very interesting. At low magnification the sample looked like normal sintered powder. However, clear faceting could be seen in the higher magnification images (Figure 4.17b-c). In some cases, there was an orientation relationship with respect to adjacent planes leading to faceted micro-crystallites with sharp edges (Figure 4.17d) whereas in some cases, no such orientation relationship was observed (Figure 4.17e). In addition to the faceting, layered growth was seen on different regions of the sample (Figure 4.17c-e). The growth of selected planes was seen clearly in

the BSE image such that the same orientation was retained (Figure 4.17f). Thus, crystallographic texture is expected in the material due to the preferential growth of selected planes.

We have discussed earlier that the relative intensities at (111) superlattice reflection as well the (220) reflection are strongly affected for the final sample after the *in situ* neutron diffraction experiment (Figure 4.13b). The (111) reflection has considerably higher intensity whereas (220) intensity is almost reduced by a factor of 2. The features were attributed to crystallographic texture but could not be confirmed as the sample was inaccessible due to activation. The faceted growth observed in the lab experiment confirms the evolution of crystallographic texture in the sample during the specific annealing procedure which explains the anomalous change in intensities as observed.

(a)	Co	Fe	Al	Si
Nominal	50	25	12.5	12.5
As-cast	48	24	14	14
Slow-cooled Powder	48	25	12.5	14.5
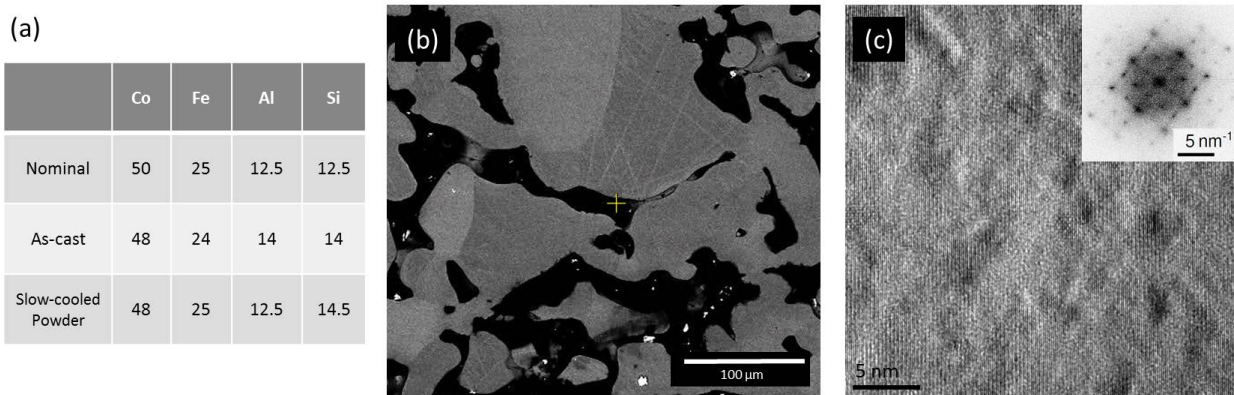
Figure 4.18: Annealed, slow-cooled Co₂FeAl₀.₅Si₀.₅ powder sample (a) EDX data along with the data for as-cast sample for comparison (b) BSE image of polished powder sample (c) High resolution TEM image showing sample homogeneity; inset shows the Fourier transform of the image. (TEM data courtesy of Dr. Felix Börrnert)

A part of the sample was embedded in resin and polished for EDX measurements shown in Figure 4.18 along with the microstructure. The composition was nominal within the error of the EDX measurement (∼2 %). Large homogeneous particles can be seen in the BSE image (Figure 4.18b). Significant grain growth took place upon annealing at 1400 K as the particles were either mono- or bicrystalline. Homogeneity was further confirmed by TEM as shown in Figure 4.18c.

X-ray diffraction was done in order to confirm the structure (Figure 4.19). The sample had cubic $Fm\bar{3}m$ structure, and no contamination or secondary phases were observed. The effect of texturing was avoided by coarsely milling the annealed sample before measurement in the transmission mode. Figure 4.19b shows the comparison between the as-cast sample and the sample quenched after annealing at 1000 K, which were measured as prior-annealed samples in neutron diffraction. The (111) superlattice reflection had substantial improvement in intensity as compared to as-cast or quenched samples, which suggests a higher $L2_1$ ordering in the sample, as expected.
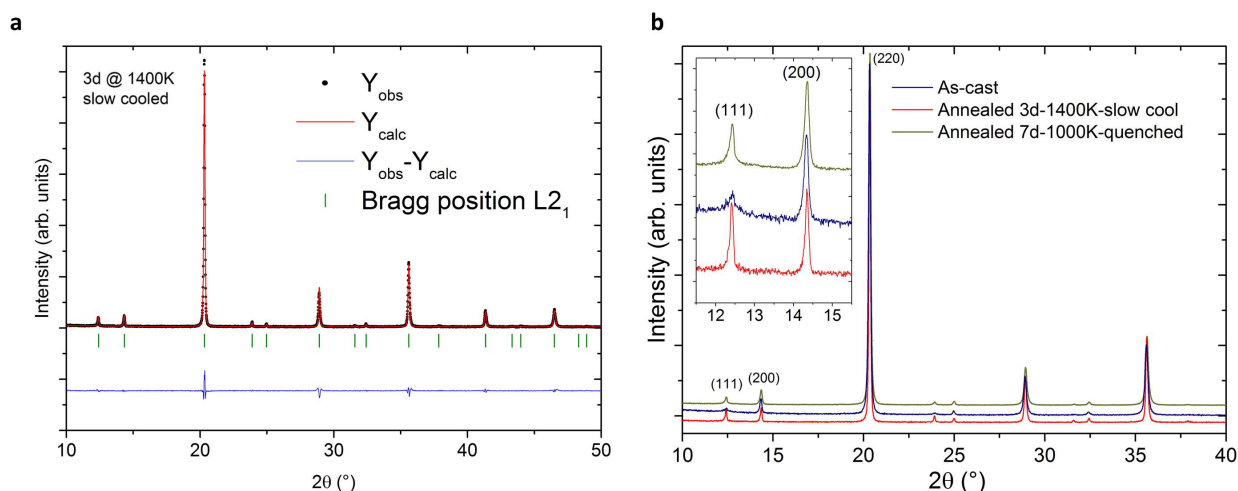
Figure 4.19: X-ray diffraction of annealed, slow-cooled $Co_2FeAl_{0.5}Si_{0.5}$ powder sample (a) Rietveld refinement (b) comparison to as-cast and 1273 K annealed (7 days; quenched) samples, plotted with a small y-axis offset.

Rietveld refinement of the data was performed so as to quantify the $L2_1$ order. The structural parameters as well as volume fraction of $B2$ disorder is listed in Table 4.2. The details of the refinement are given in Appendix A (Page 152). The values for the as-cast and quenched samples are also mentioned for comparison. The lattice constant for the slow-cooled sample does not show significant change as compared to the as-cast or the prior-annealed samples. However, there was significant reduction in $B2$ disorder ($\sim 20\%$) for the slow-cooled sample. The obtained ordering in the slow-cooled sample was found higher than those reported for the annealed and quenched samples in literature as well [66].

Table 4.2: Rietveld refinement of X-ray diffraction data for annealed $Co_2FeAl_{0.5}Si_{0.5}$ powder sample with slow cooling compared to the samples annealed prior to neutron diffraction.

Sample	Space group	Lattice (Å)	$B2$ disorder (%)
As-cast	$Fm\bar{3}m$	5.683(4)	55.1
Annealed-1000K-WQ	$Fm\bar{3}m$	5.681(4)	37.7
Annealed-1273K-WQ	$Fm\bar{3}m$	5.682(4)	41.8
Annealed-1400K-Slow	$Fm\bar{3}m$	5.682(4)	20.2

We have already seen that the sample annealed at 1273 K and subsequently quenched, where we are well above the $L2_1$-$B2$ transition, has a lesser $L2_1$ order than the sample annealed at 1000 K,

where we are below the transition. At 1400 K, we are far above the $L2_1$ regime so much so that the sample is predominantly $A2$ disordered, as seen in the *in situ* neutron diffraction (Figure 4.13a). Another important thing to note is that the slow-cooled sample has a better ordering even though it was annealed for 3 days only as compared to 7 days for the samples that were quenched.

It seems that neither the annealing temperature nor the annealing time beyond a certain point is quite as important for ordering as the cooling rate which plays a more significant role towards achieving higher $L2_1$ order. This would be advantageous for applications, as the processing time for the material can be reduced markedly.

As we have discussed earlier, it is difficult to quantify the amount of various disorders present in a material. Therefore we have performed nuclear magnetic resonance on the slow-cooled powder sample, in order to find out the exact amount of disorder after the annealing.

4.3.1 Characterization of order using nuclear magnetic resonance

Nuclear magnetic resonance (NMR) is a widely used to determine the local distribution of atoms in a material. Zero-field ^{59}Co NMR has been used in literature to quantify the amount of disorder in Co$_2$FeAl$_{1-x}$Si$_x$, both in bulk as well as films [64, 66, 297, 298]. ^{59}Co NMR was performed on the slow-cooled powder sample and the data is shown in Figure 4.20. The resulting signal profile was fitted with various nearest-neighbour and next-nearest-neighbour environments based on ordered and disordered structures (refer to Wurmehl et al. [64, 66] for further details). The NMR experiment and analysis are courtesy of Dr. Alexey Alfonsov at IFW Dresden. Based on the fitting, a presence of $\sim$70 % $L2_1$ order was obtained, which is in line with the high $L2_1$ order calculated from Rietveld refinement of our XRD data. In comparison, a recent work involving ^{59}Co NMR on bulk Co$_2$FeAl$_{0.5}$Si$_{0.5}$ samples by Wurmehl et al. reported a 59 % $L2_1$ order in an annealed sample which was quenched, whereas ordering in the as-cast was significantly lower (38 % $L2_1$ order), as expected [66].

Both NMR and XRD data show similar results with regards to a high $L2_1$ order in the slow-cooled sample. The small difference in the value of the $L2_1$ order as measured by the two techniques ($\sim$10 %) could be due to various reasons. Regarding the XRD analysis, additional factors such as slight off-stoichiometry are neglected which is seen in the NMR. The Rietveld refinement is also performed under the assumption that only $B2$ type disorder is present in the material. On the other hand, there is a 8-10 % mismatch between the NMR data and the overall fit and the 10 % difference may well be within the error bars. The values for disorder and off-stoichiometry may have small changes if a different fitting model is used. Moreover, small amounts of additional disorders such as $A2$ disorder may be present in the sample which could not be incorporated in both XRD and NMR analysis due to their small volume fraction, and this may also affect the values of order/disorder obtained.
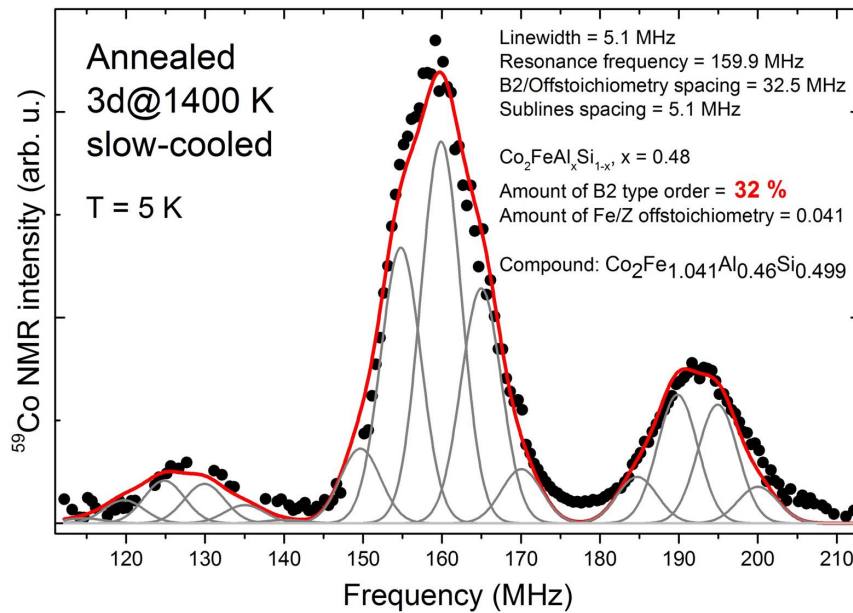
Figure 4.20: Zero-field ^{59}Co nuclear magnetic resonance data (black circle) for $Co_2FeAl_{0.5}Si_{0.5}$ powder sample slowly cooled after annealing. Gray curves are the Gaussian fits for different environments and the red curve is the overall fit. (NMR data courtesy of Dr. Alexey Alfonsov)

A possibility of a slight overestimation of the *B2*-type disorder in NMR has also been discussed in a recent report [69]. The atoms in the ordered *L2*$_1$ region which are adjacent to the antiphase domain boundary technically have partially disordered local environments. Since the NMR probes the local environments, these unit cells are also counted as part of the disordered region and would lead an overestimation of the disorder present in the material. Alfonsov et al. [69] observed that the NMR data can still be fit well while neglecting this effect, although they report a 15 % mismatch in the fit. Inclusion of such an effect in the fitting model may allow for a better evaluation of the *L2*$_1$ order. Moreover, by tracking the antiphase domain boundaries through XRD, it may be possible to give a measure of such unit cells which are overestimated towards *B2* disorder, and it might be possible to subsequently introduce corrections into the fitting model accordingly, for an improved quantification of order.

Notwithstanding the limitations of the techniques involved, a significantly higher fraction of *L2*$_1$ order has been shown in the sample slowly cooled after annealing at 1400 K, as compared to the as-cast and quenched samples.

Magnetization and calorimetric measurements were additionally performed on the slow-cooled sample, and are discussed next.

4.3.2 Physical property measurements

4.3.2.1 Magnetization and domain effects

Magnetization measurements were performed on the sample slowly cooled after annealing at 1400 K. The sample has a soft-magnetic behaviour with a slightly higher saturation moment than the Slater-Pauling value (Figure 4.21a). No transitions were observed in the sample between room temperature and 5 K. However, there seemed to be a slight smearing out of the saturation field in the magnetization versus field (M(H)) data at 5 K. Figure 4.21b shows the comparison of the M(H) curves at 5 K for as-cast, prior-annealed samples (quenched) and the slow-cooled sample. The data was normalized for easier comparison. It can be seen clearly that the saturation field for the slow-cooled sample was markedly higher than the others. The as-cast and 1000 K annealed sample were similar.
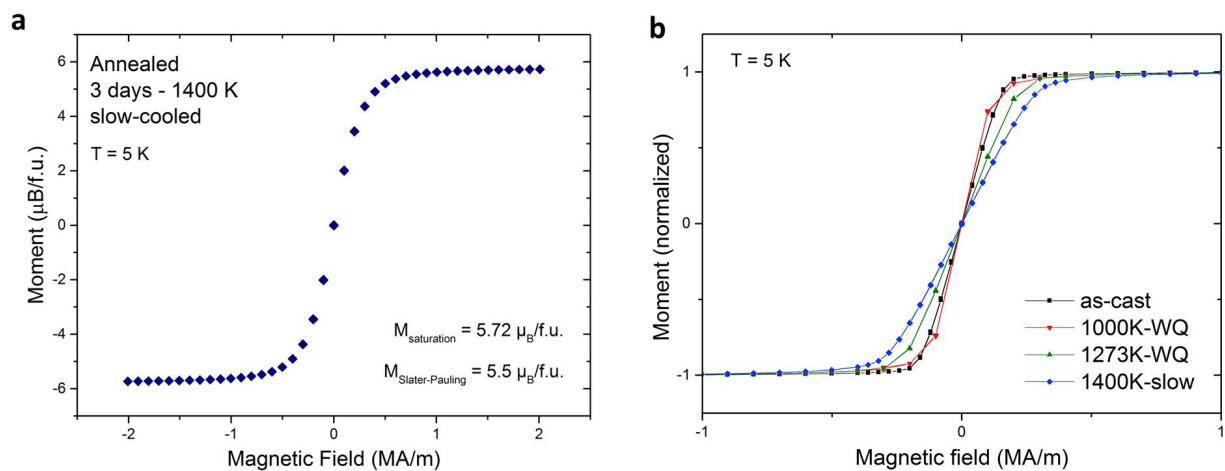
Figure 4.21: Co$_2$FeAl$_{0.5}$Si$_{0.5}$ (a) Magnetization-field (M(H)) data of the annealed slow-cooled powder sample at 5 K (b) M(H) at 5 K for slow-cooled sample in comparison with as-cast as well as samples annealed prior to neutron diffraction which were quenched. (Since all 4 samples had slightly different saturation moments, the data was normalized to highlight the difference in saturation field).

In principle, since magnetic domains are pinned at defects, a lower defect concentration should lead to faster domain magnetization dynamics. Since the slow-cooled sample is more ordered, it should need smaller field to saturate as the amount of disorder in the sample is smaller, whereas we observed the opposite of the expected phenomena. We know from the line profile analysis that selective peak broadening is minimal after the *in situ* neutron experiment. The size of individual antiphase domains (structural) are larger, although the *B2* domains have reduced in number and volume fraction (refer to Figure 4.15 and Figure 4.16 along with the relevant discussion).

It has been well studied that these antiphase domain boundaries determine the size of the magnetic

domains, and act as pinning sites for the motion of the magnetic domain walls in general [299, 300], and the same has been shown for Heusler compounds [301–304]. In addition, the magnetization and motion of magnetic domain walls has been demonstrated to be affected by antiphase boundaries in Ni$_2$Mn(Al,Ga) [304, 305]. Since both the *L2*$_1$ and *B2* domains are larger after *in situ* annealing, the magnetic domains formed at random should also be larger, and thus, a higher saturation field is needed to orient them along the field direction. This may lead to smearing out of the M(H) curve and an effective higher saturation field for the slow-cooled sample.

4.3.2.2 High temperature magnetization

Figure 4.22 shows the high temperature magnetization data for the slow-cooled sample. The $1/\chi$ near the Curie temperature is plotted in the inset. Our sample exhibited two different Curie temperatures during the heating profile, in contrast to the as-cast sample where single T_c was observed (Figure 4.5b). Moreover, the two T_cs were perceptible only during the heating part whereas only one T_c was seen during cooling.
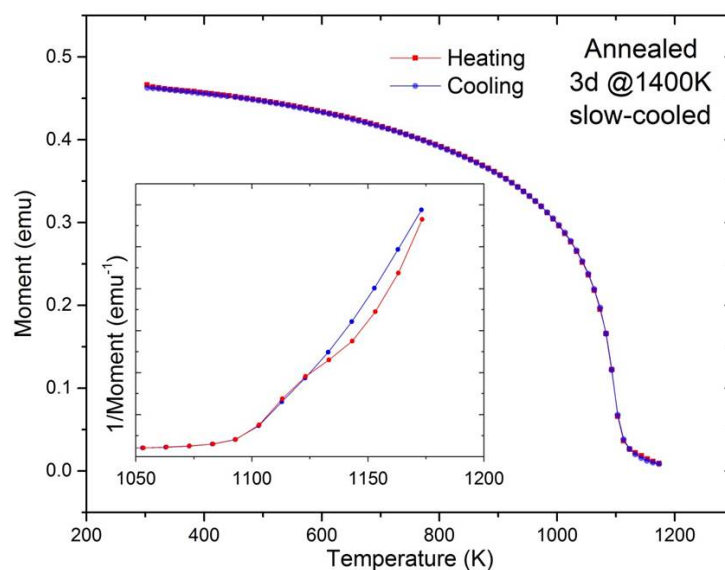
Figure 4.22: High temperature magnetization data in 1 MAm^{-1} field for the annealed slow-cooled Co$_2$FeAl$_{0.5}$Si$_{0.5}$ powder sample. Inset shows $1/\chi$ at high temperatures, showing the two different Curie temperatures during heating which smear out during cooling.

As has been already discussed, upon slow-cooling, the antiphase domains are no longer nano-sized leading to relatively larger regions of *L2*$_1$ and *B2* type ordering. The sample may essentially behave as a two-phase system of distinct *L2*$_1$ and pure *B2* ordered region. Moreover, calculations show that anti-site disorder strongly affects the T_c in double perovskites [306, 307] and the inherent magnetism of Heusler compounds is also known to be affected by disorder [40]. Therefore, complete *B2* ordered

region is expected to have a different Curie temperature than the pure $L2_1$ ordered region. This is the likely scenario in our study, that explains the two T_cs observed.

Since the sample is heated to 1173 K, well above the $L2_1$-$B2$ transition, it is likely to be predominantly $B2$ ordered. Furthermore, the magnetic ordering is at a higher temperature than the structural ordering, and therefore only one T_c is observed corresponding to the disorder structure during cooling. Since we heated the sample for considerably short duration, another possibility could be that there is still a significant amount of $L2_1$. However, it is expected that the new antiphase domains would have randomly nucleated again as well as the existing antiphase domain boundaries would have diffused. Most likely the individual ordered and disordered regions are no longer as large and distinct as was the case after slow cooling. Therefore, the two Curie temperatures are smearing out and only an effective T_c is observed during cooling.

The two Curie temperatures are not observed for the as-cast sample, as was shown in Figure 4.5b. The as-cast sample is highly disordered and the antiphase domains may be quite diffused and distributed. The individual domains are not large and distinct so as to manifest as separate Curie temperature. A similar scenario would be application for samples quenched after annealing, since quenching has been shown to lead to generation of new defects and antiphase domains as well as to diffuse and distort the existing antiphase boundaries [8, 75, 276, 308].

It is necessary to address the observation of two Curie temperatures through additional techniques involving high temperature measurements. Therefore, high resolution calorimetry has been performed, which also allowed to compare the slow-cooled sample to the literature with regards to the order-disorder transition.

4.3.2.3 Calorimetry measurements

In literature, calorimetry has been the method of choice to study order-disorder transitions, specially for Co$_2$FeAl$_{0.5}$Si$_{0.5}$ [11, 12, 84]. Therefore in order to compare to literature, as well as to have a complementary technique for the high temperature magnetization and the corresponding two Curie temperatures observed, high sensitivity differential thermal analysis (DTA) was performed on the slow-cooled sample till 1300 K with rate of 10 K/min for both heating and cooling profile. Figure 4.23 shows the DTA data for the measurement from 800 K till 1250 K, to highlight the transition because no changes were observed below 800 K.

Two distinct signals/peaks were observed in the same temperature range in the both heating and cooling profile (marked by arrows), in accordance with what has already been reported by Umetsu et al. [12]. A broad signal was seen at lower temperature, with the local maximum at ∼1115 K along both directions. The broad signal is likely due to the higher-order $L2_1$-$B2$ transition which is known to be spread over ∼100 K from the neutron diffraction. In addition, no hysteresis was seen, supporting the higher-order nature of the transition. The shoulder-like signal at ∼1150 K was

possibly due to a magnetic transition. A small change was also seen around 1050 K only during heating, which was also perceptible in the data of Umetsu et al. [12] albeit between 950-1000 K. However, they did not comment on it and no information is available in literature about any possible transitions in that temperature regime.
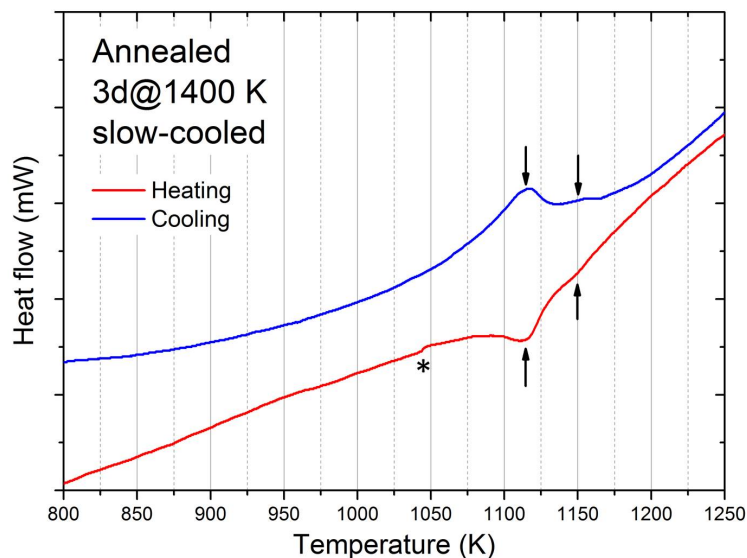
Figure 4.23: Differential thermal analysis data at 10 K/min for the $Co_2FeAl_{0.5}Si_{0.5}$ sample annealed at 1400 K and subsequently cooled slowly (the heating and cooling profiles are plotted with a small y-axis offset, as original data overlapped). The signals from structural and magnetic transitions are marked by arrows. A tiny signal is also observed around 1050 K, which could not be identified and is marked with '∗'.

The temperatures for both the signals matched to what was reported for $Co_2FeAl_{0.5}Si_{0.5}$ by Umetsu et al. [12]. In the recent work of Srinivas et al. [84], the order-disorder transition and the Curie temperatures reported for $Co_2FeAl_{0.5}Si_{0.5}$ were significantly different. We believe that there was an error with their DSC measurement. In their data, the melting peak was observed at 1461 K, which is significantly lower that our measurements from melting (∼1650 K), and moreover, no melting peak was similarly observed in the DSC data of Umetsu et al. till 1550 K [12].

Although it has been already mentioned that there is likely an error involved with the temperatures measured due to lack of adequate furnace calibration, we would like to briefly comment on the discrepancy of the temperature regime of the order-disorder transition measured in neutron diffraction and calorimetry. As was discussed earlier in Section 4.2.2.1, although the majority of the transition took place between 1000-1100 K, the maximum of the calorimetry signal was observed above 1110 K. In principle, anti-site disorders are entropy-driven and are not expected to have a sharp, first order transition temperature. A broad change over a large temperature range is rather expected, since it is a higher-order transition. This means that the associated entropy change is

also quite broadly distributed with temperature. As the sample got heated up above 1000 K, the calorimetric signal was quite low, since we were in the initial stages of the transition. The so-called peak of the signal was observed when a significantly larger fraction of material transformed near the end of transition. In calorimetric measurements, the peak signal depends on the thermal gradient as well as heat inertia or thermal lag, and may be observed later than the onset of transition [309–313]. The nature and kinetics of the transition may also affect the calorimetric response, e.g., a broad transition over ∼100 K is also observed in the DSC data for Fe-28%Al-5%Cr alloy in the work of Morris et al. [72], and interestingly the calorimetric peak is observed at the end of the order-disorder transition, as confirmed from the evolution of order parameter. Thus, the dynamics of the calorimetry measurement itself may be partly responsible for the discrepancy with the neutron diffraction data.

Another important aspect is the observation of two Curie temperatures in the high temperature magnetization data, although only one additional signal is seen in the DTA data. We believe that the two transitions observed in the magnetization above 1100 K, are indeed magnetic transitions, which arise due to distinct *L2$_1$* and *B2* ordered domains in the material. Since the lower T$_C$ is around 1100 K, it overlaps with the structural transition, and is not seen separately. In order to deconvolve the overlapping peaks, further experiments with higher resolution must be performed. The evolution of the structural and magnetics peaks upon extended thermal cycling in the DTA setup itself can also be done to complement the *in situ* neutron diffraction data and are being planned for the future.

Based on the understanding from the neutron measurements as well as the laboratory annealing experiments, we shall discuss an optimized annealing procedure in order to minimize defects and obtain higher *L2$_1$* order in Co$_2$FeAl$_{0.5}$Si$_{0.5}$.

4.3.3 Towards an optimized annealing profile

There are marked differences between the slow-cooled sample as compared to the prior-annealed samples, specifically the cooling rate after the annealing, and the temperature at which the sample was annealed. We shall now discuss both these aspects, in the context of an optimal annealing procedure, which has been one of the aims of the present study.

4.3.3.1 Quenching versus slow cooling

The amount of $L2_1$ order, antiphase domains and the resulting peak broadening show significant improvement in the slow-cooled sample as compared to prior-annealed samples which were quenched. Such marked changes are observed even though the annealing time was effectively shorter, $\sim$3 days in the slow-cooled sample as opposed to 7 days for the prior-annealed samples. We believe that the cooling rate in the annealing experiments plays quite an important role towards obtaining a higher order with lower defects.

An important aspect of the cooling rate after annealing pertains to the quenching-in of the defects. At any given temperature, there is an equilibrium defect concentration. Annealing the sample at a specific temperature equilibrates the defect density, which gets frozen-in upon quenching. Defects, in principle, are entropy-driven and thus a higher temperature would mean a higher defect concentration. Cast samples in general have a high concentration of defect density as the sample is quenched from above the melting point T_m and the defect concentration is higher than the equilibrium defect concentration at any $T < T_m$. When a cast sample with high defect density is annealed at a given temperature, the defect density becomes equal to equilibrium value at that temperature. Although compared to the cast sample, defect concentration would be less, but depending on the annealing temperature it could still be quite large, as annealing is normally done at elevated temperature to have better kinetics. Assuming that the quenching rate is fast enough that negligible defect annihilation or ordering takes place during the cooling, the quenching process freezes in the equilibrium defects and the sample cannot be improved beyond a certain extent. Quenching of vacancies after annealing has been shown recently by Neibecker et al. [154], although they utilized this aspect to obtain higher order in Ni$_2$MnAl Heusler compound which undergoes a martensitic transformation.

One may anneal at lower temperatures, but kinetics of various processes have to be kept in mind so that annealing times are realistic. For example, at a lower temperature, the rate of defect annihilation may be negligible and would thus take a really long time. The defect density can be reduced via slow cooling of the sample, allowing time for the defects to come into equilibrium at the lower temperatures. The lattice relaxation seen in XRD for the slow-cooled sample (Table 4.2) further corroborates the absence of frozen-in defects during slow-cooling as opposed to quenching.

Another disadvantage with quenching or high cooling rates, as opposed to near-equilibrium conditions during slow cooling, is the generation of additional defects, apart from the defects which might

be frozen-in. We would like to refer back to the line profile analysis of the *in situ* experiment (Section 4.2.2.1 and Section 4.2.2.2). During the initial heating to 1000 K itself, both the integral breadth and shape factor for (111) reflection reduce to values quite close to those in the final sample after annealing. On the contrary, the sample annealed at 1000 K for 7 days and subsequently quenched has both a higher integral breadth and shape factor for (111) even though just heating the sample to 1000 K leads to a sharper (111) peak, with a high Gaussian contribution. This means that the sample quenched after annealing has more defects and disorder as compared to the slow-cooled sample or even the sample at 1000 K during the initial heating in the *in situ* experiment. This is only possible through generation of additional defects/disorder during quenching which is avoided in the slow-cooling. Defects are created likely due to stress generated in the material as it is rapidly cooled, which is referred to as thermal shock. There are reports that annealing followed by quenching leads to increase in defect density, although the studies were on single crystals or pure elements [314–317] where the defect densities are small to begin with. Quenching has also been reported to induce complex dislocation substructures in a material [308]. Kogachi et al. [318] have demonstrated a direct correlation between the annealing temperature and the fraction of thermal vacancies after subsequent quenching in Co$_2$MnZ (Z = Si, Ge, Sn). Furthermore, generation of vacancies and dislocations, which nucleate preferentially at antiphase domain boundaries upon quenching of β brass (CuZn) has been shown by a detailed TEM study [75].

The defects generated due to quenching may also manifest as nanoscale antiphase domains. Quenching-in of critical fluctuations as new antiphase domains in Fe-Al alloy annealed close to the ordering temperature has been shown through TEM by Allen and Cahn [276]. In a rather recent work by Gilles et al. [319], FeCo alloys were subjected to different cooling rates after the annealing treatment and the average size of antiphase domains obtained from neutron diffraction was almost an order of magnitude smaller for the air-cooled sample (effective cooling rate of 80 K/min) as compared to the furnace-cooled sample at 1 K/min. Moreover, size of the antiphase domains became more or less equal in both the air-cooled and furnace-cooled samples as both the samples were heated to 600 °C [319]. This implies that the much smaller antiphase domains are additionally generated in the sample cooled faster after annealing. Thus, quenching or a higher cooling rate leads to antiphase domains due to random ordering and may leads to nanoscale domains, which results in selective peak broadening of superlattice reflections, as observed in our prior-annealed samples (Figure 4.2.1).

In our slow-cooled sample, the annealing temperature was 1400 K, and the sample at such high temperatures should be highly disordered as seen in neutron diffraction (Figure 4.13) where the sample is predominantly *A2* ordered. Although annealing the sample at such high temperatures seems counter-intuitive, all the *L2$_1$* domains of various sizes that may exist in the sample should be gone, as we are far above the *L2$_1$* regime. When the sample is cooled, new antiphase domains form below the order-disorder transition. As the sample is cooled further, the existing antiphase boundaries have time to grow through diffusion and the random generation of new antiphase domains

are avoided. In addition, as the sample is slowly cooled, there is less thermal shock to the material, as well the annealing process is extended till lower temperatures. Since the $L2_1$ order is more stable at lower temperatures, the $L2_1$ regions grow and the antiphase domains are further reduced during the cooling process. This leads to a much higher effective ordering in the material. Therefore, annealing experiment assisted with slow cooling may need a much shorter time for a considerable reduction in the antiphase boundaries. It is thus much more efficient in attaining higher fraction of $L2_1$ order in the samples.

In two of the earlier works on Heusler compounds, annealing followed by slow-cooling has been distinctively shown to lead to a significantly improved ordering in Pd_2MnIn as compared to quenching [33, 320]. Conversely, no significant differences between slow-cooling and quenching were observed in extended x-ray-absorption fine-structure measurement (EXAFS) and neutron diffraction study of Co_2MnSi [57]. There are significant differences between the two studies. First, in the former (Pd_2MnIn), we are dealing with $L2_1/B2$ order, whereas it is $L2_1/DO_3$ in the latter. Improvement in $L2_1$ upon slow-cooling in our case fit well to Pd_2MnIn study and may be valid for other systems with $L2_1/B2$ ordering. However, we must be very careful in generalizing the results as the different elements in different compounds means that the free energies involved would be significantly varied.

Slow-cooling therefore, offers distinct disadvantages in contrast to quenching the sample, specifically lower defects concentration and lower antiphase domain boundaries. In addition, a lower annealing time is needed to obtain a significantly higher $L2_1$ order in the material as compared to the quenched samples.

4.3.3.2 Importance of annealing temperature

We would like to briefly comment on the annealing temperature and its role in ordering. We have shown that a higher ordering is achieved by slow cooling of the sample and the annealing temperature does not seem to play a significant role. In principle, annealing the sample below transition followed by slow cooling, should be equally efficient. However, the high annealing temperature of 1400 K, may have given an unexpected advantage. Since we started with a polycrystalline sample, fine-grained structure was present in the sample. The grain boundaries, along with being high energy defects, are incoherent interfaces. Hence, they would have a pinning effect on the antiphase domains which are coherent in nature. Thus, the grain boundaries would act as inhibitors for growth of antiphase domains. Since the ordering phenomena is driven by antiphase domain coarsening, the presence of grain boundaries should, in principle, inhibit the rate and extent of ordering.

In hindsight, annealing the sample at 1400 K allowed for considerable grain growth to take place. The slow-cooled sample after annealing had mostly mono- or bi-crystalline particles as seen in Figure 4.18. Moreover, at 1400 K, we are considerably above the $L2_1$ regime, no ordering phenomenon is expected during the 3 days of annealing. All the ordering would have purely happened as the sample

was slowly cooled to room temperature. Even though no annealing time was given except during cooling, the sample had a considerably large $L2_1$ order ($\sim$70 %).

We believe that annealing the sample at 1400 K helped in growth of the antiphase domains during cooling as the grain boundaries were significantly reduced. Therefore, such a high temperature annealing step should be performed in addition to the slow cooling profile, specially in the annealing of bulk samples. The annealing time at high temperatures may be further reduced during the annealing of single crystals, or samples containing large mm sized grains, e.g., as obtained commonly for a fast Floating Zone growth.

Thus, based on the understanding gained from the *in situ* neutron diffraction as well as corresponding laboratory samples, an optimized annealing profile can be developed for obtaining a high $L2_1$ order. It must be kept in mind that precise information of order-disorder transitions in the material must be known in order to develop the annealing profile.

The sample should first be annealed at considerably high temperatures in order to facilitate grain growth as well as annihilation of quenched-in defects. The annealing time would depend on the crystalline nature of the sample, e.g., a single crystal would need a minimal annealing as compared to a polycrystalline sample. The sample should then be cooled as slowly as possible to a temperature below the order-disorder transition and held for a given amount of time. The annealing temperature in this step should be carefully chosen so that we are well below the order-disorder transition to avoid the critical fluctuations, as the order-disorder transition may be quite broad, e.g., $\sim$100 K for Co$_2$FeAl$_{0.5}$Si$_{0.5}$ as seen in our data. The annealing time in this step would depend on the order-disorder transition regime itself. The annealing time may have to be increased if the order-disorder transition are closer to room temperature, since the kinetics would be slow. Finally, the sample should be cooled as slowly as possible to room temperature.

We would like to mention that since the annealing process involves slow cooling, it would not be successful in materials which undergo a phase transformation or decomposition. However, adapting the cooling rate in certain regions may be explored in order to avoid such regions of instability. The presence of low temperature phase transformations was the main reason for adopting a quenching procedure after annealing in the case of the first Heusler compound, Cu$_2$MnAl. Cu$_2$MnAl was found to be stable at high temperatures [321], but decomposed into different phases when it was cooled slowly [322]. Later on, it was shown through neutron diffraction that slow cooling the sample may lead to a better $L2_1$ order [320]. Unfortunately, by then, the Heusler community had well adopted the quenching procedure and to this date, majority of the reports follow the popular opinion. Science is about a constant cross-examination of commonly believed ideas and the best time to learn from our mistake is in the present. We hope that we would be able to motivate the community to revisit the existing literature in the context of the points suggested in this work.

4.4 Conclusion

We examined the ordering phenomena in $Co_2FeAl_{0.5}Si_{0.5}$ in detail using *in situ* neutron diffraction and annealing experiments. The neutron diffraction measurements at room temperature on as-cast and prior-annealed samples which were quenched, showed selective peak broadening due to the presence of nanoscale antiphase domains. The two different annealing treatments involving quenching did not lead to considerable improvement in the $L2_1$ order. The reduction in peak broadening upon annealing was small as well, but followed a similar trend as the ordering phenomenon. We subsequently performed the *in situ* neutron diffraction at high temperatures till 1400 K, over multiple profiles. We found that the $L2_1$-$B2$ transition was unusually broad, spread over ∼100 K. The majority of the transition took place between 1000-1100 K and the rate of ordering was more or less linear. No $B2$-$A2$ transition regime was observed till 1400 K, as there was still a finite intensity of the (200) superlattice reflection at that temperature. The ordering in the sample was significantly improved after cooling. However, the relative intensities of the (111), (200) and (220) reflections were quite irregular, and therefore the $L2_1$ fraction could not be determined. The anomalous intensities were later confirmed through the corresponding laboratory experiments to be a result of crystallographic texture which developed in the powder sample. Furthermore, the evolution of ordering as well as the growth of antiphase domains were tracked using the line profile analysis of the *in situ* diffraction data. The final sample after the *in situ* measurement did not show any selective peak broadening.

Subsequent laboratory experiments based on the *in situ* experiment was done where the sample was annealed at 1400 K followed by a slow cooling. The slow-cooled sample showed a significantly improved ordering in the sample, which was quantitatively measured using NMR. The magnetization data showed two Curie temperatures due to the distinct $L2_1$ and $B2$ antiphase domains. However, only one T_C at higher temperature was observed in calorimetry, and we believe, that the signal from the T_C at lower temperature was overlapped with the broad signal from $L2_1$-$B2$ transition, and was therefore not perceptible.

Slow-cooling was shown to offer certain advantages in terms of defects as compared to quenching, which led to significant growth of antiphase domains and thus a higher order was achieved. Based on our present observations, we have designed an optimized annealing profile where the sample might be slowly cooled in a two-step annealing process to obtain a higher order in a material. We believe that this optimized annealing procedure may be applicable to other systems which do not undergo any additional phase transformation, given that a detailed and accurate information of the order-disorder regime in the specific system is known.

The significantly higher ordering in $Co_2FeAl_{0.5}Si_{0.5}$ should lead to an improved magnetoresistance, and hopefully, the half-metallicity could be realized.

Chapter 5

Summary and Outlook

The present thesis is devoted to the study of quaternary Heusler compounds. Heusler compounds exhibit a plethora of physical phenomena, and many additional exotic properties have been predicted in the family. The varied physical properties are an outcome of the different material aspects, but the relationship between them is quite complex and not completely understood. The aim of this work has been to unravel the entanglement between the intrinsic material attributes of Heusler compounds such as the structure, phases, defects, disorder etc., and the resulting physical properties.

We have presented our work on two cobalt-based systems, $Co_2Cr_{1-x}Fe_xAl$ and $Co_2FeAl_{1-x}Si_x$. Both the systems are predicted to be half-metallic ferromagnets with a wide band gap along the minority spin direction. Furthermore, in addition to the high Curie temperature, specific compositions in each system, $Co_2Cr_{0.6}Fe_{0.4}Al$ and $Co_2FeAl_{0.5}Si_{0.5}$ respectively, are expected to be robust to small amounts of disorder, which makes them promising towards realization of 100 % spin polarization. Unfortunately, the half-metallicity has not yet been experimentally verified and the reported physical properties are aberrant. However, the underlying cause is quite different in both materials, and therefore, we have focussed on a different aspect of the material-property correlation for each system. On one hand, we have addressed the issue of chemical instability and associated phase dynamics in $Co_2Cr_{1-x}Fe_xAl$ system, whereas, in the other case, we explored the evolution of anti-site disorder with temperature in $Co_2FeAl_{1-x}Si_x$ in order to optimize the annealing process towards a fully ordered material.

The $Co_2Cr_{1-x}Fe_xAl$ system was discussed first, where the discrepancies in physical properties of bulk samples were confirmed to be due to a phase segregation, and therefore Floating Zone (FZ) growth was performed in order to avoid the incongruent melting behaviour. Phase-pure Co_2FeAl was synthesized successfully, but both the Cr-containing compositions Co_2CrAl and $Co_2Cr_{0.6}Fe_{0.4}Al$ showed very different secondary phases in terms of structure and composition, with unusual morphologies. We performed a detailed analysis of the secondary phases, and confirmed the presence of a solid-state miscibility gap in the system, which leads to a phase transformation via spinodal decompo-

sition at low temperatures. The evolving secondary phase strongly affected the magnetic properties and the saturation moments were further lowered as compared to the phase-segregated as-cast samples. Based on the knowledge of the secondary phases, and their effect on magnetic properties, almost all the anomalies in literature for the physical properties as well as the instances/observations of chemical instability, have been accounted for. Furthermore, we have argued that a similar phase separation is likely to occur in thin films as well, since the magnetic moments and secondary phases observed in thin films fit well to our results. Thus, we have gained an understanding of the solidification and solid-state phase transformations in $Co_2Cr_{1-x}Fe_xAl$, which has helped us to elucidate on the varied data in the literature coherently.

In order to develop a recipe to obtain a phase-pure sample in a scenario with spinodal decomposition, Co_2CrAl was taken as a test case for further analysis of the immiscibility. Two approaches along different variables, namely temperature and composition, were explored. In the first case, spinodally decomposed FZ-grown Co_2CrAl samples were annealed at different temperatures. We observed that annealing does not help to remove the secondary phase due to the large extent of the immiscibility and the stability of the secondary phase. On the other hand, substitution of Cr with Al in Co_2CrAl was explored so as to move out of the miscibility gap. Off-stoichiometric $Co_2Cr_{1-x}Al_{1+x}$ compositions were grown using FZ technique, and a clear trend was observed in the reduction of the secondary phase with substitution of Cr with Al. $Co_2Cr_{0.4}Al_{1.6}$ was found to be homogeneous and phase-pure as the phase transformation via spinodal decomposition could be avoided. Based on the analysis of both the annealing and off-stoichiometry, we have been able to develop a tentative pseudo-binary phase diagram highlighting the extent of miscibility gap.

We adapted the scheme of off-stoichiometry for the $Co_2Cr_{0.6}Fe_{0.4}Al$ quaternary composition and a homogeneous phase-pure off-stoichiometric $Co_2Cr_{0.4}Fe_{0.4}Al_{1.2}$ sample was successfully grown using the FZ technique. Furthermore, the physical properties, especially the magnetization, matched well with theory, which is unprecedented in the $Co_2Cr_{1-x}Fe_xAl$ system. Band structure calculations showed that the new composition is still a half-metallic ferromagnet as well as it retains all the interesting features of the $Co_2Cr_{0.6}Fe_{0.4}Al$ composition. Thus, we have developed a new potential half-metallic ferromagnet which does not suffer from intrinsic material issues and is promising for potential applications.

In the second part of the thesis, the $Co_2FeAl_{1-x}Si_x$ system was investigated, which, unlike the $Co_2Cr_{1-x}Fe_xAl$ system, exists as a solid solution along the whole series. However, the lack of predicted half-metallic ferromagnetism, both in bulk samples as well as thin films, has been attributed to the challenge of obtaining a fully $L2_1$-ordered sample, and due to which even the observed magnetoresistance is considerably lower than the ideal value for a half-metallic ferromagnet. Therefore, the thrust has been to improve the ordering in the material for which the understanding of the order-disorder transitions is pertinent and highly desirable, but are still under debate. In order

to study the ordering phenomena in $Co_2FeAl_{0.5}Si_{0.5}$, we employed neutron diffraction studies, in contrast to indirect techniques such as calorimetry, commonly used in literature.

Firstly, we demonstrated using room temperature neutron diffraction that the popular annealing procedures employed in the community are not effective towards achieving a high $L2_1$ order. The samples are prone to the formation of antiphase domains which lead to selective peak broadening in the diffraction data. Subsequent high temperature neutron diffraction experiments offered insight in the order-disorder transformation in $Co_2FeAl_{0.5}Si_{0.5}$. The $L2_1$-$B2$ structural transition was found to be quite broad, and the transition was spread over $\sim$100 K, contrary to what is understood in literature.

Line profile analysis of the high temperature data offered a closer look at the evolution of $L2_1$ order and the corresponding order-disorder transition, as well as highlighted the evolution of antiphase domains and the corresponding reduction in selective peak broadening after the *in situ* measurement, where the sample was effectively slow-cooled. Line profile analysis also helped us to develop a better understanding of evolution of antiphase domains and domain boundaries in conjunction with the ordering phenomena.

Based on the *in situ* diffraction experiments, corresponding laboratory experiments were performed where the sample was slowly cooled after annealing at 1400 K. Similar to the *in situ* neutron diffraction, no selective peak broadening was observed. Moreover, the significantly higher $L2_1$ order in the slow-cooled sample was confirmed using nuclear magnetic resonance. In the magnetization data at low temperatures, smearing out of the saturation field in M(H) data was observed and was analysed in the context of the magnetization dynamics of magnetic domains, pinned at the antiphase domain boundaries. High temperature magnetization data on the slow-cooled sample, showed two Curie temperatures, in contrast to the as-cast sample, which we argue are due to the well defined $L2_1$ and $B2$ antiphase domains after slow cooling. However, the calorimetry data on the same sample showed only two signals corresponding to the broad order-disorder transition and the T_C at higher temperature, respectively. The T_C at the lower temperature is understood to be overlapped with the broad signal due to ordering.

In the end, we discussed the various annealing parameters in the light of understanding from the *in situ* neutron diffraction. We highlighted certain relevant disadvantages of quenching of the sample, namely freezing-in of defects from high temperatures as well as generation of additional defects and disorder due to thermal shock. We infer that these effects can be avoided with slow-cooling, and as we have already shown in our results, it leads to large distinct antiphase domains, thereby leading to an improved $L2_1$ order in the sample. The high annealing temperature well above the ordering regime was also found to be advantageous towards obtaining a higher $L2_1$ order in the sample. Finally, an optimized annealing procedure has been designed to obtain an improved $L2_1$ order, which we believe may be applicable to other similar systems, keeping in mind that the material does not undergo any phase transformations at low temperatures.

We believe we have made significant strides towards understanding the interplay between the intrinsic attributes in Heusler compounds, and the physical properties that evolve extrinsically. Developing the awareness about the transformations in the $Co_2Cr_{1-x}Fe_xAl$ system has helped us to coherently explain the inconsistent reports in literature, both in terms of the material issues and physical properties. A detailed investigation of the phase dynamics under different variables has helped us to progress to a new, propitious half-metallic ferromagnet, namely $Co_2Cr_{0.4}Fe_{0.4}Al_{1.2}$. The present work has also considerably advanced our knowledge and understanding of the ordering phenomena in $Co_2FeAl_{0.5}Si_{0.5}$ through a combination of high temperature neutron diffraction and laboratory annealing experiments. A detailed analysis of the diffraction data has brought forth the aspect of antiphase domains and their close relationship with the evolution of order in the material. We have been able to significantly enhance the $L2_1$ order in the material, and demonstrated the advantages of an alternate annealing profile involving slow cooling. The higher ordering in the material would allow us to further enhance the physical properties such as magnetoresistance. Through this work on the material properties of the $Co_2Cr_{1-x}Fe_xAl$ and $Co_2FeAl_{1-x}Si_x$ systems, we have made a significant step towards experimental realization of half-metallic ferromagnetism at elevated temperatures.

Outlook

Regarding the $Co_2Cr_{1-x}Fe_xAl$ system, although the off-stoichiometric sample is very promising, no measurements have been performed as yet to gain further insight about the spin polarization of the sample. We have performed the X-ray magnetic circular dichroism (XMCD) on the off-stoichiometric $Co_2Cr_{0.4}Fe_{0.4}Al_{1.2}$ sample, and the data is presently under analysis. We hope to extract the element-specific moments as well as quantitatively comment on the changes from the stoichiometric sample. Quadratic magneto-optical Kerr effect (QMOKE) measurements are also under way, which should also hint towards the spin polarization in the sample. Moreover, we hope that the fascinating observations of the present study will motivate the thin film community to grow the off-stoichiometric $Co_2Cr_{0.4}Fe_{0.4}Al_{1.2}$ composition, especially regarding detailed measurements of the magnetoresistance and spin polarization.

Although we have gained a deeper insight in the ordering phenomena in $Co_2FeAl_{0.5}Si_{0.5}$, the analysis, we believe, can be further improved. First and foremost, efforts are being made to do a successful Rietveld refinement of the neutron diffraction data taking into account the magnetic structure and microstructural effects. Refinement would allow us to calculate the $L2_1$ order as well as size of antiphase domains taking the magnetic contributions into account. Efforts are also being made to prepare high quality TEM samples through conventional route to obtain topographically smooth sample so that the morphology and distribution of antiphase domains in the slow-cooled sample may

be visualized. Regarding the mechanism of antiphase domain evolution, high temperature positron annihilation experiments may be performed to understand the evolution of the vacancies. Once the sample after neutron diffraction measurements is deactivated in the near future, a detailed analysis of the sample is planned, specially towards confirmation of texture and the extent of $L2_1$ order.

Additionally, quite a few aspects regarding the ordering phenomena need to be verified and there are several questions left unanswered. In order to confirm the regime of order-disorder transition, high temperature synchrotron X-ray measurements are being planned on the same sample on which neutron experiment was performed, in order to complement the neutron diffraction measurements. High resolution calorimetric measurements are planned as well, with the aim to observe the changes in the calorimetric signals of the order-disorder transition and the two magnetic transitions upon thermal cycling.

There are certain aspects related to the order-disorder that we have not been able to address in this work. We have not been able to comment on the convolution of the magnetic and structural ordering in the material. Furthermore, we have not delved into the kinetics of the order-disorder transition, which may throw more light on the ordering mechanism in the material. Study of the kinetics of order-disorder in quaternary systems is interesting as not much literature is available on this topic. However, dedicated experiments at synchrotron and neutron sources are needed for this purpose.

As a concluding remark, we strongly believe that the learnings from this work, from the point of view of phase separation and its avoidance, as well as attainment of the high degree order in the aforementioned quaternary Heusler compounds, may be directly extended to other similar systems having unresolved issues pertaining to their intrinsic attributes and physical properties.

Appendices

A Rietveld refinement of X-ray diffraction data
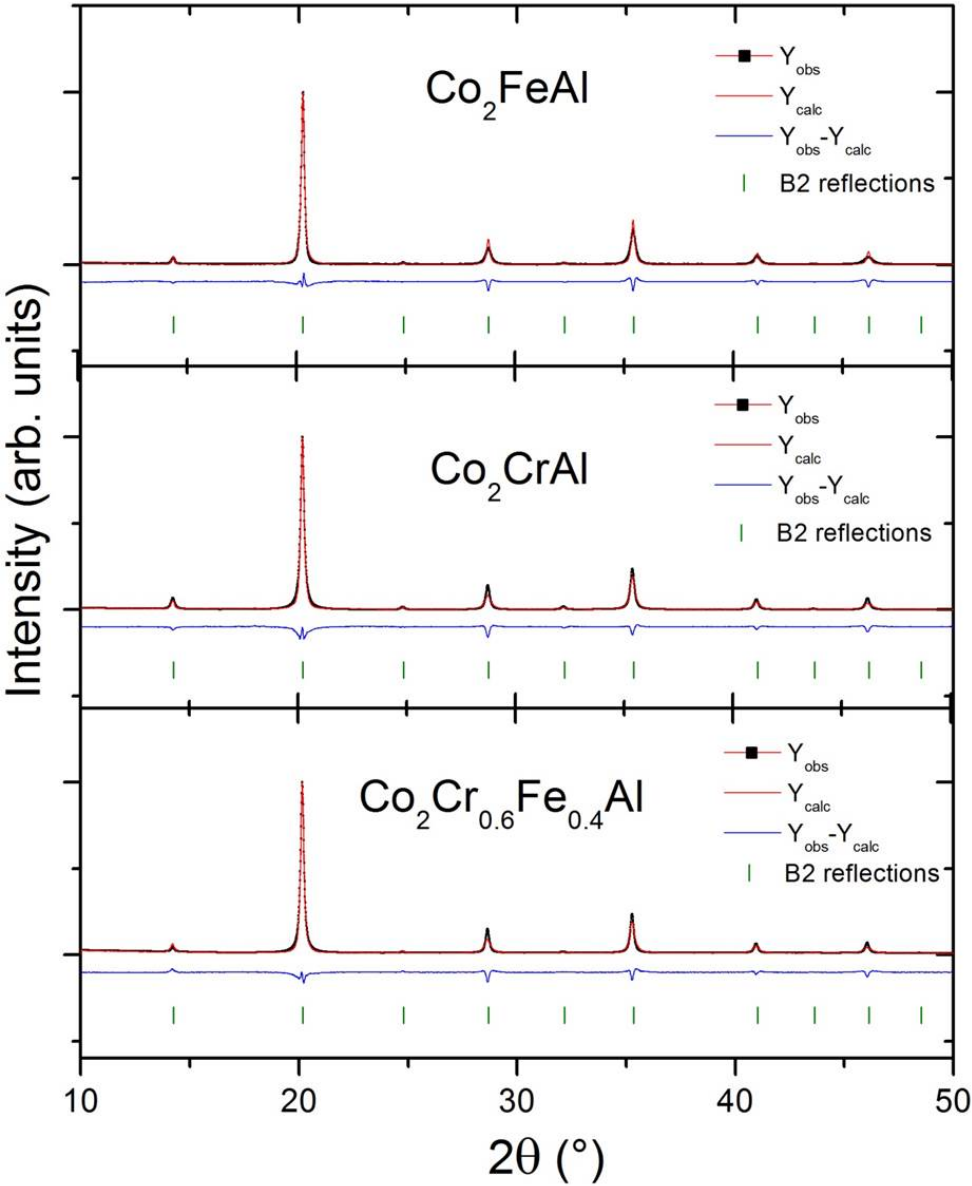
Figure A.1: X-ray diffraction pattern with refinement for as-cast $Co_2Cr_{1-x}Fe_xAl$ samples.

Table A.1: Summary of Rietveld refinement for as-cast $Co_2Cr_{1-x}Fe_xAl$ samples.

Sample	Space group	Lattice (Å)	R_{Bragg}	R_{factor}	χ^2	R_p	R_{wp}	GoF	B_{ov}
Co_2FeAl	$Pm\bar{3}m$	2.863(2)	4.12	9.49	14.1	12.5	16.5	3.8	0.698
Co_2CrAl	$Pm\bar{3}m$	2.866(2)	5.01	4.5	7.8	10.7	13.9	2.7	1.049
$Co_2Cr_{0.6}Fe_{0.4}Al$	$Pm\bar{3}m$	2.867(2)	5.23	7.01	6.46	10.3	14.1	2.5	1.183

Table A.2: Summary of Rietveld refinement for Floating Zone (FZ)-grown $Co_2Cr_{1-x}Fe_xAl$ samples.

Sample	Phase	Space group	Lattice (Å)	Vol. %	R_{Bragg}	Rf_{factor}	χ^2	R_p	R_{wp}	GoF	B_{ov}
Co_2FeAl	CoAl	$Pm\bar{3}m$	a=2.863(2)	100	5.30	6.67	11.8	11.3	15.3	3.4	0.71158
Co_2CrAl	CoAl	$Pm\bar{3}m$	a=2.867(2)	78.3(5)	3.53	3.39					1.24147
	σ-CoCr	$P4_2/mnm$	a=b=8.765(2) c=4.5360(2)	21.7(5)	13.81	17.76	10.7	7.21	9.96	3.3	0.97532
$Co_2Cr_{0.6}Fe_{0.4}Al$	CoAl	$Pm\bar{3}m$	a=2.866(2)	92.6(5)	3.43	6					1.17152
	ϵ-Co	$P6_3/mmc$	a=b=2.529(2) c=4.0725(2)	7.4(5)	11.5	10.1	8.8	7.59	10.8	3	0.92538
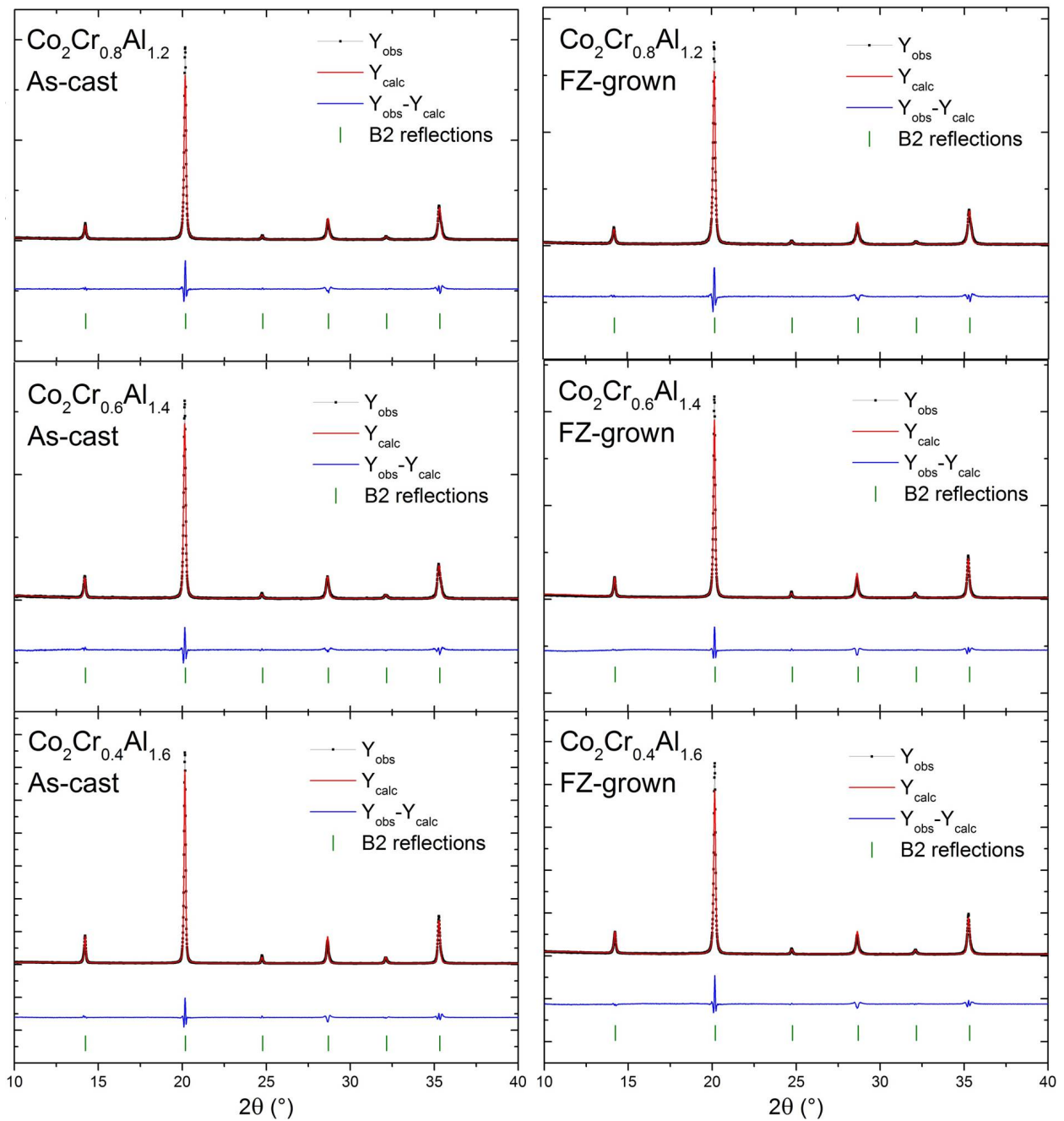
Figure A.2: X-ray diffraction pattern with refinement for as-cast and Floating Zone (FZ)-grown off-stoichiometric $Co_2Cr_{1-x}Al_{1+x}$ samples.

Table A.3: Summary of Rietveld refinement for as-cast and FZ-grown $Co_2Cr_{1-x}Al_{1+x}$ samples.

Composition	Sample	Space group	Lattice (Å)	R_{Bragg}	Rf_{factor}	χ^2	R_p	R_{wp}	GoF	B_{1a} (Cr/Al)	B_{1b} (Co)
$Co_2Cr_{0.8}Al_{1.2}$	As-cast	$Pm\bar{3}m$	2.864(2)	3.09	2.18	2.28	10.2	12.7	1.6	1.034	1.130
	FZ-grown	$Pm\bar{3}m$	2.865(2)	3.06	2.37	2.45	10.4	12.8	1.6	0.888	1.083
$Co_2Cr_{0.6}Al_{1.4}$	As-cast	$Pm\bar{3}m$	2.865(2)	3.51	3.14	1.88	9.21	11.5	1.4	0.819	0.921
	FZ-grown	$Pm\bar{3}m$	2.870(2)	4.01	3.04	4.82	9.25	11.7	2.2	0.755	0.837
$Co_2Cr_{0.4}Al_{1.6}$	As-cast	$Pm\bar{3}m$	a=2.868(2)	1.88	1.40	4.57	7.70	10.2	2.1	0.615	0.662
	FZ-grown	$Pm\bar{3}m$	2.869(2)	5.59	3.40	4.51	8.76	10.9	2.2	0.455	1.028

Table A.4: Summary of Rietveld refinement for as-cast and FZ-grown $Co_2Cr_{0.4}Fe_{0.4}Al_{1.2}$ samples.

Sample	Space group	Lattice (Å)	R_{Bragg}	$R_{ffactor}$	χ^2	R_p	R_{wp}	GoF	B_{1a} (Co)	B_{1b}
As-cast	$Pm\bar{3}m$	2.860(2)	2.37	2.09	1.86	9.40	12.0	1.3	0.732	0.766
FZ-grown	$Pm\bar{3}m$	2.869(2)	3.98	4.26	3.24	7.54	10.0	1.8	0.416	0.316
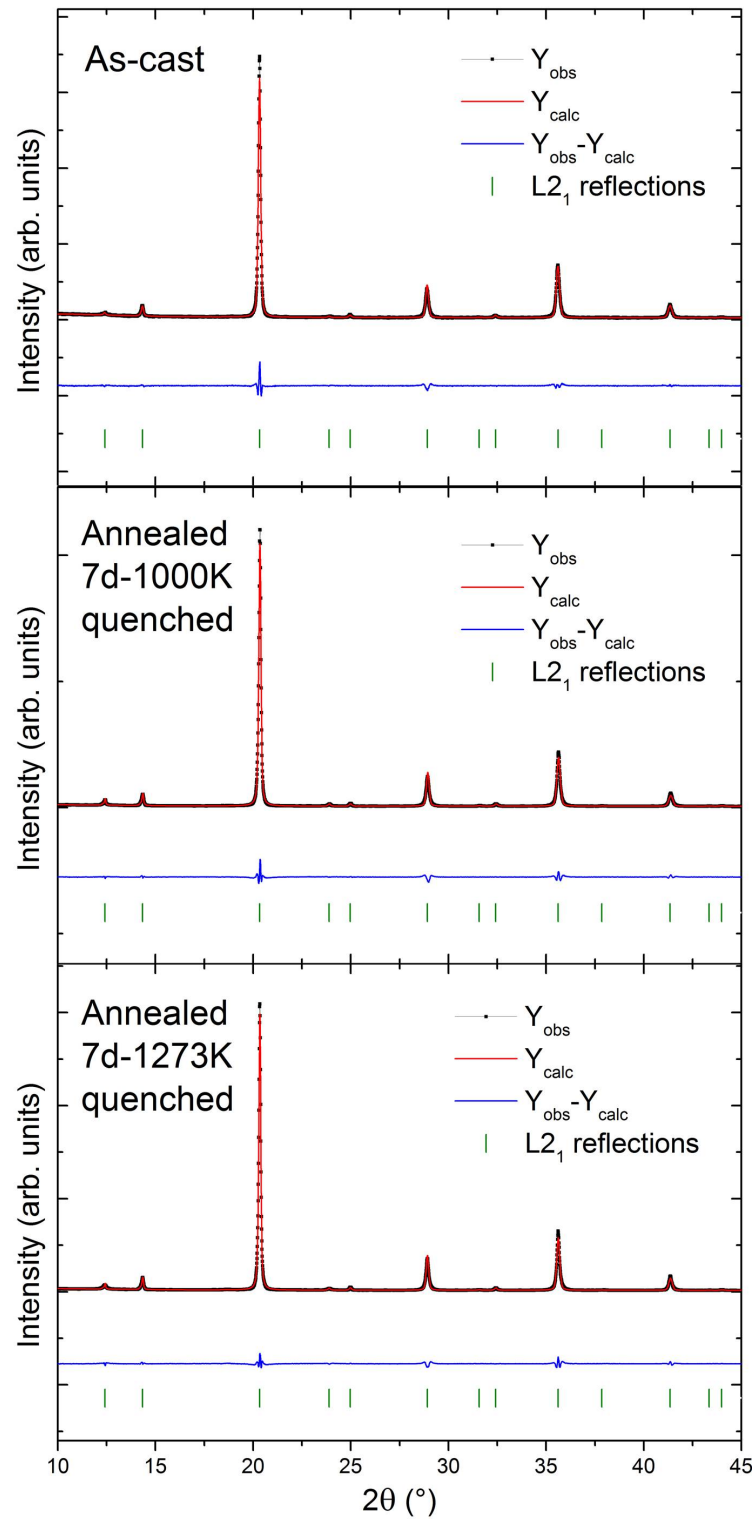
Figure A.3: X-ray diffraction pattern with refinement for as-cast and prior-annealed $Co_2FeAl_{0.5}Si_{0.5}$ samples.

Table A.5: Summary of Rietveld refinement for as-cast and annealed $Co_2FeAl_{0.5}Si_{0.5}$ samples.

Sample	Space group	Lattice (Å)	$L2_1$ (%)	R_{Bragg}	Rf_{factor}	χ^2	R_p	R_{wp}	GoF	B_{8c}	B_{4a}	B_{4b}
As-cast	$Fm\bar{3}m$	5.683(4)	55.1	2.26	3.20	2.10	6.56	8.45	1.4	0.511	0.294	0.462
Anneal-1000K-WQ	$Fm\bar{3}m$	5.681(4)	37.7	2.03	3.04	5.54	6.60	8.86	2.3	0.925	0.908	0.675
Anneal-1273K-WQ	$Fm\bar{3}m$	5.682(4)	41.8	1.78	2.34	6.53	6.49	8.99	2.5	0.908	0.849	0.692
Anneal-1400K-slow	$Fm\bar{3}m$	5.682(4)	20.2	2.14	2.02	1.48	8.19	10.8	1.2	0.583	0.496	0.288

B Background measurements for high temperature neutron diffraction
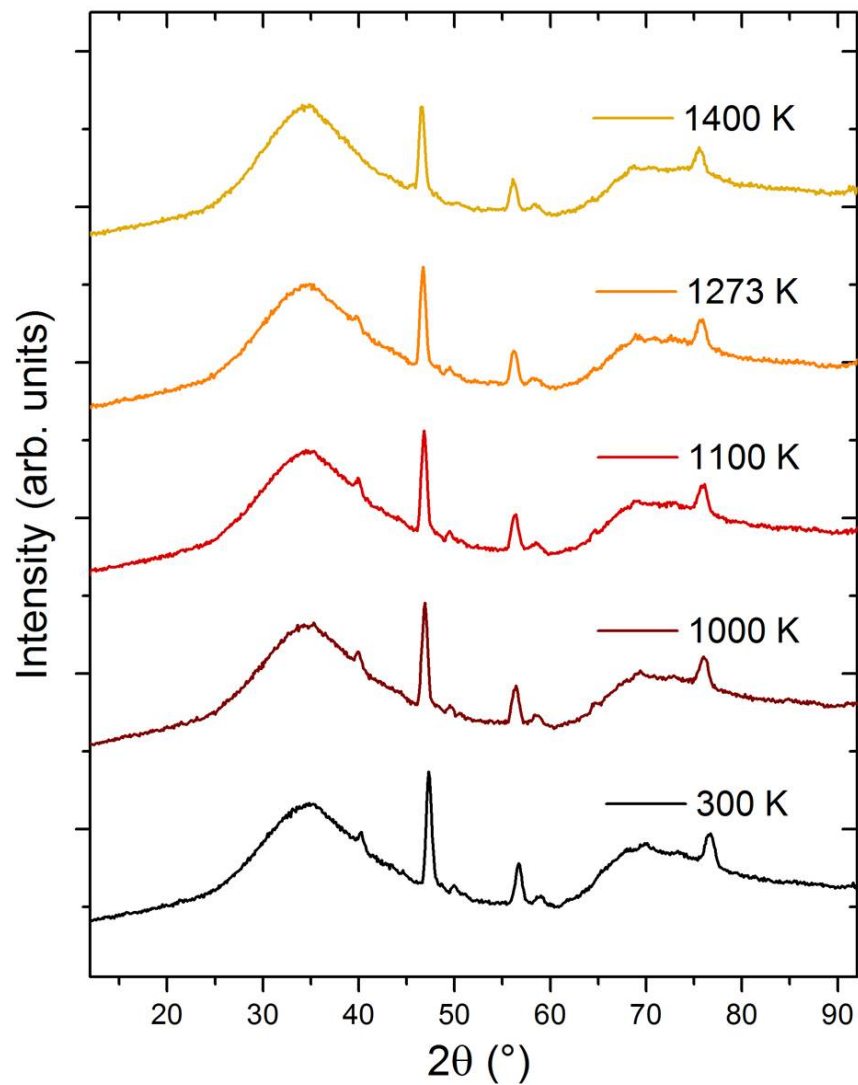
Figure B.1: Background measurements for high temperature neutron diffraction setup (data plotted with an offset along y-axis for better visualization).

Bibliography

[1] K. Ozdogan, B. Aktas, I. Galanakis, and E. Sasioglu. "Influence of mixing the low-valent transition metal atoms (Y, Y*= Cr, Mn, Fe) on the properties of the quaternary Co [Y1-xYx*] Z (Z= Al, Ga, Si, Ge, or Sn) Heusler compounds". *Journal of Applied Physics* 101 2007, 073910.

[2] P. Klaer, M. Kallmayer, C. Blum, T. Graf, J. Barth, B. Balke, G. Fecher, C. Felser, and H. Elmers. "Tailoring the electronic structure of half-metallic Heusler alloys". *Physical Review B* 80 (14) 2009, 144405.

[3] B. Balke, G. Fecher, H. Kandpal, C. Felser, K. Kobayashi, E. Ikenaga, J. Kim, and S. Ueda. "Properties of the quaternary half-metal-type Heusler alloy Co2Mn1-xFexSi". *Physical Review B* 74 (10) 2006, 104405.

[4] C. S. Lue, C. Chen, J. Lin, Y. Yu, and Y. Kuo. "Thermoelectric properties of quaternary Heusler alloys Fe2VAl1-xSix". *Physical Review B* 75 (6) 2007, 064204.

[5] I. Galanakis. "Appearance of half-metallicity in the quaternary Heusler alloys". *Journal of Physics: Condensed Matter* 16 (18) 2004, 3089.

[6] C. Felser, H.-J. Elmers, and G. H. Fecher. "The properties of Co2Cr1-xFexAl Heusler compounds". In: *Half-metallic Alloys*. Ed. by I. Galanakis and P. Dederichs. Lecture Notes in Physics. Springer, 2005, 113–152.

[7] S. Ishida, S. Kawakami, and S. Asano. "Theoretical predict of half-metals in Co-Cr-Fe-Al alloys". *Materials Transactions* 45 (4) 2004, 1065–1069.

[8] T. Nakatani, A. Rajanikanth, Z. Gercsi, Y. Takahashi, K. Inomata, and K. Hono. "Structure, magnetic property, and spin polarization of Co2FeAlxSi1-x Heusler alloys". *Journal of Applied Physics* 102 (3) 2007, 033916–033916.

[9] G. H. Fecher and C. Felser. "Substituting the main group element in cobalt–iron based Heusler alloys: Co2FeAl1- xSix". *Journal of Physics D: Applied Physics* 40 (6) 2007, 1582.

[10] Z. Gercsi and K. Hono. "Ab initio predictions for the effect of disorder and quarternary alloying on the half-metallic properties of selected Co2Fe-based Heusler alloys". *Journal of Physics: Condensed Matter* 19 (32) 2007, 326216.

[11] B. Balke, G. Fecher, and C. Felser. "Structural and magnetic properties of Co2FeAl1-xSix". *Applied Physics Letters* 90 (24) 2007, 242503–242503.

[12] R. Y. Umetsu, A. Okubo, and R. Kainuma. "Magnetic and chemical order-disorder transformations in Co2Fe(Ga1-xSix) and Co2Fe(Al1-ySiy) Heusler alloys". *Journal of Applied Physics* 111 (7) 2012, 073909.

[13] F. Heusler. "Über magnetische Manganlegieungen". *Verhandl. Deutsche Physikalische Gesellschaft* 5 1903, 219.

[14] F. Heusler, W. Stark, and E. Haupt. "Magnetisch-chemische Studien: I. Über die Synthese ferromagnetischer Manganlegierungen". *Verhandl. Deutsche Physikalische Gesellschaft* 5 1903, 220–232.

[15] A. Gray. "Note on Heusler's magnetic alloy of manganese, aluminium, and copper". *Proceedings of the Royal Society of London. Series A, Containing Papers of a Mathematical and Physical Character* 77 (516) 1906, 256–259.

[16] F. Heusler and F. Richarz. "Studien über magnetisierbare manganlegierungen". *Zeitschrift für anorganische Chemie* 61 (1) 1909, 265–279.

[17] J. Young. "XXVIII. The crystal structure of various heusler alloys by the use of X-rays". *The London, Edinburgh, and Dublin Philosophical Magazine and Journal of Science* 46 (272) 1923, 291–305.

[18] L. Harang. "On the crystal structure of the Heusler alloys". *Zeitschrift für Kristallographie* 65 1927, 261–285.

[19] F. Heusler. "Magnetismus und Kristallstruktur bei Manganaluminiumkupfer". *Zeitschrift für anorganische und allgemeine Chemie* 161 (1) 1927, 159–160.

[20] E. Persson. "Röntgenanalyse der Heuslerschen Legierungen". *Naturwissenschaften* 16 (31) 1928, 613–613.

[21] E. Persson. "Über den Bau der heuslerschen legierungen". *Zeitschrift für Physik* 57 (1-2) 1929, 115–133.

[22] H. Potter. "The X-ray structure and magnetic properties of single crystals of Heusler alloy". *Proceedings of the Physical Society* 41 (1) 1928, 135.

[23] A. Bradley and J. Rodgers. "The crystal structure of the Heusler alloys". *Proceedings of the Royal Society of London. Series A, Containing Papers of a Mathematical and Physical Character* 1934, 340–359.

[24] H. Potter. "XVIII. Magneto-resistance and magneto-caloric effects in iron and heusler alloys". *The London, Edinburgh, and Dublin Philosophical Magazine and Journal of Science* 13 (83) 1932, 233–248.

[25] J. Ashworth. "The properties of Heusler's alloy, and the true specific heat of manganese and its discontinuity". *Proceedings of the Physical Society* 48 (3) 1936, 456.

[26] W. Yager and F. Merritt. "Ferromagnetic resonance absorption in Heusler alloy". *Physical Review* 75 (2) 1949, 318.

[27] J. Hedvall and R. Hedin. "Ferromagnetic conversion and catalytic activities IV. Hydrogenation of CO and C2H4 of nickel and CO2-formation from CO of the Heusler alloy MnAlCu2". *Zeitschrift für Physikalische Chemie-Abteilung B-Chemie der Elementarprozesse Aufbau der Materie* 1935.

[28] L. A. Carapella and R. R. Hultgren. "A high magnetic saturation value for the copper-manganese-tin Heusler Alloy, Cu2MnSn". *Physical Review* 59 (11) 1941, 905.

[29] E. Hall. "The silver-based Heusler alloys". *Philosophical Magazine* 4 (42) 1959, 730–744.

[30] D. Morris, R. Preston, and I. Williams. "Search for new Heusler alloys". *Proceedings of the Physical Society* 73 (3) 1959, 520.

[31] D. Oxley, R. Tebble, and K. Williams. "Heusler alloys". *Journal of Applied Physics* 34 (4) 1963, 1362–1364.

[32] P. Webster. "Magnetic and chemical order in Heusler alloys containing cobalt and manganese". *Journal of Physics and Chemistry of Solids* 32 (6) 1971, 1221–1231.

[33] P. J. Webster. "Heusler alloys". *Contemporary Physics* 10 (6) 1969, 559–577.

[34] D. Oxley, R. Tebble, C. Slack, and K. Williams. "An anti-ferromagnetic Heusler alloy, Cu2MnSb". *Nature* 1962.

[35] K. Endo, T. Ohoyama, and R. Kimura. "Antiferromagnetism of CuMnSb". *Journal of the Physical Society of Japan* 25 (3) 1968, 907–908.

[36] C. Felser, L. Wollmann, S. Chadov, G. H. Fecher, and S. S. Parkin. "Basics and prospective of magnetic Heusler compounds". *APL Materials* 3 (4) 2015, 041518.

[37] T. Graf, C. Felser, and S. Parkin. "Simple rules for the understanding of Heusler compounds". *Progress in Solid State Chemistry* 39 (1) 2011, 1–50.

[38] C. Felser and A. Hirohata, eds. *Heusler Alloys*. Springer Series Materials, In press.

[39] T. Graf, F. Casper, J. Winterlik, B. Balke, G. Fecher, and C. Felser. "Crystal structure of new Heusler compounds". *Zeitschrift für anorganische und allgemeine Chemie* 635 (6-7) 2009, 976–981.

[40] Y. Miura, K. Nagao, and M. Shirai. "Atomic disorder effects on half-metallicity of the full-Heusler alloys Co2(Cr1-xFex)Al: A first-principles study". *Physical Review B* 69 (14) 2004, 144413.

[41] J. Soltys. "X-ray diffraction research of the order–disorder transitions in the ternary heusler alloys B2MnAl (B= Cu, Ni, Co, Pd, Pt)". *physica status solidi (a)* 66 (2) 1981, 485–491.

[42] C. Gusenbauer, T. Ashraf, J. Stangl, G. Hesser, T. Plach, A. Meingast, G. Kothleitner, and R. Koch. "Interdiffusion in Heusler film epitaxy on GaAs (001)". *Physical Review B* 83 (3) 2011, 035319.

[43] A. A. Kelly and K. M. Knowles. *Crystallography and crystal defects*. John Wiley & Sons, 2012.

[44] R. Smallman and R. Bishop. *Modern Physical Metallurgy and Materials Engineering*. Reed Educational and Professional Publishing Ltd, 1999.

[45] J. D. Walker and A. P. Grosvenor. "An X-ray absorption spectroscopic study of the metal site preference in Al1-xGaxFeO3". *Journal of Solid State Chemistry* 197 2013, 147–153.

[46] J. Mayer, L. A. Giannuzzi, T. Kamino, and J. Michael. "TEM sample preparation and FIB-induced damage". *MRS Bulletin* 32 (05) 2007, 400–407.

[47] W. Kraus and G. Nolze. "POWDER CELL–a program for the representation and manipulation of crystal structures and calculation of the resulting X-ray powder patterns". *Journal of Applied Crystallography* 29 (3) 1996, 301–303.

[48] H. Rietveld. "A profile refinement method for nuclear and magnetic structures". *Journal of Applied Crystallography* 2 (2) 1969, 65–71.

[49] Y. Takamura, R. Nakane, and S. Sugahara. "Quantitative analysis of atomic disorders in full-Heusler Co2FeSi alloy thin films using x-ray diffraction with Co Kalpha and Cu Kalpha sources". *Journal of Applied Physics* 107 (9) 2010, 09B111–09B111.

[50] G.-f. Li, Y. Honda, H.-x. Liu, K.-i. Matsuda, M. Arita, T. Uemura, M. Yamamoto, Y. Miura, M. Shirai, T. Saito, et al. "Effect of nonstoichiometry on the half-metallic character of Co2MnSi investigated through saturation magnetization and tunneling magnetoresistance ratio". *Physical Review B* 89 (1) 2014, 014428.

[51] R. E. Dinnebier and S. J. Billinge. *Powder diffraction: theory and practice.* Royal society of chemistry, 2008.

[52] B. Ravel, J. O. Cross, M. P. Raphael, V. G. Harris, R. Ramesh, and L. V. Saraf. "Atomic disorder in Heusler Co2MnGe measured by anomalous x-ray diffraction". *Applied Physics Letters* 81 (15) 2002, 2812–2814.

[53] B. A. Collins, Y. Zhong, Y. S. Chu, L. He, and F. Tsui. "Anomalous x-ray diffraction study of disorders in epitaxial films of the Heusler alloy Co2MnGe". *Journal of Vacuum Science & Technology B* 25 (3) 2007, 999–1003.

[54] K. Ziebeck and P. Webster. "A neutron diffraction and magnetization study of Heusler alloys containing Co and Zr, Hf, V or Nb". *Journal of Physics and Chemistry of Solids* 35 (1) 1974, 1–7.

[55] K. R. Kumar, B. Venkateswarlu, P. Babu, and N. H. Kumar. "Neutron diffraction studies on the full heusler alloy Co2FeGe". In: *Solid State Physics: Proceedings of The 56th DAE Solid State Physics Symposium 2011.* Vol. 1447. 1. AIP Publishing. 2012, 1213–1214.

[56] K. R. Kumar, N. H. Kumar, P. Babu, S. Venkatesh, and S. Ramakrishnan. "Investigation of atomic anti-site disorder and ferrimagnetic order in the half-metallic Heusler alloy Mn2VGa". *Journal of Physics: Condensed Matter* 24 (33) 2012, 336007.

[57] B. Ravel, M. Raphael, V. Harris, and Q. Huang. "EXAFS and neutron diffraction study of the Heusler alloy Co2MnSi". *Physical Review B* 65 (18) 2002, 184431.

[58] S. Wurmehl, J. Kohlhepp, H. Swagten, B. Koopmans, M. Wojcik, B. Balke, C. Blum, V. Ksenofontov, G. Fecher, and C. Felser. "Probing the random distribution of half-metallic Co2Mn1-xFexSi Heusler alloys". *Applied Physics Letters* 91 (5) 2007, 052506–052506.

[59] S. Wurmehl, J. T. Kohlhepp, H. J. Swagten, B. Koopmans, C. G. Blum, V. Ksenofontov, H. Schneider, G. Jakob, D. Ebke, and G. Reiss. "Off-stoichiometry in Co2FeSi thin films sputtered from stoichiometric targets revealed by nuclear magnetic resonance". *Journal of Physics D: Applied Physics* 42 (8) 2009, 084017.

[60] S. Rodan, A. Alfonsov, M. Belesi, F. Ferraro, J. Kohlhepp, H. Swagten, B. Koopmans, Y. Sakuraba, S. Bosu, K. Takanashi, et al. "Nuclear magnetic resonance reveals structural evolution upon annealing in epitaxial Co2MnSi Heusler films". *Applied Physics Letters* 102 (24) 2013, 242404.

[61] M. Wójcik, E. Jedryka, H. Sukegawa, T. Nakatani, and K. Inomata. "59Co NMR experiment as a probe of electron doping in Co2FeAl1-xSix Heusler alloys". *Physical Review B* 85 (10) 2012, 100401.

[62] D. Steil, O. Schmitt, R. Fetzer, T. Kubota, H. Naganuma, M. Oogane, Y. Ando, S. Rodan, C. G. Blum, B. Balke, et al. "Impact of local order and stoichiometry on the ultrafast magnetization dynamics of Heusler compounds". *Journal of Physics D: Applied Physics* 48 (16) 2015, 164016.

[63] S. Wurmehl and J. T. Kohlhepp. "NMR spectroscopy on Heusler thin films — A review". In: *SPIN.* Vol. 4. 04. World Scientific. 2014.

[64]   S. Wurmehl, J. T. Kohlhepp, H. J. Swagten, and B. Koopmans. "Hyperfine field distribution in the Heusler compound Co2FeAl probed by 59Co nuclear magnetic resonance". *Journal of Physics D: Applied Physics* 41 (11) 2008, 115007.

[65]   H. C. Kandpal, V. Ksenofontov, M. Wojcik, R. Seshadri, and C. Felser. "Electronic structure, magnetism and disorder in the Heusler compound Co2TiSn". *Journal of Physics D: Applied Physics* 40 (6) 2007, 1587.

[66]   S. Wurmehl, J. Kohlhepp, H. Swagten, and B. Koopmans. "59Co nuclear magnetic resonance study of the local distribution of atoms in the Heusler compound Co2FeAl0.5Si0.5". *Journal of Applied Physics* 111 (4) 2012, 043903–043903.

[67]   S. Wurmehl, J. T. Kohlhepp, H. J. Swagten, B. Koopmans, M. Wójcik, B. Balke, C. G. Blum, V. Ksenofontov, G. H. Fecher, and C. Felser. "Effects of random distribution of Mn, Fe in Co2Mn1-xFexSi Heusler compounds probed by 55Mn nuclear magnetic resonance". *Journal of Applied Physics* 103 (7) 2008, 7D706.

[68]   C.-S. Lue, C. Chen, F.-K. Chiang, and M.-W. Chu. "Annealing effect on the reduction of Fermi-level density of states in CoTiSb: NMR evidence". *Physical Review B* 80 (17) 2009, 174202.

[69]   A. Alfonsov, B. Peters, F. Yang, B. Büchner, and S. Wurmehl. "Nuclear magnetic resonance study of thin Co2FeAl0.5Si0.5 Heusler films with varying thickness". *Physical Review B* 91 (6) 2015, 064421.

[70]   S. Wurmehl, A. Alfonsov, J. Kohlhepp, H. Swagten, B. Koopmans, M. Wójcik, B. Balke, V. Ksenofontov, C. Blum, and B. Büchner. "55Mn NMR study of quaternary half-metallic ferromagnetic Co2Mn1-xFexSi Heusler compounds". *Physical Review B* 88 (13) 2013, 134424.

[71]   K. Oki, M. Hasaka, and T. Eguchi. "Kinetics of Ordering in Fe–Al Alloys". *Transactions of the Japan Institute of Metals* 15 (2) 1974, 143–149.

[72]   D. G. Morris, M. Leboeuf, S. Gunther, and M. Nazmy. "Disordering behaviour of alloys based on Fe3Al". *Philosophical Magazine A* 70 (6) 1994, 1067–1090.

[73]   D. Clegg and R. Buckley. "The disorder-order transformation in iron–cobalt-based alloys". *Metal Science* 7 (1) 1973, 48–54.

[74]   B. Fultz and H. H. Hamdeh. "Kinetics of ordering in metallic alloys". *Hyperfine Interactions* 45 (1-4) 1989, 55–72.

[75]   S. Cupschalk and N. Brown. "Observations of defects in beta brass". *Acta Metallurgica* 15 (5) 1967, 847–856.

[76]   M. Harmelin, S. Lefebvre, M. Bessiere, and Y. Calvayrac. "Study of an order-disorder transition by differential scanning calorimetry". *Thermochimica Acta* 125 1988, 59–78.

[77]   Z. Zhou, J. Du, Y. Yan, H. Yang, and S. Gu. "The order-disorder transition in Fe71Al29 alloy". *Procedia Engineering* 15 2011, 4543–4547.

[78]   S. Parida, N. Anand, R. A. Jat, and S. Kulkarni. "Calorimetric investigation of order–disorder transition in Cu0.6Pd0.4 and Cu0.85Pd0.15 alloys". *Journal of Thermal Analysis and Calorimetry* 112 (1) 2013, 173–177.

[79] R. Ducher, R. Kainuma, I. Ohnuma, and K. Ishida. "Phase equilibria and stability of B2 and L21 ordered phases in the Co–Fe–Ga Heusler alloy system". *Journal of Alloys and Compounds* 437 (1) 2007, 93–101.

[80] K. Kobayashi, R. Kainuma, and K. Ishida. "Phase separation and stability of L21-type phase in Co2(Cr1-xFex)(Ga1-yAly) alloys". *Materials Transactions* 47 (1) 2006, 20–24.

[81] A. Okubo, R. Umetsu, K. Kobayashi, R. Kainuma, and K. Ishida. "Magnetic properties and phase stability of L21 phase in Co2Mn(Ga1-xZx)(Z=Si,Ge, and Sn) Heusler alloys". *Applied Physics Letters* 96 (22) 2010, 222507–222507.

[82] R. Y. Umetsu, K. Kobayashi, A. Fujita, R. Kainuma, and K. Ishida. "Phase stability and magnetic properties of L21 phase in Co2Mn(Al1-xSix) Heusler alloys". *Scripta Materialia* 58 (9) 2008, 723–726.

[83] V. Khovailo, T. Takagi, A. Vasilev, H. Miki, M. Matsumoto, and R. Kainuma. "On order–disorder (L21-B2) phase transition in Ni2+xMn1-xGa Heusler alloys". *physica status solidi (a)* 183 (2) 2001, R1–R3.

[84] K. Srinivas, M. M. Raja, and S. Kamat. "Effect of partial substitution of silicon by other sp-valent elements on structure, magnetic properties and electrical resistivity of Co2FeSi Heusler alloys". *Journal of Alloys and Compounds* 619 2015, 177–185.

[85] R. De Groot, F. Mueller, P. Engen, and K. Buschow. "New class of materials: Half-metallic ferromagnets". *Physical Review Letters* 50 (25) 1983, 2024–2027.

[86] J. Kübler, A. William, and C. Sommers. "Formation and coupling of magnetic moments in Heusler alloys". *Physical Review B* 28 (4) 1983, 1745.

[87] M. M. Rahman, M. Kisaku, T. Kishi, D. Matsunaka, W. A. Diño, H. Nakanishi, and H. Kasai. "Ab initio study of magnetic and electronic properties of Fe-filled single-walled carbon nanotubes". *Journal of Physics: Condensed Matter* 16 (48) 2004, S5755.

[88] M. Katsnelson, V. Y. Irkhin, L. Chioncel, A. Lichtenstein, and R. De Groot. "Half-metallic ferromagnets: From band structure to many-body effects". *Reviews of Modern Physics* 80 (2) 2008, 315.

[89] J. Coey, M. Venkatesan, and M. Bari. "Half-metallic ferromagnets". In: *High Magnetic Fields*. Springer, 2001, 377–396.

[90] C. Felser and G. H. Fecher. *Spintronics: from materials to devices*. Springer Science and Business Media, 2013.

[91] K. Hanssen and P. Mijnarends. "Positron-annihilation study of the half-metallic ferromagnet NiMnSb: theory". *Physical Review B* 34 (8) 1986, 5009.

[92] K. Hanssen, P. Mijnarends, L. Rabou, and K. Buschow. "Positron-annihilation study of the half-metallic ferromagnet NiMnSb: Experiment". *Physical Review B* 42 (3) 1990, 1533.

[93] M. Julliere. "Tunneling between ferromagnetic films". *Physics Letters A* 54 (3) 1975, 225–226.

[94] R. Soulen, J. Byers, M. Osofsky, B. Nadgorny, T. Ambrose, S. Cheng, P. R. Broussard, C. Tanaka, J. Nowak, J. Moodera, J. Barry, and J. Coey. "Measuring the spin polarization of a metal with a superconducting point contact". *Science* 282 (5386) 1998, 85–88.

[95]   S. K. Upadhyay, A. Palanisami, R. N. Louie, and R. Buhrman. "Probing ferromagnets with Andreev reflection". *Physical Review Letters* 81 (15) 1998, 3247.

[96]   M. Jourdan, J. Minár, J. Braun, A. Kronenberg, S. Chadov, B. Balke, A. Gloskovskii, M. Kolbe, H. Elmers, G. Schönhense, et al. "Direct observation of half-metallicity in the Heusler compound Co2MnSi". *Nature Communications* 5 2014.

[97]   D. Ristoiu, J. Nozieres, C. Borca, B. Borca, and P. A. Dowben. "Manganese surface segregation in NiMnSb". *Applied Physics Letters* 76 (17) 2000, 2349–2351.

[98]   D. Ristoiu, J. Nozieres, C. Borca, T. Komesu, H.-K. Jeong, and P. A. Dowben. "The surface composition and spin polarization of NiMnSb epitaxial thin films". *EPL (Europhysics Letters)* 49 (5) 2000, 624.

[99]   I. Zutic, J. Fabian, and S. D. Sarma. "Spintronics: Fundamentals and applications". *Reviews of Modern Physics* 76 (2) 2004, 323.

[100]   G. Binasch, P. Grünberg, F. Saurenbach, and W. Zinn. "Enhanced magnetoresistance in layered magnetic structures with antiferromagnetic interlayer exchange". *Physical Review B* 39 (7) 1989, 4828.

[101]   M. N. Baibich, J. M. Broto, A. Fert, F. N. Van Dau, F. Petroff, P. Etienne, G. Creuzet, A. Friederich, and J. Chazelas. "Giant magnetoresistance of (001) Fe/(001) Cr magnetic superlattices". *Physical Review Letters* 61 (21) 1988, 2472.

[102]   T. Miyazaki and N. Tezuka. "Giant magnetic tunneling effect in Fe/Al2O3/Fe junction". *Journal of Magnetism and Magnetic Materials* 139 (3) 1995, L231–L234.

[103]   J. S. Moodera, L. R. Kinder, T. M. Wong, and R. Meservey. "Large magnetoresistance at room temperature in ferromagnetic thin film tunnel junctions". *Physical Review Letters* 74 (16) 1995, 3273.

[104]   A. Hirohata and K. Takanashi. "Future perspectives for spintronic devices". *Journal of Physics D: Applied Physics* 47 (19) 2014, 193001.

[105]   C. Fong, J. Pask, and L. Yang. *Half-metallic Materials and Their Properties*. Imperial College Press, 2013.

[106]   N. Tezuka, N. Ikeda, F. Mitsuhashi, and S. Sugimoto. "Improved tunnel magnetoresistance of magnetic tunnel junctions with Heusler Co2FeAl0.5Si0.5 electrodes fabricated by molecular beam epitaxy". *Applied Physics Letters* 94 (16) 2009, 162504–162504.

[107]   S. J. Hashemifar, P. Kratzer, and M. Scheffler. "Preserving the half-metallicity at the Heusler alloy Co2MnSi (001) surface: A density functional theory study". *Physical Review Letters* 94 (9) 2005, 096402.

[108]   S. Wurmehl, G. H. Fecher, H. C. Kandpal, V. Ksenofontov, C. Felser, and H.-J. Lin. "Investigation of Co2FeSi: The Heusler compound with highest Curie temperature and magnetic moment". *Applied Physics Letters* 88 2006, 032503.

[109]   G. Fecher, H. Kandpal, S. Wurmehl, J. Morais, H. Lin, H. Elmers, G. Schönhense, and C. Felser. "Design of magnetic materials: the electronic structure of the ordered, doped Heusler compound Co2Cr1-xFexAl". *Journal of Physics: Condensed Matter* 17 (46) 2005, 7237.

[110]   S. Ishida, S. Akazawa, Y. Kubo, and J. Ishida. "Band theory of Co2MnSn, Co2TiSn and Co2TiAl". *Journal of Physics F: Metal Physics* 12 (6) 1982, 1111.

[111] S. Ishida, S. Fujii, S. Kashiwagi, and S. Asano. "Search for half-metallic compounds in Co2MnZ (Z= IIIb, IVb, Vb element)". *Journal of the Physical Society of Japan* 64 (6) 1995, 2152–2157.

[112] J. C. Slater. "The ferromagnetism of nickel". *Physical Review* 49 (7) 1936, 537.

[113] L. Pauling. "The nature of the interatomic forces in metals". *Physical Review* 54 (11) 1938, 899.

[114] J. Kübler. *Theory of itinerant electron magnetism.* Oxford University Press, 2000.

[115] A. Williams, V. Moruzzi, A. Malozemoff, and K. Terakura. "Generalized Slater-Pauling curve for transition-metal magnets". *IEEE Transactions on Magnetics* 19 (5) 1983.

[116] J. Kübler. "First principle theory of metallic magnetism". *Physica B+C* 127 (1) 1984, 257–263.

[117] J. Friedel. "Metallic alloys". *Il Nuovo Cimento (1955-1965)* 7 1958, 287–311.

[118] K. Terakura and J. Kanamori. "A Calculation of the Electronic Structure of an Impurity Atom of Non-Transition Element in Nickel". *Progress of Theoretical Physics* 46 (4) 1971, 1007–1027.

[119] C. Felser, G. Fecher, and B. Balke. "Spintronics: A challenge for materials science and solid-state chemistry". *Angewandte Chemie International Edition* 46 (5) 2007, 668–699.

[120] A. Malozemoff, A. Williams, and V. Moruzzi. ""Band-gap theory" of strong ferromagnetism: Application to concentrated crystalline and amorphous Fe-and Co-metalloid alloys". *Physical Review B* 29 (4) 1984, 1620.

[121] B. Balke, S. Wurmehl, G. Fecher, C. Felser, and J. Kübler. "Rational design of new materials for spintronics: Co2FeZ (Z= Al, Ga, Si, Ge)". *Science and Technology of Advanced Materials* 9 (1) 2008, 014102.

[122] G. Fecher, H. Kandpal, S. Wurmehl, C. Felser, and G. Schonhense. "Slater-Pauling rule and Curie temperature of Co2-based Heusler compounds". *Journal of Applied Physics* 99 (8) 2006, 08J106–08J106.

[123] W. E. Pickett. "Single spin superconductivity". *Physical Review Letters* 77 (15) 1996, 3185.

[124] X. Hu. "Half-Metallic Antiferromagnet as a Prospective Material for Spintronics". *Advanced Materials* 24 (2) 2012, 294–298.

[125] T. Kanomata, K. Shirakawa, and T. Kaneko. "Effect of hydrostatic pressure on the Curie temperature of the Heusler alloys Co2TiAl AND Co2TiGa". *Le Journal de Physique Colloques* 49 (C8) 1988, C8–143.

[126] S. Wurmehl, G. H. Fecher, H. C. Kandpal, V. Ksenofontov, C. Felser, H.-J. Lin, and J. Morais. "Geometric, electronic, and magnetic structure of Co2FeSi: Curie temperature and magnetic moment measurements and calculations". *Physical Review B* 72 (18) 2005, 184434.

[127] Y. Kakehashi and O. Hosohata. "Curie-temperature "Slater-Pauling curve"". *Journal de Physique* 49 (C8) 1988, C8–73–C8–74.

[128] J. Kübler. "Ab initio estimates of the Curie temperature for magnetic compounds". *Journal of Physics: Condensed Matter* 18 (43) 2006, 9795.

[129] J. Kübler, G. Fecher, and C. Felser. "Understanding the trend in the Curie temperatures of Co2-based Heusler compounds: Ab initio calculations". *Physical Review B* 76 (2) 2007, 024414.

[130] J. Kübler. "Curie temperatures of zinc-blende half-metallic ferromagnets". *Physical Review B* 67 (22) 2003, 220403.

[131] P. Webster and M. Ramadan. "Magnetic order in palladium-based Heusler alloys. Part 3: The effects of disorder in Pd2MnIn1-xSn and Pd2MnIn1-ySb". *Journal of Magnetism and Magnetic Materials* 20 1980, 271–276.

[132] H. Ebert and G. Schütz. "Theoretical and experimental study of the electronic structure of PtMnSb". *Journal of Applied Physics* 69 (8) 1991, 4627–4629.

[133] D. Orgassa, H. Fujiwara, T. Schulthess, and W. Butler. "First-principles calculation of the effect of atomic disorder on the electronic structure of the half-metallic ferromagnet NiMnSb". *Physical Review B* 60 (19) 1999, 13237.

[134] D. Orgassa, H. Fujiwara, T. Schulthess, and W. Butler. "Disorder dependence of the magnetic moment of the half-metallic ferromagnet NiMnSb from first principles". *Journal of Applied Physics* 87 (9) 2000, 5870–5871.

[135] P. J. Hasnip, C. H. Loach, J. H. Smith, M. I. Probert, D. Gilks, J. Sizeland, L. Lari, J. Sagar, K. Yoshida, M. Oogane, et al. "The effect of cobalt-sublattice disorder on spin polarisation in Co2FexMn1-xSi Heusler alloys". *Materials* 7 (3) 2014, 1473–1482.

[136] I. Galanakis, K. Ozdogan, B. Aktas, and E. Sasioglu. "Effect of doping and disorder on the half metallicity of full Heusler alloys". *Applied Physics Letters* 89 (4) 2006, 042502.

[137] Y. Kudryavtsev, V. Uvarov, V. Oksenenko, Y. Lee, J. Kim, Y. Hyun, K. Kim, J. Rhee, and J. Dubowik. "Effect of disorder on various physical properties of Co2CrAl Heusler alloy films: Experiment and theory". *Physical Review B* 77 (19) 2008, 195104.

[138] J. Dubowik, I. Goscianska, Y. Kudryavtsev, and V. Oksenenko. "Structure and magnetism of Co2CrAl Heusler alloy films". *Materials Science-Poland* 25 (4) 2007, 1281–1287.

[139] S. Lee, T. Lee, P. Blaha, and K. Schwarz. "Magnetic and half-metallic properties of the full-Heusler alloys Co2TiX (X= Al, Ga; Si, Ge, Sn; Sb)". *Journal of Applied Physics* 97 (10) 2005, 10C307–10C307.

[140] S. Picozzi, A. Continenza, and A. Freeman. "Role of structural defects on the half-metallic character of Co2MnGe and Co2MnSi Heusler alloys". *Physical Review B* 69 (9) 2004, 094423.

[141] S. Picozzi, A. Continenza, and A. Freeman. "Role of Mn antisite defects on half-metallicity in Co2MnSi Heusler alloy". *Journal of Magnetism and Magnetic Materials* 272 2004, 315–316.

[142] S. Picozzi, A. Continenza, and A. Freeman. "Spin injection at Heusler/semiconductor interfaces: First-principles determination of potential discontinuity and half-metallicity". *Journal of Applied Physics* 94 (7) 2003, 4723–4725.

[143] K. Ozdogan and I. Galanakis. "Effect of order on the half-metallic gap in Heusler compounds". *Journal of Applied Physics* 110 (7) 2011, 076101–076101.

[144] M. Raphael, B. Ravel, Q. Huang, M. Willard, S. Cheng, B. Das, R. Stroud, K. Bussmann, J. Claassen, and V. Harris. "Presence of antisite disorder and its characterization in the predicted half-metal Co2MnSi". *Physical Review B* 66 (10) 2002, 104429.

[145] Y. Huang, M. Karppinen, H. Yamauchi, and J. Goodenough. "Systematic studies on effects of cationic ordering on structural and magnetic properties in Sr2FeMoO6". *Physical Review B* 73 (10) 2006, 104408.

[146] E. V. Vidal, H. Schneider, and G. Jakob. "Influence of disorder on anomalous Hall effect for Heusler compounds". *Physical Review B* 83 (17) 2011, 174410.

[147] C. Venkatesh, V. Srinivas, V. Rao, S. Srivastava, and P. S. Babu. "Effect of site disorder on the electronic properties of Fe2VAl Heusler alloy". *Journal of Alloys and Compounds* 577 2013, 417–425.

[148] B. Suh, S. Baek, and J. Rhee. "Antisite disorder and superparamagnetism in Heusler-like Fe2VAl: A 51V and 27Al NMR study". *Journal of Korean Physical Society* 28 (2) 2006, 288–292.

[149] Y. Kudryavtsev, V. Oksenenko, N. Lee, Y. Lee, J. Rhee, and J. Dubowik. "Effect of structural disorder on some physical properties of the Cu2MnAl Heusler alloy films". *Journal of Applied Physics* 97 (11) 2005, 113903.

[150] Y. Kudryavtsev, Y. Lee, and J. Rhee. "Dependence of the optical and magneto-optical properties and electronic structures on the atomic order in Ni2MnIn Heusler alloys". *Physical Review B* 69 (19) 2004, 195104.

[151] M. Zhou, L. Chen, W. Zhang, and C. Feng. "Disorder scattering effect on the high-temperature lattice thermal conductivity of TiCoSb-based half-Heusler compounds". *Journal of Applied Physics* 98 (1) 2005, 013708.

[152] P. Kharel, Y. Huh, N. Al-Aqtash, V. Shah, R. Sabirianov, R. Skomski, and D. Sellmyer. "Structural and magnetic transitions in cubic Mn3Ga". *Journal of Physics: Condensed Matter* 26 (12) 2014, 126001.

[153] A. Hirohata, S. Ladak, N. Aley, and G. Hix. "Si segregation in polycrystalline Co2MnSi films with grain-size control". *Applied Physics Letters* 95 (25) 2009, 252506.

[154] P. Neibecker, M. Leitner, G. Benka, and W. Petry. "Increasing the achievable state of order in Ni-based Heusler alloys via quenched-in vacancies". *Applied Physics Letters* 105 (26) 2014, 261904.

[155] K. Ozdogan, E. Sasioglu, and I. Galanakis. "Vacancy-induced minority-spin states in half-metallic Heusler alloys". *physica status solidi (RRL)-Rapid Research Letters* 1 (5) 2007, 184–186.

[156] A. Slebarski, A. Jezierski, M. Neumann, and S. Plogmann. "Influence of vacancies on the electronic structure of Co ZrSn Heusler alloys". *The European Physical Journal B-Condensed Matter and Complex Systems* 12 (4) 1999, 519–523.

[157] A. Jezierski. "Effect of vacancies on the electronic structure of PdxTiSn alloys". *Journal of Physics: Condensed Matter* 12 (37) 2000, 8127.

[158] Y. Chen, B. Wu, H. Yuan, Y. Feng, and H. Chen. "The defect-induced changes of the electronic and magnetic properties in the inverse Heusler alloy Ti2CoAl". *Journal of Solid State Chemistry* 221 2015, 311–317.

[159] Q.-L. Fang, J.-M. Zhang, K.-W. Xu, and V. Ji. "The effect of defects on the magnetic properties and spin polarization of Ti 2 FeAl Heusler alloy". *Journal of Magnetism and Magnetic Materials* 351 2014, 25–28.

[160]   B. A. Alhaj and B. Hamad. "The effect of defects on the electronic and magnetic properties of Co2CrAl Heusler alloy". *Journal of Physics and Chemistry of Solids* 74 (2) 2013, 265–271.

[161]   N. Mahmoud, J. Khalifeh, B. Hamad, and A. Mousa. "The effect of defects on the electronic and magnetic properties of the Co2VSn full Heusler alloy: Ab-initio calculations". *Intermetallics* 33 2013, 33–37.

[162]   B. Hamad and Q.-M. Hu. "The effect of defects on the electronic and magnetic properties of Fe2MnSi Heusler alloy". *physica status solidi (b)* 248 (12) 2011, 2893–2898.

[163]   L. Jodin, J. Tobola, P. Pecheur, H. Scherrer, and S. Kaprzyk. "Effect of substitutions and defects in half-Heusler FeVSb studied by electron transport measurements and KKR-CPA electronic structure calculations". *Physical Review B* 70 (18) 2004, 184207.

[164]   Q. F. Li, H. F. Zhao, X. Zhong, and J. L. Su. "Co doping effects on structural, electronic and magnetic properties in Mn2VGa". *Journal of Magnetism and Magnetic Materials* 324 (7) 2012, 1463–1467.

[165]   B. Hamad, J. Khalifeh, I. Abu Aljarayesh, C. Demangeat, H.-B. Luo, and Q.-M. Hu. "The electronic structure and spin polarization of Fe3-xMnxSi and Fe3-yMnSi y alloys". *Journal of Applied Physics* 107 (9) 2010, 093911–093911.

[166]   I. Galanakis, K. Ozdogan, and E. Sasioglu. "Role of defects and disorder in the half-metallic full-Heusler compounds". In: *Advances in Nanoscale Magnetism.* Springer, 2009, 1–19.

[167]   Z. Zhu, Y. Cheng, and U. Schwingenschlögl. "Vacancy induced half-metallicity in half-Heusler semi-conductors". *Physical Review B* 84 (11) 2011, 113201.

[168]   Y. W. Chai, K. Yoshioka, and Y. Kimura. "Intrinsic point defects in thermoelectric half-Heusler alloys". *Scripta Materialia* 83 2014, 13–16.

[169]   A. Nayak, M. Nicklas, S. Chadov, C. Shekhar, Y. Skourski, J. Winterlik, and C. Felser. "Large zero-field cooled exchange-bias in bulk Mn2PtGa". *Physical Review Letters* 110 (12) 2013, 127204.

[170]   A. K. Nayak, M. Nicklas, S. Chadov, P. Khuntia, C. Shekhar, A. Kalache, M. Baenitz, Y. Skourski, V. K. Guduru, A. Puri, et al. "Design of compensated ferrimagnetic Heusler alloys for giant tunable exchange bias". *Nature Materials* 2015.

[171]   H. S. Nair, T. Chatterji, and A. M. Strydom. "Antisite disorder-induced exchange bias effect in multiferroic Y2CoMnO6". *Applied Physics Letters* 106 (2) 2015, 022407.

[172]   S. K. Bux, J.-P. Fleurial, and R. B. Kaner. "Nanostructured materials for thermoelectric applications". *Chemical Communications* 46 (44) 2010, 8311–8324.

[173]   A. Minnich, M. Dresselhaus, Z. Ren, and G. Chen. "Bulk nanostructured thermoelectric materials: current research and future prospects". *Energy and Environmental Science* 2 (5) 2009, 466–479.

[174]   J.-F. Li, W.-S. Liu, L.-D. Zhao, and M. Zhou. "High-performance nanostructured thermoelectric materials". *NPG Asia Materials* 2 (4) 2010, 152–158.

[175]   M. Schwall and B. Balke. "Phase separation as a key to a thermoelectric high efficiency". *Physical Chemistry Chemical Physics* 15 (6) 2013, 1868–1872.

[176]   S. Paul, A. Kundu, B. Sanyal, and S. Ghosh. "Anti-site disorder and improved functionality of Mn2NiX (X= Al, Ga, In, Sn) inverse Heusler alloys". *Journal of Applied Physics* 116 (13) 2014, 133903.

[177] S. Singh, I. Glavatskyy, and C. Biswas. "The influence of quench atomic disorder on the magnetocaloric properties of Ni–Co–Mn–In alloys". *Journal of Alloys and Compounds* 601 2014, 108–111.

[178] V. Alijani, J. Winterlik, G. H. Fecher, and C. Felser. "Tuning the magnetism of the Heusler alloys Mn3-xCoxGa from soft and half-metallic to hard-magnetic for spin-transfer torque applications". *Applied Physics Letters* 99 (22) 2011, 222510.

[179] S. Chadov, S. W. D'Souza, L. Wollmann, J. Kiss, G. H. Fecher, and C. Felser. "Chemical disorder as an engineering tool for spin polarization in Mn3Ga-based Heusler systems". *Physical Review B* 91 9 2015, 094203.

[180] J. W. Gibbs. *Scientific Papers: Thermodynamics.* Vol. 1. Dover Publications, 1961.

[181] F. C. Campbell. *Phase diagrams: Understanding the basics.* ASM International, 2012.

[182] A. Bondar'. "Aluminium-Cobalt-Chromium". In: *Ternary Alloys.* Vol. 4. VCH, 1991, 159–167.

[183] D. R. F. West and N. Saunders. *Ternary phase diagrams in Materials Science.* Maney for the Institute of Materials, 2002.

[184] A. Kodentsov, G. Bastin, and F. Van Loo. "The diffusion couple technique in phase diagram determination". *Journal of Alloys and Compounds* 320 (2) 2001, 207–217.

[185] J.-C. Zhao. "The diffusion-multiple approach to designing alloys". *Annual Review of Material Research* 35 2005, 51–73.

[186] J.-C. Zhao. *Methods for phase diagram determination.* Elsevier, 2011.

[187] R. Hermann, G. Behr, G. Gerbeth, J. Priede, H.-J. Uhlemann, F. Fischer, and L. Schultz. "Magnetic field controlled FZ single crystal growth of intermetallic compounds". *Journal of Crystal Growth* 275 (1) 2005, e1533–e1538.

[188] T. Ito, T. Ushiyama, Y. Yanagisawa, Y. Tomioka, I. Shindo, and A. Yanase. "Laser-diode-heated floating zone (LDFZ) method appropriate to crystal growth of incongruently melting materials". *Journal of Crystal Growth* 363 2013, 264–269.

[189] S. Koohpayeh, D. Fort, A. Bradshaw, and J. Abell. "Thermal characterization of an optical floating zone furnace: A direct link with controllable growth parameters". *Journal of Crystal Growth* 311 (8) 2009, 2513–2518.

[190] A. Balbashov and S. Egorov. "Apparatus for growth of single crystals of oxide compounds by floating zone melting with radiation heating". *Journal of Crystal Growth* 52 1981, 498 –504.

[191] *Internal report, Reseach Technology Division.* Leibniz-Institut für Festkörper- und Werkstoffforschung Dresden. 2008.

[192] G. Behr, W. Löser, N. Wizent, P. Ribeiro, M.-O. Apostu, and D. Souptel. "Influence of heat distribution and zone shape in the floating zone growth of selected oxide compounds". *Journal of Materials Science* 45 (8) 2010, 2223–2227.

[193] G. Behr, W. Löser, D. Souptel, G. Fuchs, I. Mazilu, C. Cao, A. Köhler, L. Schultz, and B. Büchner. "Crystal growth of rare earth-transition metal borocarbides and silicides". *Journal of Crystal Growth* 310 (7) 2008, 2268–2276.

[194]   *Annual internal report.* Leibniz-Institut für Festkörper- und Werkstoffforschung Dresden. 2008.

[195]   N. Wizent, N. Leps, G. Behr, R. Klingeler, B. Büchner, and W. Löser. "The effect of process parameters on floating zone crystal growth of selected cuprates". *Journal of Crystal Growth* 401 2014, 596–600.

[196]   N. Wizent. "Hochdruckkristallzüchtung ausgewählter Oxidverbindungen". PhD thesis. Technische Universität Dresden, 2009.

[197]   H. B. Cao, Z. Y. Zhao, M. Lee, E. S. Choi, M. A. McGuire, B. C. Sales, H. D. Zhou, J.-Q. Yan, and D. G. Mandrus. "High pressure floating zone growth and structural properties of ferrimagnetic quantum paraelectric BaFe12O19". *APL Materials* 3 (6), 062512 2015.

[198]   J. Rodriguez-Carjaval. "An Introduction To The Program Fullprof" 2001.

[199]   T. Block, S. Wurmehl, C. Felser, and J. Windeln. "Powder magnetoresistance of Co2Cr0.6Fe0.4Al/Al2O3 powder compacts". *Applied Physics Letters* 88 (20) 2006, 202504–202504.

[200]   C. Herbort, E. A. Jorge, and M. Jourdan. "Morphology induced magnetoresistance enhancement of tunneling junctions with the Heusler electrode Co2Cr0.6Fe0.4Al". *Applied Physics Letters* 94 (14) 2009, 142504–142504.

[201]   E. Clifford, M. Venkatesan, R. Gunning, and J. Coey. "Magnetoresistance in point contacts of the Heusler alloy Co2Cr0.6Fe0.4Al". *Solid State Communications* 131 (1) 2004, 61–64.

[202]   J. De Teresa, D. Serrate, R. Córdoba, and S. Yusuf. "Correlation between the synthesis conditions and the compositional and magnetic properties of Co2(Cr1-xFex)Al Heusler alloys". *Journal of Alloys and Compounds* 450 (1) 2008, 31–38.

[203]   S. Wurmehl, G. Fecher, K. Kroth, F. Kronast, H. Dürr, Y. Takeda, Y. Saitoh, K. Kobayashi, H. Lin, G. Schönhense, and C. Felser. "Electronic structure and spectroscopy of the quaternary Heusler alloy Co2Cr1-xFexAl". *Journal of Physics D: Applied Physics* 39 (5) 2006, 803.

[204]   T. Block, C. Felser, G. Jakob, J. Ensling, B. Mühling, P. Gütlich, and R. Cava. "Large negative magnetoresistance effects in Co2Cr0.6Fe0.4Al". *Journal of Solid State Chemistry* 176 (2) 2003, 646–651.

[205]   H. Elmers, G. Fecher, D. Valdaitsev, S. Nepijko, A. Gloskovskii, G. Jakob, G. Schönhense, S. Wurmehl, T. Block, C. Felser, et al. "Element-specific magnetic moments from core-absorption magnetic circular dichroism of the doped Heusler alloy Co2Cr0.6Fe0.4Al". *Physical Review B* 67 (10) 2003, 104412.

[206]   S. Okamura, A. Miyazaki, N. Tezuka, S. Sugimoto, and K. Inomata. "Epitaxial growth of ordered Co2(Cr1-xFex)Al full-Heusler alloy films on single crystal substrates". *Materials Transactions* 47 (1) 2006, 15–19.

[207]   K. Inomata, S. Okamura, A. Miyazaki, M. Kikuchi, N. Tezuka, M. Wojcik, and E. Jedryka. "Structural and magnetic properties and tunnel magnetoresistance for Co2(Cr,Fe)Al and Co2FeSi full-Heusler alloys". *Journal of Physics D: Applied Physics* 39 (5) 2006, 816.

[208]   S. Okamura, R. Goto, S. Sugimoto, N. Tezuka, and K. Inomata. "Structural, magnetic, and transport properties of full-Heusler alloy Co2Cr1-xFexAl thin films". *Journal of Applied Physics* 96 (11) 2004, 6561–6564.

[209] M. Zhang, A. L. Wolf, L. Zhang, O. Tegus, E. Bruck, G. Wu, and F. R. de Boer. "The structure, magnetism, and electrical-transport properties of the Heusler alloys Co2Cr1-xFexAl". *Journal of Applied Physics* 97 (10) 2005, 10C301–10C301.

[210] R. Kelekar and B. Clemens. "Epitaxial growth of the Heusler alloy Co2Cr1-xFexAl". *Journal of Applied Physics* 96 2004, 540–543.

[211] K. Kobayashi, R. Umetsu, R. Kainuma, K. Ishida, T. Oyamada, A. Fujita, and K. Fukamichi. "Phase separation and magnetic properties of half-metal-type Co2Cr1-xFexAl alloys". *Applied physics letters* 85 (20) 2004, 4684–4686.

[212] S. Karthik, A. Rajanikanth, Y. Takahashi, T. Ohkubo, and K. Hono. "Microstructure and spin polarization of quaternary Co2Cr1-xVxAl, Co2V1-xFexAl and Co2Cr1-xFexAl Heusler alloys". *Acta Materialia* 55 (11) 2007, 3867–3874.

[213] C. Felser, B. Heitkamp, F. Kronast, D. Schmitz, S. Cramm, H. Dürr, H. Elmers, G. Fecher, S. Wurmehl, T. Block, et al. "Investigation of a novel material for magnetoelectronics: Co2Cr0.6Fe0.4Al". *Journal of Physics: Condensed Matter* 15 (41) 2003, 7019.

[214] R. Kelekar and B. Clemens. "Existence of a second A3 phase in B2 epitaxial Co2Cr1-xFexAl thin films". *Solid State Communications* 145 (4) 2008, 223–226.

[215] Y. Takahashi, T. Ohkubo, K. Hono, S. Okamura, N. Tezuka, and K. Inomata. "Transmission electron microscopy of Co2Cr1-xFexAl sputtered films and their magnetic tunneling junctions". *Journal of Magnetism and Magnetic Materials* 313 (2) 2007, 378–382.

[216] G. Jakob, F. Casper, V. Beaumont, S. Falk, N. Auth, H.-J. Elmers, C. Felser, and H. Adrian. "Thin epitaxial films of the Heusler compound Co2Cr0.6Fe0.4Al". *Journal of Magnetism and Magnetic Materials* 290 2005, 1104–1107.

[217] K. Matsuda, T. Kasahara, T. Marukame, T. Uemura, and M. Yamamoto. "Epitaxial growth of Co2Cr0.6Fe0.4Al Heusler alloy thin films on MgO (001) substrates by magnetron sputtering". *Journal of Crystal Growth* 286 (2) 2006, 389–393.

[218] A. Omar, M. Dimitrakopoulou, C. Blum, H. Wendrock, S. Rodan, S. Hampel, W. Loser, B. Buchner, and S. Wurmehl. "Phase dynamics and growth of Co2Cr1-xFexAl Heusler compounds: A key to understand their anomalous physical properties". *Crystal Growth Design* 13 (9) 2013, 3925–3934.

[219] J. Thomas, J. Schumann, M. Dománková, and T. Gemming. "Microstructure and phase formation of Heusler thin film compounds: Dedicated to Professor Dr. Dr. hc Klaus Wetzig on the occasion of his 65th birthday". *Zeitschrift für Metallkunde* 96 (9) 2005, 1015–1023.

[220] D. Seol, S. Hu, Y. Li, J. Shen, K. Oh, and L. Chen. "Computer simulation of spinodal decomposition in constrained films". *Acta Materialia* 51 (17) 2003, 5173–5185.

[221] T. Kozakai and T. Miyazaki. "Experimental and theoretical studies on phase separations in the Fe-Al-Co ordering alloy system". *Journal of Materials Science* 29 (3) 1994, 652–659.

[222] T. Kozakai, T. Koyama, and M. Doi. "Spinodal decomposition in Fe-rich Fe-Co-Al ordered alloy". In: *The Fourth Pacific Rim International Conference on Advanced Materials and Processing*. Japan Institute of Metals, 2001.

[223] T. Kozakai, T. Koyama, and M. Doi. "Effect of Ti addition on the phase equilibria in Fe-Al-Co ordering system and A2+B2+D03 three-phase field". In: *The Fourth Pacific Rim International Conference on Advanced Materials and Processing.* Japan Institute of Metals, 2001.

[224] T. Kozakai, T. Koyama, and M. Doi. "Phase decomposition and precipitation of metastable A2 phase in B2 ordered Co–Al–Fe alloys". *Zeitschrift für Metallkunde* 97 (3) 2006, 266–272.

[225] C. Colinet, G. Inden, and R. Kikuchi. "CVM Calculation of the phase diagram of b.c.c. Fe-Co-Al". *Acta Metallurgica et Materialia* 41 1993, 1109–1118.

[226] E. Moskvitina, V. Kuznetsov, and L. Guzei. "Refinement of the Co-Cr-Al phase diagram". *Moscow University Chemistry Bulletin* 47 (4) 1992, 70–71.

[227] B. Livshits and N. Myuller. "Investigation of the phase equilibria in the system Cobalt-Chromium-Aluminum". In: *Nauchn. Dokl. Vyssh. Shk. Metall.* Vol. 1. 1958, 201–206.

[228] D. A. Young. *Phase diagrams of the elements.* University of California, Lawrence Livermore Laboratory, 1975.

[229] C.-S. Yoo, P. Söderlind, and H. Cynn. "The phase diagram of cobalt at high pressure and temperature: the stability of-cobalt and new-cobalt". *Journal of Physics: Condensed Matter* 10 (20) 1998, L311.

[230] M. Sagoi, R. Nishikawa, and T. Suzuki. "Microstructural inhomogeneity and magnetic properties in Co-Cr sputtered films". *IEEE Transactions on Magnetics* 22 (5) 1986, 1335–1340.

[231] K. Ishida and T. Nishikawa. "Cobalt-Chromium". In: *ASM Binary Alloy Phase Diagram Database.* ASM International, 1996.

[232] L. Wilde, J. Schumann, J. Thomas, I. Bächer, N. Mattern, T. Gemming, R. Kaltofen, D. Elefant, and S. Oswald. "Microstructure of Co2Cr1-xFexAl thin films for magneto-electronic applications". *Thin Solid Films* 515 (17) 2007, 6781–6790.

[233] A. Omar, C. G. Blum, W. Löser, B. Büchner, and S. Wurmehl. "Effect of annealing on spinodally decomposed Co2CrAl grown via floating zone technique". *Journal of Crystal Growth* 401 2014, 617–621.

[234] Q. Ran and. MSIT®. "The Al-Co binary system". In: *MSI Eureka in SpringerMaterials.* Ed. by G. Effenberg. MSI Materials Science International Services GmbH, 1991.

[235] H. Ebert, D. Koedderitzsch, and J. Minar. "Calculating condensed matter properties using the KKR-Green's function method—recent developments and applications". *Reports on Progress in Physics* 74 (9) 2011, 096501.

[236] S. Vosko, L. Wilk, and M. Nusair. "Accurate spin-dependent electron liquid correlation energies for local spin density calculations: a critical analysis". *Canadian Journal of Physics* 58 (8) 1980, 1200–1211.

[237] S. Ami and K. Maki. "Pinning effect due to periodic variation of impurity concentration in type II superconductors". *Progress of Theoretical Physics* 53 (1) 1975, 1–20.

[238] C. Blum, C. Jenkins, J. Barth, C. Felser, S. Wurmehl, G. Friemel, C. Hess, G. Behr, B. Büchner, A. Reller, et al. "Highly ordered, half-metallic Co2FeSi single crystals". *Applied Physics Letters* 95 (16) 2009, 161903.

[239] J. Kondo. "Resistance minimum in dilute magnetic alloys". *Progress of Theoretical Physics* 32 (1) 1964, 37–49.

[240] W. Meissner and B. Voigt. "Messungen mit Hilfe von flüssigem Helium XI Widerstand der reinen Metalle in tiefen Temperaturen". *Annalen der Physik* 399 (8) 1930, 892–936.

[241] R. Umetsu, N. Endo, A. Fujita, R. Kainuma, A. Sakuma, K. Fukamichi, and K. Ishida. "Electronic specific heat coefficient and magnetic properties of L21 phase in Co2YGa (Y= Cr, Mn and Fe) Heusler alloys". In: *Journal of Physics: Conference Series*. Vol. 200. 6. IOP Publishing. 2010, 062036.

[242] T. Graf, G. H. Fecher, J. Barth, J. Winterlik, and C. Felser. "Electronic structure and transport properties of the Heusler compound Co2TiAl". *Journal of Physics D: Applied Physics* 42 (8) 2009, 084003.

[243] S. Rodan. "Nuclear magnetic resonance and specifc heat studies of half-metallic ferromagnetic Heusler compounds". PhD thesis. Technische Universität Dresden, Submitted.

[244] K. Wong, E. Wohlfarth, and D. Hum. "Density of states and effective electron interaction in hexagonal cobalt". *Physics Letters A* 29 (8) 1969, 452–453.

[245] C. Park, B. Lee, and J. Lee. "Spin-asymmetry of the density of states for bulk and surface Fe, Co, and Ni". *Journal of the Korean Physical Society* 47 (4) 2005, 655–665.

[246] V. A. de la Pena O'Shea, I. de PR Moreira, A. Roldan, and F. Illas. "Electronic and magnetic structure of bulk cobalt: The alpha, beta, and epsilon-phases from density functional theory calculations". *The Journal of Chemical Physics* 133 (2) 2010, 024701.

[247] N. Tezuka, N. Ikeda, A. Miyazaki, S. Sugimoto, M. Kikuchi, and K. Inomata. "Tunnel magnetoresistance for junctions with epitaxial full-Heusler Co2FeAl0.5Si0.5 electrodes with B2 and L21 structures". *Applied Physics Letters* 89 (11) 2006, 112514–112514.

[248] N. Tezuka, N. Ikeda, S. Sugimoto, and K. Inomata. "175 percent tunnel magnetoresistance at room temperature and high thermal stability using Co2FeAl0.5Si0.5 full-Heusler alloy electrodes". *Applied Physics Letters* 89 (25) 2006, 252508–252508.

[249] W. Wang, H. Sukegawa, R. Shan, and K. Inomata. "Large tunnel magnetoresistance in Co2FeAl0.5Si0.5/ MgO/Co2FeAl0.5Si0.5 magnetic tunnel junctions prepared on thermally oxidized Si substrates with MgO buffer". *Applied Physics Letters* 93 (18) 2008, 182504–182504.

[250] N. Tezuka, N. Ikeda, S. Sugimoto, and K. Inomata. "Giant tunnel magnetoresistance at room temperature for junctions using full-Heusler Co2FeAl0.5Si0.5 electrodes". *Japanese Journal of Applied Physics* 46 (5L) 2007, L454.

[251] R. Shan, H. Sukegawa, W. Wang, M. Kodzuka, T. Furubayashi, T. Ohkubo, S. Mitani, K. Inomata, and K. Hono. "Demonstration of half-metallicity in fermi-level-tuned Heusler alloy Co2FeAl0.5Si0.5 at room temperature". *Physical Review Letters* 102 (24) 2009, 246601.

[252] N. Tezuka. "New materials research for high spin polarized current". *Journal of Magnetism and Magnetic Materials* 324 (21) 2012, 3588–3592.

[253] K. Inomata, M. Wojcik, E. Jedryka, N. Ikeda, and N. Tezuka. "Site disorder in Co2Fe(Al,Si) Heusler alloys and its influence on junction tunnel magnetoresistance". *Physical Review B* 77 (21) 2008, 214425.

[254] S. Trudel, G. Wolf, J. Hamrle, B. Hillebrands, P. Klaer, M. Kallmayer, H.-J. Elmers, H. Sukegawa, W. Wang, and K. Inomata. "Effect of annealing on Co2FeAl0.5Si0.5 thin films: A magneto-optical and x-ray absorption study". *Physical Review B* 83 (10) 2011, 104412.

[255] T. Chatterji, ed. *Neutron Scattering from Magnetic Materials*. Elsevier Science, 2005.

[256] I. Ohnuma, H. Enoki, O. Ikeda, R. Kainuma, H. Ohtani, B. Sundman, and K. Ishida. "Phase equilibria in the Fe–Co binary system". *Acta Materialia* 50 (2) 2002, 379–393.

[257] B. Sundman, I. Ohnuma, N. Dupin, U. R. Kattner, and S. G. Fries. "An assessment of the entire Al–Fe system including D03 ordering". *Acta Materialia* 57 (10) 2009, 2896–2908.

[258] T. Degen, M. Sadki, E. Bron, U. König, and G. Nénert. "The HighScore suite". *Powder Diffraction* 29 (S2) 2014, S13–S18.

[259] G. Will. *Powder diffraction: The Rietveld method and the two stage method to determine and refine crystal structures from powder diffraction data*. Springer Science & Business Media, 2006.

[260] E. J. Mittemeijer and U. Welzel. "The "state of the art" of the diffraction analysis of crystallite size and lattice strain". *Zeitschrift für Kristallographie International journal for structural, physical, and chemical aspects of crystalline materials.* 223 (9) 2008, 552–560.

[261] M. Marcinkowski and N. Brown. "Direct observation of antiphase boundaries in the Fe3Al superlattice". *Journal of Applied Physics* 33 (2) 1962, 537–552.

[262] R. Fisher and M. Marcinkowski. "Direct observation of antiphase boundaries in the AuCu3 superlattice". *Philosophical Magazine* 6 (71) 1961, 1385–1405.

[263] U. Prakash, R. Buckley, and H. Jones. "Formation of B2 antiphase domains in rapidly solidified Fe-Al alloys". *Philosophical Magazine A* 64 (4) 1991, 797–805.

[264] J. Perez, P. Shang, D. Morris, and I. Jones. "The structure, thickness and chemistry of antiphase domain boundaries in heat-treated, rapidly solidified Ni3Al". *Philosophical Magazine A* 79 (1) 1999, 179–192.

[265] P. Swann, W. Duff, and R. Fisher. "The electron metallography of ordering reactions in Fe-Al alloys". *Metallurgical Transactions* 3 (2) 1972, 413–423.

[266] B. Prasad. "Theory of X-ray diffraction from stacking faults and antiphase domain boundaries in the DO19-type ordered hcp structures". *Acta Crystallographica Section A: Crystal Physics, Diffraction, Theoretical and General Crystallography* 31 (2) 1975, 240–245.

[267] M. Yamaguchi and Y. Umakoshi. "The deformation behaviour of intermetallic superlattice compounds". *Progress in Materials Science* 34 (1) 1990, 1–148.

[268] P. Ghosal. "Diffraction effects on antiphase boundaries in ordered structures: An overview". In: *Advanced X-ray Techniques in Research and Industry*. Ed. by A. Singh and I. Defence Metallurgical Research Laboratory Hyderabad. IOS Press, 2005.

[269] R. W. Cheary and R. Squadrito. "Electron and X-ray diffraction from antiphase domains in the barium magnesium hollandite Ba1.33Mg1.33Ti6.67O16". *Acta Crystallographica Section A: Foundations of Crystallography* 48 (1) 1992, 15–27.

[270] P. Önnerud, Y. Andersson, R. Tellgren, P. Nordblad, F. Bourée, and G. André. "The crystal and magnetic structures of ordered cubic Pd3MnD0.7". *Solid State Communications* 101 (6) 1997, 433–437.

[271] R. Cheary and N. Grimes. "Investigation of antiphase domains in lithium ferrite by analysis of the broadened X-ray lines". *Acta Crystallographica Section A: Crystal Physics, Diffraction, Theoretical and General Crystallography* 34 (1) 1978, 74–84.

[272] T. Kamiyama, T. Shinohara, S. Tomiyoshi, Y. Minonishi, H. Yamamoto, H. Asano, and N. Watanabe. "Effect of deformation on Pd2MnSn Heusler alloy studied with transmission electron microscopy, profile analysis of neutron powder diffraction pattern, and magnetization measurement". *Journal of Applied Physics* 68 (9) 1990, 4741–4750.

[273] B. Warren. *X-ray diffraction*. Addison-Wesley series in metallurgy and materials engineering. Dover Publications, 1969.

[274] W. David. "Powder diffraction: least-squares and beyond". *Journal of Research of the National Institute of Standards and Technology* 109 (1) 2004, 107.

[275] J. Cahn and S. Allen. "A microscopic theory for domain wall motion and its experimental verification in Fe-Al alloy domain growth kinetics". *Le Journal de Physique Colloques* 38 (C7) 1977, C7–51.

[276] S. M. Allen and J. W. Cahn. "A microscopic theory for antiphase boundary motion and its application to antiphase domain coarsening". *Acta Metallurgica* 27 (6) 1979, 1085–1095.

[277] J. Cahn. "Antiphase domain growth in Cu3Au". *Scripta Metallurgica* 14 (1) 1980, 93–94.

[278] D. Mikkola and K. Rundman. "The kinetics of ordering and antiphase domain growth vs. the kinetics of spinodal decomposition and coarsening". *Scripta Metallurgica* 6 (11) 1972, 1095–1098.

[279] H. Ishikawa, R. Umetsu, K. Kobayashi, A. Fujita, R. Kainuma, and K. Ishida. "Atomic ordering and magnetic properties in Ni2Mn(GaxAl1-x) Heusler alloys". *Acta Materialia* 56 (17) 2008, 4789–4797.

[280] S. Cupschalk and N. Brown. "Kinetics of antiphase domain growth". *Acta Metallurgica* 16 (5) 1968, 657–666.

[281] F. Livet, F. Bley, J.-P. Simon, R. Caudron, J. Mainville, M. Sutton, and D. Lebolloc'h. "Statics and kinetics of the ordering transition in the AuAgZn 2 alloy". *Physical Review B* 66 (13) 2002, 134108.

[282] C. Abromeit and S. Matsumura. "Kinetics of antiphase domain boundaries during an L12 order-disorder phase transformation: A Monte Carlo simulation". *Philosophical Magazine A* 82 (11) 2002, 2287–2302.

[283] A. Ardell, N. Mardesich, and C. Wagner. "Antiphase domain growth in Cu3Au: Quantitative comparison between theory and experiment". *Acta Metallurgica* 27 (7) 1979, 1261–1269.

[284] R. Cahn. "The place of atomic order in the physics of solids and in metallurgy". In: *Physics of New Materials*. Ed. by F. Fujita. Vol. 27. Springer Series in Materials Science. Springer Berlin Heidelberg, 1994, 179–225.

[285] C. Liu, R. Cahn, and G. Sauthoff. *Ordered Intermetallics: Physical Metallurgy and Mechanical Behaviour*. Nato Science Series E: Springer Netherlands, 2012.

[286] R. Gilles, M. Hofmann, Y. Gao, F. Johnson, L. Iorio, M. Larsen, F. Liang, M. Hoelzel, and B. Barbier. "Probing the relationship of long-range order in nanodomain FeCo alloys with ternary additions using neutron diffraction". *Metallurgical and Materials Transactions A* 41 (5) 2010, 1144–1150.

[287] M. Zhang, K. Yang, Z. Chen, Y. Wang, and X. Fan. "Microscopic phase-field study on order-disorder transition of the antiphase domain boundary formed between L12 phases". *Science China Technological Sciences* 54 (12) 2011, 3409–3414.

[288] M. Porta, C. Frontera, E. Vives, and T. Castán. "Effect of the vacancy interaction on antiphase domain growth in a two-dimensional binary alloy". *Physical Review B* 56 (9) 1997, 5261.

[289] C. Frontera, E. Vives, and A. Planes. "Antiphase domain growth in BCC metallic alloys via vacancies". *Zeitschrift für Physik B Condensed Matter* 96 (1) 1994, 79–86.

[290] E. Vives and A. Planes. "Kinetics of a vacancy-driven order-disorder transition in a two-dimensional binary alloy". *Physical Review Letters* 68 (6) 1992, 812.

[291] A. Y. Volkov, V. Baraz, O. Novikova, and E. Polovnikova. "Kinetics of the disorder-order transformation in the Cu-47 at. % Pd alloy". *Russian Physics Journal* 55 (11) 2013, 1258–1265.

[292] J. Soltys and R. Kozubski. "A simple model of the order—disorder phase transitions in ternary alloys and its application to several selected Heusler alloys". *physica status solidi (a)* 63 (1) 1981, 35–44.

[293] R. McCormack, D. De Fontaine, and J. Hoyt. "Order-disorder transformations in the heusler alloy Cd2AgAu". *Journal of Phase Equilibria* 18 (6) 1997, 580–587.

[294] R. McCormack and D. De Fontaine. "First-principles study of multiple order-disorder transitions in Cd2AgAu Heusler alloys". *Physical Review B* 54 (14) 1996, 9746.

[295] Y. Murakami, Y. Watanabe, and S. Kachi. "Kinetics of the Heusler-type ordering in AuAgZn2 Alloy". *Transactions of the Japan Institute of Metals* 21 (11) 1980, 714–720.

[296] Y. Murakami. "Kinetics of order-disorder transformations in the heusler AuAgZn2 alloy". *Acta Metallurgica* 33 (2) 1985, 167–174.

[297] B. Peters, A. Alfonsov, C. Blum, S. J. Hageman, P. Woodward, S. Wurmehl, B. Büchner, and F. Yang. "Epitaxial films of Heusler compound Co2FeAl0.5Si0.5 with high crystalline quality grown by off-axis sputtering". *Applied Physics Letters* 103 (16) 2013, 162404.

[298] M. Emmel, A. Alfonsov, D. Legut, A. Kehlberger, E. Vilanova, I. Krug, D. Gottlob, M. Belesi, B. Büchner, M. Kläui, P. Oppeneer, S. Wurmehl, H. Elmers, and G. Jakob. "Electronic properties of Co2FeSi investigated by X-ray magnetic linear dichroism". *Journal of Magnetism and Magnetic Materials* 368 (0) 2014, 364 –373.

[299] H. Zijlstra. "Coping with Brown's paradox: The pinning and nucleation of magnetic domain walls at antiphase boundaries". *IEEE Transactions on Magnetics* 15 (5) 1979, 1246–1250.

[300] T. Asaka, X. Yu, Y. Tomioka, Y. Kaneko, T. Nagai, K. Kimoto, K. Ishizuka, Y. Tokura, and Y. Matsui. "Strong pinning effect and magnetic nanodomain formation by coupling between magnetic and crystallographic domains in the ordered double perovskite Ba2FeMoO6". *Physical Review B* 75 (18) 2007, 184440.

[301]   A. Lapworth and J. Jakubovics. "Effect of antiphase boundaries on the magnetic properties of Cu-Mn-Al Heusler alloys". *Philosophical Magazine* 29 (2) 1974, 253–273.

[302]   Y. Murakami, D. Shindo, K. Kobayashi, K. Oikawa, R. Kainuma, and K. Ishida. "TEM studies of crystallographic and magnetic microstructures in Ni-based ferromagnetic shape memory alloys". *Materials Science and Engineering: A* 438 2006, 1050–1053.

[303]   Y. Murakami, D. Shindo, K. Oikawa, R. Kainuma, and K. Ishida. "Magnetic domain structure in a ferromagnetic shape memory alloy Ni51Fe22Ga27 studied by electron holography and Lorentz microscopy". *Applied Physics Letters* 82 (21) 2003, 3695–3697.

[304]   T. Yano, Y. Murakami, R. Kainuma, and D. Shindo. "Interaction between magnetic domain walls and antiphase boundaries in Ni2Mn(Al,Ga) studied by electron holography and Lorentz microscopy". *Materials Transactions* 48 (10) 2007, 2636.

[305]   Y. Murakami, K. Yanagisawa, K. Niitsu, H. Park, T. Matsuda, R. Kainuma, D. Shindo, and A. Tonomura. "Determination of magnetic flux density at the nanometer-scale antiphase boundary in Heusler alloy Ni50Mn25Al12.5Ga12.5". *Acta Materialia* 61 (6) 2013, 2095–2101.

[306]   C. Frontera and J. Fontcuberta. "Configurational disorder and magnetism in double perovskites: A Monte Carlo simulation study". *Physical Review B* 69 1 2004, 014406.

[307]   A. S. Ogale, S. Ogale, R. Ramesh, and T. Venkatesan. "Octahedral cation site disorder effects on magnetization in double-perovskite Sr2FeMoO6: Monte Carlo simulation study". *Applied Physics Letters* 75 (4) 1999, 537–539.

[308]   R. Nicholson. "Quenching defects in solid solutions and their effect on precipitation". *Le Journal De Physique et Le Radium* 23 (10) 1962, 824–827.

[309]   T. Ozawa. "A critique on the analysis of DSC and DTA curves". *Netsusokutei* 4 (2) 1977, 45–51.

[310]   Y. Janssen, M. Angst, K. Dennis, R. McCallum, and P. Canfield. "Differential thermal analysis and solution growth of intermetallic compounds". *Journal of Crystal Growth* 285 (4) 2005, 670–680.

[311]   M. E. Brown. *Introduction to thermal analysis: techniques and applications.* Vol. 1. Springer Science & Business Media, 2001.

[312]   P. Holba and J. Sesták. "Heat inertia and its role in thermal analysis". *Journal of Thermal Analysis and Calorimetry* 2015, 1–5.

[313]   J. Sesták and P. Holba. "Heat inertia and temperature gradient in the treatment of DTA peaks". *Journal of Thermal Analysis and Calorimetry* 113 (3) 2013, 1633–1643.

[314]   E. Macho, J. Llopis, A. Remón, C. Ballesteros, and J. Piqueras. "Optical study of defects in quenched MgO crystals". *physica status solidi (a)* 82 (1) 1984, 111–117.

[315]   R. Maddin and A. Cottrell. "LXXXIII. Quench hardening in aluminium single crystals". *The London, Edinburgh, and Dublin Philosophical Magazine and Journal of Science* 46 (378) 1955, 735–743.

[316]   I. Johnston, P. Dobson, and R. Smallman. "The effect of multiple quenching on the stability and growth of defect tetrahedra: Correspondence". *Philosophical Magazine* 17 (150) 1968, 1289–1293.

[317]   A. Khellaf, A. Seeger, and R. M. Emrick. "Ultra-high purity metals. II. Quenching studies of lattice vacancies in high-purity aluminium". *Materials Transactions* 43 (2) 2002, 186–198.

[318] M. Kogachi, T. Fujiwara, and S. Kikuchi. "Atomic disorder and magnetic property in Co-based Heusler alloys Co2MnZ (Z= Si, Ge, Sn)". *Journal of Alloys and Compounds* 475 (1) 2009, 723–729.

[319] R. Gilles, M. Hofmann, F. Johnson, Y. Gao, D. Mukherji, C. Hugenschmidt, and P. Pikart. "Analysis of antiphase domain growth in ternary FeCo alloys after different cooling rates and annealing treatments using neutron diffraction and positron annihilation". *Journal of Alloys and Compounds* 509 (2) 2011, 195–199.

[320] P. Webster and R. Tebble. "The magnetic and chemical ordering of the heusler alloys Pd2MnIn, Pd2MnSn and Pd2MnSb". *Philosophical Magazine* 16 (140) 1967, 347–361.

[321] R. Kimura, K. Endo, and T. Ohoyama. "A partially ordered structure of the Heusler alloy Cu2MnAl at high temperature". *Journal of the Physical Society of Japan* 17 1962, 723.

[322] R. Kimura, T. Ohoyama, and K. Endo. "On the decomposition of the ferromagnetic phase of the Heusler alloy, Cu2MnAl". *Journal of the Physical Society of Japan* 16 1961, 1266.

List of Figures

List of Tables

Publications

- **A. Omar**, M. Dimitrakopoulou, C. Blum, H. Wendrock, S. Rodan, S. Hampel, W. Löser, B. Büchner, and S. Wurmehl. "Phase dynamics and growth of $Co_2Cr_{1-x}Fe_xAl$ Heusler compounds: A key to understand their anomalous physical properties". *Crystal Growth & Design* 13 (9) **2013**, 3925–3934.

- **A. Omar**, C. G. Blum, W. Löser, B. Büchner, and S. Wurmehl. "Effect of annealing on spinodally decomposed Co_2CrAl grown via floating zone technique". *Journal of Crystal Growth* 401 **2014**, 617–621.

Acknowledgements

growth lab at IFW Dresden. I also thank Gesine Kreutzer, Dina Lohse, Tina Sturm for their technical assistance. I sincerely thank Kerstin Höllerer, Katja Schmiedel and Manja Maluck for all the administrative help and guidance that they so kindly provided. I also thank Dr. Uwe Hinz for his timely help and suggestions. I thank everyone at IFW Dresden for the cooperation, help and the nice working environment.

I am indebted to so many people for an unforgettable experience in Germany. I thank all the members of the crystal growth group at IFW Dresden especially, Sabine, Christian, Markus, Hannes, Franzi, Rhea, Sai,, Biene, Alexey and Michael, for a great time both at work and outside. Special thanks go to Markus and Ellen, and the lovely Cäcelie and Odelie, for their warmth, kindness and hospitality, making me feel at home in Germany. I thank Ashwin and Gayatri for the late-night discussions, cooking sessions, creative collaborations, great experiences and an amazing time. I also thank Steve and Jaena for the fun times at tea and lunch, great memories, and the many new experiences. Many thanks to Prashanth, Raghu and Vamshi for their camaraderie. To Ruchi, Haritha, Nida, Vasanth, Osama and Abhishek, even though you all are far away, I am grateful to have you all in my life. I also thank Shreya and Tushar for the great company and the homely atmosphere outside work. I also thank Amartya, Mira, Parthi, Shiv, Supriyo, Pranab, and Anamika as well as everyone else at IFW and outside, for all the nice memories.

Finally, to my dear parents, who have been my constant source of support, encouragement, guidance, motivation and love, for you no words can suffice. This is to you. To my dear elder brother, sister-in-law, Ozair, and the beautiful Alia, thank you from the bottom of my heart for all the love, guidance and support. You have made it worthwhile.

Thanks to all the friends and family, of near and far, for being a part of this journey.

Dankeschön!

An ode to PhD

The nuclei with spins
Or martensitic twins
Without a single crystal
Would there be any win

This vast Heusler family
$L2_1$, cubic, ternary,
Everyone makes samples
Arc-melting, like alchemy

Though thou are magnetic
Please half be metallic
Like diamonds we polish
Structures like magic

Orient with the laue
Much fun with xray
But samples will only be
As thermodynamics say

Phases at boundary
And disorders many
$A2$, $B2$, some DO_3
Or spinodal, may even be?

So many ways of imaging
Of quenching post aging
In neutrons annealing
That swiss of a feeling

On the zone that is floating
That oxide of a coating
Some Slater some Pauling
In search of my calling

A lot has been learnt and lot was to see
Great times I had in this beautiful city

Much thanks to all, and coffee and tea
Has come to an end finally, my PhD

Erklärung

Hiermit versichere ich, dass ich die vorliegende Arbeit ohne unzulässige Hilfe Dritter und ohne Benutzung anderer als der angegebenen Hilfsmittel angefertigt habe. Die aus fremden Quellen direkt oder indirekt übernommenen Gedanken sind als solche kenntlich gemacht. Die Arbeit wurde bisher weder im Inland noch im Ausland in gleicher oder ähnlicher Form einer anderen Prüfungsbehörde vorgelegt.

Diese Arbeit wurde unter Betreuung von Prof. Dr. Bernd Büchner am Institut für Festkörperforschung (IFF) des Institutes für Festkörper- und Werkstoffforschung Dresden e.V. (IFW Dresden) angefertigt. Es haben keine früheren erfolglosen Promotionsverfahren stattgefunden.

Ich erkenne hiermit die Promotionsordnung der Fakultät Mathematik und Naturwissenschaften der Technischen Universität Dresden vom 23.02.2011 an.

Ahmad Omar

Dresden, September 2015